Fabrication, Mechanical Characterization, and Modeling of 3D Architected Materials upon Static and Dynamic Loading

Thesis by
Carlos M. Portela

In Partial Fulfillment of the Requirements for the
Degree of
Doctor of Philosophy

CALIFORNIA INSTITUTE OF TECHNOLOGY
Pasadena, California

2019
Defended May 16, 2019

Carlos M. Portela
ORCID: 0000-0002-2649-4235

ACKNOWLEDGEMENTS

I am honored to have been part of this remarkable institution. Besides providing me with unique opportunities and resources, it allowed me to learn from and interact with leading researchers in a variety of fields. My time at Caltech was pivotal in forming the person I am today, and I am forever grateful for that.

My deepest gratitude goes to my advisors Professors Julia R. Greer and Dennis M. Kochmann for their unparalleled support, guidance, and patience throughout these five years at Caltech. I am grateful for the freedom they entrusted me with, which enabled me to explore a wide range of interesting topics, and for constantly encouraging me to become a better colleague, leader, and researcher. Julia's infinite passion for science and open-mindedness will continue to inspire me for decades to come. I am lucky to have been able to learn from Dennis' deep knowledge of mechanics and his meticulous approaches, and I am thankful for my time working with him at ETH Zürich.

I would like to also thank my thesis committee members Professors Chiara Daraio and Guruswami Ravichandran for their kind advice and generous time throughout the last years of my graduate studies. Their ideas and feedback encouraged me to venture into fields that were previously unknown to me and helped me grow as a researcher. Additionally, I would like to thank Professor Sergio Pellegrino for his guidance and mentorship throughout my graduate studies; I truly enjoyed his lectures and appreciated his perspective on the topics I was studying.

I am also thankful to Professor Andrea M. Hodge, who believed in me when I was a young undergraduate engineering student and encouraged me to apply to graduate school. My Caltech experience would not have been the same without the friendship and advice from Gregory P. Phlipot and William J. Schill; two remarkable researchers I had the pleasure of working with and learning from during my time here. None of this work would have been possible without my outstanding Greer Group colleagues. To name a few, I would like to thank Professor Lucas R. Meza and Dr. Ottman Tertuliano for serving as my mentors during my first few years, Daryl W. Yee and Bryce W. Edwards for being great friends and office mates, and Andrey Vyatskikh, Xiaoxing Xia, and Widianto P. Moestopo for being great collaborators. I would also like to acknowledge the financial support from the Office of Naval Research (ONR) throughout most of my graduate studies.

Lastly, I would like to thank my girlfriend Jenny, my sisters (María del Mar, María Alexandra, and María Camila), and especially my parents Carlos A. and Gloria E. for always being there for me throughout my graduate studies. They encouraged me to pursue my dreams and continuously motivated me to put in the work that made all of this possible. For their unconditional love and unwavering support, I am forever indebted to them.

Carlos M. Portela
June 4, 2019
Pasadena, CA

ABSTRACT

Architected materials have been ubiquitous in nature, enabling unique properties that are unachievable by monolithic, homogeneous materials. Inspired by natural processes, man-made three-dimensional (3D) architected materials have been reported to enable novel mechanical properties such as high stiffness- and strength-to-density ratios, extreme resilience, or high energy absorption. Furthermore, advanced fabrication techniques have enabled architected materials with feature sizes at the nanometer-scale, which exploit material size effects to approach theoretical bounds. However, most architected materials have relied on symmetry, periodicity, and lack of defects to achieve the desired mechanical response, resulting in sub-optimal mechanical response under the presence of inevitable defects. Additionally, most of these nano- and micro-architected materials have only been studied in the static regime, leaving the dynamic parameter space unexplored.

In this work, we address these issues by: (*i*) proposing numerical and theoretical tools that predict the behavior of architected materials with non-ideal geometries, (*ii*) presenting a pathway for scalable fabrication of tunable nano-architected materials, and (*iii*) exploring the response of nano- and micro-architected materials under three types of dynamic loading. We first explore lattice architectures with features at the micro- and millimeter scales and provide an extension to the classical stiffness scaling laws, enabled by reduced-order numerical models and experiments at both scales. After discussing the effect of nodes (i.e., junctions) on the mechanical response of lattice architectures, we propose alternative node-less geometries that eliminate the stress concentrations associated with nodes to provide extreme resilience. Using natural processes such as spinodal decomposition, we present pathways to fabricate a version of these materials with samples sizes on the order of cubic centimeters while achieving feature sizes on the order of tens of nanometers. In the dynamic regime, we design, fabricate, and test micro-architected materials with tunable vibrational band gaps through the use of architectural reconfiguration and local resonance. Lastly, we present methods to fabricate carbon-based materials at the nano- and centimeter scales and test them under supersonic impact and blast conditions, respectively. Our work provides explorations into pathways that could enable the use of nano- and micro-architected materials for applications that go beyond small-volume, quasi-static mechanical regimes.

PUBLISHED CONTENT AND CONTRIBUTIONS

CHAPTER 2 has been adapted from:

1) L.R. Meza, G.P. Phlipot, C.M. Portela, A. Maggi, L.C. Montemayor, A. Comella, D.M. Kochmann & J.R. Greer. "Reexamining the mechanical property space of three-dimensional lattice architectures". *Acta Materialia* (2017) 140, pp. 424–432. DOI: 10.1016/j.actamat.2017.08.052.
CONTRIBUTIONS: fabricated a portion of the samples, conducted a portion of the experiments and analyzed the data, performed a portion of the computational analysis, and participated in the writing of the manuscript.

CHAPTER 3 has been adapted from:

2) C.M. Portela, J.R. Greer & D.M. Kochmann. "Impact of node geometry on the effective stiffness of non-slender three-dimensional truss lattice architectures". *Extreme Mechanics Letters* (2018) 22, pp. 110–138. DOI: 10.1016/j.eml.2018.06.004.
CONTRIBUTIONS: designed and fabricated samples, performed and analyzed the experiments, performed the computational analysis, and wrote the manuscript.

CHAPTER 4 has been adapted, in part, from:

3) N.G. Dou, R.A. Jagt, C.M. Portela, J.R. Greer & A.J. Minnich. "Ultralow Thermal Conductivity and Mechanical Resilience of Architected Nanolattices". *Nano Letters* (2018) 18, 8 pp. 4755–4761. DOI: 10.1021/acs.nanolett.8b01191.
CONTRIBUTIONS: performed mechanical experiments and analyzed the data, performed the computational analysis, and participated in the writing of the manuscript.

and from:

4) C.M. Portela, A. Vidyasagar[†], S. Krödel[†], T. Weissenbach, D.Y. Yee, J.R. Greer & D.M Kochmann. "Extreme mechanical resilience of self-assembled nanolabyrithine materials". *Under Review* (2020)
CONTRIBUTIONS: fabricated samples, performed mechanical experiments and analyzed the data, performed the computational analysis, and wrote the manuscript.

Chapter 5 has been adapted, in part, from:

5) X. Xia, A. Afshar, H. Yang, C.M. Portela, D.M. Kochmann, C.V. Di Leo & J.R. Greer. "Electrochemically Reconfigurable Architected Materials". *Nature* (2019) 573, 7773 pp. 205–213. DOI: 10.1038/s41586-019-1538-z.
Contributions: computed the numerical dispersion relations and participated in the writing of the manuscript.

Chapter 6 has been adapted from:

6) C.M. Portela, A. Vyatskikh & J.R. Greer. "Fabrication and Design of Composites with Architected Layers". *U.S. Patent Application No. 16/206,163 and PCT International Patent Application No. PCT/US18/63306* (November 30, 2018)
Contributions: participated in the conception and design of the project, fabricated samples, performed mechanical tests and analyzed the data, and participated in the writing of the application.

7) C.M. Portela, B.W. Edwards, D. Veysset, Y. Sun, K. Nelson, D.M. Kochmann & J.R. Greer. "Supersonic Impact on Nano-architected Carbon Materials". *In Preparation* (2020)
Contributions: participated in the conception and design of the project, designed and fabricated samples, participated in the mechanical testing and analyzed the data, and wrote the manuscript.

Not directly adapted in this thesis:

8) A. Vyatskikh, S. Delalande, A. Kudo, X. Zhang, C.M. Portela & J.R. Greer. "Additive manufacturing of 3D nano-architected metals". *Nature Communications* (2018) 9, 1 pp. 593. DOI: 10.1038/s41467-018-03071-9.
Contributions: partially performed nanomechanical tests and analyzed the data.

9) L.A. Shaw, F. Sun, C.M. Portela, R.I. Barranco, J.R. Greer & J.B. Hopkins. "Computationally efficient design of directionally compliant metamaterials". *Nature Communications* (2019) 10, 1 pp. 291. DOI: 10.1038/s41467-018-08049-1.
Contributions: fabricated micro-scale samples, performed nanomechanical tests and analyzed the data, performed the mechanical numerical analysis, and participated in the writing of the manuscript.

10) C.M. Portela, G.P. Phlipot, J.R. Greer & D.M. Kochmann. " Approaches for Efficient Modeling of the Mechanical Response of Complex Periodic Truss Architectures". *SAMPE Technical Paper* (2019). DOI: 10.33599/nasampe/s.19.1428.

CONTRIBUTIONS: performed experiments and analyzed the data, performed part of the numerical analysis, wrote the manuscript.

TABLE OF CONTENTS

LIST OF ILLUSTRATIONS

LIST OF TABLES

NOMENCLATURE

E_s. *Constituent material's Young's modulus* — Young's modulus of the material that makes up the architected material.

σ_{ys}. *Constituent material's strength* — Strength of the material that makes up the architected material.

$\overline{\rho}$. *Relative density* — A dimensionless parameter representing the fill fraction in a unit cell, or more generally, the ratio between the density of an architected material ρ and that of the constituent material ρ_s.

E^*. *Effective Young's modulus* — serves as an estimate of a material's actual Young's modulus E, i.e., a measure of stiffness for a finite volume of a material.

σ_y^*. *Effective strength* — serves as an estimate of a material's actual yield/failure strength σ_y, i.e., a measure of strength for a finite volume of a material.

Chapter 1

INTRODUCTION TO ARCHITECTED MATERIALS

1.1 The Concept of Architected Materials

Almost all engineering applications, ranging from the aerospace to the biomedical field, require precise control of material properties to enable a particular performance for any given machine, structure, or device. Prior to the last two centuries, humankind was limited to using readily available or engineered monolithic materials such as stone, wood[1], and metal alloys to fabricate tools or structures. While this proved to be satisfactory for a few millennia, it resulted in overly heavy and inefficient structures such as the pyramids of Giza.

Throughout the last ~100+ years, the concept of structural architecture enabled the construction of significantly more efficient designs, epitomized by the Eiffel tower. Although a significant advancement for mankind, the material choices then were still limited to readily available materials including stiff but heavy metals such as iron or steel. Plotting the properties of all known monolithic materials, such as Young's modulus (i.e., the stiffness) versus the density brings to light a significant void in this parameter space corresponding to lightweight-but-stiff materials (Fig. 1.2). The efficient design of the Eiffel tower does not qualify to reach into that void, since the discrete nature of its struts and arches is evident to the naked eye, exemplifying an architected *structure* instead of an architected *material*.

To understand this important distinction between an architected structure and an architected material, we need to consider not only the length scale l of the effective "building blocks", but also that of the overall structure or fields of interest (i.e., stresses, strains, and deformation), L. To be able to call a given structure a *material*, we require the scale of structural features to be orders of magnitude smaller than the characteristic length over which the fields of interest vary, i.e.,

$$\epsilon = \frac{l}{L} \ll 1, \tag{1.1}$$

such that we can assume a proper *separation of scales*. This implies that making man-made architected materials requires the miniaturization of this concept of architected structures, to the point that the discrete features of a given material cannot

[1] Although wood is inherently not monolithic if analyzed at the microscale, most of its applications do not benefit from this architected nature.

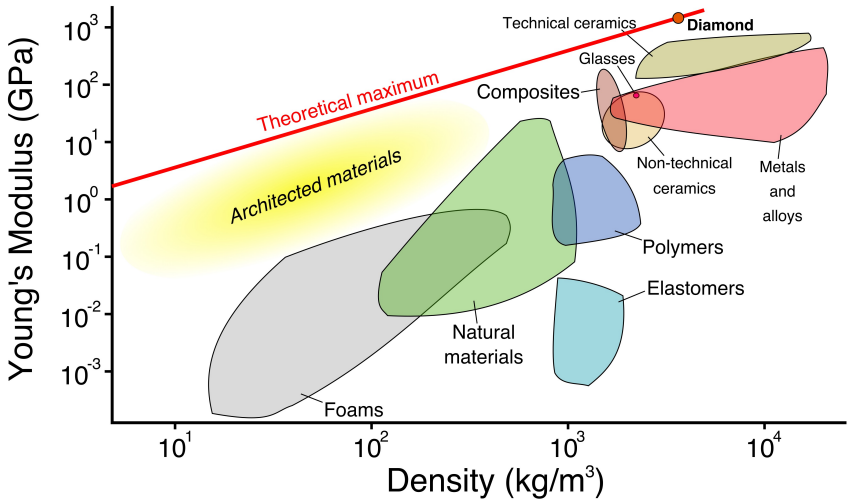

FIGURE 1.1 | STIFFNESS VS. DENSITY IN GENERAL MATERIAL CLASSES

be discerned or are sufficiently small compared to the applied boundary conditions (i.e., loads or displacements).

1.2 Natural Architected Materials

Architected materials have been ubiquitous in nature, enabling unique properties that are unachievable by monolithic, homogeneous materials. An example of these are the spicules in *Euplectella aspergillum* sea sponges [96] or nacre [6], which utilize structural hierarchy to attain strength and toughness values superior to those of their constituent ceramics. Another example of hierarchy that spans several order of magnitude in scale is that of human bone [98, 131, 142], which uses mechanisms at scales ranging from the mm-diameter of trabeculae to the nm-diameter of fibrils that make up the lamellae within a single trabecula. All of these natural materials portray orders-of-magnitude separation of scales, which is key to enabling their unique properties.

Although not strictly classifiable as architected materials, the atomic lattices that make up the crystalline structure of most metals are directly relatable to their mechanical properties such as their anisotropy (i.e., direction-dependent properties) or plasticity (i.e., inelastic flow). These lattices, along with the microstructures found in nacre and bone, have served as inspiration for a new age of nature-inspired and biomimetic man-made architected materials [38, 40, 111]. Atomic-lattice inspired materials, in particular, present a lightweight design approach which will be discussed in this thesis.

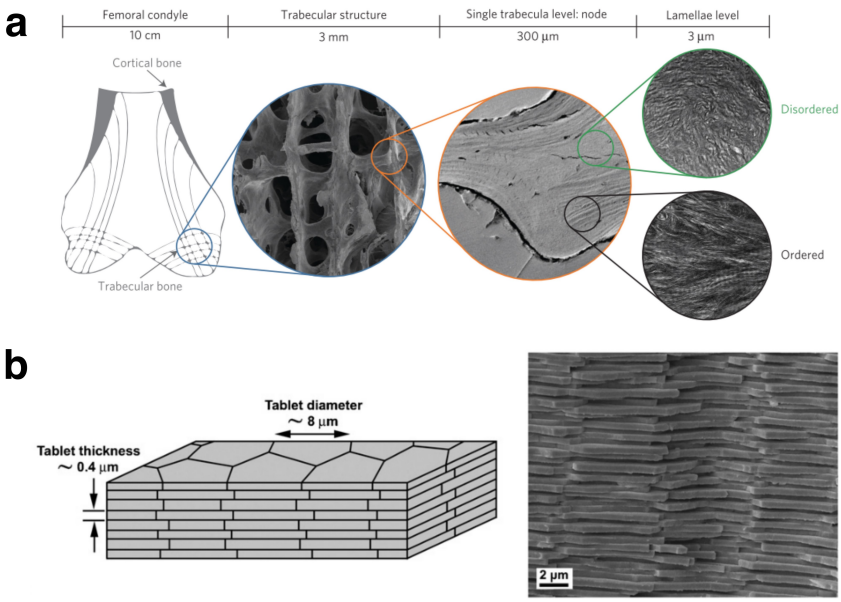

FIGURE 1.2 | ARCHITECTURE IN BONE AND NACRE
(a) Hierarchical microstructure of human bone, reprinted by permission from Springer Nature: Nature Materials, Tertuliano and Greer [131] ©(2016), and **(b)** schematic and micrograph of microstructure in nacre, reprinted from the Journal of the Mechanics and Physics of Solids, 55, Barthelat et al. [6], 306–337 ©(2007), with permission from Elsevier.

1.3 Cellular Solids

The most commonly available man-made architected materials, foams, can be categorized as a form of a cellular solid. In its essence, a cellular solid is composed of a network of struts, plates, or shells that make up a cell, which is then tessellated in two dimensions or three dimensions (i.e., 2D or 3D) to make up the overall material. Taking a statistically significant number of cells as the representative volume element (RVE), cellular solids can be characterized based on their strut connectivity or number of faces and edges (if they are open or closed cells, respectively) as well as the volume of solid material in each cell. Taking the ratio between the volumes of solid material and that of a box encompassing each cell, gives rise to the concept of relative density $\overline{\rho}$, which is a measure of the fill fraction. As we will see throughout this thesis, this measure of relative density can sometimes (not always) be related to a specific mechanical response of the material. The constituent material properties that make up these foams are equally important in predicting the response, since they can range from stiff and brittle in ceramic foams, to compliant and ductile in polymeric foams.

Although the notion of periodicity is assumed when analyzing a representative vol-

ume element, most scalable man-made architected materials have irregular architecture, owing to their fabrication techniques. In these cases, a statistically significant RVE consists of a large number of cells to obtain an on-average, homogenized response. A type of foams that exhibit unique properties albeit with a semi-irregular architecture are nanoporous metallic foams (np-foams) [53, 107], which benefit from the nanoscale size effects of its ligaments [18] and provide strength values that approach theoretical bounds. Similar geometries to those of np-foams can be achieved via segregated polymeric microemulsions [7, 155], albeit with slightly larger features, which provide further geometric tunability of the microstructure based on mixture ratios and processing parameters.

1.3.1 Fabrication Techniques

At the macroscale, i.e., with mm- or μm-scale feature sizes, cellular solids can be fabricated in a variety of forms. Polymeric foams are often formed by introducing some form of gas to a monomer or a hot polymer, which causes bubbling. Upon stabilization of the formed bubbles, the mixture can be polymerized to become solid [46]. Some metal foams are formed via liquid processing of the molten metal, either by mechanical agitation or by introducing particles which cause foaming [46].

Metallic np-foams can be synthesized by methods such as free corrosion or electrochemically driven dealloying [53]. The latter method can lead to extremely fine ligaments, on the order of a few tens-of-nm, which has resulted in optimal material properties [18]. A commonly studied system for np-foam production is that of Ag_xAu_x alloys, which forms almost-pure Au foams upon dealloying.

Polymeric nanoporous or microporous foams can be fabricated by mixing several types of block co-polymers which segregate into ordered or disordered phases [78, 136, 155]. Following equilibrated segregation, the system can be cross-linked to retain its configuration, and one or more of the phases can be selectively etched out to produce pores [136]. Minimal changes in any of several variables such as phase concentrations, molecular weights, temperature, and pressure can give rise to drastically different configurations, some of which are highly ordered and become truss-like rather than foam-resembling [7]. We classify the disordered phases in these systems as foams, while particular highly ordered configurations will be discussed in the truss-based architected materials category in this chapter.

1.3.2 Mechanical Properties: Classical Scaling Laws

The configuration of foam cells typically leads to geometric arrangements which preferentially deform through bending of its members. Assuming a simplistic open-celled foam configuration [46] with slender struts of circular cross-section and radius r and length l such as in Fig. 1.3a, the relative density can be approximated as

$$\overline{\rho} \propto \left(\frac{r}{l}\right)^2, \tag{1.2}$$

obtained by the ratio of the volume of the struts $V_s \propto r^2 l$ and that of the box encompassing the unit cell $V_{\text{UC}} \propto l^3$.

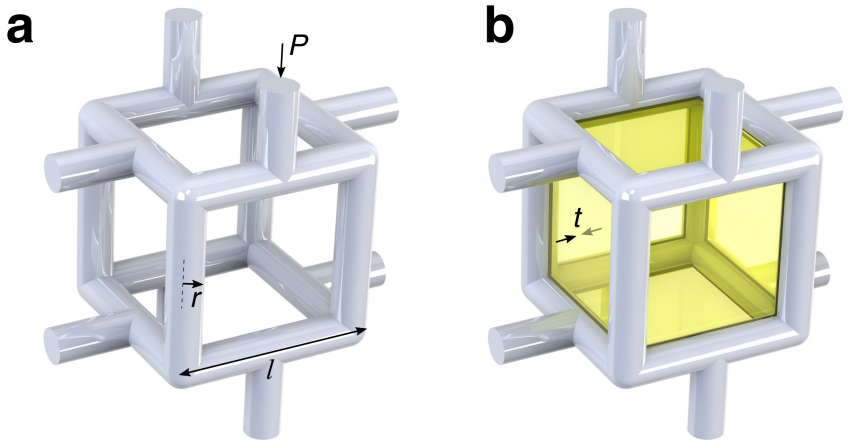

Figure 1.3 | Open vs. Closed Cell Foam

Using simple Euler-Bernoulli beam theory [132], the effective Young's modulus of the foam can be approximated by studying the deflection of a beam with a load P at its center. The deflection δ can then be approximated as

$$\delta \propto \frac{P l^3}{E_s I}, \tag{1.3}$$

where E_s is the constituent material's Young's modulus and $I \propto r^4$ is the second area moment of the beam. Assuming proper separation of scales, this deformation can be assumed to be characteristic of all cells in the foam, and the whole foam can be assumed to deflect by a magnitude proportional to δ. It also follows that the uniaxial stress σ (i.e., area-normalized load) can be assumed to be

$$\sigma \propto \frac{P}{l^2}. \tag{1.4}$$

Defining the uniaxial strain on the foam to be $\varepsilon \propto \delta/l$, the effective Young's modulus of this foam is estimated as

$$E^* \propto \frac{\sigma}{\varepsilon} \propto E_s \overline{\rho}^2. \tag{1.5}$$

In practice, the normalized effective modulus is presented as

$$\frac{E^*}{E_s} = C_1 \overline{\rho}^2, \tag{1.6}$$

where C_i is a proportionality constant that accounts for geometric parameters.

If the cell is closed (Fig. 1.3b), the cell walls of thickness t can add to the effective stiffness, assuming its contribution can be superimposed to that of Eq. 1.17. From an energetic perspective, the work done by the external load P to deform the closed cell is proportional to $\frac{1}{2}P\delta$, and it is distributed between the strain energy of the beams $\frac{1}{2}\frac{E_s I}{l^3}\delta^2$, and that of the stretching in the cell walls $\frac{1}{2}E_s\varepsilon^2 V_w$, where V_w is the volume of the walls. Solving for P in the energy balance described above, and assuming again $E^* \propto (P/l^2)/(\delta/l)$ (also relating t/l to the overall relative density, see Gibson and Ashby [46]), the normalized effective modulus for a closed-cell foam is expressed as [122]

$$\frac{E^*}{E_s} = C_2\phi^2\overline{\rho}^2 + C_3(1-\phi)\overline{\rho}, \tag{1.7}$$

where $\phi \in [0, 1]$ is the relative distribution of solid in the beams.

Performing the same type of dimensional analysis, expressions for the collapse of the cells (i.e., the strength) have been obtained of the form [46]

$$\frac{\sigma_y^*}{\sigma_{ys}} = D_1\overline{\rho}^{3/2}, \tag{1.8}$$

for open-cell foams, and

$$\frac{\sigma_y^*}{\sigma_{ys}} = D_2(\phi\overline{\rho})^{3/2} + D_3(1-\phi)\overline{\rho}, \tag{1.9}$$

for closed-cell foams, where σ_{ys} corresponds to the yield strength of the constituent material and D_i is again a proportionality constant.

1.4 Periodic Architected Materials

Thus far, quasi-ordered foams have been discussed in a general sense due to their large variety of geometries (and vast number of variables that lead to them). Recent developments in advanced manufacturing techniques have enabled types of cellular solids with deterministic, repeatable, and (approximately) periodic cells. Very broadly, we will categorize them into beam-based designs and plate- or shell-based designs.

1.4.1 Beam-based designs

Enabled mainly by 3D-printing processes, materials consisting of a network of struts connected at joints constitute the most common type of periodic architected material [8, 92, 118, 153]. Due to the highly controlled geometries within these materials, a single unit cell is usually sufficient to be taken as the RVE and can be used to fully characterize each material.

Unit cells can be described by their number of struts, vertices, and faces but this becomes ambiguous, for instance, when drastically different geometries with the same number of struts exist. To categorize these structures more generally, they can be defined based on their structural rigidity as explained in the following section. As we will see in later sections, this categorization will provide insight not only on the topology of the architectures, but also on their mechanical behavior.

Defining Structural Rigidity

Assuming a given structure is composed of pin joints (i.e., no resistance for the struts to rotate), it can be categorized as *statically* and *kinematically* determinate or indeterminate. *Static* determinacy requires the forces in each bar to be known from the equilibrium equations while *kinematic* determinacy implies that the unique position of each joint can be determined based on the lengths of the struts. We define a *rigid* architecture as one that requires stretching of one or more struts for any of the joints to change position, implying that a rigid structure may be statically determinate or indeterminate, but it necessarily has to be kinematically determinate. Static indeterminacy in these structures can occur when redundant struts exist which allow a state of *self-stress* without the influence of any external forces. On the other hand, a *non-rigid* architecture is kinematically indeterminate since the joints can freely move in space without the need of stretching in any of the struts, defined as a zero-energy *mechanism*.

To formally understand this categorization, we will briefly describe the mathematical foundation presented by Pellegrino and Calladine [110], which uses the geometry of a given structure to form a linear-algebra framework that provides answers on each level of determinacy. For a structure that is attached to a rigid foundation via any k number of constraints (to prevent rigid-body motions), Maxwell's rule states that a necessary condition for static and kinematic determinacy is

$$b = 3j, \tag{1.10}$$

where b is the number of struts and J is the number of joints that are not attached to the foundation. Since this is a necessary but not sufficient condition, some structures that satisfy this rule can be kinematically indeterminate, which leaves room for a more in-depth analysis.

To this end, the vector of forces $\boldsymbol{f} \in \mathbb{R}^{dj-k}$ at each joint in d-dimensions can be related to the tension $\boldsymbol{t} \in \mathbb{R}^{b}$ in each strut in the form

$$\boldsymbol{f} = \boldsymbol{A}\boldsymbol{t}, \tag{1.11}$$

where $\boldsymbol{A} \in \mathbb{R}^{(dj-k)\times b}$ is the equilibrium matrix. Similarly, the extension of each strut $\boldsymbol{e} \in \mathbb{R}^{b}$ can be related to the displacements of each joint $\boldsymbol{d} \in \mathbb{R}^{dj-k}$ in the form

$$\boldsymbol{e} = \boldsymbol{B}\boldsymbol{d}, \tag{1.12}$$

where $\boldsymbol{B} \in \mathbb{R}^{b\times(dj-k)}$ is the kinematic matrix, which can also be expressed as

$$\boldsymbol{B} = \boldsymbol{A}^{\mathrm{T}}. \tag{1.13}$$

The fundamental subspaces of these rank-r matrices $\boldsymbol{A}$ and $\boldsymbol{B}$ can then provide information on the existence of zero-energy mechanisms or states of self-stress. Specifically, the number of states of self-stress s corresponds to the dimension of the nullspace of $\boldsymbol{A}$, while the number of mechanisms m corresponds to that of $\boldsymbol{B}$. Therefore, Maxwell's law can be replaced by

$$s = b - r, \tag{1.14}$$

$$m = 3j - k - r, \tag{1.15}$$

expressed together as

$$s - m = b - 3j + k. \tag{1.16}$$

Assembling the equilibrium matrix for a given unit cell geometry then allows categorization of a material's architecture as rigid or non-rigid, based on the number of mechanisms.

1.4.2 Plate- and Shell-based designs

Several plate-based designs (i.e., no curvature) have emerged using the vertices of a beam-based lattice as a template, but with solid plates corresponding to each face [15, 128]. Large variations of these structures can be made by superimposing

different basis lattices and also varying the plate thickness in each lattice. By definition, most of these materials have closed cells (unless specifically designed to have holes) and their density is highly dependent on the fluid encompassed within each cell.

Alternatively, periodic materials made out of curved shells have also been designed using a beam-based lattice architectures as templates [19, 20]. These materials have utilized the surfaces corresponding to each beam as a shell, along with curved features such as fillets or spheres at junctions. More mathematically elaborate designs, termed triply periodic minimal surfaces (TPMS) [1, 49, 50, 101], have been fabricated in a variety of topologies belonging to that family. TPMS materials are unique in the sense that their mean curvature is zero or constant and the domains on each side of the shells are continuous, by definition. Further variations of TPMS materials (although not shell-based) arise when one of the two domains is filled [65, 86].

1.4.3 Fabrication Methods

Nano- and Micro-Fabrication Techniques

At the micro- to nano-scale, polymer-containing materials have been most prevalent due to advanced lithography techniques. Two-photon lithography processes have enabled the fabrication of polymeric features with sub-micron resolution and sample volumes on the order a cubic millimeter [8, 92–94, 128]. Subsequent pyrolysis or sintering of specific resins has also enabled the fabrication of carbon and metal architectures with features sizes below to ~200 nm [9, 139, 152]. Additionally, conformally coating these templates with nanometer-thick ceramic [8, 93, 120] or metal coatings has enabled the fabrication of ceramic/metal-polymer composites. Removing the polymeric template from these composites has produced hollow, shell-based ceramic [92] and metal [97] materials.

Larger sample volumes, with features on the order of tens to hundreds of micrometers, have been achieved via large area projection microstereolithography methods [153, 154]. Overall sample sizes produced through this method can reach volumes on the order of $\sim 10\,\mathrm{cm}^3$, and have enabled multiscale materials with dimensions spanning from tens of nanometers to tens of centimeters [154]. A wide range of material arrangements, ranging from ceramic or metallic shells to monolithic ceramics have been reported using this method [153].

Nano- and micro-architected materials have also been fabricated via self-assembly processes. The use of block copolymers to assemble a truss-like periodic patterns

has been reported to fabricate metallic (Ni) truss-like thin films [65]. At the microscale, particle-stabilized emulsion gels (bijels) have produced macroporous architected materials with features on the order of $\sim 10\,\mu m$ [79].

Macro-Fabrication Techniques

We define macro-scale fabrication techniques in this work as those capable of fabricating volumes larger than $\sim 10\,cm^3$, with feature sizes greater than a few tens of micrometers. Most of the well-established additive manufacturing techniques fall in this regime, along with some lithography techniques. One such lithography technique is that of self-propagating polymer waveguides, which can achieve truss-like polymeric scaffolds [60] that can be coated and etched to produce ultralight metallic materials [118] or pyrolyzed to form vitreous carbon structures [61]. Similar material systems, with a larger range of printable geometries, have been made available by 3D-printing techniques such as stereolithography [75] or laser sintering [12].

Looking beyond metallic coatings at the macro-scale, monolithic metal architected materials have been fabricated through techniques such as selective electron beam melting (SEBM) or selective laser melting (SLM). Several periodic architected materials have been fabricated through these processes with constituent materials such as stainless steel 316L [19, 20, 51, 127] and Ti-6Al-4V [141]. Lattice-core sandwich plates have been fabricated as well via sheet perforation and followed by folding or snap-fitting components, requiring no additive manufacturing techniques [129, 147, 149].

1.4.4 Static Mechanical Properties

The structural rigidity of an architecture, as defined in section 1.4.1, provides simple predictive tools on the mechanical response of a material containing that architecture. For instance, the classical scaling law for the stiffness of foams (Eq. 1.17) applies to non-rigid structures

$$\left(\frac{E^*}{E_s}\right)_{\text{non-rigid}} = C_1\bar{\rho}^2, \tag{1.17}$$

since their deformation is inherently bending-dominated. Due to periodicity (lacking in foams), beam-based periodic materials will achieve a higher scaling constant C_1 than foams.

An equally simple approximation for a rigid-architecture-containing material consists of an arrangement of bars and pin-joints in three dimensions [35], which ne-

glect bending deformation and provide a scaling law of the form

$$\left(\frac{E^*}{E_s}\right)_{\text{rigid}} = C_1\overline{\rho}, \tag{1.18}$$

where the value of C_1 should be higher than that of a non-rigid architecture material of the same constituent material and relative density.

An extensive body of literature has explored the effective scalings (both for stiffness and strength) for a variety of beam-based periodic architected materials. In the stiffness realm, several works have have reported scalings that differ from the ones presented above [9, 93, 117, 118, 127], usually presenting higher-than-linear scalings for rigid architectures (Fig. 1.4a). This has been shown in both experiments and simulations, confirming that this deviation is likely due to the non-slender struts that are used in these materials which go beyond the assumptions made by beam theory (a topic that will be discussed in detail in chapters 2 and 3). For non-rigid geometries (Fig. 1.4b), experiments show higher-than-quadratic scalings along with extreme variations in the scalings predicted by simulations which are highly affected by the choice of boundary conditions employed [117].

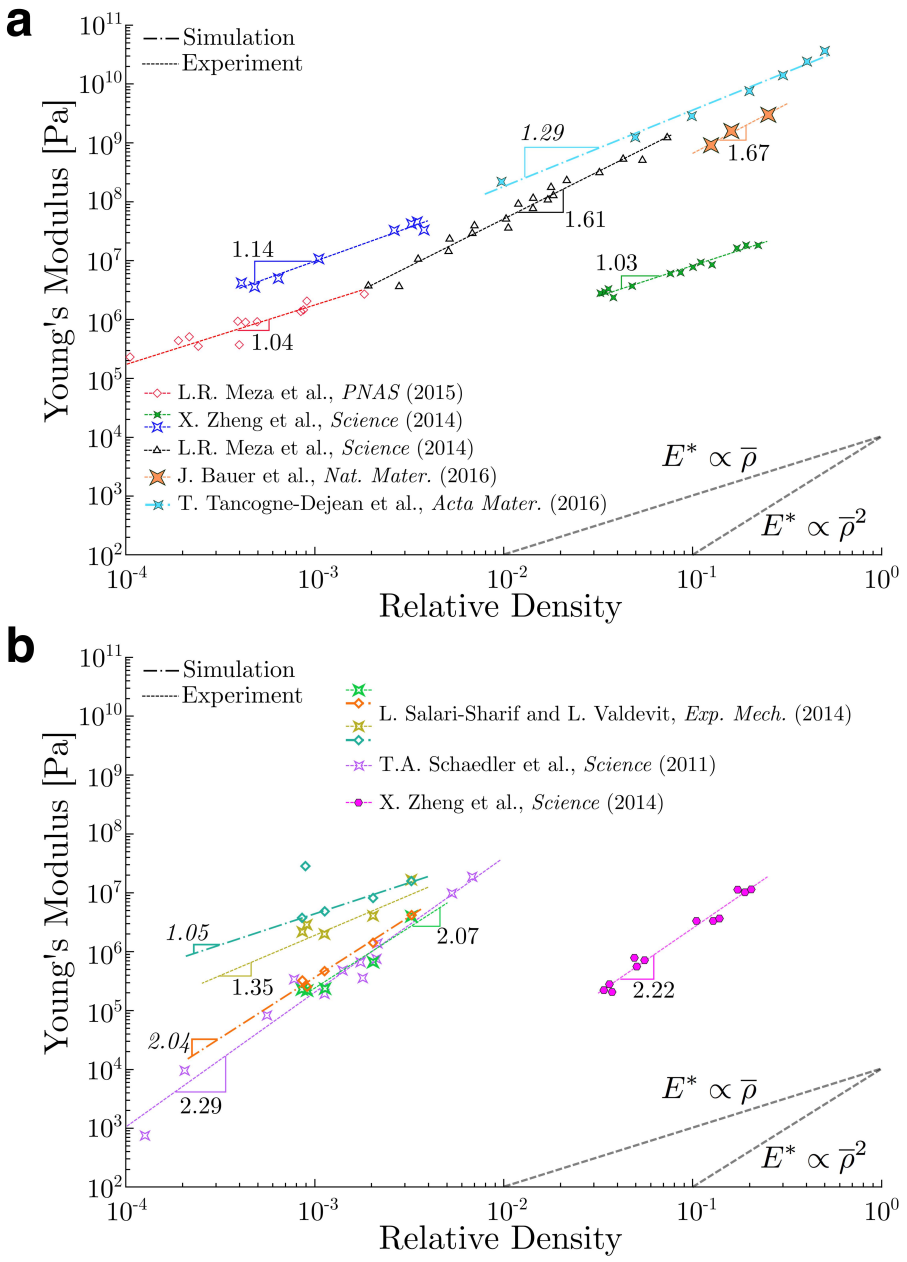

FIGURE 1.4 | STIFFNESS SCALINGS OF SELECTED BEAM-BASED PERIODIC ARCHITECTED MATERIALS Experiments and simulations on **(a)** rigid and **(b)** non-rigid architectures.

The strength scalings and failure mechanisms of these types of materials at the nano- and micro-scales have been shown to be diverse, mainly due to the dominant effect of inevitable defects (both structural- and material-related) on these properties. Depending on the geometry of structural features and the constituent material, both ductile-like and brittle failure have been observed, relating to beam/shell buckling or material fracture, respectively. Ductile-like failure followed by struc-

tural recovery has been reported in nano-architected materials enabled by elastic shell-buckling of thin ceramic beam walls [92, 93]. Although structural recovery is observed, the material is substantially weaker due to fracture at nodes where stress concentrations arise. Brittle failure has been observed when beam-wall thicknesses increase [92, 93] or when the struts are monolithic or composite [8, 153]. Additionally, some monolithic-beam materials with sub-micron beam dimensions made out of carbon have approached the theoretical bounds for strength [9, 152] by harnessing material size effects. Analogous to their nano-architected counterparts, hollow metallic lattices with larger dimensions have also reported buckling and yielding failure regimes depending on the struts' geometric parameters [134], and are strongly affected by the compliance of hollow nodes. This important effect of stress concentrations at nodes has been shown to be slightly mitigated if fillets are added to strut junctions [75]. Recently, some works have explored the fracture behavior of beam-based architected materials at both the nano- and macro-scales [87, 103] and have also highlighted the importance of nodal effects in this regime.

Looking beyond beam-based architectures, plate- and shell-based materials that have been fabricated at the micro-scale have exhibited stiffnesses that are close to the theoretical bounds [128]. Doubly curved geometries based on triply periodic minimal surfaces (and doubly curved derivations of truss geometries) [1, 20, 49, 50] showed mechanical performance equal or superior to beam-based architectures at the same relative density, including close-to-linear stiffness scalings. A benefit from the mechanical response of these doubly curved architectures is the lack of nodes at which stress concentrations could occur and smoother collapse responses compared to truss architectures [20].

1.4.5 Dynamic Mechanical Properties

The propagation of mechanical waves in periodic 3D architected materials has been explored extensively numerically and analytically, while experimental studies have only recently been made possible. In particular, the use of lumped masses [88] and buckling of beam-like components [140, 141] have shown to be mechanisms to achieve vibrational band gaps in these materials at centimeter scales. At the micro- and nano-scale, lattice architectures submerged in water have exhibited the formation of ultrasonic acoustic band gaps with modifications at the nodes [69] as well as frequency-dependent group velocities [71].

Dynamic non-elastic deformation such as compaction has also been studied exper-

imentally. The dynamic compression of stainless steel lattices with feature sizes on the order of hundreds of micrometers to a few millimeters and strain rates of 10^3 s^{-1} have reported that effective dynamic strength increases [127] and high energy absorption [51] are achievable with the use of architecture. Similar experiments on aluminum-alloy truss-core sandwich plates explored the effect of temperature on energy absorption during compaction and showed improved performance at temperatures as low as $-170\,°C$ [129]. Comparable experiments on polymeric lattice architectures with beam diameters of $\sim 30\,\mu m$ and compaction velocities of $\sim$300 m/s showed evidence of constant-velocity compaction waves regardless of architecture, hinting to an inertia-dependent process [52]. Auxetic polymeric micro-lattices studied at strain rates of $\sim 1000\,s^{-1}$ show beam buckling as a mechanism to enhance energy absorption in these materials under compaction [73].

The impact and blast response of 3D periodic architected materials has been mostly explored in truss-core sandwich plate configurations which usually consist of a small tessellation of unit cells in the thickness direction (just one unit cell in some cases). Low-velocity drop-weight impact experiments on additively manufactured metallic and polymeric truss cores, with impact velocities of up to $\sim$5 m/s, reported energy absorption values comparable to aluminum honeycombs of the same density [95, 149] as well as an important effect of architecture [12] in this regime. At higher strain rates, the dependence on geometric parameters in the truss core has been explored analytically and numerically for millimeter-scale monolithic [145] and micro-scale hollow metallic struts [41], both showing the potential of these materials to sustain higher blast impulses than a monolithic plate of the same weight. The ballistic impact response of metallic truss-core sandwich plates to maximum velocities of 1,300 m/s showed comparable energy absorption response to monolithic plates, and showed a diminishing effect of architecture beyond a critical velocity at which full sample penetration occurred [147].

1.5 Numerical Modeling of Architected Materials

Due to the immense parameter space associated with 3D periodic architected materials, numerical models have become necessary to predict and optimize the response of lattice architectures. Depending on the problem on interest (i.e., linear response, non-linear response) and the size of tessellation to be modeled, several numerical approaches have been proposed.

1.5.1 Finite Periodic Tessellations

Discrete beam-element models [37, 130] and beam homogenization models [11, 106, 112, 138] have provided efficient approaches to model large tessellations of unit cells, although they are applicable only to slender geometries where beam theory applies. Furthermore, these models fall short in predicting the response of complex architectures such as the hollow-beam geometries used in Meza et al. [93] or Schaedler et al. [118]. With these limitations in mind, these types of models have been used both in the static and dynamic regimes and have provided estimates on phenomena ranging from tensile viscoelastic response [130] to elastic wave directionality [10, 90, 148] in lattice architectures.

More computationally demanding representations that use 3D finite elements have been reported to provide more accurate results when beam theory becomes insufficient, but pose additional challenges due to the added computational cost [19, 127].

1.5.2 Homogenization

The periodicity inherent in these materials allows for numerical homogenization using periodic boundary conditions (PBCs), which effectively predicts the response of an infinite tessellation of unit cells. Since the work presented in this thesis utilizes numerical homogenization methods in both the static and dynamic regimes, these concepts will be explained in more detail below.

Static Response

We begin by assuming a heterogenous RVE under strain field $\boldsymbol{\varepsilon}$, whose linearized stress field $\boldsymbol{\sigma}$=$\boldsymbol{\sigma}(\boldsymbol{x}, \boldsymbol{\varepsilon})$ and density $\rho = \rho(\boldsymbol{x})$ undergo variations from point to point. Assuming separation of scales is achieved, we aim to express the problem in a homogenized form such that these properties of the *effective material* are $\boldsymbol{\sigma}(\boldsymbol{x})$=$\boldsymbol{\sigma}^*$ and $\rho(\boldsymbol{x})$=ρ^*. Using conservation of mass we can define the effective density of a material volume V as

$$\rho^* V = \int_\Omega \rho(\boldsymbol{x}) \, \mathrm{d}V \Rightarrow \boxed{\rho^* = \langle \rho \rangle}, \tag{1.19}$$

where Ω represents the domain of the whole RVE. In the same manner, the effective stress and strain fields are defined as

$$\boxed{\boldsymbol{\sigma}^* = \langle \boldsymbol{\sigma} \rangle} \text{ and } \boxed{\boldsymbol{\varepsilon}^* = \langle \boldsymbol{\varepsilon} \rangle}. \tag{1.20}$$

Thus, conservation of energy in the small strain regime requires the strain energy density of the macroscale to be equal to that of the microscale

$$\boldsymbol{\sigma}^* \cdot \boldsymbol{\varepsilon}^* = \langle \boldsymbol{\sigma}(\boldsymbol{x}) \cdot \boldsymbol{\varepsilon}(\boldsymbol{x}) \rangle. \tag{1.21}$$

This energetic equivalence is attained by exploiting periodicity in the heterogeneous material and applying periodic boundary conditions enforcing

$$u^+ - u^- = \boldsymbol{\varepsilon}(\boldsymbol{x}^+ - \boldsymbol{x}^-) \text{ and } \boldsymbol{t}^+ = \boldsymbol{t}^- \text{ on } \partial\Omega, \tag{1.22}$$

where $\boldsymbol{u}^{+/-}$ and $\boldsymbol{t}^{+/-}$ are the displacements and tractions on the plus and minus boundaries ($\partial\Omega$) of the RVE (with coordinates $\boldsymbol{x}^+$ and $\boldsymbol{x}^-$), respectively.

This approach has been used to predict the effective response of periodic materials by just modeling one unit cell [20, 94, 117, 126, 128, 134], which then implies an infinite tessellation in all directions. If separation of scales is indeed achieved in experimental samples, this computational technique provides an efficient approach to approximate their response.

Wave Propagation Response

Periodicity can also be employed to predict the propagation of elastic waves in periodic materials using Bloch wave analysis [59]. This analysis begins by characterizing an infinite periodic material using three basis vectors, namely $\boldsymbol{a}_1$, $\boldsymbol{a}_2$, and $\boldsymbol{a}_3$ which fully define the tessellation of an elementary unit cell that composes the infinite material. Thus, the position of a specific point $\boldsymbol{\alpha}$ can be expressed in the unit cell's local coordinate system as $\boldsymbol{r}_0$, and in global coordinates as

$$\boldsymbol{r}_\alpha = \boldsymbol{r}_0 + n_1\boldsymbol{a}_1 + n_2\boldsymbol{a}_2 + n_3\boldsymbol{a}_3, \tag{1.23}$$

where $n_i \in \mathbb{Z}$ correspond to the tessellation integers of the unit cell of interest. Bloch's theorem then relates the displacement $\boldsymbol{u}$ of a point in global coordinates to the point in the unit-cell coordinate system by the expression

$$\boldsymbol{u}(\boldsymbol{r}_\alpha) = \boldsymbol{u}(\boldsymbol{r}_0)\boldsymbol{e}^{-i\boldsymbol{k}\cdot(\boldsymbol{r}_\alpha - \boldsymbol{r}_0)}, \tag{1.24}$$

where $\boldsymbol{k}$ is the wave vector. We note that periodicity is enforced by ensuring that the wave vector is defined by reciprocal lattice vectors [67] given by

$$\boldsymbol{b}_1 = 2\pi\frac{\boldsymbol{a}_2 \times \boldsymbol{a}_3}{\boldsymbol{a}_1 \cdot (\boldsymbol{a}_2 \times \boldsymbol{a}_3)}, \quad \boldsymbol{b}_2 = 2\pi\frac{\boldsymbol{a}_3 \times \boldsymbol{a}_1}{\boldsymbol{a}_2 \cdot (\boldsymbol{a}_3 \times \boldsymbol{a}_1)}, \quad \boldsymbol{b}_3 = 2\pi\frac{\boldsymbol{a}_1 \times \boldsymbol{a}_2}{\boldsymbol{a}_3 \cdot (\boldsymbol{a}_1 \times \boldsymbol{a}_2)}, \tag{1.25}$$

in the form

$$\boldsymbol{k} = k_1\boldsymbol{b}_1 + k_2\boldsymbol{b}_2 + k_3\boldsymbol{b}_3, \tag{1.26}$$

with $k_i \in \mathbb{R}$. Using the finite element framework and assembling the appropriate mass and stiffness matrices for the RVE, $\boldsymbol{M}$ and $\boldsymbol{K}$, respectively, the solution to the problem can be expressed as

$$\boldsymbol{M}\ddot{\boldsymbol{U}} + \boldsymbol{K}\boldsymbol{U} = \boldsymbol{F}, \tag{1.27}$$

where $\ddot{\boldsymbol{U}}$, $\boldsymbol{U}$, and $\boldsymbol{F}$ are the acceleration, displacement, and force vectors, respectively. Seeking a plane-wave solution of the form $\boldsymbol{U}(\boldsymbol{r}_0) = \boldsymbol{U}_0 e^{-i\omega t}$, with frequency ω, and applying Bloch's theorem (Eq. 1.24) yields the eigenvalue problem

$$(\boldsymbol{K} - \omega^2\boldsymbol{M})\boldsymbol{U}_0 = \boldsymbol{F}, \tag{1.28}$$

subject to

$$\boldsymbol{U}_0^+ = \boldsymbol{U}_0^- e^{-i\boldsymbol{k}\cdot(\boldsymbol{x}^+ - \boldsymbol{x}^-)} \qquad \boldsymbol{F}^+ = -\boldsymbol{F}^- e^{-i\boldsymbol{k}\cdot(\boldsymbol{x}^+ - \boldsymbol{x}^-)}, \tag{1.29}$$

where $\boldsymbol{x}^{+/-}$ are the coordinates of the corresponding points in the plus and minus faces of the RVE and $(\cdot)^{+/-}$ are the quantities corresponding to those faces. The dispersion relation of the infinite periodic material is then obtained by exploiting periodicity to define an irreducible Brillouin zone (IBZ) [21] in k-space and solving for the eigenfrequencies ω while sweeping the wave vector $\boldsymbol{k}$ along the edges of the IBZ.

This analysis has been used extensively for architected materials with both beam- and continuum-element representations, and serves as the guiding principle for validation experiments [2, 26, 69, 88]. These dispersion relations obtained numerically can be used to predict the existence of band gaps [83, 141] and provide insight on the phase and group velocities of waves traveling in periodic materials [10, 71, 90, 109].

1.6 Significance of Architected Materials

As highlighted in previous sections, architecting structural materials at the micro- and nanoscale has enabled novel mechanical properties unattainable by homogeneous materials. Their high mechanical tunability has enabled their use in previously unrelated fields pertaining to cell mechanics, electrochemistry, and impact absorption among others.

Recent developments in the architected-material field have enabled the fabrication of increasingly larger volumes with nano- and micro-scale features, bridging the

gap between interesting material size effects and everyday applications. Future progress in this field has the potential to completely close this gap and thus drastically change the materials parameter space presented in Fig. 1.2.

1.7 Outline

This thesis presents an exploration on the mechanical response of architected materials with dimensions ranging from the nanometers to centimeters, presenting novel fabrication and testing methods along the way. Furthermore, the first part of the thesis pertains to the response of these materials under quasi-static loading, while the second part explores their response in the dynamic regime. In doing so, it encompassing mechanical loading ranging from uniaxial compression, to mechanical vibrations in the MHz regime, and ultimately to blast loading and supersonic impact with velocities of up to ~1 km/s.

Chapter 2 begins by analytically, experimentally, and numerically studying the mechanical property space of nano-architected beam-based periodic materials, specifically relating geometric parameters such as unit cell topology and beam slenderness to the effective mechanical response. This chapter concludes by showing that architectures that are manufacturable by current methods deviate from the mechanical response predicted by classical scaling laws and qualitatively associates this deviation to emerge from non-slender nodes (i.e., junctions).

Chapter 3 expands on the exploration from the previous chapter and describes a systematic, quantitative experimental and numerical study of the effect of nodes on non-slender beam architectures, additionally showing that this effect is scale-independent. In this chapter, we propose an efficient reduced-order numerical model that accurately captures the effect of nodes on the linear mechanical response of lattice architectures and provides an extension to the classical stiffness scaling laws to account for the deviation observed in non-slender geometries.

We enhance our exploration in chapter 4 by moving beyond beam-based architectures and instead study node-less, shell-based geometries that do not suffer from the issues presented in the previous chapters. As part of this exploration, we present a self-assembly method for scalable fabrication of nano-architected materials with sample volumes of up to a few cubic centimeters consisting of smooth doubly curved ceramic shells. Harnessing the tunable nature of self-assembly processes, we numerically and experimentally showcase the extreme resilience and overall superior performance of these materials compared to other architected materials.

The next portion of the thesis consists of the exploration of these materials in the dynamic mechanical regime, with chapter 5 describing the propagation of mechanical waves in micro-architected beam-based architectures. In this chapter we explore the use of reconfigurable geometries and added micro-inertia to elicit the emergence of vibrational band gaps, also presenting a novel experimental method that enables dynamic testing of small-volume micro-architected materials.

Chapter 6 further enters the dynamic regime by studying the response of carbon-based lattice architectures, both at the nano- and centimeter scales, under supersonic impact and blast loading conditions. We also present methods to fabricate these carbon-based materials at both scales (including a type of 3D architected carbon composite at the larger scale), and experimentally show their potential to dissipate energy in these conditions.

Lastly, we summarize and provide an outlook based on the lessons learned from the above explorations.

Chapter 2

IDENTIFYING THE EFFECT OF NODES ON LATTICE ARCHITECTURES

This chapter has been adapted from

L.R. Meza, G.P. Phlipot, C.M. Portela, A. Maggi, L.C. Montemayor, A. Comella, D.M. Kochmann & J.R. Greer. "Reexamining the mechanical property space of three-dimensional lattice architectures". *Acta Materialia* (2017) 140, pp. 424–432. DOI: 10.1016/j.actamat.2017.08.052.
CONTRIBUTIONS: fabricated a portion of the samples, conducted a portion of the experiments and analyzed the data, performed a portion of the computational analysis, and participated in the writing of the manuscript.

2.1 Chapter Summary

In the process of studying the mechanical parameter space of lattice architectures we conducted systematic nanomechanical experiments and finite element analysis on nanolattices made from two different material systems (i.e., solid and hollow beams), with four different topologies each. We found that the mechanical properties of nanolattices in a currently experimentally realizable property space are nearly independent of architecture, and that the strength and stiffness of rigid and non-rigid topologies (as defined in Section 1.4.1) at these relative densities are nearly identical. This result represents a significant point of departure from theories relating mechanical properties to the rigidity of the lattice topology [34, 35, 43, 46, 48, 154]. Uniaxial compression experiments reveal a non-linear scaling of strength and stiffness with relative density, with exponents between $m = 1.41 - 1.83$ for stiffness and $n = 1.45 - 1.92$ for strength for all nanolattice topologies and material systems. Finite element simulations reproduce the observed nonlinear scaling within the range of relative densities tested experimentally for both solid and hollow-beam nanolattices. They further reveal that for solid lattices with relative densities of $\overline{\rho} < 5\%$, the stiffnesses of rigid and non-rigid topologies deviate from one another to show good agreement with existing bending- and stretching-dominated scaling laws [46]. For hollow lattices, finite element simulations reveal a highly complex parameter space with orders-of-magnitude deviations in stiffness arising from small variations in pa-

rameters. We propose a simple analytical framework that provides insight into the stiffness scaling of solid-beam lattices, and we investigate some of the mechanisms for the large variances in hollow-beam lattice properties. We postulate that the convergence of strength and stiffness in solid lattices at higher densities is caused by the increased influence of beam intersections at the nodes. These results suggest that the existing classification of nanolattice topologies as solely stretching- or bending-dominated is insufficient, and new theories must be developed to accurately capture the effect of both nodal interferences in solid-beam lattices and empty nodes in hollow-beam lattices on the mechanical properties. This chapter sets the groundwork for more advanced analysis on the effect of nodes presented in chapter 3.

2.2 Experimental Framework

2.2.1 Fabrication

Polymer nanolattices were fabricated using a two-photon lithography direct laser writing process in IP-Dip photoresist using the Photonic Professional lithography system (Nanoscribe GmbH). Structures were written using laser powers of 6-14 mW and writing speeds of $\sim 50\,\mu m\,s^{-1}$. Laser power is used to control the beam diameters. As a byproduct of the fabrication process, all beams were elliptical, with an aspect ratio of ~3:1. Beams can be made to be circular by writing structures using a layer-by-layer process, but this writing method results in structures with larger dimensions. The smallest beam dimensions that can be written using this process are on the order of ~200 nm, and in this work the beam dimensions range from ~400 nm to ~2 μm. Unit cell sizes of fabricated nanolattices ranged from 3 to 15 μm, and overall sample dimensions were between 25 and 85 μm.

Hollow structures were written using the polymer nanolattices as a base scaffold; polymer surfaces were conformally coated in alumina (Al_2O_3) using atomic layer deposition (ALD). Deposition was done at 150 °C in a Cambridge Nanotech S200 ALD system using the following steps: H_2O is pulsed for 15 ms, the system is purged for 20 s, trimethyl aluminum (TMA) is pulsed for 15 ms, the system is purged for 20 s, and the process is repeated. The carrier gas is nitrogen, flown at a rate of 20 sccm (standard cubic centimeters per minute). The process was cycled for between 50 and 1200 cycles to obtain the desired thickness coatings on the nanolattices, which ranged from 5 to 120 nm. The thickness of the coatings was verified using spectroscopic ellipsometry with an alpha-SE Ellipsometer (J.A. Wollam Co., Inc.). After deposition, two outer edges of the coated nanolattices were

removed using focused ion beam (FIB) milling in an FEI Nova 200 Nanolab system to expose the polymer to air. After this exposure, the samples were placed into an O_2 plasma barrel asher for a time period between 50 and 75 hours with a 300 sccm flow rate of O_2 under 100 W of power to fully remove the polymer. This process is nearly identical to that reported by Meza et al. [92].

2.2.2 Nanomechanical Experiments

Monotonic and cyclic uniaxial compression experiments were performed on nanolattices in a G200 XP Nanoindenter (Agilent Technologies). Structures were compressed uniaxially to ~50% strain at a rate of 10^{-3} s^{-1} to determine their yield stress σ_y, Young's modulus E and overall deformation characteristics. The data obtained from nanolattice compression experiments performed in this work had a wide range of stress-strain responses, which required the formulation of a consistent method to measure meaningful effective Young's moduli and yield strengths. In every sample tested, the stress-strain data was comprised of a toe region, a linear region, and a failure region. The toe region is a non-linear segment of data at the beginning of loading, and generally corresponds to slight misalignments and imperfections between the sample and the indenter tip. For each sample, a subset of stress-strain data was taken starting at the beginning of loading and going to the onset of failure. The maximum slope of this data subset was defined as the effective Young's modulus, E. This is done to mitigate the effect of the toe region on the stiffness measurement. In polymer samples, or any sample with ductile yielding, a line with slope E is determined using a 0.2% strain offset from the obtained Young's modulus fit, and the intersection of this line and the stress-strain data is taken to be the effective yield strength σ_y. In hollow Al_2O_3 samples, or any sample with a brittle yielding, the yield strength is taken to be the peak stress before failure. It should be noted that edge effects that arise due to the finite sample size can affect the strength and stiffness, particularly for non-rigid topologies, so the strength and stiffness of lattices here is an *effective* structural response that approximates the properties of an infinite lattice.

2.2.3 Results

We fabricated four nanolattice topologies with varying degrees of rigidity and average nodal connectivity (Z): (*i*) an octet-truss (rigid, $Z = 12$), (*ii*) a cuboctahedron (periodically rigid, $Z = 8$), (*iii*) a 3D Kagome (periodically rigid, $Z = 6$), and (*iv*) a tetrakaidecahedron (non-rigid, $Z = 4$) (Fig. 2.1). Each nanolattice was constructed

out of solid polymer and hollow Al_2O_3 beams with elliptical cross sections, which arise as a result of the fabrication method [92, 93]. Octet-truss, cuboctahedron and tetrakaidecahedron samples were made with $5 \times 5 \times 5$ unit cells, and 3D Kagome samples were made with $6 \times 6 \times 3$ unit cells. The relative densities of fabricated samples ranged from $\overline{\rho} = 1.1\%$ to 62.6% for solid polymer and $\overline{\rho} = 0.14\%$ to 9.1% for hollow Al_2O_3 and spanned at least one order of magnitude within each topology. The slenderness of the beams ranged from $\lambda = 13.8$ to 62.8 for polymer samples and $\lambda = 12.0$ to 59.8 for Al_2O_3 samples, defined as $\lambda = \sqrt{(AL^2/I)}$, with A being the cross-sectional area and I being the area moment of inertia of the beam. Despite the high relative density of some of the samples, each individual architecture remained topologically identical throughout its relative density range, and most samples had $\overline{\rho} \leq 30\%$.

We experimentally investigated strength and stiffness scaling relations of the form

$$E = BE_s\overline{\rho}^m, \tag{2.1}$$

$$\sigma_y = C\sigma_{ys}\overline{\rho}^n, \tag{2.2}$$

where B and C are proportionality constants, E_s and σ_y are the constituent material's properties, and m and n are the scaling coefficients, across all nanolattice topologies, dimensions, and material systems. We found that in the monolithic polymer samples the scaling exponents for stiffness range from $m = 1.41$ to 1.83 and those for strength range from $n = 1.63$ to 1.92, and in the hollow Al_2O_3 samples, the stiffness exponents range from $m = 1.46$ to 1.73 and the strength exponents range from $n = 1.45$ to 1.77. Table 2.1 provides the scaling and proportionality constants for all topologies and material systems explored in this work. The plots of strength and stiffness vs. density in Fig. 2.2 show that the mechanical properties of all topologies at the same density effectively collapse onto each other for each material system. Little variation exists in the proportionality constants or scaling exponents for Young's modulus between the two material systems, and the strength proportionality constants and scaling exponents of the polymer nanolattices are slightly higher than those of the Al_2O_3 nanolattices. These results demonstrate that in the range of relative densities tested for both materials systems, virtually no correlation exists between the rigidity of the samples and their strength and stiffness scaling. This finding is surprising because it indicates that topology has a less significant role in controlling the strength and stiffness of lattices than commonly theorized [35, 43, 46].

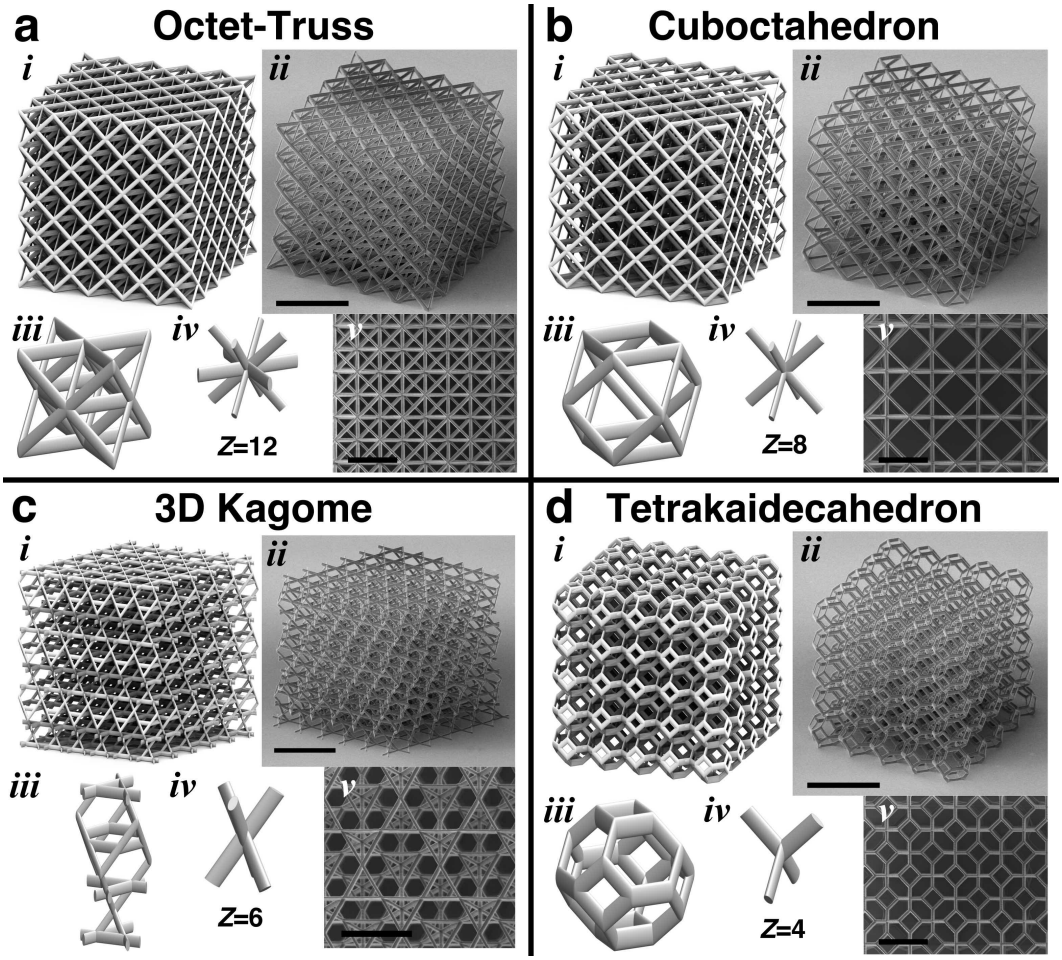

FIGURE 2.1 | RIGID AND NON-RIGID NANOLATTICE TOPOLOGIES
The four nanolattice topologies tested in this chapter: **(a)** octet-truss, **(b)** cuboctahedron, **(c)** 3D Kagome, and **(d)** tetrakaidecahedron. Figures (*i*) are CAD models of the full structures, (*ii*) are SEM images of the full structures, (*iii*) are CAD models of the unit cells, (*iv*) are representative nodes showing the average nodal connectivity, and (*v*) are SEM images from the top of the structures. Scale bars in (*ii*) and (*v*) are 10 μm and 5 μm, respectively.

Material	Topology	*B*	*m*	*C*	*n*
Polymer	Octet-truss	0.82	1.77	1.31	1.88
	Cuboctahedron	1.09	1.83	1.59	1.92
	3D Kagome	0.43	1.41	0.97	1.68
	Tetrakaidecahedron	0.57	1.60	0.84	1.63
Al_2O_3	Octet-truss	0.39	1.63	1.14	1.71
	Cuboctahedron	0.52	1.69	0.82	1.64
	3D Kagome	0.26	1.46	0.44	1.45
	Tetrakaidecahedron	0.95	1.73	0.67	1.55

TABLE 2.1 | EXPERIMENTAL SCALING PARAMETERS FOR SOLID- AND HOLLOW-BEAM NANOLATTICES
Experimentally derived scaling constants (*m* and *n*) and the proportionality constants (*B* and *C*) of the stiffness and strength scaling relationships respectively for each topology and each material system tested.

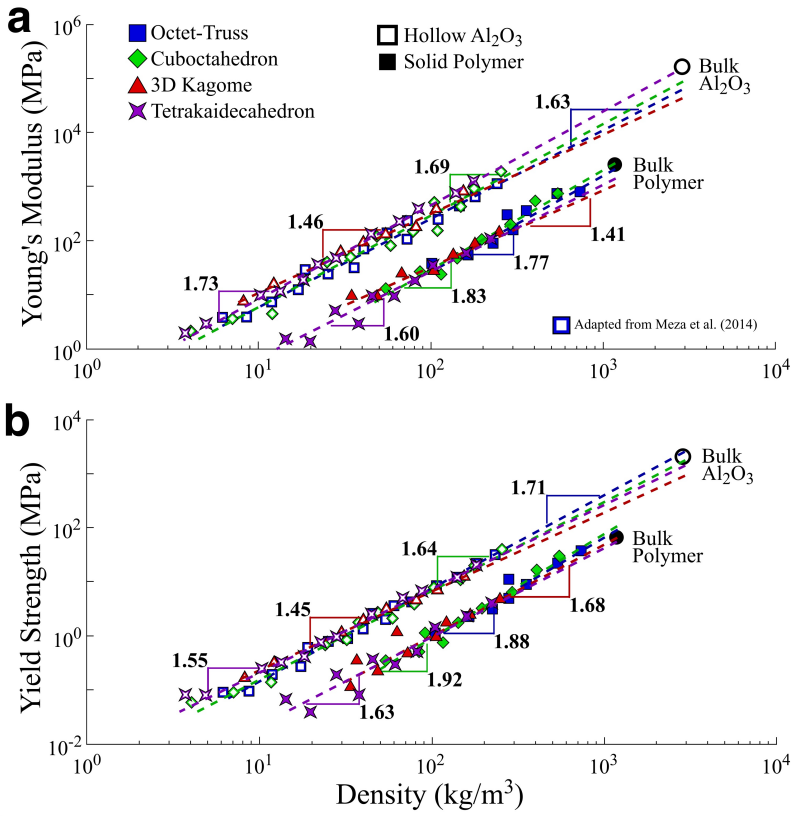

FIGURE 2.2 | STRENGTH AND STIFFNESS VS. DENSITY OF DIFFERENT NANOLATTICE TOPOLOGIES
Logarithmic plots of **(a)** Young's modulus vs. relative density and **(b)** yield strength vs. relative density of every sample tested from all four regular topologies and both material systems. The values of the fully dense constituent materials are also plotted. Trend lines for each set of samples are meant to graphically illustrate the scaling relations.

2.3 Analytical Framework: accounting for stretching and bending

The mechanical properties of periodic lattices are commonly modeled using the bending or stretching behavior of the constituent beams [8, 35, 43, 45, 70, 153]. In classical formulations, beams in a lattice are assumed to be slender and are approximated as Euler-Bernoulli or Timoshenko beams [46, 63]. Deformation modes like shearing and torsion in the beams and compression and bending of the nodes are often neglected in these simplified analyses because of the complexity associated with incorporating them into models and their negligible influence in slender beam lattices. In a non-rigid lattice comprised of solid Euler-Bernoulli beams with a characteristic cross-sectional dimension R and length L, the stiffness is assumed to be dominated by bending of the beams, giving rise to a scaling of $E \propto (R/L)^4$ [3, 46]. In a rigid lattice, this scaling is $E \propto (R/L)^2$ and arises from the assumption that

stiffness is governed by stretching and compression of the beams [3, 35]. In lattices with very slender beams (i.e., $\lambda \gtrsim 20$), the relative density can be approximated to scale as $\overline{\rho} \propto (R/L)^2$, where the slenderness is again defined as $\lambda = \sqrt{(AL^2/I)}$, with A being the cross-sectional area and I being the area moment of inertia of the beam. These three relationships give rise to the classical stiffness scaling of $E \propto \overline{\rho}^2$ for "bending-dominated" and $E \propto \overline{\rho}$ for "stretching-dominated" cellular solids.

These simplified relations begin to break down when the beams in a lattice cannot be approximated as slender. Simplified relative density relations are obtained by ignoring the relative contribution of beams intersecting at the nodes. Accounting for the effects of nodal intersections, we derived the relative densities of lattices with solid and hollow circular beams as a function of R/L and t/R to have the functional forms

$$\overline{\rho}_{\text{solid}} = C_1 \left(\frac{R}{L}\right)^2 + C_2 \left(\frac{R}{L}\right)^3, \tag{2.3}$$

$$\overline{\rho}_{\text{hollow}} = C_1 \left(\frac{R}{L}\right)^2 f\left(\frac{t}{R}\right) + C_2 \left(\frac{R}{L}\right)^3 g\left(\frac{t}{R}\right), \tag{2.4}$$

where C_1 and C_2 are geometry-dependent constants and are equal in solid and hollow lattices with the same geometry. The function $f\left(\frac{t}{R}\right) = 2\left(\frac{t}{R}\right) - \left(\frac{t}{R}\right)^2$ is the hollow-cylinder correction, and $g\left(\frac{t}{R}\right) = 3\left(\frac{t}{R}\right) - 3\left(\frac{t}{R}\right)^2 - \left(\frac{t}{R}\right)^3$ is the hollow-sphere correction. This model accurately predicts relative density scaling over a wide range of beam slendernesses, and notably diverges from models that do not account for nodal corrections in solid and hollow lattices when beam slenderness is $\lambda < 20$.

Classical stiffness models ignore the combined influence of stretching and bending in beams by assuming that one has a dominant effect over the other. In real lattices, this assumption no longer holds, and beams in a non-slender lattice are subject to both bending and stretching, in addition to other effects such as shearing, torsion and nodal interactions. To account for some of these effects, we developed a simple analytical model that accurately captures the stiffness of rigid and non-rigid lattices by representing them as 3D networks of solid Euler-Bernoulli beams subject to bending and axial compression and tension.

As shown in Fig. 2.3, 3D non-rigid and rigid lattice topologies are reduced to their 2D analogs and then further reduced using symmetry to representative one- and two-beam models, respectively. The stiffness of these simplified one- and two-beam models is then generalized to non-rigid and rigid lattice topologies. This analysis considers lattices comprised of beams with uniform solid circular cross-

sections, radius R, length L, and a constituent Young's modulus E_s. All beams are subject to a combination of stretching and bending, and beams are modeled using Euler-Bernoulli theory [132] for slender elastic beams. Nodes are all taken to be welded joints. Additional effects such as nodal compliance, torsion or shearing of beams, and imperfections like misalignment or waviness are ignored, as in classical theories for slender beams.

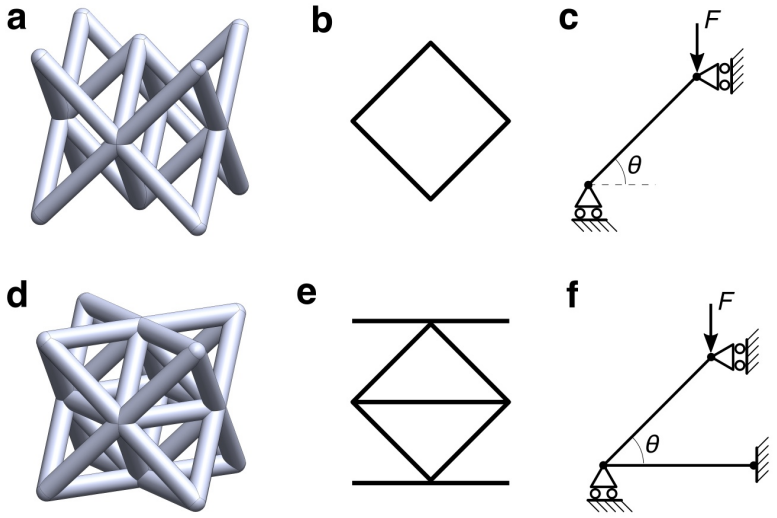

Figure 2.3 | Non-Rigid and Rigid Simplified Model Systems
(a) Model non-rigid nanolattice topology, **(b)** 2D analog of the non-rigid 3D lattice in (a). **(c)** Simple one-beam model constructed using symmetry of the 2D lattice in B and assuming rigid nodes. **(d)** Model rigid lattice topology (octet-truss). **(e)** 2D analog of the rigid 3D lattice in (d). **(f)** Simple two-beam model constructed using symmetry of the 2D lattice in (e) and assuming rigid nodes.

The stiffness S of any material is defined as the amount of deflection δ subject to a given load F, expressed as $S = F/\delta$. The effective stiffness of the simplified non-rigid and rigid beam models shown in Figs. 2.3c,f, respectively, are taken to be the deflection in the vertical direction under an applied load. The diagonal beams are taken to have length L, cross-sectional area A, area moment of inertia I, constituent material stiffness E_s, and are oriented at an angle θ with respect to horizontal. The axial stiffness of the horizontal beam in the rigid-beam model is taken to be a factor α different than the diagonal beam; this factor is intended to account for differences in length and/or cross-sectional area. The stiffness of these one- and two-beam model systems is found to be, respectively,

$$S_{\text{non-rigid}} = \frac{E_s}{\frac{L^3}{12I}\cos^2\theta + \frac{L}{A}\sin^2\theta}, \tag{2.5}$$

$$S_{\text{rigid}} = \frac{E_s\left[1 + \alpha\left(\cos^2\theta + \frac{AL^2}{12I}\sin^2\theta\right)\right]}{\frac{L^3}{12I}\left(\cos^2\theta + \alpha\right) + \frac{L}{A}\sin^2\theta}. \tag{2.6}$$

In the simple case where $\theta = \pi/4$ and $\alpha = 1$, these equations reduce to

$$S_{\text{non-rigid}} = \frac{2E}{\frac{L^3}{12I} + \frac{L}{A}}, \tag{2.7}$$

$$S_{\text{rigid}} = \frac{E\left(3 + \frac{AL^2}{12I}\right)}{\frac{L^3}{4I} + \frac{L}{A}}. \tag{2.8}$$

The stiffness of the non-rigid beam model can be identified as a Reuss model construction of a bending and stretching beam in series, where the axial stiffness of a beam is $S_{\text{axial}} = E_s A/L$ and the stiffness of an Euler-Bernoulli beam in bending is $S_{\text{bend}} = CE_s I/L^3$ and C is a constant depending on the boundary conditions. The stiffness of the rigid beam model is similar to the non-rigid model but has an additional term in the numerator. This additional term arises because the horizontal beam provides a reaction force proportional to the ratio between the stiffnesses of the two beams, which can be expressed as $F_{\text{react}} \propto F_{\text{applied}}(S_{\text{horz}}/S_{\text{bend}} + S_{\text{horz}}/S_{\text{axial}})$. In the extreme case where $\alpha \to \infty$, which represents a diagonal beam fixed on a rigid surface, this equation reduces to the Voigt model construction of a bending and stretching beam as

$$S_{\text{rigid}}\big|_{\alpha\to\infty} = E_s\left(\frac{12I}{L^3}\cos^2\theta + \frac{A}{L}\sin^2\theta\right). \tag{2.9}$$

In regular lattices, such as those shown in Figs. 2.3a,d, the structure can be approximated as a repeating periodic arrangement of the simple reduced non-rigid and rigid beam models. The stiffness of the lattice can then be approximated to be proportional to the stiffness of the reduced model systems, and the stiffness of non-rigid and rigid lattices can be expressed as

$$S_{\text{non-rigid}} = \frac{E_s}{A_1\frac{L^3}{I} + A_2\frac{L}{A}}, \tag{2.10}$$

$$S_{\text{rigid}} = \frac{E_s\left(1 + B_1\frac{AL^2}{I}\right)}{B_2\frac{L^3}{I} + B_3\frac{L}{A}}. \tag{2.11}$$

Here, A_1, A_2, B_1, B_2, and B_3 are constants that depend on the number of diagonal and horizontal beams in a structure, the angle θ, and the horizontal beam stiffness α. The effective (structural) Young's modulus E of a lattice can then be identified as the

ratio of stress (force normalized by the effective area A_{eff}) and strain (displacement normalized by the effective height H_{eff}), so that $E = S\frac{H_{\text{eff}}}{A_{\text{eff}}}$. The height and area of a unit cell with beams of length L are approximately $H_{\text{eff}} \sim L$ and $A_{\text{eff}} \sim L^2$, giving $E \approx S/L$. Taking a lattice constructed from circular beams, the area and area moment of inertia are $A_s = \pi R^2$ and $I_s = \frac{\pi}{4}R^4$, respectively. From this, the expression for Young's modulus of a rigid and non-rigid lattice are, respectively,

$$E_{\text{non-rigid}} = \frac{E_s}{A_1\left(\frac{R}{L}\right)^{-4} + A_2\left(\frac{R}{L}\right)^{-2}}, \tag{2.12}$$

$$E_{\text{rigid}} = \frac{E_s\left[1 + B_1\left(\frac{R}{L}^{-2}\right)\right]}{B_2\left(\frac{R}{L}\right)^{-4} + B_3\left(\frac{R}{L}\right)^{-2}}. \tag{2.13}$$

In the extreme case of very slender beams (i.e., $R/L \ll 1$), these equations approach $E_{\text{non-rigid}} \approx A_1 E_s\left(\frac{R}{L}\right)^4$ and $E_{\text{rigid}} \approx B_1 E_s\left(\frac{R}{L}\right)^2$, which are the previously derived analytical models for a bending- and stretching-dominated solid, respectively [46]. Neither the proposed models nor the previous analytical models account for shear in the beams or stiffness of the nodes, both of which are likely to be dominant factors affecting the stiffness of the lattices. Despite this, the proposed rigid and non-rigid stiffness models serve to explain deviations from power-law scaling at high R/L-ratios by accounting for both bending and stretching in the beams.

2.4 Finite-element Models

2.4.1 Beam-element Models

In order to account for stretching and bending of struts in rigid and non-rigid topologies, initial finite element analyses were performed with three-dimensional two-node Euler-Bernoulli and Timoshenko beam elements in an in-house finite element code. The beam elements are equipped with six degrees of freedom per node and include a small-strain assumption. A linear elastic material model was used, and each strut was refined into an appropriate number of elements to ensure mesh-independent results. For the octahedron, cuboctahedron, and tetrakaidecahedron topologies, the full $5 \times 5 \times 5$ unit cell lattice was modeled. For the 3D Kagome, the full $6 \times 6 \times 3$ unit cell was modeled. All nodes in the bottom face of the unit cell were fixed (translations and rotations), and the top nodes were only constrained in the z-direction; a 1% compressive strain was applied to extract the effective vertical stiffness.

2.4.2 Full-resolution 3D-element Models

Finite element simulations of the solid and hollow unit cells were also performed using the commercial finite element code Abaqus. All simulations were performed statically with linear perturbations to obtain the linear stiffness of each topology. The solid unit cell simulations were performed using C3D10 10-node quadratic tetrahedral elements, and the hollow simulations used S3R 3-node shell elements to represent the discretized unit cells. An isotropic linear elastic material model was used for both solid and hollow structure simulations, and stiffnesses for the constituent polymer and Al_2O_3 were obtained from literature [14, 93]. Solid unit cell simulations had between 25,000 and 250,000 elements and hollow unit cell simulations had between 25,000 and 100,000 elements; the exact number of elements varied depending on the unit cell and structural parameters used.

Simulations of the full-scale lattices tested in the experiments required prohibitively expensive computational resources, so single unit cells subject to periodic boundary conditions (PBCs) were simulated to obtain the effective stiffness of the periodic lattices. PBCs were manually implemented in a similar fashion to [143]. To simulate uniaxial stressing of the periodic structure, the z-component of the volume-averaged strain was imposed, while the transverse components remained unconstrained and periodicity of the unit cell was enforced by solving for the unknown relative displacements U_i^Δ on the X- and Y-faces below. The procedure of implementing the PBCs is summarized below.

LOA 1 | Periodic Boundary Conditions

Require: periodic mesh within tol.
  for node i on X^+ face **do**
    find matching X^- face node
Ensure: $U_1^+ - U_1^- = U_1^\Delta$ (constrain transverse displacements)
Ensure: $U_2^+ = U_2^-, U_3^+ = U_3^-$ (constrain in-plane displacements)
Ensure: $\theta_j^+ = \theta_j^-$ **for** $j = \{1, 2, 3\}$ (constrain rotations)
  end for
  Repeat for Y- and Z-faces
Ensure: $U_3^\Delta = \Delta z$ (constrain volume-averaged strain in z-direction)

Note that the rotation constraint was only needed for the hollow simulations since the tetrahedron elements used in the solid unit cell simulations do not have rotational degrees of freedom. The effective stiffness of the periodic lattice was calculated as the ratio between the average strain and the average stress of the unit cell

in the z-direction. Taking F to be the reaction force across the top surface and L to be the unit cell side length, the modulus was calculated as

$$E = \frac{\sigma_{\text{avg}}}{\varepsilon_{\text{avg}}} = \frac{F}{L\Delta z}. \tag{2.14}$$

2.4.3 Results

The beam-element models, in general, failed to match the response of the experiments and the 3D-element models but provide insight on the sources of deviation from classical scalings. The beam models for the cuboctahedron and octet-truss lattices matched the theoretical scaling of the form $E \propto (R/L)^b$ at low (R/L) ratios, with $b = 2.003$. Both of these models showed a deviation from this theoretical scaling at higher (R/L) ratios, although the deviation was not as significant as that observed in the full resolution, 3D-element models. The beam model for the 3D Kagome lattice failed to match the theoretical scaling at low density and underpredicted the 3D-element model's results. Larger tessellations of the 3D Kagome lattices ($18 \times 18 \times 9$ unit cells) were necessary to approach the stiffness from the full-resolution models at low densities. This response is attributed to the finite size of the tessellated lattice, since the free boundaries activate intrinsic zero-energy mechanisms and make beam-element models fundamentally unable to match the stiffness of the periodic (infinite) lattice for this geometry (i.e., such as with periodic boundary conditions). The non-rigid tetrakaidecahedron models, on the other hand, initially matched the theory with a scaling of $b \approx 4$, but showed a similar deviation from the power-law fit at higher (R/L) ratios. Since the beam models inherently ignore the effect of the intersection volume at nodes, the models in Fig. 2.4 diverge from the full-resolution simulations at higher (r/l) ratios for all topologies except the 3D Kagome, which are observed to converge at higher (R/L) ratios. This unexpected convergence is likely an artifact caused by the relatively high sensitivity of the 3D Kagome lattice to the boundary conditions. Fitting the Euler-Bernoulli beam simulations with their respective rigid and non-rigid models (Eqs. 2.12, 2.13) yielded a correlation coefficient of $R^2 = 1.000$ for all cases (Fig. 2.4).

The same beam-model simulations were performed for the hollow geometries, also failing to agree with the full-resolution simulations (Fig. 2.5). Both the Timoshenko and Euler-Bernoulli beams significantly over-predicted the stiffness of all four topologies across all relative densities. This is attributed to the compliant hollow nodes that are not correctly modeled in the simple slender-beam simulations.

Full-resolution finite element (FE) simulations of monolithic polymer lattices help

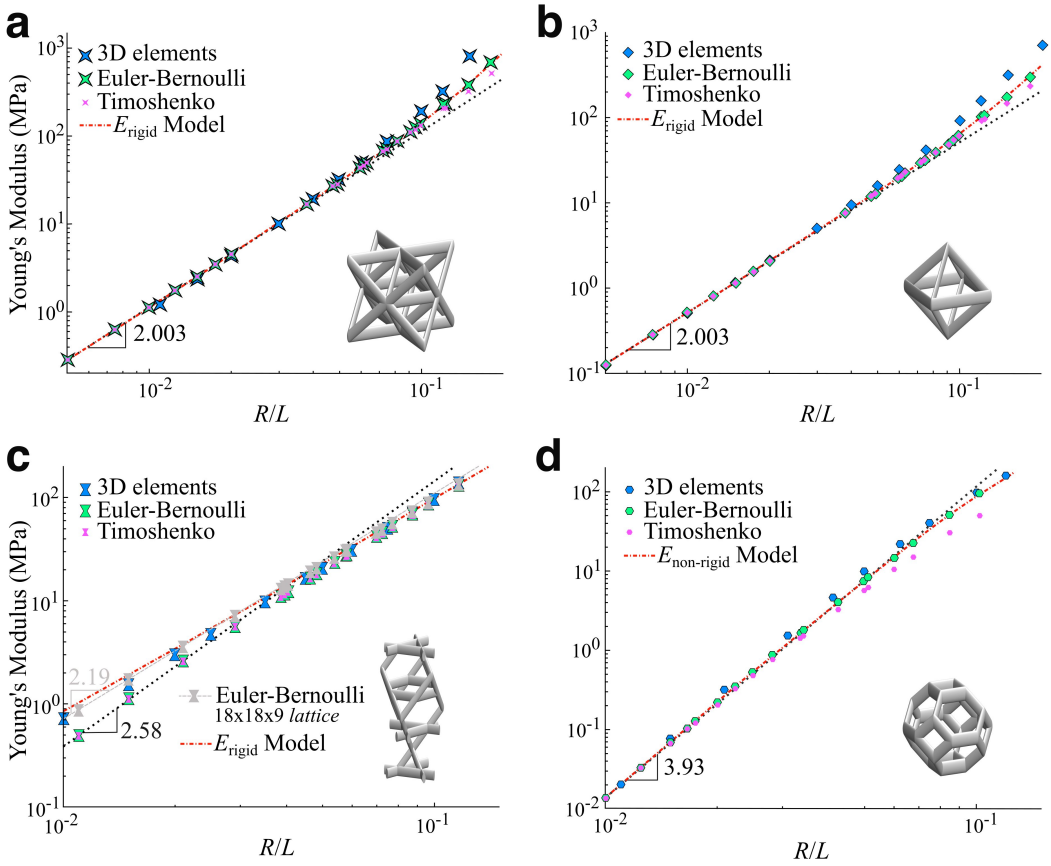

FIGURE 2.4 | SOLID EULER-BERNOULLI AND TIMOSHENKO BEAM SIMULATIONS VS. FULL-RESOLUTION 3D-ELEMENT MODELS

(a) Octet unit cell, **(b)** cuboctahedron unit cell, **(c)** 3D Kagome, and **(d)** tetrakaidecahedron unit cell. The black trend line denotes the scaling exponent b at low relative densities, calculated using the lowest three relative density simulations. The red fit lines correspond to the E_{rigid} and $E_{\text{non-rigid}}$ models, which yielded a correlation coefficient of $R^2 = 1.000$ in all cases. For the 3D Kagome unit cell (c), a strong dependence on boundary conditions was observed, meaning that a much larger lattice ($18 \times 18 \times 9$) was needed to approach the full-detail simulations. The E_{rigid} Model line for the 3D Kagome is fit to the data for the $18 \times 18 \times 9$ model.

shed more light onto the underlying causal mechanisms for this observed deviation from analytical predictions. Figure 2.6 shows that at the relative densities investigated in the experiments, the simulated stiffnesses are in excellent agreement with the experimental results and show a similar nonlinear scaling. At relative densities below experimentally attainable ones, the simulations show a transition to a different, topology-dependent scaling relation. For the rigid octet-truss and periodically rigid cuboctahedron, we identified a transition in the stiffness scaling from $m \approx 2$ when the beams have slendernesses of $\lambda < 25$ ($\overline{\rho} \gtrsim 10\%$) to $m \approx 1$ when the beams

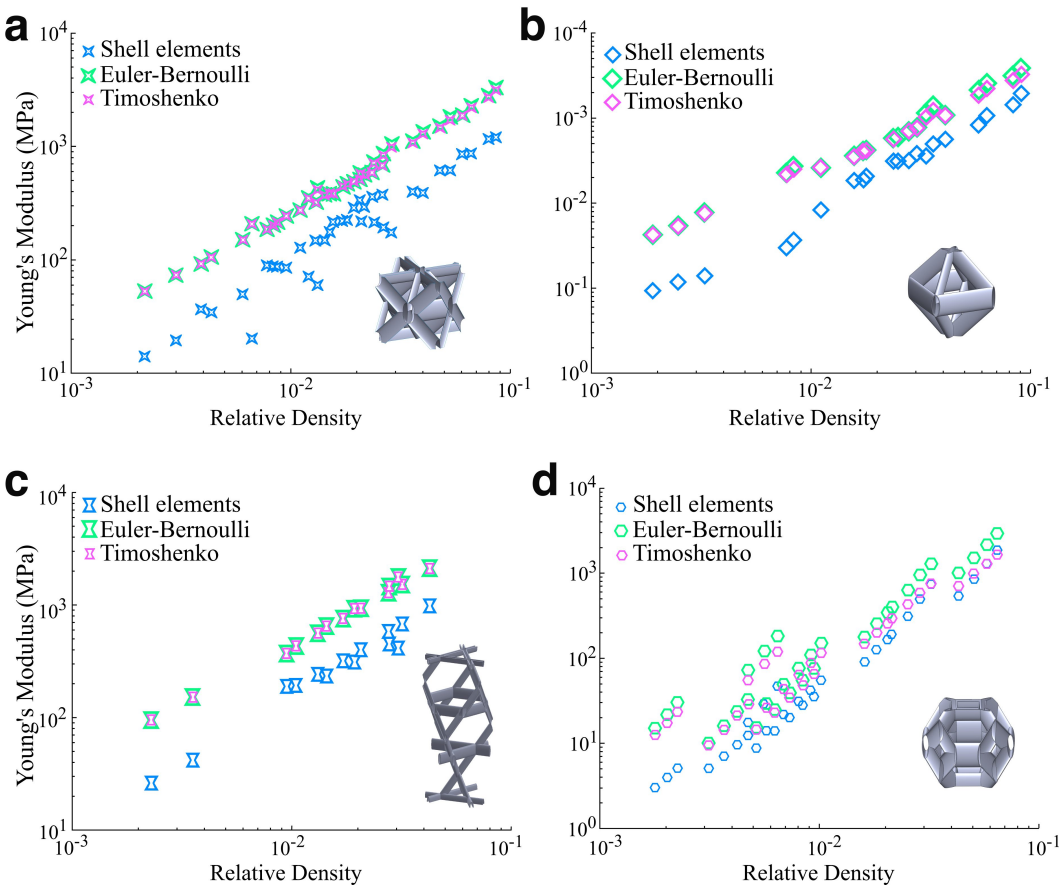

FIGURE 2.5 | HOLLOW EULER-BERNOULLI AND TIMOSHENKO BEAM SIMULATIONS VS. FULL-RESOLUTION SHELL-ELEMENT MODELS
(a) Hollow octet unit cell, **(b)** hollow cuboctahedron unit cell, **(c)** hollow 3D Kagome, and **(d)** hollow tetrakaidecahedron unit cell.

have slendernesses of $\lambda > 25$ ($\overline{\rho} \lesssim 10\%$). Similarly, a transition from $m \approx 1.4$ when beams have slendernesses of $\lambda < 27$ ($\overline{\rho} \gtrsim 9\%$) to $m \approx 1$ when beams have slendernesses of $\lambda > 27$ ($\overline{\rho} \lesssim 9\%$) exists for the periodically rigid 3D Kagome. For the non-rigid tetrakaidecahedron, a similar transition occurs from a scaling of $m \approx 1.5$ when the beams have slendernesses of $\lambda < 7$ ($\overline{\rho} \gtrsim 7\%$) to $m \approx 2$ when the beams have slendernesses of $\lambda > 7$ ($\overline{\rho} \lesssim 7\%$), which matches the analytic prediction for a non-rigid topology of $E \propto \overline{\rho}^2$. The FE scaling fits shown in Figure 2.6 are taken using the 4 densest and 4 least dense points, which is the reason for the slight discrepancy from the experimentally obtained scaling coefficients.

Finite element simulations of hollow Al_2O_3 nanolattices with the same structural parameters as used in experiments corroborated most of the experimental findings. Simulations for octet, cuboctahedron, and 3D Kagome lattices match experimen-

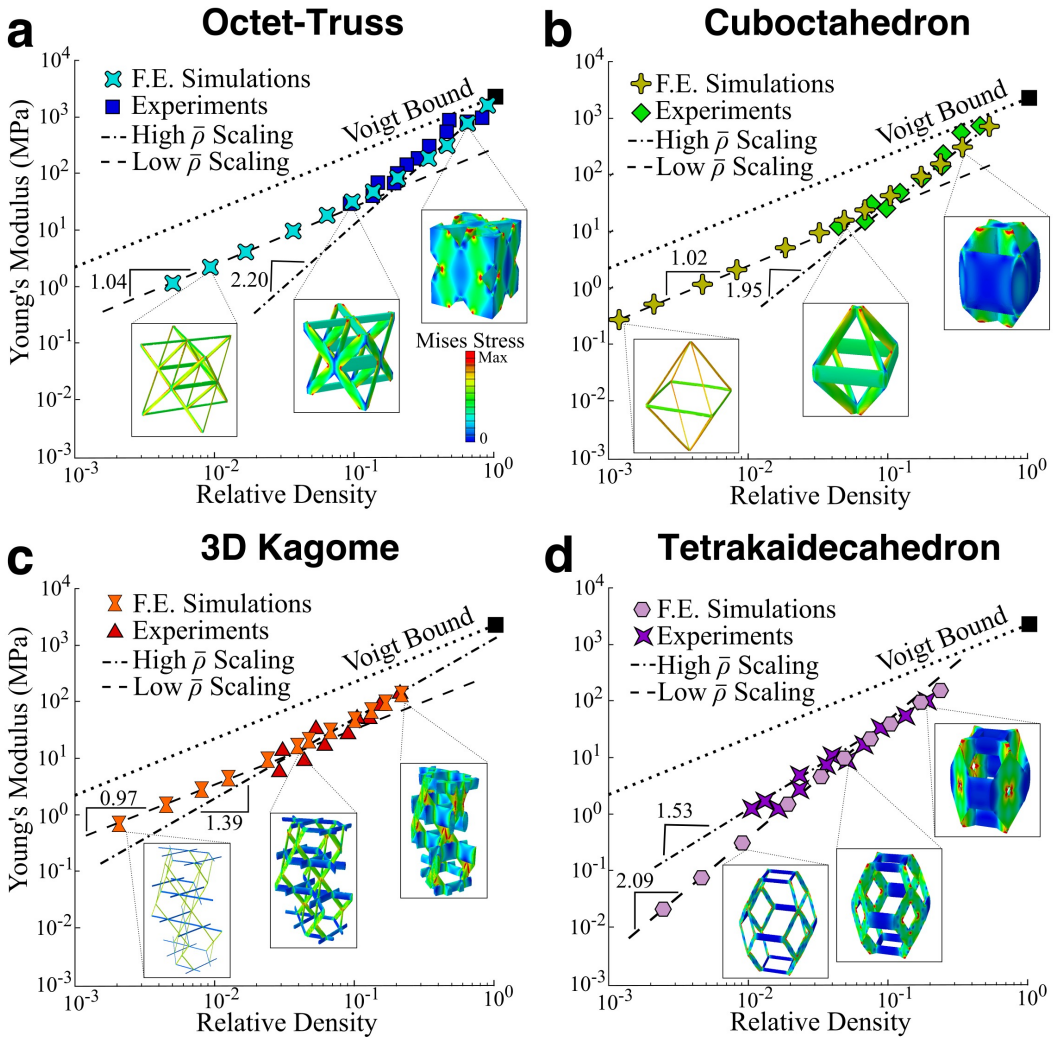

FIGURE 2.6 | SOLID-BEAM NANOLATTICES FE AND EXPERIMENTAL YOUNG'S MODULUS VS. RELATIVE DENSITY
Illustration of the comparison between FE and experimental results for **(a)** octet-truss, **(b)** octahedron, **(c)** 3D Kagome, and **(d)** tetrakaidecahedron lattices. The plots demonstrate the transition to the theoretical scaling relations at low density, as well as the agreement between experimental and FE results at low density. Insets show the stress distribution in the compressed lattices.

tal results at high relative densities ($\overline{\rho} \gtrsim 1\%$) and are at most a factor of 2–3 higher than experimental results at the lowest relative densities ($\overline{\rho} \lesssim 1\%$) (Fig. 2.7a,b). The simulated tetrakaidecahedron stiffness matches experimental results across the entire range of relative densities (Fig. 2.7c). Simulations of hollow nanolattices with structural parameters that span beyond those that were tested experimentally reveal a more complex landscape. A highly non-linear relationship between Young's mod-

ulus and relative density emerges in hollow octet-truss simulations when the beam wall thickness-to-length ratio (t/L) is held constant and the beam semi-minor axis-to-length ratio (R/L) is varied, with large deviations from experimental stiffness scaling (Fig. 2.8a). We observed a similar deviation from linearity in the hollow tetrakaidecahedron, but the result is less pronounced (Fig. 2.8b).

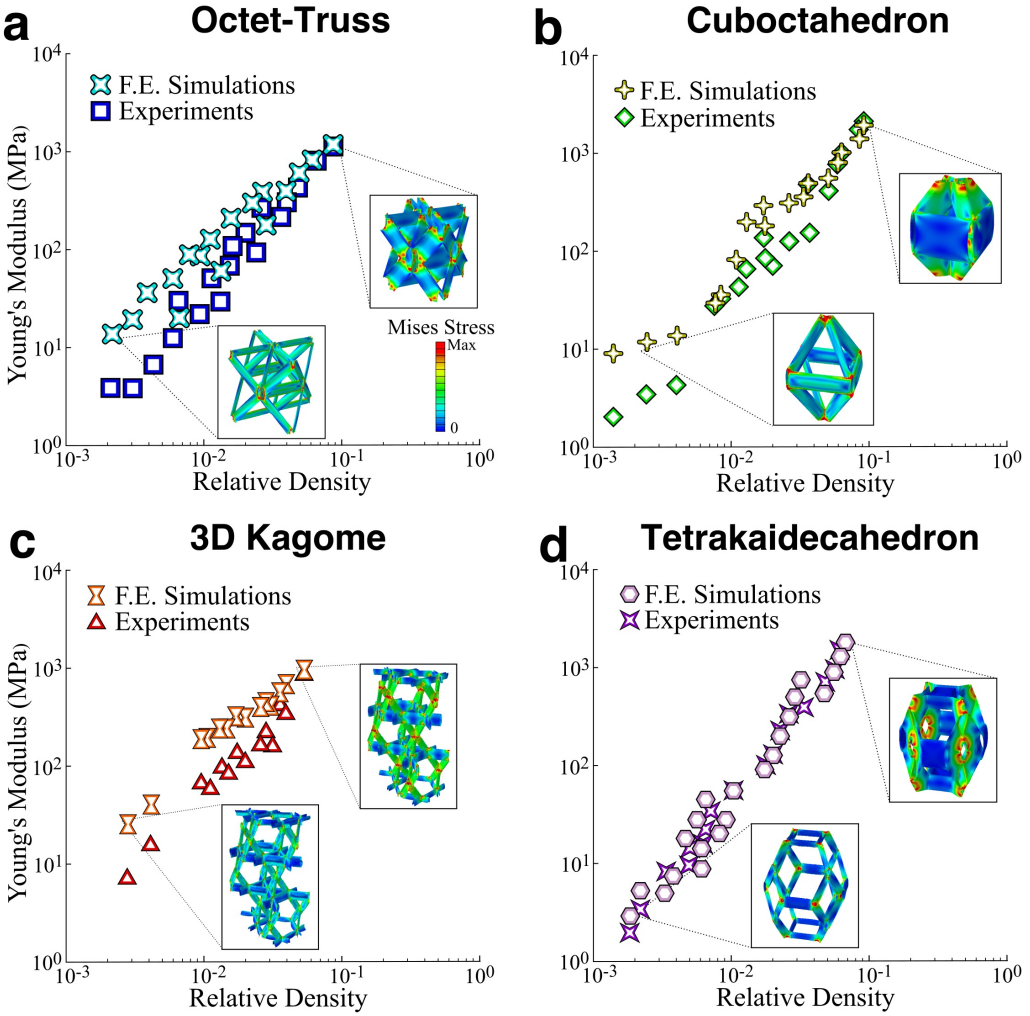

FIGURE 2.7 | HOLLOW-BEAM NANOLATTICES FE AND EXPERIMENTAL YOUNG'S MODULUS VS. RELATIVE DENSITY

Illustration of the comparison between FE and experimental results for **(a)** octet-truss, **(b)** octahedron, **(c)** 3D Kagome, and **(d)** tetrakaidecahedron lattices, showing convincing agreement between experimental and FE results across the range of structural parameters tested experimentally. Insets show the stress distribution in the compressed lattices.

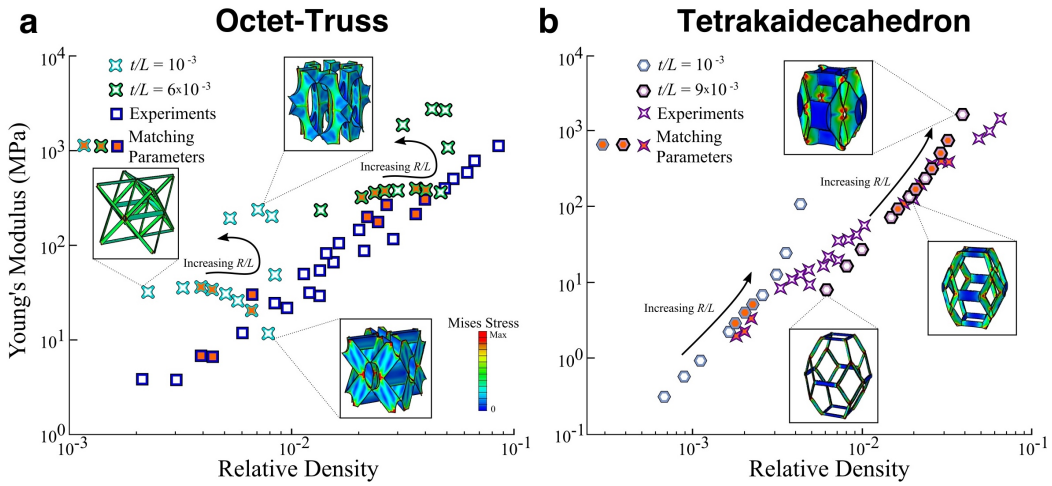

FIGURE 2.8 | EXTENDED HOLLOW-BEAM OCTET-TRUSS AND TETRAKAIDECAHEDRON NANOLATTICE SIMULATION RESULTS
Comparison of the stiffness data of **(a)** octet-truss and **(b)** tetrakaidecahedron lattices obtained from experiments and from finite element simulations. Two t/L values were studied for each geometry over a wide range of R/L values. Simulation and experimental data points with matching R/L and t/L values are filled with orange.

2.5 Discussion

2.5.1 Solid beam nanolattices

The strong agreement between FE and experimental results for solid nanolattices across all relative densities and topologies suggests that the FE models accurately capture the dominant features that govern the elastic behavior (Fig. 2.6). The small variance between the two results can be attributed to factors like waviness in the beams [94], non-uniformity of the cross sections [121], surface roughness [94], misalignment of the nodes, and edge effects from the finite size of the samples in experiments. Solid-beam nanolattices in low-density regimes are difficult to realize experimentally because of their high sensitivity to defects and external processing parameters. All nanolattices with beams that had slendernesses of $\lambda > 70$ were prone to spontaneous collapse because small stresses that arise during writing and developing of the photopolymer can cause premature buckling of the highly slender beams. This is what set the relative density limit of the solid polymer samples in this work.

The close agreement between the FE, Euler-Bernoulli and Timoshenko beam results at low densities ($\overline{\rho} < 1\%$) suggests that beam theories are adequate to predict lattice stiffnesses in these regimes (Fig. 2.4). At higher relative densities, Euler-Bernoulli

beam lattice simulations show a divergence from power law scaling that is similar to experimental data and FE results and generally underpredict the magnitude of the stiffness (ig. 2.4). Simulations using Timoshenko beam models, which account for shear deformation and are used to model less slender beams, have a lower stiffness than Euler-Bernoulli beam models and further underpredict the stiffness. The simplified stiffness model in Eq. 2.13 provides insights into the mechanisms for the scaling of rigid and non-rigid solid beam lattices, viz. that there are contributions from both bending and stretching of beams at high relative densities, which leads to a stiffening behavior, but it does not fully capture the mechanisms behind the observed deviation. The incorrect stiffness prediction of beam-based models occurs primarily because they fail to account for the contribution of the nodes to the overall mechanical properties. In solid-beam lattices, the nodes form solid joints that hinder beam rotation, shortening the effective length of the constituent beams and generally leading to higher stiffnesses. While beam models that capture shearing behavior, such as Timoshenko models, can be used to more accurately capture the behavior of short beams [76, 91], they lead to a drop in the effective stiffness, which is opposite from the trend observed here. Accurately replicating the mechanics of solid lattices with computationally efficient models, similar to what is done using beam elements, requires in-depth investigations into the role of nodes on the mechanical properties, which is outside the scope of this work.

At the lowest simulated relative densities ($\overline{\rho} < 1\%$), the FE results show that Young's modulus of monolithic polymer cuboctahedron and octet-truss lattices scales as $E = E_s\overline{\rho}/8.7$ and $E = E_s\overline{\rho}/9.0$, respectively (Fig. 2.6a,b). These moduli agree well with the existing analytic prediction for the modulus of $E = \overline{\rho}E_s/9$ using pin-jointed bars [35], and are well matched by Euler-Bernoulli and Timoshenko beam models. For the 3D Kagome lattices, FE results predict a stiffness scaling of $E = E_s\overline{\rho}/6$ at low relative densities (Fig. 2.6c). This result is different than both the Euler-Bernoulli and Timoshenko beam simulations (Fig. 2.4). This difference occurs because the 3D Kagome lattice is periodically rigid and has a low connectivity, making it highly sensitive to imperfections and boundary conditions. The FE simulations were performed using periodic boundary conditions, making the lattice effectively infinite; the Euler-Bernoulli simulations were performed on a finite lattice, rendering them sensitive to boundary conditions and preventing them from attaining a linear scaling at low relative densities. This suggests that it is impossible in a practical sense to fabricate a 3D Kagome lattice with a perfectly linear stiffness scaling at any relative density.

2.5.2 Hollow-beam nanolattices

The mechanical behavior of hollow-beam nanolattices is notably different from that of solid-beam nanolattices. Two main factors affect the stiffness of hollow lattices: (*i*) the hollow nodes in thin-walled beams become highly compliant in bending and lead to a reduced overall stiffness, and (*ii*) the surface roughness that arises from beam waviness inherent in the manufacturing process can cause a significant drop in both axial and bending stiffness at low wall thicknesses. Euler-Bernoulli and Timoshenko beam simulations for hollow lattices fail to capture the effect of the hollow nodes and, as a result, consistently over-predict the stiffness (Fig. 2.5).

Fully resolved finite element simulations of the hollow lattices capture the effect of the nodes, and, because they are performed on ideal structures, the observed discrepancy from experiments can primarily be attributed to the imperfections. Octet-truss, cuboctahedron and 3D Kagome lattices transmit load relatively uniformly throughout their beams (Fig. 2.7a-c), rendering their thinner-walled variations highly sensitive to roughness. This thin-walled sensitivity correlates well with the observed overprediction of the stiffness in the FE simulations at low relative densities (Fig. 2.7). The non-rigid tetrakaidecahedron lattices accommodate macroscopic deformation through local deformation at the nodes (Fig. 2.7d), which causes them to be sensitive to nodal compliance and less sensitive to the beam waviness. The primary imperfections at the nodes exist in the form of misalignment [62], which have a minimal effect on the stiffness [91] and lead to an agreement between FE and experimental results across the tested range of relative densities.

The complex parameter space revealed by FE simulations of hollow nanolattices (Fig. 2.8) arises because the relative density and stiffness depend on two dimensionless parameters: R/L and t/L, where R is the minor axis of the elliptical beam, t is the wall thickness, and L is the length of the beam. The highly non-linear relationship between relative density and these dimensionless parameters (Eq. 2.4) can give rise to hollow nanolattices with different R/L and t/L that have identical relative density. This leads to situations where samples can have the same geometry, wall thickness, and relative density but can have over an order-of-magnitude difference in stiffness. For example, simulations of two different hollow octet unit cells with the same wall-thickness-to-length ratio, $t/L = 10^{-3}$, and with two different cross-sectional dimensions of $R/L = 0.1$ ($\overline{\rho} = 0.78\%$) and $R/L = 0.15$ ($\overline{\rho} = 0.81\%$), have stiffnesses of 11 MPa and 205 MPa, respectively. These samples are visually distinct (Fig. 2.8a), with one appearing more similar to a solid beam lattice and

the other more closely resembling a membrane structure, but they are topologically identical. This complex parameter space reveals that classical scaling laws that depend only on architecture and relative density are incapable of fully capturing the mechanical properties of hollow lattices, and new theories that incorporate the effect of hollow nodes are needed to accurately predict their stiffness. It should be noted that the ellipticity of the beams will have an effect on the stiffness of the lattices, particularly for low-slenderness beams, but quantifying this effect is beyond the scope of this work.

2.6 Generalization to Macroscopic Experiments and Larger Tessellations

To support the generality of the results presented in this work, we fabricated and tested octet-truss lattices at the macro- and microscopic scale with tessellations of $5 \times 5 \times 5$ and $7 \times 7 \times 7$ unit cells. We fabricated the macroscopic lattices out of PR-48 resin using an Ember 3D Printer (Autodesk) and compressed them using an Instron mechanical testing machine, while the microscopic samples were fabricated and tested in the same manner as the other samples in this study. These polymer "macro"-lattices had ~2.65 mm-long beams with 450 μm to 850 μm-diameter circular cross-sections, 3.75 mm unit cells, and overall sample dimensions of $19 \times 19 \times 19$ mm and $27 \times 27 \times 27$ mm (Fig. 2.9).

Figure 2.10 shows the Young's modulus and yield strength as a function of relative density for polymer octet-truss nanolattices and polymer octet-truss macrolattices. This plot reveals that the nano- and macro-lattices have nearly identical scaling coefficients of $m = 1.77$ and $m = 1.91$ for stiffness and of $n = 1.88$ and $n = 1.86$ for strength, respectively. The tessellation seems to not play a significant role in the stiffness or strength scalings, indicating that the $5 \times 5 \times 5$ tessellation is a satisfactory approximation of larger, continuum-like representative volumes of an octet-truss material. The slight offset in the strength and stiffness between the two lattice systems is a result of the slightly weaker properties of the PR-48 polymer (macro-lattices) compared to the IP-Dip polymer (nanolattices) and the circular beams in the macro-lattices compared to the elliptical ones in the nanolattices. The properties of the PR-48 polymer were determined through uniaxial compression experiments in an Intron testing machine, using a cylindrical specimen with a 15 mm-diameter and a height-to-diameter ratio of 2, revealing a constituent stiffness of $E = 1.30 \pm 0.03$ GPa and strength of $\sigma_y = 33.0 \pm 1.0$ MPa. These results directly support the applicability of the conclusions drawn in this chapter to solid-beam lattices of any material and absolute dimensions within the relevant ranges of

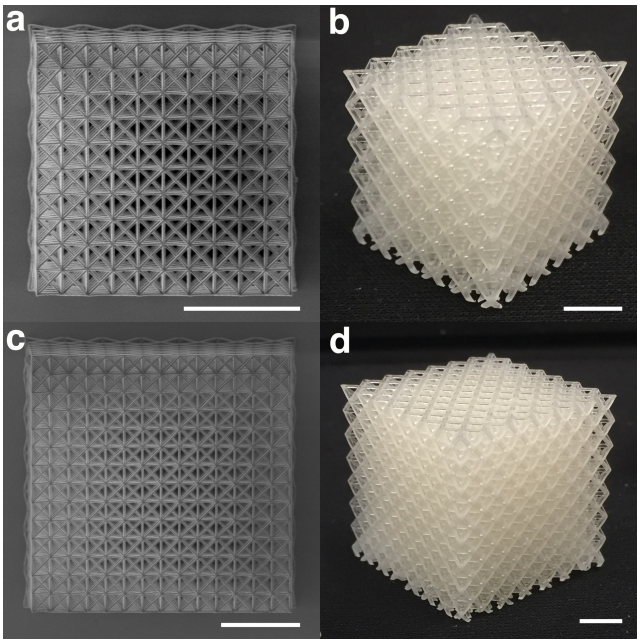

Figure 2.9 | Polymeric Nano- and Macro-Scale Octet Trusses of Variable Tessellations
Polymeric $5 \times 5 \times 5$ **(a)** nanolattices and **(b)** macro-lattices, and self-similar $7 \times 7 \times 7$ **(c)** nanolattices and **(d)** macro-lattices. Scale bars in (a),(c), 20 µm, and (b),(d), 1 cm.

R/L.

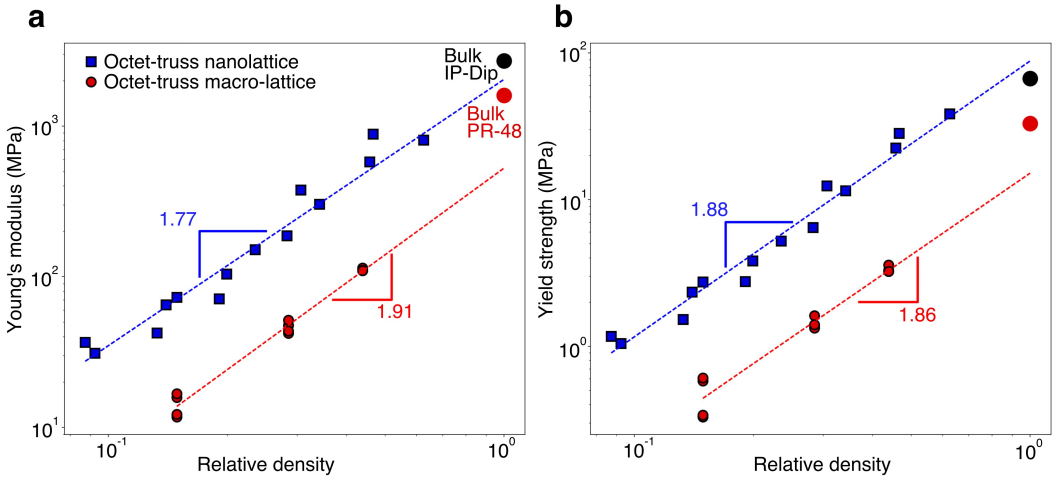

Figure 2.10 | Properties of Nano- and Macro-Scale Octet Trusses of Variable Tessellations
(a) Stiffness scaling and **(b)** strength scaling for samples at both scales and both $5 \times 5 \times 5$ and $7 \times 7 \times 7$ tessellations.

2.7 Conclusion

In this chapter we provided an in-depth exploration of the parameter space of solid- and hollow-beam nanolattices using experiments, finite element analysis, and beam-based numerical simulations and models. Our work establishes that the strength and stiffness of solid- and hollow-beam nanolattices does not correlate with topology alone, but is instead governed by an intricate combination of geometry and structural parameters. Nanolattices with widely different topologies can have nearly identical strength and stiffness at the same relative density, and hollow nanolattices with the same topology and relative density can have widely different stiffness. We postulate that the convergence of strength and stiffness in solid lattices at higher densities is caused by the increased influence of beam intersections at the nodes. The strength and stiffness parameter space of hollow lattices is highly complex and dependent upon changes in beam length, radius and wall thickness, and a detailed study of these parameters must be conducted before their relative influence can be quantified. These results suggest that the existing classification of nanolattice topologies as solely stretching- or bending-dominated is insufficient, and new theories must be developed to accurately capture the effect of both nodal interferences in solid-beam lattices and empty nodes in hollow-beam lattices on the mechanical properties.

Chapter 3

IMPACT OF NODE GEOMETRY ON NON-SLENDER LATTICE ARCHITECTURES

This chapter has been adapted from

C.M. Portela, J.R. Greer & D.M. Kochmann. "Impact of node geometry on the effective stiffness of non-slender three-dimensional truss lattice architectures". *Extreme Mechanics Letters* (2018) 22, pp. 110–138. DOI: 10.1016/j.eml.2018.06.004.

Contributions: designed and fabricated samples, performed and analyzed the experiments, performed the computational analysis, and wrote the manuscript.

3.1 Chapter Summary

As discussed in in previous chapters, three-dimensional (3D), lattice-based micro- and nano-architected materials can possess desirable mechanical properties that are unattainable by homogeneous materials. Manufacturing these so-called structural metamaterials at the nano- and microscales typically results in non-slender architectures (e.g., struts with a high radius-to-length ratio r/l), for which simple analytical and computational tools are inapplicable since they fail to capture the effects of nodes at strut junctions, which was the source of the deviation observed in chapter 2. Building upon the results in that chapter, we report a detailed analysis that quantifies the effect of nodes on the effective Young's modulus (E^*) of lattice architectures with different unit cell geometries through (*i*) simple analytical constructions, (*ii*) reduced-order computational models, and (*iii*) experiments at the milli- and micrometer scales. The computational models of variable-node lattice architectures match the effective stiffness obtained from experiments and incur computational cost that are three orders-of-magnitude lower than alternative, conventional methods. We highlight a difference in the contribution of nodes to rigid versus non-rigid architectures and propose an extension to the classical stiffness scaling laws of the form $E^* \propto C_1(r/l)^\alpha + C_2(r/l)^\beta$, which holds for slender and non-slender beam-based architectures, where constants C_1 and C_2 change with lattice geometry. We find the optimal scaling exponents for rigid architectures to be $\alpha = 2$ and $\beta = 4$, and $\alpha = 4$ and $\beta = 6$ for non-rigid architectures. These analytical, computational,

and experimental results confirm and quantify the specific contribution of nodes to the effective stiffness of beam-based architectures and highlight the necessity of incorporating their effects into calculations of the structural stiffness. This work provides new, efficient tools that accurately capture the mechanics and physics of strut junctions in 3D beam-based architected materials and brings to light the insufficiency of classifying cellular solids as either stretching- or bending-dominated over the manufacturable parameter space.

3.2 Theory

We begin with simple, representative 2D beam-element networks of rigid and non-rigid geometries to provide intuition on their stiffness scaling as a function of beam slenderness. Using linear two-node Euler-Bernoulli beam elements with circular cross-sections (radius r, modulus E, and length l), we define the beam slenderness as the radius-to-length (r/l) ratio. To account for the effect of the nodes, i.e., the beam junctions, we utilize variable-stiffness rotational springs at junctions in addition to beam elements. With at most two beam elements connected at a given junction in the model, each junction has two translational and two rotational degrees of freedom, the latter of which are coupled by a rotational spring with stiffness k_θ (Fig. 3.1a). The total strain energy density of a structure with n_b beams and n_θ rotational springs assembled in this manner takes the form

$$W_{\text{tot}} = \sum_{i=1}^{n_b} W_b^i + \sum_{j=1}^{n_\theta} W_\theta^j, \tag{3.1}$$

where W_b^i and W_θ^j are the energy densities of the ith linear Euler-Bernoulli beam and the jth rotational spring, respectively. The rotational spring energy is assumed of the form

$$W_\theta^j = \frac{1}{2} k_\theta (\theta_1^j - \theta_2^j)^2, \tag{3.2}$$

where θ_1^j and θ_2^j are the rotational degrees of freedom of the two beams connected at joint j, while the beam energy consists of the classical axial stretching and bending contributions [29].

Upon solving the system of equations, we calculate an effective stiffness for each structure as $k^* = F/u_{\text{top}}$, where F is an applied vertical load at the top node and u_{top} is the resulting vertical displacement of that node. In the limit $k_\theta \to 0$, the deformation transforms into the stretching-only behavior of a rigid structure, while letting $k_\theta \to \infty$ recovers the classical Euler-Bernoulli solution based on fixed nodal connections. The non-rigid structure has zero stiffness in the limit $k_\theta \to 0$, since this

activates a zero-energy mode, i.e., a mechanism. The behavior of the rigid-structure model in the limits resembles the stretching-to-bending transition observed in other works [36, 94], where k_θ can be interpreted as the degree of nodal influence with decreasing beam slenderness.

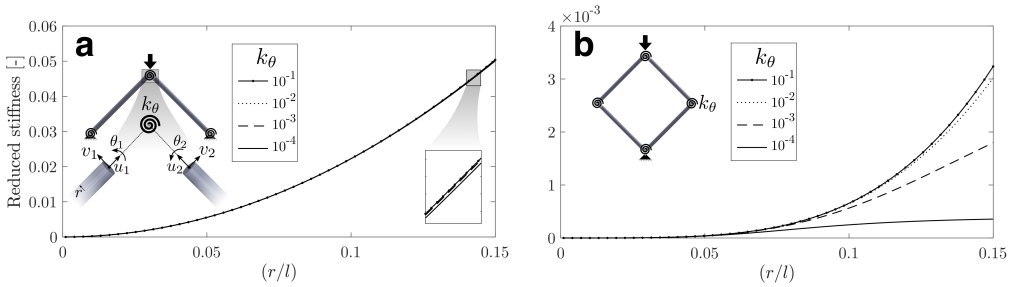

Figure 3.1 | Beam-Spring Model System for Rigid and Non-Rigid Architectures
Effective structural stiffness $\bar{k} = k^*/(El)$ of beam-theory models applied to **(a)** rigid and **(b)** non-rigid geometries that contain rotational springs (variable stiffness k_θ) at all junctions. A significantly more pronounced effect of the nodal stiffness k_θ is observed in the non-rigid structure than in the rigid one.

From the effective stiffness we calculate a dimensionless reduced stiffness $\bar{k} = k^*/(El)$ for the two representative rigid and non-rigid structures shown in Fig. 3.1 and explore their behavior as a function of (r/l) and k_θ. Fig. 3.1a shows negligible changes in the rigid structure's stiffness as k_θ is varied, indicating that nodal geometry is expected to have a small effect on the stiffness behavior of rigid architectures. For the range of spring stiffnesses studied, the effective structural stiffness takes the form $k^* \propto (r/l)^c$ with $c = 2$, which agrees with the classical stiffness scaling laws for highly slender structures since $\bar{\rho} \propto (r/l)^2$ when $(r/l) \ll 1$. In comparison, the non-rigid structure in Fig. 3.1b shows significant changes in stiffness as k_θ varies. Varying the spring stiffness from $k_\theta = 10^{-4}$ to 10^{-1} changes the scaling exponent c from 2.57 to 3.98, which implies that a more pronounced effect of nodal geometry exists for non-rigid architectures compared to rigid ones. In the following, we aim to properly quantify these effects for specific lattice architectures in order to understand the influence of node geometry and the associated nodal stiffness on the effective stiffness of non-slender lattice architectures with refined analysis tools.

3.3 Design of Variable Node Geometry

We designed lattice architectures with tailorable node geometries, isolating nodes as the variable of interest in this work. We systematically explored different node geometries by spatially varying the cross-section of individual struts near their junc-

tions. Starting with a constant-cross-section cylindrical strut of a given radius-to-length ratio (r/l), the node-contributing regions of the strut were defined as those that extend inwards a distance of $(a + b)r$ from the ends[1] (Fig. 3.2b).For the (r/l) range studied in this work, we chose $a = 1.5$ and $b = 1$ to ensure that the nodes did not comprise more than 75% of the strut in the least slender case. The node-contributing region at each end of the strut was segmented into a *modified section*, with a constant designed cross-section, and a *transition section*, with a cross-section that approached the original circular geometry from the modified one (Fig. 3.2c) via a G0 continuous surface with a constant (linear) tangent vector. The *modified sections* were designed to extend inwards from the strut ends a distance ar, while the *transition sections* extended a distance br further from the ends of the *modified sections*. The remaining central *gauge section* of the strut was unmodified, retaining the original circular cross-section. This setup allowed us to arbitrarily modify the nodal geometry independent of the strut cross-section.

When arranging the struts into a desired architecture, the node-contributing regions of connecting struts combine into what we define as a *node* in this work. A node for an architecture with Z struts meeting at a junction corresponds to the combination of Z node-contributing regions belonging to those struts. Three different node geometries were constructed by selecting the *modified* cross-sections of the struts to be (*i*) a circle (i.e., an unmodified strut for reference), (*ii*) a square, and (*iii*) an isotoxal four-point star. The second area moment of the *modified* cross-section ranged from $I_0 = \frac{\pi}{4}r^4$ for the circular strut to $1.05I_0$ for the square strut, and $1.3I_0$ for the star strut. The struts were designed under the constraint that the cross-sectional area remained constant throughout, resulting in equal strut volumes, identical *gauge section* radii r, and unchanged lengths l. Building any desired architecture with each of the three types of struts resulted in unit cells with effectively constant relative densities $\bar{\rho}$ (at most $\pm 0.7\%$ variation) — and equal slenderness ratios (r/l) — that differed only by the node geometry.

To study the effect of different-geometry nodes on lattice stiffness for rigid versus non-rigid architectures, we designed variable-node octahedron (periodically rigid), octet (rigid), tetrakaidecahedron (non-rigid), and pyramidal (non-rigid) lattices. From these four geometries, we selected the octahedron as a representative rigid and tetrakaidecahedron as a representative non-rigid architecture to conduct

[1] This choice is not unique; it was deemed practicable and reasonable in numerical experiments and is expected to not significantly alter the drawn conclusions.

an in-depth analysis via newly developed reduced-order models and experiments at multiple scales.

3.4 Hybrid-Element Numerical Models

We developed reduced-order finite element models for the octahedron and tetrakaidecahedron architectures to capture the non-classical, i.e., non-slender-beam, stiffness of typical experimental sample sizes, such as $5 \times 5 \times 5$ unit cell tessellations. Modeling the actual tessellation of the samples avoided using periodic boundary conditions, which assume an infinite tessellation and neglect any potential boundary effects, see e.g. Latture et al. [74, 75]. Our models were composed of quadratic tetrahedral element substructures for the lattice nodes, and the *gauge sections* were represented by Timoshenko beam elements[2] (Fig. 3.2d,f). This hybrid-element formulation significantly reduced the computational costs compared to a fully 3D solid-element representation.

We created node substructures with circle, square, and star *modified* cross-sections for each architecture type. Each substructure included the node-contributing regions of all struts connecting at a lattice junction and terminated at the circular ends of the *transition sections* of the connecting struts. The octahedron node substructures had eight terminal circular cross-sections ($Z = 8$, Fig. 3.2e); the tetrakaidecahedron node substructures had four ($Z = 4$, Fig. 3.2g). After meshing the substructures with quadratic tetrahedral elements, we performed a static condensation of degrees of freedom (DOFs) (see section 3.4.1) which reduced the substructures to six DOFs per terminal circular cross-section (three translations and three rotations associated with the centroid of each face). This condensation step significantly reduced the computation time, since it is performed only once for each unique node, regardless of the total number of nodes in the periodic lattice. For octahedron node substructures, the problem size was condensed from $15,000$ – $27,000$ DOFs ($3,000$ – $6,000$ elements) to 48 DOFs (six per terminal circular cross-section). For tetrakaidecahedron node substructures, the problem size was reduced from $8,000$ – $12,000$ DOFs ($1,600$ – $2,300$ elements) to 24 DOFs (six per terminal circular cross-section). This condensation procedure assumes linear elastic material behavior for all effective stiffness calculations and will need refined strategies when handling nonlinear or inelastic strut behavior. The resulting condensed-node substructures were tessellated to form a $5 \times 5 \times 5$ lattice, and were connected to each other through

[2] Using the commercial FE code Abaqus, we employed C3D10 tetrahedral elements for the node substructures and B31 Timoshenko beam elements for the struts.

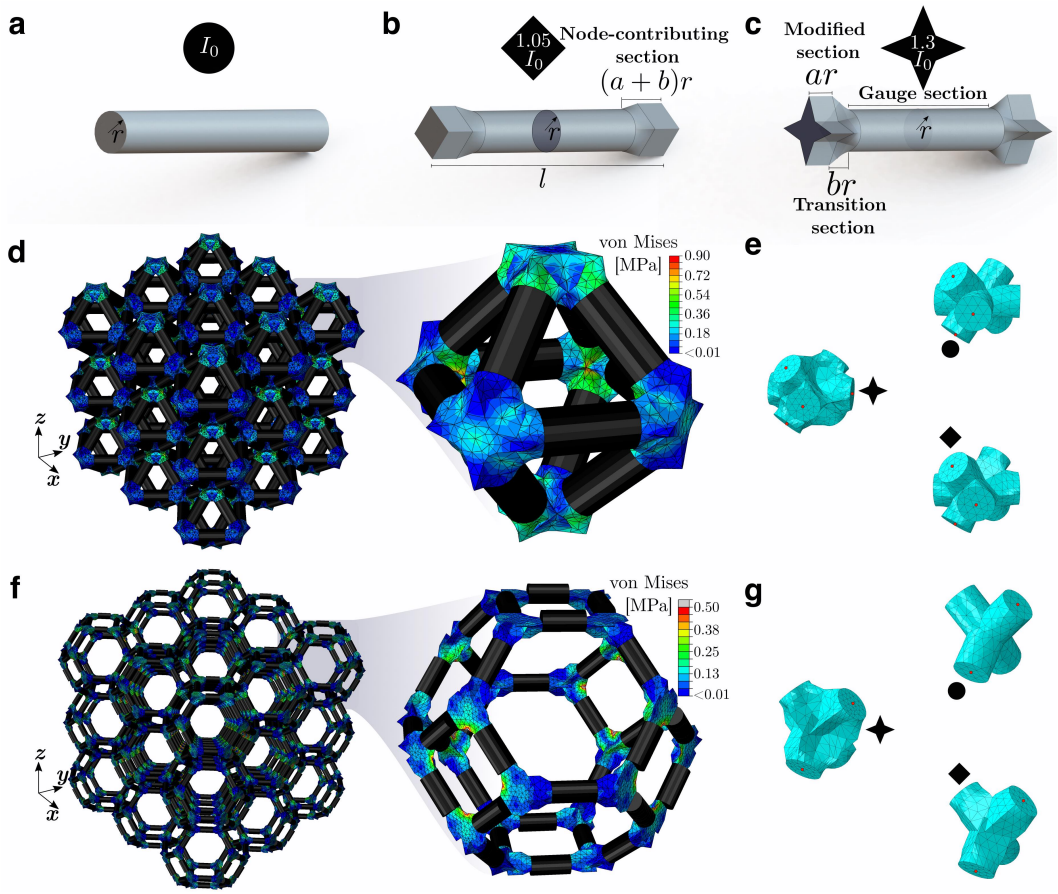

FIGURE 3.2 | NODE MODIFICATION AND IMPLEMENTATION OF REDUCED-ORDER MODELS
Truss architecture and geometry definitions: **(a)** unmodified circular strut of radius r and length l, **(b)** square-modified strut, **(c)** star-modified strut, **(d)** uniaxial compression of a $3 \times 3 \times 3$ reduced-order octahedron model, **(e)** octahedron node substructures depicting the tetrahedral mesh and the retained DOF points in red, **(f)** uniaxial compression of a $3 \times 3 \times 3$ reduced-order tetrakaidecahedron model, and **(g)** tetrakaidecahedron node substructures depicting the tetrahedral mesh and the retained DOF points in red.

ten Timoshenko beam elements per strut, which represented the *gauge section*. The beam elements' DOFs at the ends of the *gauge section* were coupled to the six retained DOFs at each termination circular cross-section.

Throughout this work, we probed the octahedron and tetrakaidecahedron geometries along the $\langle 001 \rangle$ direction, corresponding to nominally stretching- and bending-dominated directions, respectively. The effective modulus E^* of the described lattices was determined via a linear perturbation step by applying uniaxial compression of $\varepsilon = 1\%$ in the z-direction, while constraining in-plane translations and all rotations at the top and bottom surfaces of the lattice. This closely resembles ex-

perimental conditions where the substrate and the indenter tip pose similar constraints. We used an isotropic linear elastic material model with the Young's moduli determined in section 3.5.2, and a Poisson's ratio of $\nu = 0.49$ [93]. To validate the described reduced-order models, we compared the effective stiffness of a substructured versus a fully-resolved unit cell—for different node geometries and (r/l) ratios—and found that the relative difference between the two was at most 3%, while reducing the problem size to 0.02–0.3% of the fully resolved problem (see section 3.4.2 for details).

3.4.1 Substructuring Implementation and Theory

To reduce the number of degrees of freedom (DOFs) at the node substructures, a static condensation of degrees of freedom was performed. For each node substructure, only Z computational nodes were retained, one at each centroid of the Z terminal faces (see Fig. 3.2e,g). The retained computational nodes were not part of the tetrahedral elements on the terminal face, but their six DOFs were coupled to those of the tetrahedral-element nodes at the face. The retained DOFs at a given terminal face were subsequently coupled to the six DOFs of the Timoshenko beam-element node at the edge of the strut representation. In particular, the translational DOFs were forced to on-average match those of the connecting Timoshenko beam, while the rotational DOFs were coupled to the mean rotation of the tetrahedral face nodes.

The condensation process begins by assembling the stiffness equations in the form [29]

$$\begin{bmatrix} \boldsymbol{K}_{rr} & \boldsymbol{K}_{ri} \\ \boldsymbol{K}_{ir} & \boldsymbol{K}_{ii} \end{bmatrix} \begin{bmatrix} \boldsymbol{u}_r \\ \boldsymbol{u}_i \end{bmatrix} = \begin{bmatrix} \boldsymbol{f}_r \\ \boldsymbol{f}_i \end{bmatrix}, \tag{3.3}$$

where $\boldsymbol{u}_r$ and $\boldsymbol{u}_i$ are the retained and internal DOFs, respectively; $\boldsymbol{f}_r$ and $\boldsymbol{f}_i$ are their respective nodal forces, and $\boldsymbol{K}_{rr}$, $\boldsymbol{K}_{ri}$, $\boldsymbol{K}_{ir}$, and $\boldsymbol{K}_{ii}$ are the corresponding stiffness submatrices. Solving the second matrix equation in Eq. 3.3 for the internal DOFs (exploiting that $\boldsymbol{K}_{ii}$ is nonsingular) yields

$$\boldsymbol{u}_i = \boldsymbol{K}_{ii}^{-1} \left(\boldsymbol{f}_i - \boldsymbol{K}_{ir} \boldsymbol{u}_r \right). \tag{3.4}$$

Substitution into the first matrix equation in Eq. 3.3 yields the condensed set of equations as

$$\overline{\boldsymbol{K}_{rr}}\, \boldsymbol{u}_r = \overline{\boldsymbol{f}_r}, \tag{3.5}$$

where the condensed stiffness matrix and force vector are, respectively

$$\overline{\boldsymbol{K}_{rr}} = \boldsymbol{K}_{rr} - \boldsymbol{K}_{ri}\, \boldsymbol{K}_{ii}^{-1}\, \boldsymbol{K}_{ir}, \qquad \overline{\boldsymbol{f}_r} = \boldsymbol{f}_r - \boldsymbol{K}_{ri}\, \boldsymbol{K}_{ii}^{-1}\, \boldsymbol{f}_i. \tag{3.6}$$

The condensed equations are used to obtain the linear response of the substructure while significantly reducing the computational cost. After solving for the condensed DOFs, the internal DOFs are obtained from Eq. 3.4.

3.4.2 Reduced-order Model Validation

To validate the reduced-order models, we compared the effective stiffness of a single octahedron unit cell with substructures to that of a fully refined unit cell. The sides of both types of unit cells were left traction-free and a 1% strain compression was applied in the z-direction, while leaving the x-y displacements of top and bottom faces unconstrained. The node substructures used in the validation consisted of half of the internal node substructures depicted in Figs. 3.2e,g, which simplified the process of applying the boundary conditions. The relative effective stiffness error, Δk^*, between the fully meshed octahedron unit cell (10^5 to 10^6 tetrahedral elements, 1×10^6 to 5×10^6 DOFs, depending on node geometry) and the described substructure-containing unit cell was $\Delta k^* < 3\%$ (Fig. 3.3). The relative stiffness error of a few percent came with a concomitant problem size reduction to 0.02–0.3% of the fully meshed problem size.

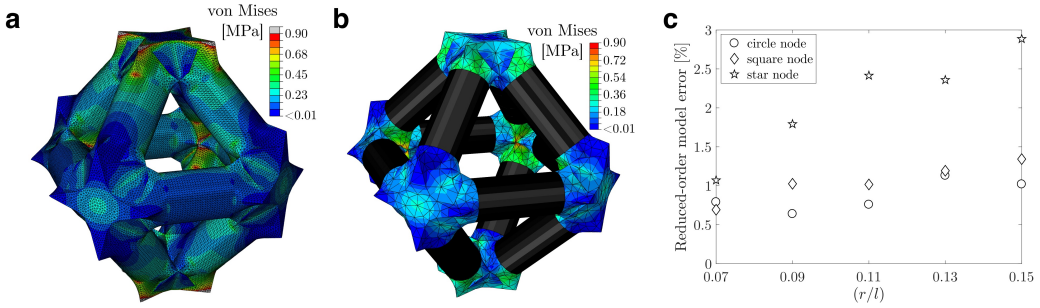

Figure 3.3 | Reduced-Order Model Validation and Error
(a) Full-detail simulation of uniaxial compression of a star-node $(r/l) = 0.11$ octahedron unit cell, with rollers at the top/bottom and unconstrained at the sides (10^6 elements); **(b)** the same simulation with the reduced-order method (126 effective elements); **(c)** summary of the reduced-order model error for all node geometry types and a range of (r/l) values, calculated as the relative difference in the calculated effective stiffness: $\Delta k^* = \frac{k^*_{\text{reduced}} - k^*_{\text{full}}}{k^*_{\text{full}}}$.

3.5 Experimental Framework

3.5.1 Sample Fabrication and Experiments

We fabricated two sets of octahedron and tetrakaidecahedron lattices at different length scales. Microlattices were fabricated using Two-Photon Lithography (TPL) direct laser writing (Photonic Professional GT, Nanoscribe GmbH) out of IP-Dip

photoresist with the same variable-node geometries used in the reduced-order models. These samples consisted of a $5 \times 5 \times 5$ tessellation of 60 µm unit cells, with effective strut diameters ranging from 3.0 µm to 12.7 µm, resulting in overall sample dimensions of $300 \times 300 \times 300$ µm (Fig. 3.5d). A laser power of 15 mW and a scan speed of 10 mm s^{-1} were used for the writing process on a Si substrate. Arrays of 15 µm-diameter and 30 µm-height micropillars with identical process parameters were also written to directly measure the material properties of cross-linked IP-Dip under uniaxial compression (see section 3.5.2).

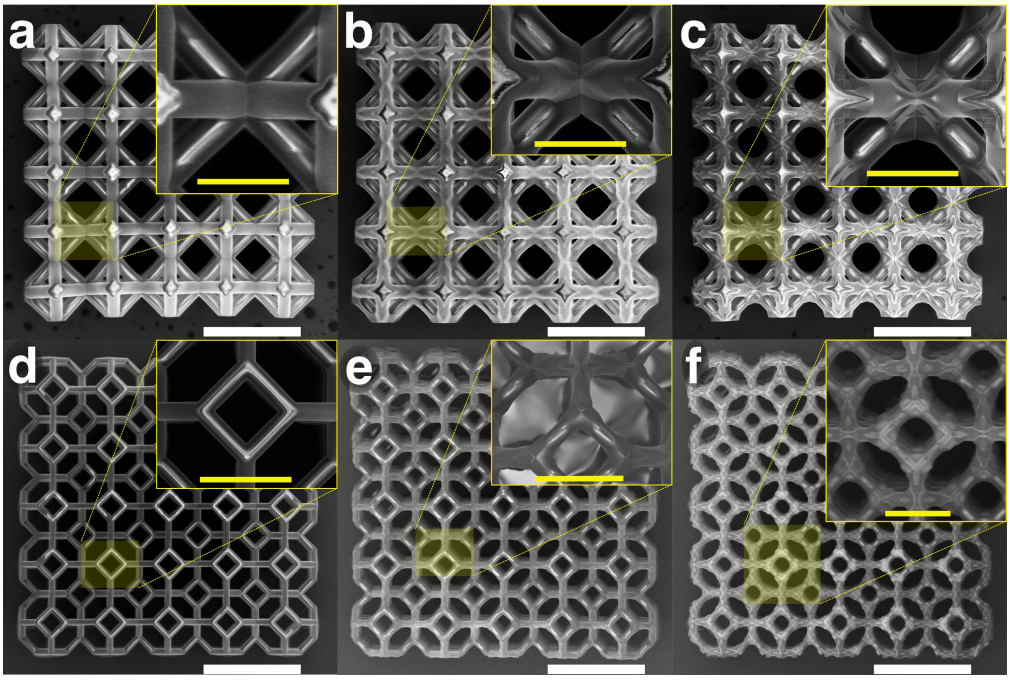

Figure 3.4 | Detailed View of TPL-Lattice Modified Nodes
Micrographs presenting detailed views of the nodes in the TPL lattices with $(r/l) = 0.15$. Octahedron lattices with **(a)** circle, **(b)** square, and **(c)** star nodes. Tetrakaidecahedron lattices with **(d)** circle, **(e)** square, and **(f)** star nodes. Scale bars in white correspond to 100 µm and yellow bars in insets are 30 µm.

Larger, self-similar lattices were manufactured using a 3D Digital Light Processing (DLP) Ember printer (Autodesk, Inc.) out of the PR-48 (Colorado Photopolymer Solutions) polymer resin. These lattices also had a $5 \times 5 \times 5$ tessellation of 7.2 mm unit cells, with strut diameters ranging from 0.55 mm to 1.60 mm, and overall sample dimensions of $36 \times 36 \times 36$ mm (Fig. 3.5h). In addition, cylinders with diameters of 15 mm and heights of 30 mm were fabricated using identical printing parameters to obtain the material properties of PR-48 under uniaxial compression (see sec-

tion 3.5.2). Besides the difference in dimensions, the geometry across all lattices was kept constant.

We fabricated TPL and DLP samples to span an (r/l) range from 0.07 to 0.15, focusing on the regime where the deviation from classical stiffness scalings becomes significant [94]. Microlattices with beam slenderness ratios of $(r/l) = 0.07$, 0.1, and 0.15 as well as lattices with beam slenderness ratios $(r/l) = 0.07$, 0.11, and 0.15 were fabricated, with several samples for each of the three node geometries. The relative densities, $\bar{\rho}$, of the octahedron samples ranged from 5.8 % to 22.6 % (Fig. 3.5a-c), and those of the tetrakaidecahedron samples ranged from 1.5 % to 6.7 % (Fig. 3.5e-g).

We performed uniaxial compression experiments along the ⟨001⟩ direction on all samples at a strain rate of $\dot{\varepsilon} = 10^{-3}\,\mathrm{s}^{-1}$, up to $\varepsilon = 50\,\%$ using a G200 XP Nanoindenter (Agilent Technologies) for the microlattices and an Instron 5500 load frame for the larger lattices. The Young's moduli of the cross-linked IP-dip and PR-48, E_s , were determined from the stress-strain data obtained from the compression of individual cylinders deformed under the same conditions. The slope of the linear loading portion of the stress-strain response was used to estimate the effective Young's modulus E^* of the lattices, as well as E_s for the pillar compression tests. The stress-strain data also convey the effective strength of the samples, which is beyond the scope of this study (the specifically designed node geometries create complex stress concentrations that could not be studied systematically within the given setup). To compare the stiffness across the two different polymers in this work as well as to other published material systems, we use the relative modulus of the structures E^*/E_s in the following, where E_s is the Young's modulus of the corresponding constituent material.

3.5.2 Constituent Material Properties

To determine the mechanical properties of the constituent material in the TPL microlattice and 3D DLP lattice samples, we fabricated pillars at each length scale using the same printing parameters as the $5 \times 5 \times 5$ lattice architectures. The cylindrical specimens had diameters of 15 µm and 15 mm for TPL and DLP samples, respectively, and a height-to-diameter ratio of 2. We performed uniaxial compression experiments on several specimens of each type, up to $\sim$ 10% strain, at a strain rate of 10^{-3} s^{-1}. Micropillar compressions were carried out in a G200 XP Nanoindenter (Agilent Technologies), while centimeter-scale pillars were compressed in

an Instron 5500 load frame.

Using the stress-strain response of each pillar, Young's modulus E_s and yield strength σ_y of Ip-Dip (TPL) and PR-48 (3D DLP) were calculated. Young's modulus was obtained by calculating the slope of the linear load regime, while the strength was determined by the intersection of the stress-strain response with a 0.2% strain offset line from the linear regime. An initial non-linear toe region is commonly observed in the stress-strain response due to slight misalignments between the samples and the indenter tip (or compression head) [94], so the largest slope of the linear load regime was used for the modulus approximation. $E_s = 2.68 \pm 0.07$ GPa and $\sigma_y = 75 \pm 2$ MPa were calculated for Ip-Dip, while $E_s = 1.30 \pm 0.03$ GPa and $\sigma_y = 33 \pm 1$ MPa were obtained for PR-48.

3.6 Results

Fig. 3.5i shows that the computational models of $5 \times 5 \times 5$ octahedron (rigid) lattices reveal subtle effects of nodal geometry on the effective lattice stiffness. The star-node structures were consistently stiffer, followed by the square-node and circular-node structures (Fig. 3.5i). For the most slender beams, with $(r/l) = 0.07$, modifying the nodal geometries yielded a maximum stiffness difference of 1%, compared to 6% for the least slender $(r/l) = 0.15$ case. The Young's moduli obtained from compression experiments on octahedron samples showed good agreement with those predicted by the reduced-order models. The experiments did not reveal a clear distinction in stiffness among the octahedron lattices of all node types, which may be attributed to the imperfections introduced by the manufacturing process. The Two-Photon Lithography process, e.g., was not capable of retaining the nodal integrity at slenderness ratios of $(r/l) = 0.15$.

Significant effects of node geometry on the effective lattice stiffness were observed in the reduced-order models of $5 \times 5 \times 5$ tetrakaidecahedron (non-rigid) lattices (Fig. 3.5j), as expected from the theoretical considerations described in section 3.2. Modifying the nodal geometries in the computational models yielded a maximum stiffness increase of 17% for the lattices with beams having $(r/l) = 0.07$; a 28% stiffness increase was observed for those with $(r/l) = 0.15$. As in the case of the octahedron lattices, the star-node tetrakaidecahedron structures consistently achieved the highest stiffness, followed by the square-node and circular-node architectures. The more marked effects of nodes in these non-rigid architectures were also reflected in the experiments, particularly for the least slender architectures. Mechani-

cal testing of centimeter-scale DLP tetrakaidecahedron samples with beams whose (r/l) was below 0.15 was not possible due to printing failures attributed to the low relative density of these samples.

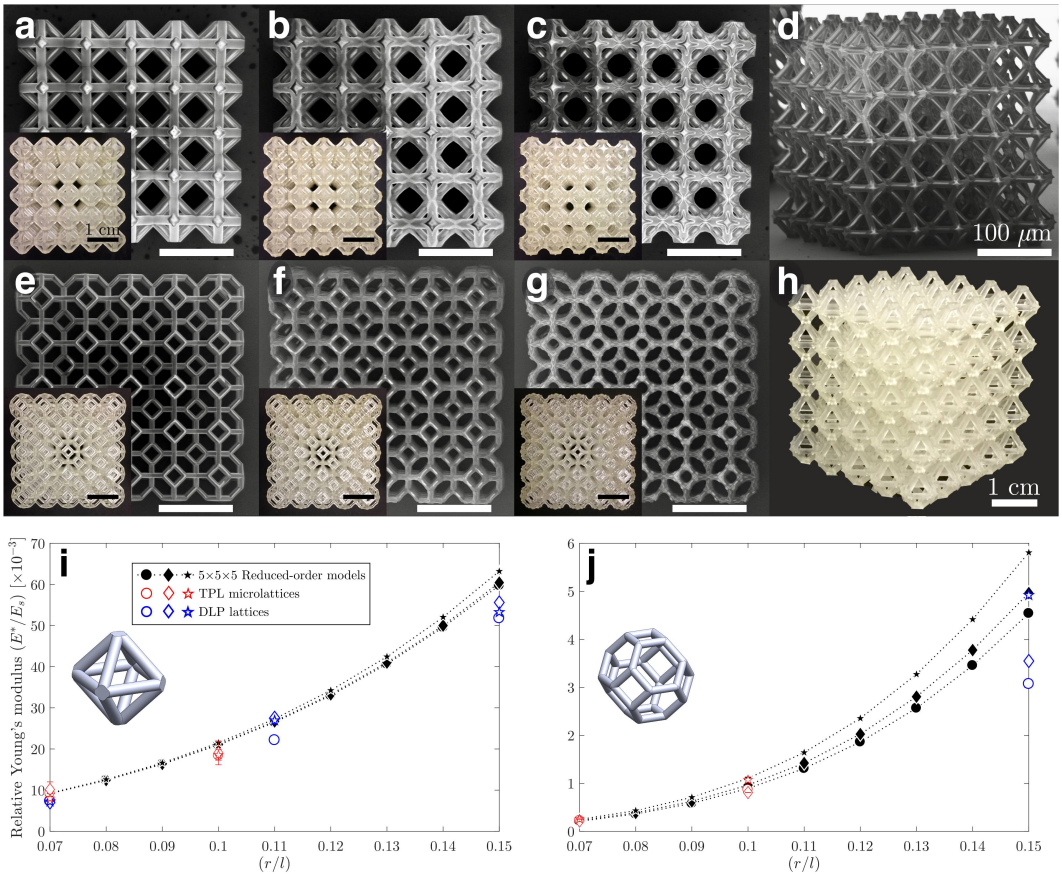

Figure 3.5 | TPL and DLP Lattice Samples and Comparison to Models
Representative top-view of octahedron TPL and DLP (inset) **(a)** circle-, **(b)** square-, and **(c)** star-node samples; **(d)** perspective view of a star-node octahedron $(r/l) = 0.15$ TPL microlattice. Representative top-view of tetrakaidecahedron TPL and DLP (inset) **(e)** circle-, **(f)** square-, and **(g)** star-node samples; **(h)** perspective view of a star-node tetrakaidecahedron $(r/l) = 0.15$ 3D DLP lattice (node detail presented in Fig. 3.4). Relative Young's moduli of reduced-order models (in black) and two-scale experiments for **(i)** $5 \times 5 \times 5$ octahedron lattices, and **(j)** $5 \times 5 \times 5$ tetrakaidecahedron lattices, with microlattice samples in red and cm-scale lattices in blue. Error bars (where visible) are presented for the TPL microlattice compressions and represent the standard deviation of the calculated relative Young's modulus for at least three identical samples. The TPL samples depicted in this figure were not tested due to manufacturing defects at some nodes, but are included for comparison to the larger, self-similar, DLP lattices.

In addition to accurately capturing the experimental lattice stiffness in the beam slenderness range studied, the reduced-order models confirm the observation from

the spring-beam models in section 3.2 that for a given slenderness, the effect of node geometry is more pronounced in non-rigid architectures than in rigid ones. This differing effect can be quantified and explained by extracting the strain energy from a finite $1 \times 1 \times 1$ tessellation[3] and comparing its distribution among the nodes and the struts (see Fig. 3.6). In these simulations, a 1% uniaxial strain was imposed in the z-direction, the x-y displacements at the top and bottom faces were unconstrained, and the lateral faces were left traction-free. The rigid octahedron geometry undergoes a transition from having most of the total strain energy concentrated within the struts for $(r/l) < 0.11$, to having most of it localized at nodes for less slender structures. This shift in strain energy distribution further confirms that the octahedron undergoes a transition from stretching- to bending-dominated deformation as the slenderness ratio increases. It also supports the finding that node geometry has marginal effects at low slenderness ratios and only becomes slightly pronounced at higher slenderness ratios. The non-rigid tetrakaidecahedron, on the other hand, has most of the strain energy localized at the nodes throughout the entire (r/l) range which indicates bending-dominated deformation and higher sensitivity to node geometry throughout.

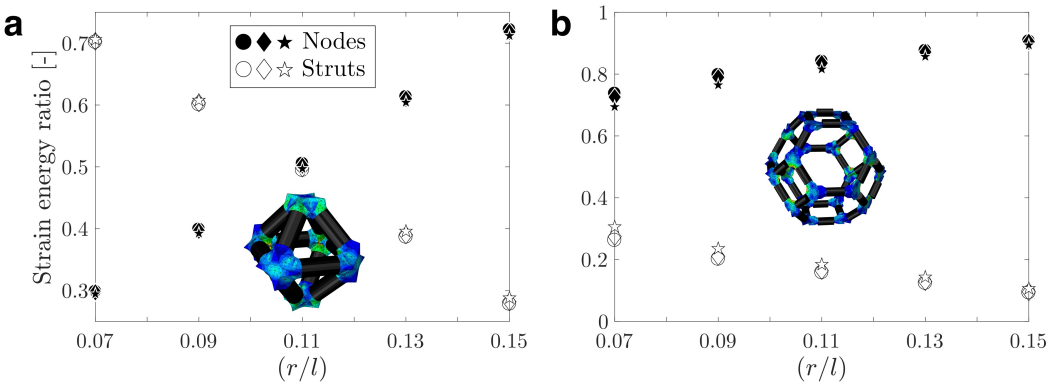

FIGURE 3.6 | STRAIN ENERGY DISTRIBUTION IN UNIT CELLS
Strain energy distribution in a $1 \times 1 \times 1$ reduced-order model. **(a)** Octahedron geometry (rigid), and **(b)** tetrakaidecahedron geometry (non-rigid). The strain energy ratio for each component type (struts or nodes) is defined as the sum of the strain energies of all nodes/struts in the simulation, normalized by the total strain energy in the unit cell.

[3]This choice of tessellation and boundary conditions was selected as the simplest case that enables the effect of free boundaries associated with compression experiments such as the ones presented in this work.

3.7 Extension of Classical Scaling Laws

The close agreement between reduced-order models and experiments suggests that it is the effects of the nodes in lattices that cause the observed non-classical stiffness scaling at high relative densities (low beam slenderness ratios) [94]. To generalize and quantify these findings, we studied additional rigid and non-rigid architectures through FE models, and compared their stiffnesses to those of the octahedron and tetrakaidecahedron geometries.

In this numerical study, we modeled individual unit cells of: (*i*) rigid architectures: octahedron and octet (Fig. 3.7a), and (*ii*) non-rigid ones: tetrakaidecahedron and pyramidal[4] (Fig. 3.7b). Each unit cell had variable node geometries analogous to the ones in the reduced-order models and was fully represented using quadratic tetrahedral elements (1.4×10^4 to 3.5×10^5 elements, depending on unit cell and node geometries). To avoid boundary effects present in finite $n \times n \times n$ tessellations, we applied periodic boundary conditions to the unit cell [143] and implemented a linear perturbation step with uniaxial compression in the z-direction. For a unit cell of side length L, an effective Young's modulus E^* along the $\langle 001 \rangle$ direction was calculated by normalizing the reaction force of the unit cell by its footprint area (i.e., the volume-averaged stress $\sigma_{\text{avg}} = F/L^2$) and dividing by the volume-averaged applied uniaxial strain ($\varepsilon_{\text{avg}} = \Delta z/L$):

$$E^* = \frac{\sigma_{\text{avg}}}{\varepsilon_{\text{avg}}} = \frac{F}{L\Delta z}. \tag{3.7}$$

To gain deeper understanding of the transition from classical to non-classical stiffness scaling as a function of slenderness ratio, the beams in all architectures and node geometries spanned the range of (r/l) from 0.03 to 0.15. The calculated moduli in Figs. 3.7c,d show that, in the low (r/l) regime, these models agree with the classical scaling law which has the form

$$\frac{E^*}{E_s} = C\left(\frac{r}{l}\right)^{\alpha} \tag{3.8}$$

for $(r/l) \ll 1$. Here, C is a scaling constant determined by the architecture, and α is the scaling exponent that is equal to 2 for rigid and to 4 for the non-rigid architectures [3]. The individual unit cell models diverged from the classical scaling as (r/l) increased to $(r/l) \gtrsim 0.07$. Throughout the slenderness ratios probed, the unit cell models were in agreement with the reduced-order models in that the star-node geometries were stiffer than the circle-node ones by approximately 1% to 5% for octahedron geometries and 17% to 35% for tetrakaidecahedron geometries.

[4] Same topology studied by Valdevit et al. [134], except without hollow struts.

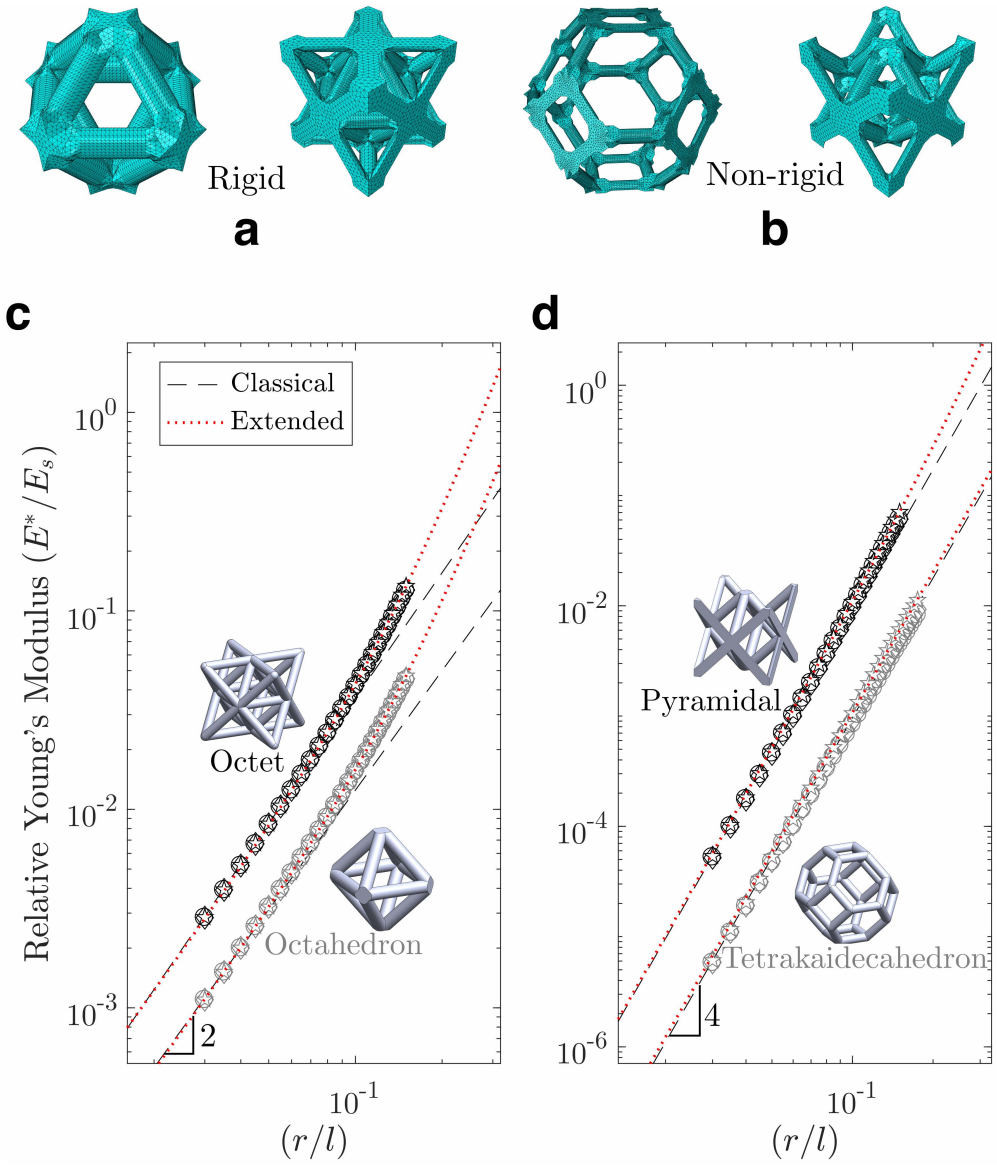

FIGURE 3.7 | EXTENSION OF CLASSICAL STIFFNESS SCALINGS
Generalization of nodal effects through numerical models. **(a)** Representative star-node octahedron and octet finite element meshes (r/l = 0.11) and **(b)** representative star-node tetrakaidecahedron and pyramidal unit cells (r/l = 0.11) used for periodic boundary condition (PBC) simulations. Classical and extended stiffness scaling fits on PBC simulations of **(c)** rigid architectures, and **(d)** non-rigid architectures. The simulations used for the fits are represented by hollow markers depicting the node geometry (i.e., circle, square, and star). As expected, the relative moduli for non-rigid architectures are orders-of-magnitude smaller than those of rigid architectures for the same beam slenderness range.

To capture the divergence of the simulations from classical stiffness predictions at higher (r/l) ratios, we include a higher-order term to the classical scaling law

Architecture	Node Type	C_1	α	C_2	β
Octahedron	○	1.19	2.0	34.9	3.99
	◇	1.19	2.0	35.5	3.98
	★	1.20	2.0	47.1	4.10
Octet	○	2.95	2.0	103.3	3.93
	◇	2.97	2.0	103.7	3.93
	★	3.02	2.0	142.7	4.06
Tetrakaidecahedron	○	10.39	4.1	1.31	5.94
	◇	12.42	4.1	2.38	5.92
	★	17.42	4.2	3.99	5.90
Pyramidal	○	150.5	4.2	842	5.90
	◇	140.8	4.2	1015	5.90
	★	167.7	4.3	1340	5.90

Table 3.1 | Extended Stiffness Scaling Fit Parameters for Rigid and Non-Rigid Architectures

Fitted parameters for PBC simulations assuming the form $E^*/E_s = C_1\,(r/l)^{\alpha} + C_2\,(r/l)^{\beta}$ while only constraining the initial guess for α to be 2 or 4 for rigid and non-rigid architectures, respectively.

(Eq. 3.8):

$$\frac{E^*}{E_s} = C_1\left(\frac{r}{l}\right)^{\alpha} + C_2\left(\frac{r}{l}\right)^{\beta}, \tag{3.9}$$

where C_1 and C_2 are scaling constants, α is the classical scaling exponent, and β is a higher-order scaling exponent that corrects for the non-slender beam geometries. This form of the extended stiffness scaling approaches the classical scaling for small (r/l). Using Eq. 3.9, we fit the unit cell models constraining α to approximate the corresponding rigid or non-rigid classical scaling exponent (i.e., 2 or 4). The resulting extended scaling fits shown as red dotted lines in Fig. 3.7c,d agree with the models throughout the entire (r/l) regime, with the parameters presented in Table 3.1.

To gain physical intuition for the parameters presented in Table 3.1, we use dimensional analysis as a form of characterizing the stiffness scaling relation for an arbitrary lattice architecture. The effective stiffness E^* of a given lattice architecture can be broadly expressed as a function of its constituent material properties and unit cell geometrical parameters. Assuming perfectly linear constitutive behavior, the material can be characterized by its Young's modulus E_s, presenting the familiar form of a stiffness scaling law:

$$\frac{E^*}{E_s} = f(\text{geom.}). \tag{3.10}$$

The geometry of the unit cell can be generally described by the strut radius r, the strut length l, and the number of zero-energy mechanisms m; while the nodes of the unit cell can be described by the idealized node radius r_n (assuming the nodal volume to be $V_n = \frac{4}{3}\pi r^3$), the nodal connectivity Z, and the three second area moments of the strut cross-sections at the nodes I_1, I_2, and I_3.

The group of all variables associated with the stiffness scaling of a lattice architecture admit a basis of three dimensions: a mass dimension M, a length dimension L, and a time dimension T. The variables can be grouped as (*i*) the mechanical properties

$$[E^*] = ML^{-1}T^{-2}, \qquad [E_s] = ML^{-1}T^{-2}, \tag{3.11}$$

(*ii*) the unit cell topology variables

$$[r] = L, \qquad [l] = L, \qquad [m] = -, \tag{3.12}$$

and (*iii*) the nodal geometry variables

$$[r_n] = L, \qquad [I_1] = L^4, \qquad [I_2] = L^4, \qquad [I_3] = L^4, \qquad [Z] = -. \tag{3.13}$$

Applying the Buckingham Π theorem and assembling a dimensional matrix $\boldsymbol{M}$ of all variables (where the rows correspond to the fundamental dimensions M, L, and T) yields

$$\boldsymbol{M} = \begin{array}{c} \\ M \\ L \\ T \end{array} \begin{array}{c} \begin{array}{cccccccccc} E_s & E^* & r & l & r_n & I_1 & I_2 & I_3 & Z & m \end{array} \\ \begin{bmatrix} 1 & 1 & 0 & 0 & 0 & 0 & 0 & 0 & 0 & 0 \\ -1 & -1 & 1 & 1 & 1 & 4 & 4 & 4 & 0 & 0 \\ -2 & -2 & 0 & 0 & 0 & 0 & 0 & 0 & 0 & 0 \end{bmatrix} \end{array}, \tag{3.14}$$

whose null space

$$\boldsymbol{\Pi} = \begin{array}{c} \\ E_s \\ E^* \\ r \\ l \\ r_n \\ I_1 \\ I_2 \\ I_3 \\ Z \\ m \end{array} \begin{array}{c} \begin{array}{cccccccc} \Pi_1 & \Pi_2 & \Pi_3 & \Pi_4 & \Pi_5 & \Pi_6 & \Pi_7 & \Pi_8 \end{array} \\ \begin{bmatrix} -1 & 0 & 0 & 0 & 0 & 0 & 0 & 0 \\ 1 & 0 & 0 & 0 & 0 & 0 & 0 & 0 \\ 0 & -1 & -1 & -4 & -4 & -4 & 0 & 0 \\ 0 & 1 & 0 & 0 & 0 & 0 & 0 & 0 \\ 0 & 0 & 1 & 0 & 0 & 0 & 0 & 0 \\ 0 & 0 & 0 & 1 & 0 & 0 & 0 & 0 \\ 0 & 0 & 0 & 0 & 1 & 0 & 0 & 0 \\ 0 & 0 & 0 & 0 & 0 & 1 & 0 & 0 \\ 0 & 0 & 0 & 0 & 0 & 0 & 1 & 0 \\ 0 & 0 & 0 & 0 & 0 & 0 & 0 & 1 \end{bmatrix} \end{array} \tag{3.15}$$

identifies the dimensionless groups pertinent to the stiffness behavior of lattice architectures. This provides eight dimensionless numbers

$$\begin{aligned} \Pi_1 &= \frac{E^*}{E_s}, & \Pi_2 &= \frac{r}{l}, \\ \Pi_3 &= \frac{r_n}{r}, & \Pi_4 &= \frac{I_1}{r^4}, \\ \Pi_5 &= \frac{I_2}{r^4}, & \Pi_6 &= \frac{I_3}{r^4}, \\ \Pi_7 &= Z, & \Pi_8 &= m, \end{aligned} \tag{3.16}$$

which can be generally grouped into (*i*) mechanical response groups (Π_1), (*ii*) unit cell groups (Π_2,Π_8), and (*iii*) nodal groups (Π_3,Π_4,Π_5,Π_6,Π_7).

The proposed stiffness scaling form in Eq. 3.9

$$\frac{E^*}{E_s} = C_1 \left(\frac{r}{l}\right)^{\alpha} + C_2 \left(\frac{r}{l}\right)^{\beta},$$

can then be expressed in terms of the dimensionless parameters in Eq. 3.16 as

$$\Pi_1 = C_1 \Pi_2^{\alpha} + C_2 \Pi_2^{\beta}, \tag{3.17}$$

where $\alpha = f(\Pi_8)$, $\beta = f(\Pi_8)$, $C_1 = f(\Pi_3, \Pi_4, \Pi_5, \Pi_6, \Pi_7, \Pi_8)$, and $C_2 = f(\Pi_3, \Pi_4, \Pi_5, \Pi_6, \Pi_7, \Pi_8)$. Linking the constants C_1 and C_2 to nodal geometry agrees with the parameter trends observed in Table 3.1, where the magnitude of C_2 is directly related to the stiffening effect of a particular node.

Although β was not constrained, the fitting process produced an optimal $\beta \simeq 4$ for rigid architectures and $\beta \simeq 6$ for the non-rigid ones. For the former, this higher-order term resembles the classical scaling (Eq. 3.8) for bending-dominated architectures with $\alpha = 4$. This indicates that this term accounts for the bending of the beams enabled by the nodes at high (r/l) ratios [94]. The proposed extended scaling for rigid architectures with $\alpha = 2$ and $\beta = 4$ accounts for the combined influence of stretching and bending without assuming a dominant behavior of either. For the non-rigid architectures, we study the simplest 2D representation of a diamond structure shown in Fig. 3.1b (except without rotational springs) to understand the nature of the higher-order exponent. The effective Young's modulus of this structure under vertical compression is given by [94]

$$\frac{E^*}{E_s} = \frac{1}{A_1 \left(\frac{r}{l}\right)^{-4} + A_2 \left(\frac{r}{l}\right)^{-2}}, \tag{3.18}$$

where A_1 and A_2 are geometrical constants. Performing a Taylor expansion of Eq. 3.18 about $r/l = 0$ results in

$$\frac{E^*}{E_s} \approx B_1 \left(\frac{r}{l}\right)^4 - B_2 \left(\frac{r}{l}\right)^6 + O\left[\left(\frac{r}{l}\right)^8\right], \tag{3.19}$$

with B_1 and B_2 as constants (depending on A_1, A_2), which matches the form of Eq. 3.9. As in the case of rigid architectures, accounting for a combined influence of bending and stretching provides an extended scaling law for non-rigid architectures that captures stiffness throughout the admissible (r/l) regime. It must be noted that the above analysis can be translated to other anisotropic moduli and loading directions, such as the case of a nominally stretching-dominated direction of an anisotropic non-rigid architecture. In such cases, the nominal behavior of the given direction will dictate the choice of the scaling exponents α and β.

3.8 Conclusions

We have analyzed the effect of nodes on the stiffness scaling of lattice architectures and quantified the nodal contribution to the deviation of this scaling from classical laws in non-slender-beam lattices. We developed efficient reduced-order models, which capture the mechanics of the nodes in full detail, allowing us to simulate full lattice tessellations at a computational cost orders-of-magnitude below traditional approaches. Stiffnesses predicted by these models match experiments on non-slender-beamed lattices at the milli- and micrometer scales. Experiments and simulations revealed a more pronounced effect of the nodes on the stiffness of non-rigid lattice architectures than that of rigid ones. We have proposed a modification to the classical stiffness scaling laws for lattice architectures, in which higher order (r/l) terms account for the non-slender beam effects. Dimensional analysis on the proposed modified scaling laws provides physical intuition for the resulting parameters and confirms that these deviations can be attributed to the effects of node geometry. These results confirm and quantify the non-negligible contribution of nodes to the mechanical properties of lattice architectures and bring to light the insufficiency of classifying cellular solids as either stretching- or bending-dominated over the manufacturable parameter space.

Chapter 4

NODELESS ARCHITECTURES VIA SELF-ASSEMBLED GEOMETRIES

Section 4.2 has been adapted from:

N.G. Dou, R.A. Jagt, C.M. Portela, J.R. Greer & A.J. Minnich. "Ultralow Thermal Conductivity and Mechanical Resilience of Architected Nanolattices". *Nano Letters* (2018) 18, 8 pp. 4755–4761. DOI: 10.1021/acs.nanolett.8b01191.

CONTRIBUTIONS: performed mechanical experiments and analyzed the data, performed the computational analysis, and participated in the writing of the manuscript;

and the rest of this chapter has been adapted from:

C.M. Portela, A. Vidyasagar†, S. Krödel†, T. Weissenbach, D.Y. Yee, J.R. Greer & D.M Kochmann. "Extreme mechanical resilience of self-assembled nano-labyrithine materials". *In Preparation* (2019)

CONTRIBUTIONS: fabricated samples, performed mechanical experiments and analyzed the data, performed the computational analysis, and wrote the manuscript.

4.1 Chapter Summary

Low-density materials with tailorable properties have attracted attention for decades, yet stiff materials systems that can resiliently tolerate extreme forces and deformation, while being manufactured at large scales, have remained a rare find [154]. Designs inspired by nature such as hierarchically designed composites and foams [15, 38, 40, 93] and atomic-lattice-mimicking architectures such as the micro-trusses and nanolattices [9, 87, 92, 152, 153] studied in previous chapters have achieved optimal combinations of mechanical parameters but suffer from limited mechanical tunability, limited long-term stability, and low throughput volumes. In particular, we have studied the detrimental effect of nodes which prevent these materials from achieving an optimal linear scaling. Most of these architected materials have also relied on symmetry, periodicity, and lack of defects to achieve the desired mechanical response [94, 101], and as as a result symmetry-breaking defects cause localized deformation and failure, which significantly affects the material's resilience upon

further loading [39, 47, 111]. Shell-type designs [1, 20, 49, 57, 151], on the other hand, avoid stress concentrations and flaws but all realizations have come with high densities and limited recoverability.

By harnessing natural self-assembly processes [84, 133, 136], we here present scalable non-periodic ceramic-shell architectures of ultralow density (reaching 4 mg/cm^3) with features on the order of tens of nanometers and sample volumes on the order of cubic centimeters, whose engineered curvature distribution achieves close-to-optimal stiffness scaling and, moreover, whose careful combination of topology, geometry and base material results in superior mechanical resilience compared to previously reported architected materials. We show the capability of these architectures to maintain more than 50% of their original stiffness and strength after ten cycles of compression up to 30% with no discernible permanent deformation. Guided by theory and computations, we experimentally demonstrate precise control over material morphology, which elicits prescribed (an)isotropic material response, whose directional stiffness distribution remains the same over a wide range of shell thicknesses and relative densities. Our approach provides a pathway to harness self-assembly methods in the design and scalable fabrication of architected materials with simultaneous directionally tunable, high stiffness and unsurpassed recoverability to 10 cycles with marginal deterioration.

4.2 Detrimental Effect of Nodes to Resilience

To understand the negative effect of nodes beyond the non-ideal stiffness scalings explored in previous chapters, we will briefly discuss their impact on the damage and deterioration of beam-based architected materials. Several beam-based hollow architectures have harnessed size effects of nm-thick struts to enable structural recovery after large deformation, characterizing structural recovery solely by the ratio between the original and the post-compression sample heights while acknowledging the presence of significant cracks at nodes [39, 92] as shown in Fig. 4.1. These micro-cracks at nodes are the result of stress concentrations emerging at the junction of two or more struts which makes them inevitable in any beam- or plate-based geometry where two or more discrete components meet. The mechanical effect of this type of failure at hollow nodes has been observed as a drastic decrease in the effective stiffness and strength of the materials [39, 92, 93], and has also been identified in the cyclic response of ceramic-polymer microlattices [120]. Furthermore, the detrimental effect of nodes has recently been identified as the main determining factor for tensile failure and crack propagation in lattice materials [87].

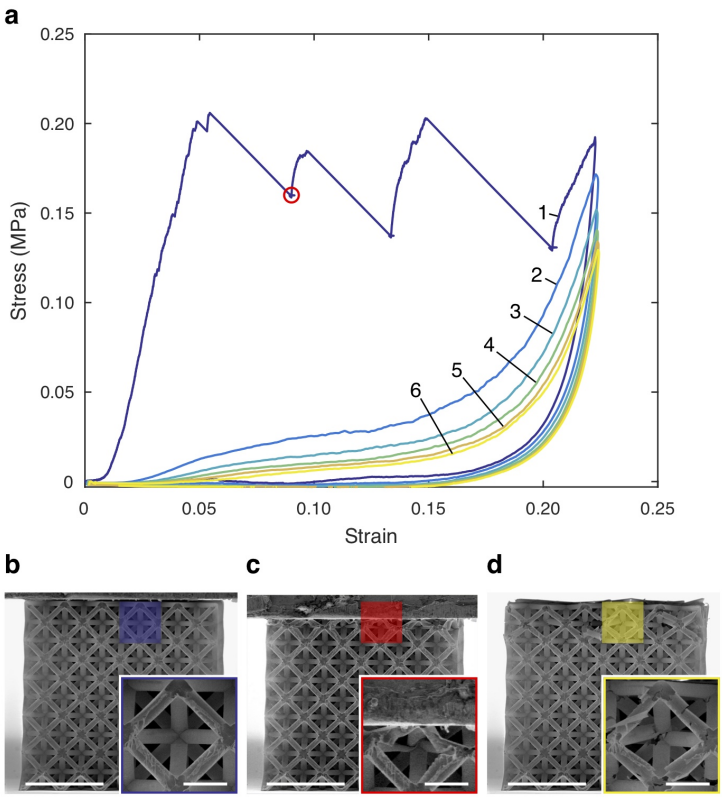

FIGURE 4.1 | CYCLIC RESPONSE OF Al_2O_3 24-NM-WALL-THICKNESS OCTET NANOLATTICES
(a) Stress and strain recorded during a 6-cycle compression test of a 24 nm wall thickness nanolattice. Curves are labeled with the cycle number. SEM images **(b)** before, **(c)** during, and **(d)** after the test show 98% structural recovery although significant cracks emerge at nodes. The circular marker indicates the stress and strain of the partially compressed nanolattice shown in (c). Zoomed images (insets) illustrate the contribution of beam buckling, shell buckling, and fracture. Scale bars are 50 µm for (b)–(d) and 10 µm for insets.

In light of this, extreme resilience in architected materials can only be enabled by architectures that lack nodes or junctions, while still harnessing size effects at the nano-scale.

4.3 Eliminating Nodes in Architected Materials

The design of architected cellular materials to date has heavily relied on truss-based geometries, which achieve desirable mechanical properties such as high stiffness- or strength-to-density ratios [9, 92, 118, 153], flaw tolerance [87], high energy absorption [127], and vibration mitigation [69]. Truss-based architectures, like open-cell foams, typically engage their structural members in bending, increasingly so for slender features regardless of architecture. This compliant deformation mode is

responsible for poor, higher-than-linear scaling of the effective truss stiffness with density [94, 115]. Alternatively, plate- and shell-based geometries have been shown to mitigate such bending and to reach theoretical stiffness bounds [15, 128] by improving the load distribution within their members as compared to trusses, but usually exhibit poor recoverability: the truss- and plate-based designs suffer from stress concentrations at junctions, resulting in permanent damage and material failure. As a solution to this, smooth shell architectures such as triply periodic minimal surfaces (TPMS) avoid sharp junctions and attain high stiffness owing to double curvature in its components. This concept of nonzero Gaussian curvature, first introduced by Gauss in his *Theorema Egregium*, provides mechanical benefits to doubly curved surfaces [113] and has been identified in nature, for instance, in providing rigidity to egg shells [77] and plant leaves [80, 99]. Recently, this concept has led to smooth shell architectures that achieve stretching-dominated behavior and have superior energy absorption capabilities than trusses [1, 20, 49, 151].

The beneficial mechanical properties of synthesized truss-, plate-, and beam-based architected materials are largely enabled by the periodicity of symmetric unit cells, all of which are susceptible to symmetry-breaking defects and effects of free boundaries [74, 101]. Materials with such geometries are typically only achievable using additive manufacturing techniques at small scales that are defect-prone and non-scalable, inevitably resulting in their lower-than-theoretical strength- and stiffness-scaling with density. As a point of departure from periodicity, materials that are formed through natural evolution processes like nanoporous foams [18], can be non-periodic and are often comprised of bi-continuous networks of smooth, doubly curved solid morphologies corresponding to different phases. Further morphology tunability, with the potential for direction-dependent properties, can be achieved via molecular processes like self-assembly of block copolymers [13, 65] or polymeric micro-emulsions [7, 133, 155]. These processes enable orders-of-magnitude increase in fabrication volumes [79, 100] compared to additively manufactured materials and expand the parameter space to allow drastically different features with sizes ranging from tens of nanometers to tens of micrometers, all by simple changes in phase concentrations, molecular weights, or temperature [136]. Architectures obtained through these processes may be particularly resilient against defects [57] not only since they do not rely on periodicity, but also because they could simultaneously benefit from double curvature if they are reduced to thin shells at the boundary between phases. Exploring non-periodic, shell-based architectures with double curvature provides a promising scalable pathway to attain low-density architected

materials with extremely low weight, high stiffness, and extreme resilience.

4.4 Sample Fabrication

To this end, we developed a fabrication method (Fig. 4.2a) that harnesses the self-assembly capabilities of polymeric emulsions to create bi-continuous, doubly curved shell-based materials with throughput volumes on the order of cubic centimeters. With pore sizes on the order of tens of micrometers, and smooth walls on the order of tens of nanometers, our materials span six orders-of-magnitude from the smallest feature dimension to the overall sample dimensions and present the first realization of a scalable self-assembled nano-architected material. We fabricated the porous bi-continuous template (Fig. 4.2b) exploiting the spinodal decomposition of an epoxy-based emulsion (see Methods), which produced a fully interconnected solid phase upon polymerization with consistent pore morphologies on the order of tens of micrometers [133]. This template was then coated with a 79 nm conformal coating of ALD-deposited Al_2O_3, followed by O_2 plasma ashing to remove the epoxy template and yield the resulting nano-labyrinthine shell-based material. The polymerization-induced phase separation process that creates the initial bi-continuous templates gives these nano-labyrinthine materials the potential to be fully tunable using thermal, chemical, or mechanical stimuli during self assembly, which could lead to controllable morphologies that conform to desired specifications.

To systematically explore the parameter space enabled by this fabrication method, we computed several bi-continuous morphologies achievable through the separation process and experimentally probed their response as thin shell-based nano-labyrinthine materials. To obtain the bi-continuous morphologies, we first describe a phase separation process during self-assembly of a generic two-phase system using a Cahn-Hilliard-type phase field model [137], in which $\varphi(\boldsymbol{X}, t) = [0, 1]$, defined at position $\boldsymbol{X}$ and time t, separates solid ($\varphi = 1$) from void ($\varphi = 0$) domains. To control the characteristics of the resulting porous bi-continuous microstructures, we fix the average fill fraction at 50% and tune the surface energy of the interface between the two phases to modify the resulting feature morphology. Drawing inspiration from nanoporous foams and block copolymers whose morphology and directionality can be controlled by properly choosing the alloying [72, 107] or mixing ratios [108], we computed anisotropic shell architectures that mimic such directional tunability [84]. To enable this, we prescribe the anisotropic surface energy $\gamma(\boldsymbol{n})$ as a function of the surface normal $\boldsymbol{n}$) to penalize growth along a particular set of directions defined by $\{\boldsymbol{m}_1, \ldots, \boldsymbol{m}_n\}$, which produces bi-continuous shapes that

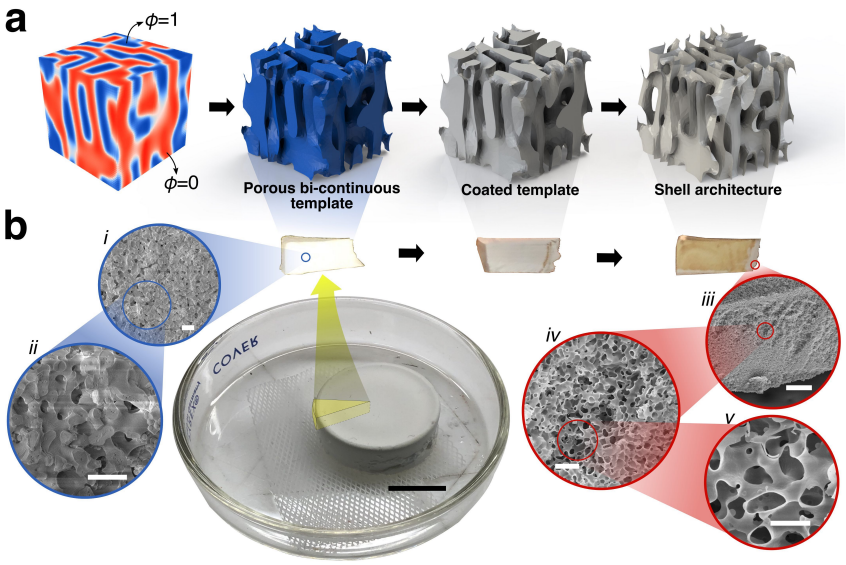

FIGURE 4.2 | SELF-ASSEMBLED NANO-LABYRINTHINE SHELL-BASED MATERIAL
(a), Schematic of fabrication process starting with spinodal decomposition of an epoxy resin and polyethylene glycol (PEG) emulsion, which is thermally cured to produce a porous bi-continuous template after extraction of PEG. The template is then conformally coated with atomic layer deposited (ALD) Al_2O_3 which, after removing the epoxy phase via O_2 plasma ashing, composes the resulting nano-labyrinthine shell architectures. **(b)**, Extraction of a wedge from a disk-shaped porous template and SEM micrographs at different stages in the fabrication process. Black scale bar, 1 cm. Scale bars in (*i*),(*ii*) 10 µm, (*iii*) 100 µm, (*iv*) 10 µm, and (*v*) 5 µm.

are arranged in energetically favorable directions perpendicular to the $\boldsymbol{m}_i$-directions and possess, in principle, any prescribed elastic symmetry. Conformally coating the computed solid phase with a thin layer of another material whose thickness is uniform and below 10% of the average feature size, and subsequently removing the solid phase, creates the designed thin-shell architectures corresponding to the interface regions with $\varphi = 0.5$. Lastly, we note that the resulting average pore size and the curvatures of the interface can be further tuned to match the fabricated materials by setting a time limit for the phase separation process to take place.

We fabricated a few examples of the computed architectures out of thin-shell alumina using a three-step process: (*i*) two-photon lithography direct laser writing (Nanoscribe GmbH) to create 3D scaffolds with prescribed shapes out of IP-Dip photoresist, (*ii*) atomic layer deposition (ALD) of 11, 44, or 168 nm-thick conformal coatings of Al_2O_3 onto the scaffolds, and (*iii*) removing polymer templates by selectively etching small perforations in the coating using a focused ion beam (FIB) and ashing the samples in O_2 plasma. Details of this fabrication process are pro-

vided in section 4.9 and in Fig. 4.4. The resulting nano-labyrinthine-sample form factors were cubic, with overall dimensions of 125 × 125 × 125 µm, and porous feature sizes on the order of ~10 µm, to approximate the pores of nano-labyrinthine samples from Fig. 4.2b. These bi-continuous surface architected materials had a relative density $\overline{\rho}$ (i.e., fill fraction) of approximately 0.15 % to 2.4 %, which corresponds to 4 to 62 mg/cm^3, depending on shell thickness. Five representative examples that showcase the wide range of self-assembly-like architectures are shown in (Fig. 4.3). The scanning electron microscopy (SEM) images include columnar (Fig. 4.3a), lamellar (Fig. 4.3c), isotropic (Fig. 4.3d), cubic (Fig. 4.3e), and trigonal (Fig. 4.3f) architectures, with their numerically computed Young's moduli (i.e., stiffness) in each direction shown as contour surfaces in the image insets which is described in the following.

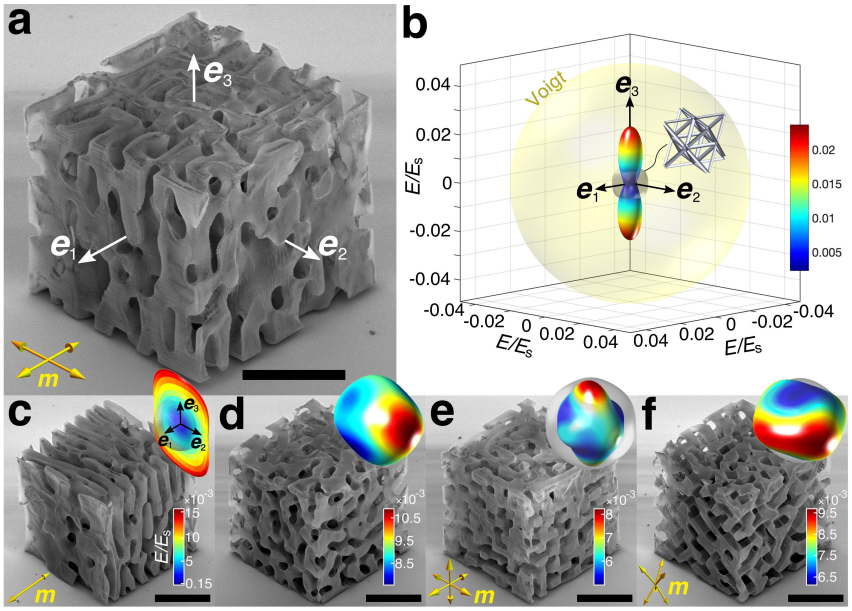

Figure 4.3 | Anisotropic Al_2O_3 Shell-Based Bi-Continuous Geometries
(a) Columnar shell geometry with 11 nm thickness and **(b)** corresponding elastic surface at $\overline{\rho} = 4.8 \pm 0.3\%$ showing the computed anisotropy as compared to that of an equally dense octet (grey surface). **(c)** Lamellar, **(d)** isotropic, **(e)** cubic, and **(f)** trigonal geometries with the corresponding elastic surfaces as insets (same $\overline{\rho}$ as in **b**). The Voigt bound of $E/E_s = 0.048$ is presented as a golden spherical surface. When not visible, the octet elastic surface is contained within the bi-continuous material's surface. The preferential ***m*** vectors are depicted where applicable. Scale bar, 50 µm.

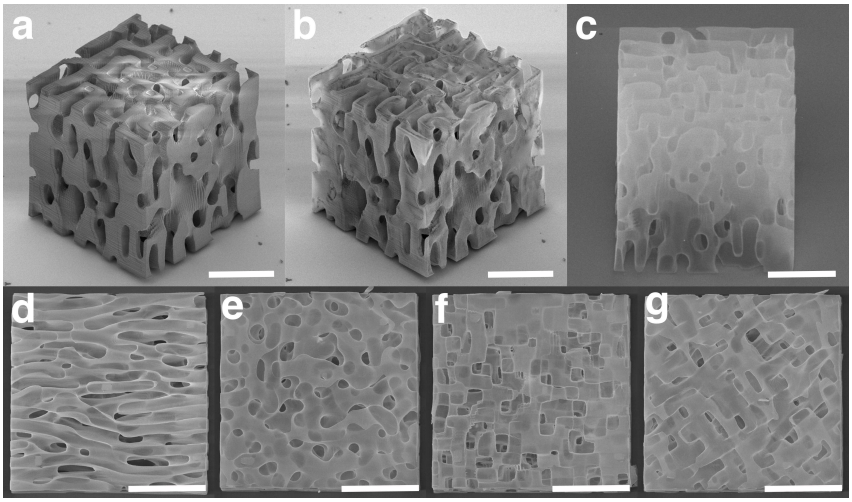

Figure 4.4 | Nano-Labyrinthine Sample Fabrication Details
(a) Columnar bi-continuous architecture fabricated using two-photon lithography with an 11 nm Al_2O_3 coating, with five rectangular perforations at the top obtained via focused ion beam milling; **(b)** hollow shell-based sample after 80 hours in an O_2 plasma ashing system; **(c)** micrograph of a columnar sample obtained at a high imaging voltage (10 kV) showing the hollow nature of the samples; high-voltage micrographs for the 11 nm **(d)** lamellar, **(e)** isotropic, **(f)** cubic, and **(g)** trigonal architectures. Scale bar, 50 μm.

4.5 Elastic Surface Calculation

The mechanical anisotropy of such shell-based architectures is highlighted by the elastic surfaces (Fig. 4.3), which convey the orientation-dependent sample stiffness, i.e., Young's modulus E, calculated using linear elastic shell finite element models with the constituent properties of ALD Al_2O_3 [14] (see Methods). We first simulated uniaxial compression of each architecture along each $\boldsymbol{e}_i$ direction for $i = \{1, 2, 3\}$ (i.e., the [100], [010], and [001] directions, respectively), resembling actual experimental boundary conditions, to allow comparison to experimental anisotropy values in those three directions. Additionally, we implemented a homogenization scheme with periodic boundary conditions to calculate the modulus in all directions, first obtaining the full elastic modulus tensor $\mathbb{C}$ and then using it to compute the compliance tensor $\mathbb{S} = \mathbb{C}^{-1}$, which provided E along any direction. The contoured elastic surfaces were then plotted using all values of E normalized by the Young's modulus of ALD alumina, E_s, where colors represent the magnitude of the normalized modulus (Fig. 4.3b, insets). The deviation of elastic surfaces from spherical shape is quantitatively related to the elastic anisotropy and is typically maximized along directions perpendicular to the preferential $\boldsymbol{m}$ vectors. Fig. 4.3b shows two ellipsoidal lobes along the [001] direction that comprise the elastic sur-

face of the columnar architecture shown in Fig. 4.3a, along with lower and upper surfaces for reference: that of an octet truss lattice (one of the most extensively explored stiffer *periodic* architectures [35, 94, 115, 153]) represented by a small gray surface centered at the origin, and that of the Voigt theoretical upper bound (defined by the rule of mixtures between Al_2O_3 and air) shown as a golden sphere. This plot reveals that for this representative case of $\overline{\rho} = 4.8 \pm 0.3\%$, the maximum elastic modulus of the columnar architecture outperforms the equivalently lightweight octet truss by a factor of 3.6 and reaches 48% of the Voigt bound. The contoured elastic surfaces also reveal a stiff omnidirectional response in the absence of preferential directions within the architecture, an example of which is shown in Fig. 4.3d, where the architecture's response is close to isotropic as would be the case, for example, in nanoporous materials [85] and stochastic foams [57]. The elastic surface of the octet is fully contained within that of the isotropic shell architecture (Fig. 4.3d), which demonstrates that the non-periodic bi-continuous architectures in this work are substantially stiffer in all directions than equally dense periodic truss architectures. The columnar (Fig. 4.3a), lamellar (Fig. 4.3c), cubic (Fig. 4.3e), and trigonal (Fig. 4.3f) geometries all appear to have tunable stiffness variations. In the case of the columnar architecture, the anisotropy induced by the selected preferential directions promotes material arrangement in stress-bearing columnar features along the [001] direction, which renders its relative modulus E/E_s in this direction the highest for all studied geometries. The lamellar structure (Fig. 4.3d) displays the highest degree of anisotropy, $E_{[001]}/E_{[100]}$ of 177, driven by sheet-like, low inter-connectivity material arrangements along the [010] and [001] directions. These computational results demonstrate that introducing preferential $\boldsymbol{m}$ directions into non-periodic architectures allows for prescribing substantial elastic anisotropy and provides a mechanism to design the elastic response along any chosen direction in a single material, attaining performance superior to some periodic architectures. All computed elastic responses appear to be below the theoretical upper bound since enforcing shell bi-continuity requires some material arrangement in less-than-ideal configurations, yet the connectivity is achieved without sharp corners or edges (opposite of what is typical in periodic architectures) which will become essential in giving these nano-labyrithine materials exceptional properties beyond stiffness.

4.6 Nanomechanical Experiments

To test the computational predictions, we conducted uniaxial compression experiments on each architected sample along their ⟨100⟩ directions in a nanoindenter

(G200 XP, KLA) with a flat punch tip to strains of $\varepsilon = 35\%$ at a quasistatic rate of $\dot{\varepsilon} = 10^{-3}$ s^{-1}. Additional cyclic compressions on selected architectures were performed *in situ*, in a custom nanomechanical instrument inside of an SEM chamber [92] (Quanta 200 FEG, Thermo Fisher). We compressed a minimum of three samples for each configuration: geometry, orientation, and shell thickness, and converted the load vs. displacement data produced by the instrument into stresses and strains by normalizing by the sample footprint area and height, respectively. We then obtained the effective elastic modulus $E^*_{[\cdot]}$ and material strength $\sigma^*_{y,[\cdot]}$ from the stress-strain data by obtaining the slope of the linear loading regime and the corresponding load at the onset of nonlinearity (see Methods). Representative stress vs. strain data sets are shown in Fig. 4.5 which reveal the characteristic linear and nonlinear responses of samples at the three different shell thicknesses.

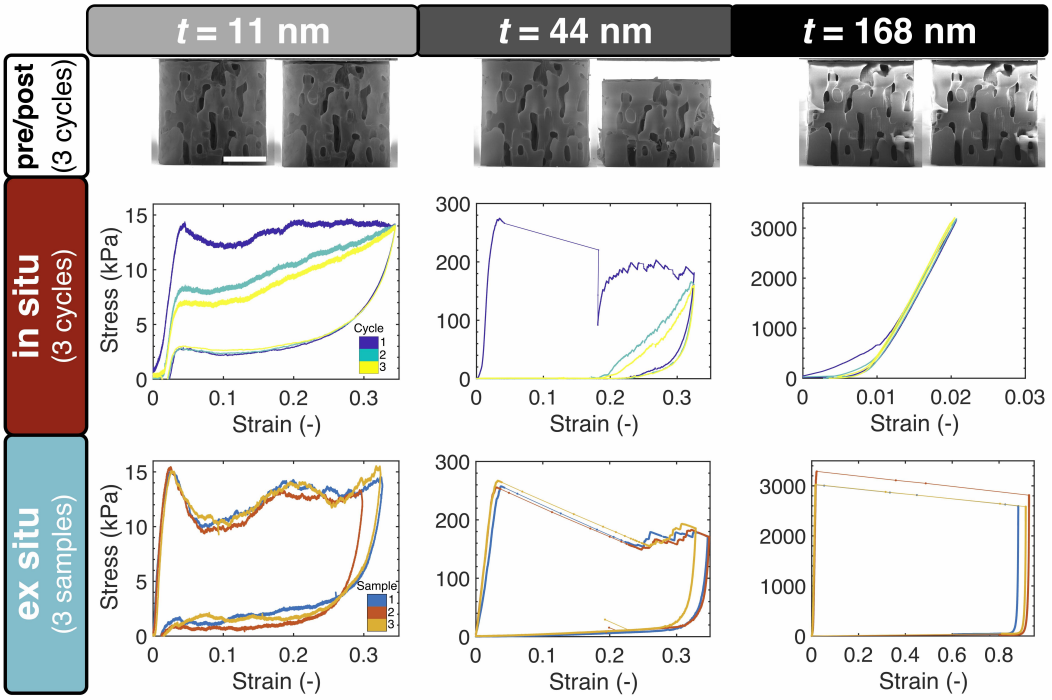

Figure 4.5 | Compressions of Columnar Samples at Different Thicknesses
Top row: micrographs before and after 3-cycle *in situ* uniaxial compressions to $\varepsilon = 30\%$ (the maximum load in the nanoindenter was reached prior to failure of the 168 nm sample). Middle row: stress-strain response for the *in situ* cycles. Bottom row: stress-strain response for *ex situ* compression on 3 distinct samples for each thickness. Scale bar, 50 µm.

The 163 nm shell thickness samples ($\overline{\rho} = 2.3 \pm 0.1\%$) exhibited the predicted two-order-of-magnitude anisotropy for the lamellar architecture, with an experimental $E^*_{[001]}/E^*_{[100]}$ ratio of 0.057 compared to 0.014 predicted by simulations. The close-

to-isotropic and columnar samples approximated the numerical models' overall anisotropy with experimental $E^*_{[001]}/E^*_{[100]}$ ratios of 0.87 and 3.0 compared to the numerical ones of 0.92 and 7.2, respectively. The inherent surface waviness of the samples caused by the layer-by-layer 3D printing process slightly undermines the mechanical properties (Extended Data Figure 4.10), but preserves the desired qualitative anisotropic response. Thinner-walled samples (i.e., $t = 11$ and 44 nm) exhibited the same anisotropic behavior and had higher knockdown factors caused by fabrication defects.

Our experiments reveal that the nano-labyrinthine ceramic architectures possess high and tunable directional stiffness and do not contain stress concentrations like those at the junctions of all periodic architectures [39, 75, 87, 120], which enables their extraordinary mechanical resilience as shown in Figs. 4.6 and 4.7. Our *in situ* experiments reveal that the 11 nm-thick samples exhibited full recovery, with no visible microcracks, after ten compressive cycles to strains of up to 35 %. This is in contrast to all other thin-walled ceramic and polymer beam-based architected materials at this scale, which fail by the creation of microcracks at the nodes and whose strength and energy-absorption hysteresis deteriorate by an order of magnitude or more after just one loading cycle [39, 93, 120]. While both hollow-beam and nano-labyrinthine architectures structurally recover due to elastic shell buckling, the nano-labyrinthine samples in this work are the only ones that do not visibly fracture and maintain substantial mechanical performance with cycling. For instance, the columnar architecture (Fig. 4.6) compressed along the [001] direction exhibited a linear loading regime followed by the onset of elastic buckling of the Al_2O_3 shells from a strain of 5% to 10%, beyond which they underwent nonlinear buckling and self-contact, ultimately recovering to their original geometry after each cycle characterized by self-similar hysteretic behavior. This hysteresis corresponds to significant energy dissipation, most likely through friction and the nonlinear buckling processes, without any permanent structural deformation or evident microcrack formation (see Supplementary Videos 1–4). Increasing the shell thickness to 44 nm changed the failure mechanism to mostly fracture-dominated with structural recovery enabled by marginal elastic buckling (see Supplementary Videos 5–9), while the 163 nm samples underwent mostly catastrophic failure during the first cycle with their structural integrity compromised (see Extended Data Figure 4.5 & Supplementary Videos 10–14). This is consistent with the competing effects of elastic buckling and material failure found previously for hollow-shell truss architectures [92], which showed significant cyclic degradation driven

by stress concentrations at truss junctions. It is also in line with observations of improved effective strength in lattice materials [74] where fillets are used to decrease the curvature at truss nodes.

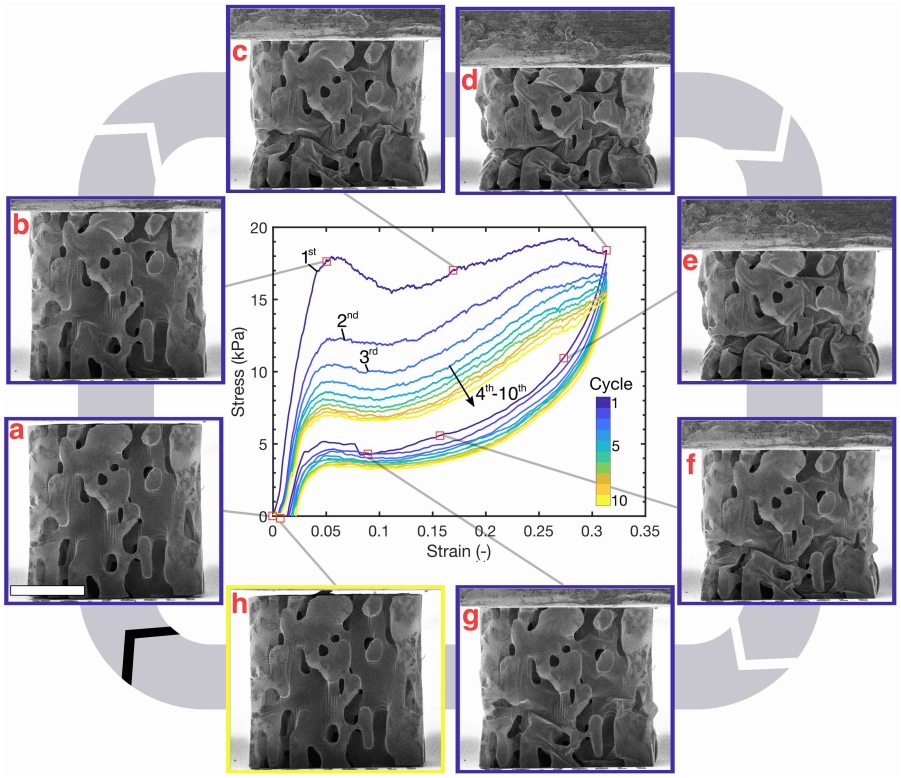

Figure 4.6 | Cyclic Loading and Recovery of Columnar Sample
Cyclic loading of a 11 nm-thick columnar architecture: **(a)** initial geometry, **(b)** end of linear regime and onset of buckling, **(c)** nonlinear buckling regime, **(d)** end of loading regime, **(e)**-**(g)** unloading regime showing elastic recovery, and **(h)** final geometry after 10 cycles showing no permanent microcracks. The panel border color matches the cycle number of the stress-strain plot. Scale bar, 50 μm.

We attribute the observed mechanical resilience to the double-curvature of the alumina surfaces. The low principal curvatures minimize the formation of stress concentrations, which prevents localized material failure. We quantify the architectural morphology by extracting the point-wise mean and Gaussian curvatures and calculating the principal curvature probability distribution (i.e., the distribution of κ_1 and κ_2). For the columnar architecture, Fig. 4.8a shows that most of its features have dimensionless principal curvatures, i.e., $\hat{\kappa}_i = \kappa_i L$ where L is the sample characteristic dimension, whose absolute value $|\hat{\kappa}_i|$ is less than 20. Performing the same analysis for the octet architecture shows significantly larger curvatures and their bimodal distribution, with a peak curvature dominated by the struts' non-zero $\hat{\kappa}_2$

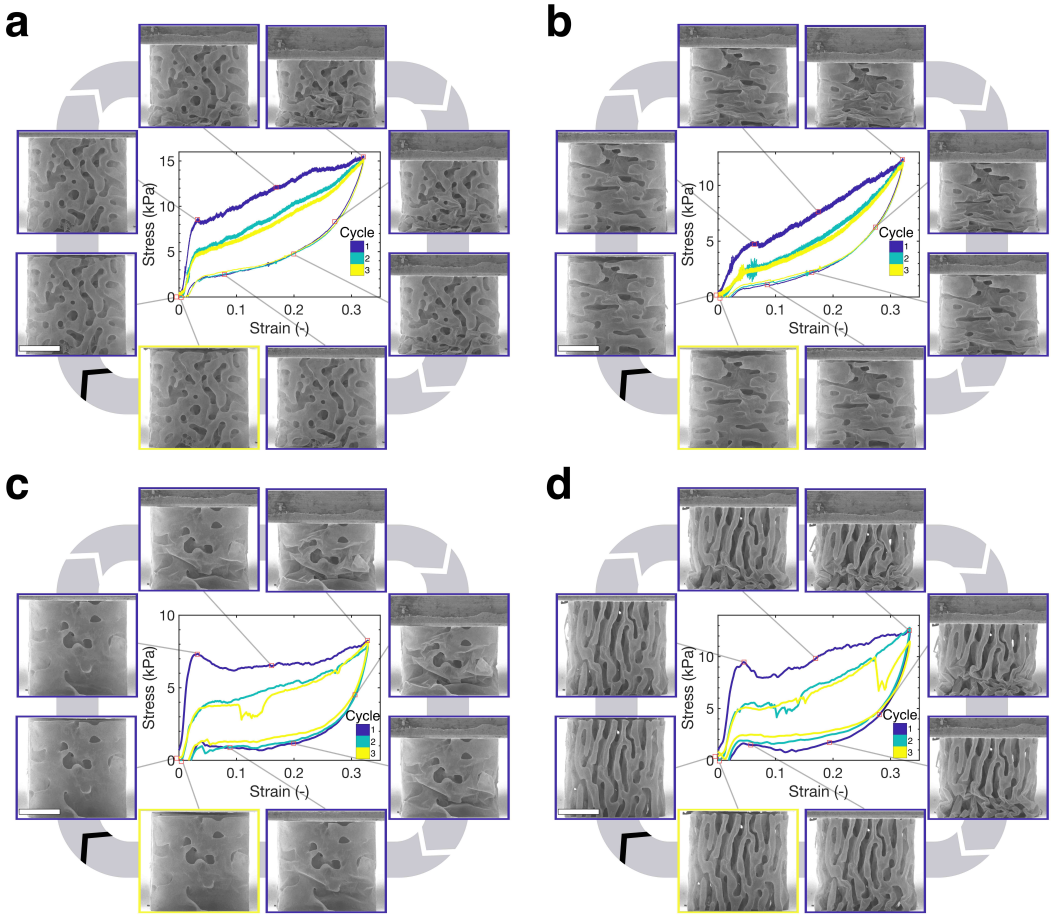

Figure 4.7 | Cyclic Resilience of Various 11-nm Nano-Labyrinthine Architectures
(a) Isotropic architecture, **(b)** columnar architecture along the [100] direction, **(c)** lamellar architecture along the [001] direction, and **(d)** lamellar architecture along the [010] direction. Scale bars, 50 µm.

curvature and another peak at $|\hat{\kappa}_i| \gg 20$ corresponding to the nodal joints. Experiments mitigate such singularities and introduce a finite-sized joint radius: the parameter space in Fig. 4.8b contains curvature distributions of octet-trusses for fillets with radii $0.5r$ and r (where r is the strut radius) that serve as conservative upper bounds. We matched the surface area-to-volume ratio of these unit cells with that of the bi-continuous columnar architecture (Fig. 4.9) to ensure equivalent relative densities.

We chose the columnar samples as a representative case to compare the cyclic performance of nano-labyrinthine architectures in this work to that of hollow-tube octet lattices. We fabricated $5 \times 5 \times 5$ octet tessellations with the same alumina wall thickness and relative density as the 11 nm samples and performed the same *in-*

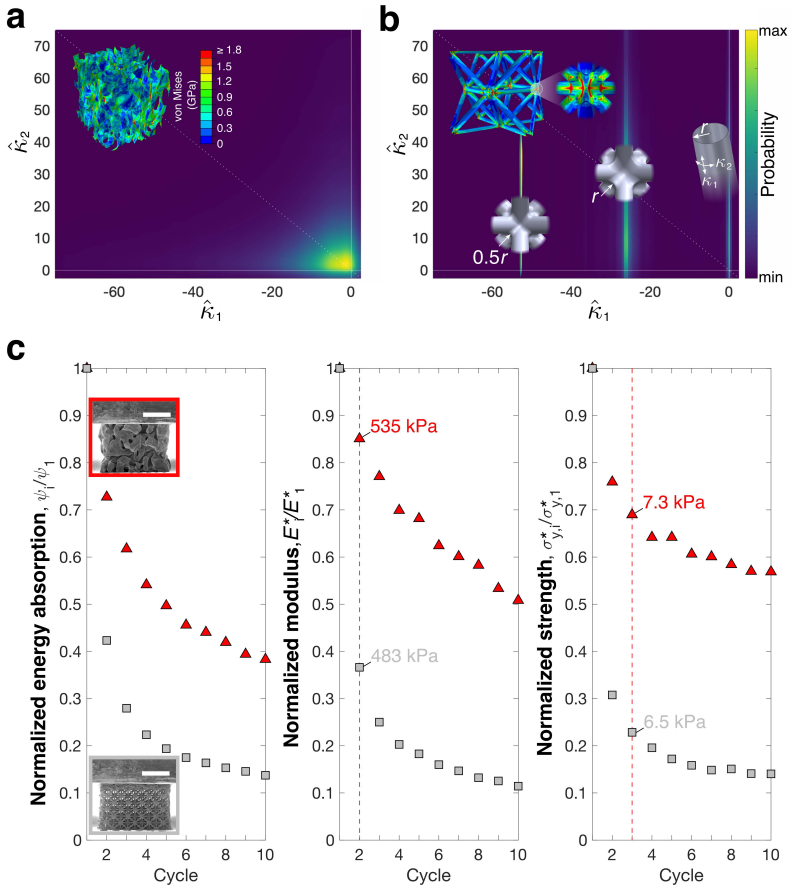

Figure 4.8 | Curvature Distribution and Cyclic Mechanical Performance
(a) Dimensionless curvature probability distribution for the columnar bi-continuous architecture with the stress distribution for uniaxial loading (inset), $\hat{\kappa}_i = \kappa_i L$, where L is the sample characteristic dimension; **(b)** two octet architectures with fillets of radii $0.5r$ and r, where r is the strut radius, and stress distribution for the $0.5r$ case in uniaxial loading (inset, same color map as **a**). The normalized curvatures are defined as $\hat{\kappa}_i = \kappa_i L$ where κ_i is a principal curvature and L is the unit cell dimension. **(c)** Evolution of first-cycle-normalized mechanical properties through cyclic loading for hollow octet and columnar bi-continuous material of relative density $\overline{\rho} = 0.15\%$, and 11 nm shells. Insets depict both architectures at maximum compression in an in situ experiment. Inset scale bar, 50 µm.

situ cyclic compressions along the [001] direction (see Fig. 4.9 & Supplementary Video 15). We tracked the degradation of the measured modulus E^*_i, strength $\sigma^*_{y,i}$, and the absorbed energy density $\psi_i = \frac{1}{2}\oint_i \sigma \mathrm{d}\varepsilon$, graphically represented as the enclosed area in the stress-strain response for a given i-th cycle. Fig. 4.8c summarizes how these three performance metrics, normalized by their values in the first cycle, evolved over ten load cycles. These plots convey that between the first and second cycles, the energy absorption decreased by 27% for the columnar architecture and

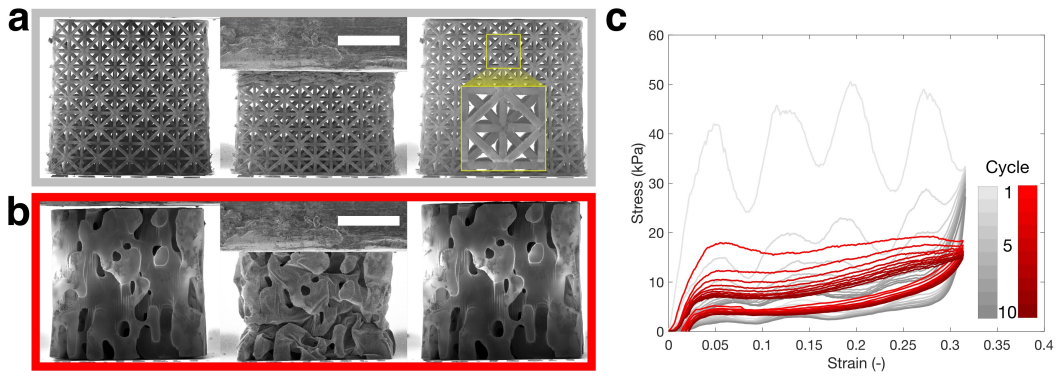

FIGURE 4.9 | CYCLIC RESPONSE OF OCTET AND COLUMNAR Al_2O_3 ARCHITECTURES
Micrographs of *in situ* uniaxial compressions depicting sample morphologies before, at maximum compression ($\varepsilon = 30\%$), and after 10 cycles for **(a)** an octet $5 \times 5 \times 5$ tessellation and **(b)** a columnar architecture, both of equal relative density and 11-nm wall thickness. **(c)** Cyclic stress-strain response for both samples showing self-similar response for the columnar architecture and significant decay in the octet architecture's response.

by 58% for the octet, asymptotically approaching the tenth-cycle limit of 38% of the original energy storage capacity for the columnar and 14% for the octet architectures. Young's modulus showed a second-cycle drop of 15% for the columnar architecture compared to 63% for the octet. This significant drop in the octet's mechanical response is caused by the localized material failure and a loss of load-bearing capacity at multiple nodes, whose number increases with cycling. The less-than-half relative drop in energy absorption and a factor-of-3 lower reduction in the Young's modulus between 1st and 2nd cycles of the columnar architectures, when compared with octets, stem from likely internal micro-cracks and variations in the self-contact process that weaken but not necessarily disable load-bearing shells (no cracks were observed on the structure's outer surfaces). Strength performance also appears to be superior for the columnar architecture showing a first-to-second-cycle degradation of 24% degradation compared to 70% for the octet, with the absolute strengths being greater than those of octet beyond the second cycle. Despite the knock-down factor in stiffness and strength caused by shell waviness (Fig. 4.10), the columnar architecture shows considerably superior mechanical performance compared to periodic architectures through (at least) ten cycles. Since the deformation mechanisms exhibited by the columnar and octet architectures are representative of nano-labyrinthine and periodic truss architectures, respectively, the benefits of non-periodic, low-curvature shells can be harnessed to produce architected nano-labyrinthine materials with superior mechanical performance than that of an equiv-

alent periodic architecture.

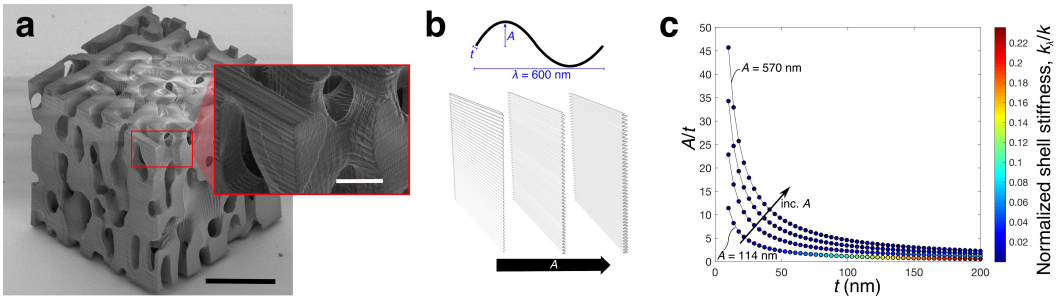

Figure 4.10 | Effect of Shell Waviness
(a) Columnar bi-continuous architecture fabricated using two-photon lithography showing shell waviness due to the layer-by-layer nature of the fabrication process; **(b)** finite element models of a corrugated sheet with varying thicknesses t and amplitudes A, for a constant wavelength $\lambda = 600$ nm (corresponding to two printing layers); **(c)** stiffness of the corrugated sheets k_λ normalized by the stiffness of a flat sheet k, for various amplitude-thickness combinations, upon loading from the top with roller boundary conditions on the sides. At small thicknesses, two-order-of-magnitude knockdown can be attributed to corrugation. Black and white scale bars, 50 µm and 10 µm, respectively.

4.7 Quasi-Linear Stiffness Scaling

The Atomic Layer Deposition (ALD) process used in this work allowed for a wide range of shell thicknesses, from 11 to 168 nm, which enabled the nano-labyrinthine architectures to span a relative density range from 0.15 % to 2.4 %. To explore the effect of relative density on stiffness and anisotropy, we performed finite element simulations of three types of architectures with the same relative densities: columnar nano-labyrinthine, hollow octet truss, and the Schwarz Primitive triply periodic minimal surface (TPMS). Fig. 4.11 shows a plot of the normalized elastic modulus $E_{[001]}/E_s$ (top plot) as a function of relative density for these three architectures along with their elastic surfaces at three different relative densities (bottom panels). These simulations demonstrate a close-to-constant anisotropy for the columnar architecture (red), with virtually identical lobular elastic surfaces, and a quasi-linear stiffness scaling exponent of $\alpha = 1.17$ (fit of the type $E_{[\cdot]} \propto \overline{\rho}^{\alpha}$) at relative densities below 5%. The TPMS (blue) and octet (grey) geometries exhibit significant transformations in anisotropy, with both having a scaling exponent of ~1.4, and with the octet gradually changing its direction of maximal stiffness from [001] to [111] throughout the studied relative density regime. This anisotropy in trusses arises from the competing effects of beam bending and stretching [126] and presents an additional challenge when designing truss-based materials. Nano-labyrinthine ar-

chitectures appear to be immune to significant changes in wall thickness as they retain their target elastic anisotropy throughout the full explored density range.

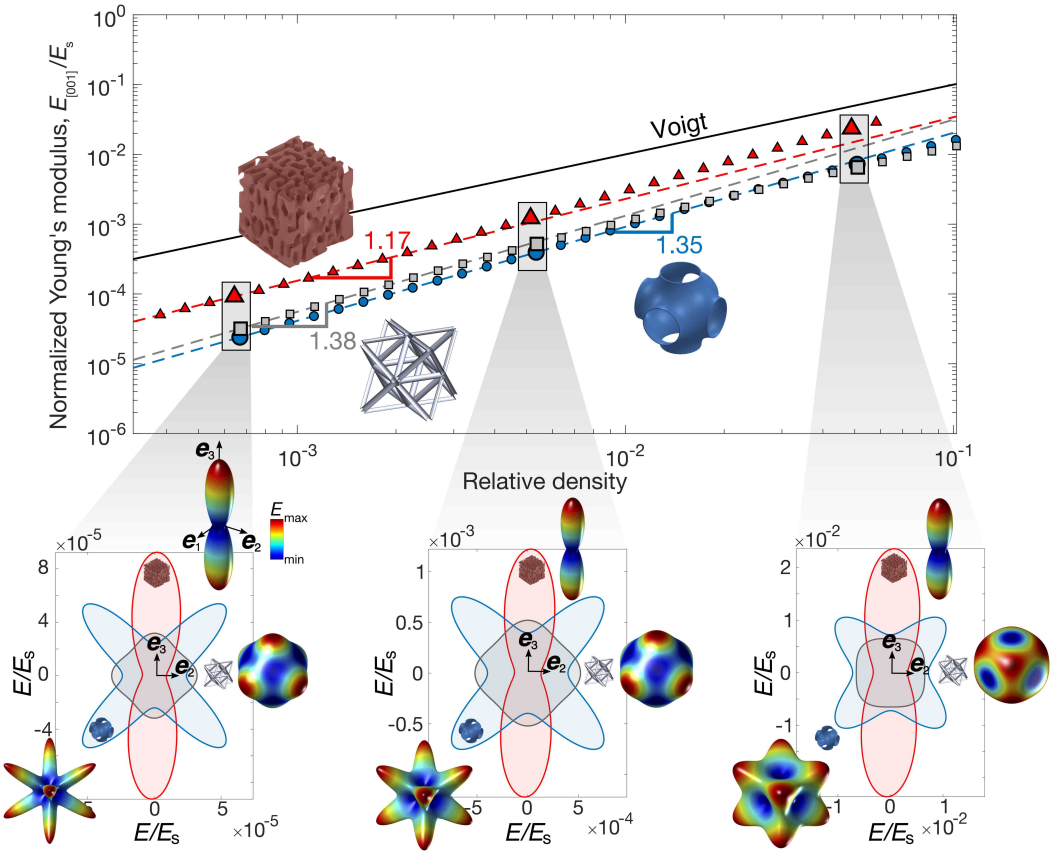

Figure 4.11 | Stiffness Scaling and Elastic Surface Variations in Nano-Labyrinthine Architectures
Normalized Young's modulus $E_{[001]}/E_s$ as a function of relative density $\overline{\rho}$ for bi-continuous columnar (red), Schwarz Primitive TPMS (blue), and hollow octet (gray) architectures. Fits for the ten lowest relative densities from each architecture are depicted as dashed lines, using a fit of the form $E_{[\cdot]}/E_s = C\,\overline{\rho}^{\alpha}$, with the corresponding scaling exponent α next to each fit. The elastic surfaces for each structure, along with their 2D projections, are shown for three selected relative densities. Close to constant anisotropy is observed for the bi-continuous architecture as opposed to the TPMS and octet geometries.

The stiffness scaling of nano-labyrintine architectures reveals another counter-intuitive feature, previously shown only for thick polymeric shells [57]: all architectures display an almost linear stiffness scaling with relative density. Performing the same analysis for the rest of the nano-labyrinthine architectures was consistent with the stiffness scaling of the columnar one with scaling exponents ranging from 1.16 to 1.21 in the ⟨100⟩ directions, remaining below the scaling exponents computed for

the TPMS and octet architectures. Linear scaling is considered to be optimal, as it corresponds to the rule of mixtures, and is generally associated with stretching as the primary deformation mechanism; bending manifests in $\alpha = 2$. Although the double-curvature morphology explains the enhanced resilience observed for all architectures, the fact that their elastic deformation is stretching-dominated seems counter-intuitive at first—but is also tied to the double curvature. In the limit of very thin shells of thickness t, the bending stiffness (scaling with t^3) is comparably less than the stretching stiffness (scaling with t), so that membrane theory effectively describes the deformation behavior.

To further understand the effect of double-curvature on the load distribution within the shells, we analyzed first-order approximations of the columnar architecture since the exact morphology of nano-labyrinthine architectures is challenging to quantify. We approximated the columnar topology as: (*i*) an ideal array of cylindrical shells with $\kappa_1 = 0$ and $\kappa_2 > 0$ having zero Gaussian curvature (i.e., $\kappa_1\kappa_2 = 0$), (*ii*) an array of doubly-curved *barreled* nearly-cylindrical shells with $\kappa_1 > 0$ and $\kappa_2 > 0$ having positive Gaussian curvature, and (*iii*) an array of doubly-curved *waisted* nearly-cylindrical shells with $\kappa_1 < 0$ and $\kappa_2 > 0$ having negative Gaussian curvature (see Fig. 4.12). The curvature distribution presented in Fig. 4.8a demonstrates that the negative Gaussian curvature approximation is most appropriate for these architectures. For the idealized cylindrical shell arrangement case ($\kappa_1\kappa_2 = 0$), we find that applying an arbitrary distribution of axial load N on one end of the shells produces a solution of straight lines carrying the load throughout the shell, analogous to an arrangement of straight rods. In the nearly-cylindrical case with a negative Gaussian curvature, the solution still has a straight distribution of axial load N, with no decay from the prescribed value at one end (see Supplementary Information for derivation). Since this would not be the case if the simplified structure had positive Gaussian curvature, such as a barrel-like cylinder, it is evident that the negative Gaussian curvature adds rigidity to axial loads in the form of membrane-stress carrying ability [22, 116], as depicted by the simulations on these elementary strucures in Fig. 4.12. This figure also shows vertically aligned domains in the uniaxial compression simulations of the columnar architecture along which the principal stresses are non-decaying and maximal, resembling the non-decaying solution of the *waisted* cylindrical shells [22, 116]. Given that this solution only applies while the membrane hypothesis is valid (i.e., small thicknesses and relative densities), it is expected that bending will take a more prominent role at higher relative densities yielding slightly higher scaling exponents due to less ideal stress distributions.

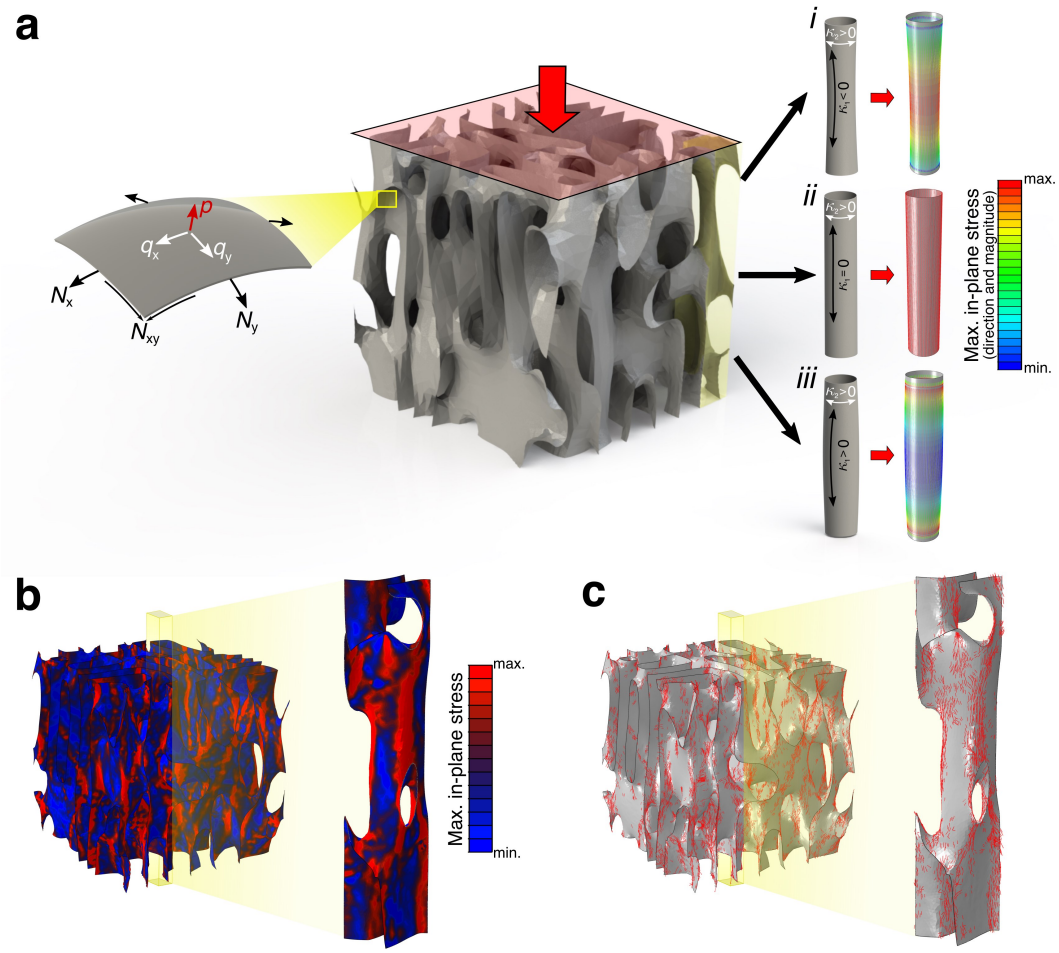

Figure 4.12 | Effect of Double Curvature on Load Distribution
(a) Elementary doubly curved shell section depicting the stress resultants (left), and uniaxial compression simulations of three simplified representative structures for the columnar architecture under the same boundary conditions (right). In particular, we show the compression of: (*i*) a *waisted* shell with negative Gaussian curvature (i.e., $\kappa_1\kappa_2 < 0$) showing in-plane stress intensification, (*ii*) a cylindrical shell with zero Gaussian curvature showing the ideal case of constant in-plane stress, and (*iii*) a *barreled* shell with positive Gaussian curvature showing attenuation of vertical in-plane stress. **(b)**, **(c)** Finite element models of uniaxial compression on the columnar architecture with maximum in-plane stress regions shown in red (b) along with the vectors corresponding to their orientation (c), presenting evidence of no attenuation in vertically aligned domains.

4.8 Conclusion

In this chapter we present the first fabrication method that enables self-assembly of nano-architected materials with up to cubic-centimeter volumes and numerically and experimentally showcase their mechanical tunability and unsurpassed resilience. This method presents a significant advancement in the fabrication and

design of architected materials at any scale, since it bypasses the need for slow and defect-prone additive manufacturing processes. These nano-labyrinthine ceramic-shell architectures also are the first to overcome the common high-stiffness-high-resilience exclusivity while maintaining controllable constant anisotropy over a wide range of relative densities, namely from 0.15% to 2.4%. Our architectures combine two beneficial design strategies explored only independently before: extremely thin shells yielding material size effects and reducing material failure, on the one hand, and smooth double-curvature structural architectures providing high stiffness, on the other hand. The consequence are high-tunable-stiffness, high-resilience metamaterials which promise potential for scalable fabrication at large scales through self-assembly.

4.9 Detailed Methods Description

4.9.1 Sample Fabrication

The centimeter-scale bi-continuous polymer was synthesized according to the method reported by Tsujioka et al. [133]. In brief, 2.34 g of diglycidyl ether of bisphenol A (DGEBA), 0.86 g of 4,4'-methylenebis(cyclohexylamine) (MBCHA), and 8.01g of polyethylene glycol (PEG) 200 were added to a 20 mL vial, mixed vigorously in a vortex mixer to form a clear homogenous solution and then ultrasonicated for 10 s to remove any bubbles formed. 1.5 mL of this solution was added to a 1 dram vial (15 mm-diameter) and then cured at 130 °C for 3 hrs to form a white solid. After polymerization, the sample was immersed in water for 24 hrs to extract out the PEG 200 porogen, followed by drying in vacuum at room temperature for another 24 hrs. The polymer was then sectioned and the inner cores were were conformally coated in Al_2O_3 using an atomic layer deposition (ALD) process (Cambridge Nanotech S200). The chamber was held at 150 °C with a recipe consisting of pulsing H_2O for 15 ms, purging for 20 s, pulsing trimethyl aluminum (TMA) for 15 ms, purging again for 20 s, and repeating the process for the desired layer thickness. The system was run for 750 cycles (corresponding to 79 nm) with N_2 as the carrier gas at a flow rate of 20 sccm. The coating thickness was verified via spectroscopic ellipsometry using an alpha-SE Ellipsometer (J.A. Wollam Co., Inc). To expose the epoxy component after coating, we made sacrificial cuts on some edges using a razor. The exposed samples were inserted in an O_2 plasma asher between 100 h to 200 h, in a 300 sccm flow rate at 100 W power output, until the epoxy component was fully removed.

The computed geometries were fabricated at the microscale using a two photon

lithography (TPL) process in a Photonic Professional GT system (Nanoscribe GmbH). A laser power of 15 mW and a scan speed of 10 mm s^{-1} on an Ip-Dip photoresist. To prevent excessive warping during the developing process, we dried the samples using a critical point drying process in an Autosamdri-931 system (Tousimis). Following the drying process, the samples were conformally coated in Al_2O_3 using the atomic layer deposition (ALD) process described above. Depending of the sample, the system was run for 100, 400, or 1600 cycles. After deposition, we introduced perforations on the top ceramic coating using focused ion beam milling (FIB) in an FEI Nova 200 Nanolab system (see Fig. 4.4). The exposed samples were inserted in an O_2 plasma asher between 80 h to 100 h, in a 300 sccm flow rate, at 100 W power output. Using a high imaging voltage (~10 kV) in a scanning electron microscope, it was possible to determine when the totality of the polymer had been removed.

4.9.2 Computational Framework

The sample geometries were computed using the numerical framework presented by Vidyasagar et al. [137]. In this approach, the evolution of a phase field describing anisotropic spinodal decomposition was simulated using a stabilized Fourier spectral technique. The phase field, existing in stable equilibrium at either of the binary phases (i.e., $\phi = 0, 1$) describes microstructure formation given a particular non-convex potential energy, respective volume fractions, and preferential directions of anisotropy. The Ginzburg-Landau form of the binary potential ensured that the mixture underwent reverse diffusive processes and formed stable phases. The interface energy introduces anisotropy by penalizing normal gradients along particular directions. The stabilization and regularization of the Fourier spectral method, which was chosen to exploit the computational efficiency of Fast Fourier Transforms, ensured that interfacial ringing artifacts caused by non-convexity of interface energy were largely mitigated. This is performed using finite difference stencils to obtain asymptotically consistent acoustic wave vectors. The simulations were initiated with smooth initial Gaussian distributions for probabilistic pattern formation and evolution. The interfaces resulting from the simulated spinodal decomposition, i.e., with $\phi = 0.5$, were extracted to yield the geometries used to generate the metamaterials.

The geometries derived from the computational spinodal decomposition process were meshed using three-node shell elements (S3R) in Abaqus (Simulia). A mesh convergence study was performed to ensure mesh-independent results, which led to 237,000 to 266,000 elements per model, depending on geometry type. Following

a corresponding mesh convergence study, the geometries for the octet and TPMS architectures consisted of 16,000 and 63,000 elements, respectively.

To compare the response of the uniaxial compression experiments to simulations, we performed a set of linear perturbation simulations to establish the linear response of each geometry. Depending on the parameter being probed, we applied a compression strain of 1% in the selected direction by constraining the out-of-plane displacement degrees of freedom (dofs) on the plus and minus faces, while leaving the in-plane displacement dofs and all rotations unconstrained. The remaining four faces in the cubic representative volume element (RVE) were left unconstrained, as in the experiments.

To predict the full elastic response of the architectures (i.e., elastic surfaces and Young's moduli in all directions), we implemented a numerical homogenization scheme. Upon applying proper periodic boundary conditions, we sequentially imposed each column of the strain tensor $\tilde{\boldsymbol{\varepsilon}} \in \mathbb{R}^{6\times6}$ of the form $\tilde{\boldsymbol{\varepsilon}} = \alpha \boldsymbol{I}$ (with $\alpha = 0.01$), and computed the resulting stresses to populate the corresponding effective stress tensor $\tilde{\boldsymbol{\sigma}} \in \mathbb{R}^{6\times6}$. Following Hooke's law $\boldsymbol{\sigma} = \mathbb{C}\boldsymbol{\varepsilon}$ (or $\sigma_{ij} = \mathbb{C}_{ijkl}\varepsilon_{kl}$ following Einstein's summation convention), where $\boldsymbol{\sigma}$ and $\boldsymbol{\varepsilon}$ are corresponding columns of $\tilde{\boldsymbol{\sigma}}$ and $\tilde{\boldsymbol{\varepsilon}}$, respectively, the full elastic modulus tensor $\mathbb{C}$ was obtained. Lastly, the compliance tensor $\mathbb{S} = \mathbb{C}^{-1}$ was calculated to obtain the Young's modulus $E(\boldsymbol{d})$ in any direction $\boldsymbol{d}$ as $E^{-1}(\boldsymbol{d}) = \mathbb{S}_{ijkl}d_i d_j d_k d_l$.

4.9.3 Nanomechanical Experiments

We performed nanomechanical experiments on the shell-based architectures to determine their effective stiffness, strength, and recoverability along the ⟨100⟩ directions. We performed *ex situ* uniaxial compression experiments on a minimum of three samples per configuration (i.e., each geometry, thickness, and orientation) using a G200 XP Nanoindenter (KLA). The samples were compressed to strains of up to $\varepsilon = 35\%$, at a strain rate of $\dot{\varepsilon} = 10^{-3}$ s^{-1}, using a 400 μm flat punch tip. The *in situ* compressions were performed using an inSEM II Nanoindenter (Nanomechanics) under the same conditions as in the *ex situ* compressions. Cyclic compressions of up to ten cycles were performed *in situ* observe the failure mechanisms and to quantify the cycle-specific dissipated energy and recovery. For all experiments, the effective Young's modulus was approximated by the loading slope of each cycle's linear stress-strain regime. For samples exhibiting catastrophic failure (i.e., some of the 44 nm samples and all of the 168 nm samples), the strength was approximated as the maximum load prior to collapse. For the recoverable samples (i.e., some of

the 44 nm samples and all of the 11 nm samples), the strength was calculated via the 0.2% strain offset method.

Chapter 5

VIBRATION MITIGATION VIA LATTICE ARCHITECTURES

Section 5.2 has been adapted from:

X. Xia, A. Afshar, H. Yang, C.M. Portela, D.M. Kochmann, C.V. Di Leo & J.R. Greer. "Electrochemically Reconfigurable Architected Materials". *Nature* (2019) 573, 7773 pp. 205–213. DOI: 10.1038/s41586-019-1538-z.

CONTRIBUTIONS: computed the numerical dispersion relations and participated in the writing of the manuscript;

and section 5.3 is part of a collaboration with Jinwoong Cha and Chiara Daraio.

CONTRIBUTIONS: designed and implemented the experimental setup, designed and fabricated the samples, computed the numerical dispersion relations, and conducted the experiments and analyzed the data.

5.1 Chapter Summary

At this point in the thesis we have thoroughly explored the static mechanical parameter space of beam- and shell-base architectures but no explorations into their dynamic response have been done. This chapter will provide an exploration into the dynamic realm by studying the propagation of mechanical waves in micro-architected beam-based materials of two types.

We will first present a method to fabricate microlattices that utilize electrochemistry to undergo reconfiguration, providing a method to actively modulate the propagation of waves in this material. We numerically explore the dynamic response of this material and analyze the emergence of vibrational band gaps upon tunable and reversible reconfiguration.

The second part of this chapter presents a custom experimental technique that enables probing the response of small-volume micro-architected materials upon ultrasonic stimuli in the MHz regime, which is used to measure the emergence of band gaps upon adding micro-inertia to a polymeric microlattice.

5.2 Vibration Band Gaps via Reconfigurable Architectures

The dynamic response of architected materials is an active field of research due to their ability to exhibit tunable properties such as vibrational band gaps [2, 10, 16, 59] or nonlinear wave propagation [33] on top of their already unique static mechanical properties. Unlike homogeneous materials, the highly tunable microstructure of these materials has enabled designs that achieve reconfiguration by mechanical deformation [104] and instabilities [30, 44], hydration-induced swelling [64, 125], or magnetic actuation [66]. Such smart, multi-functional materials would have a long-lasting impact on implantable, deployable, and dynamically tunable devices if they could overcome the challenges of (*i*) requiring bulky external control, (*ii*) only toggling between "on" and "off" states, and (*iii*) reverting to the initial structure once the external stimulus is removed. Furthermore, most of these reconfigurable systems are small and idealized; increasing the number of repeating units in periodic architected materials could potentially induce inhomogeneities similar to defects, gradients or grain boundaries in classical materials [17, 31].

In this section, we demonstrate a mechanism to achieve reconfigurability in architected materials by exploiting electrochemical alloying/dealloying reactions that enable continuous, stable, and reversible structural transformations. Using the alloying couple of silicon and lithium as a prototype system notorious for ~300% volumetric expansion [89], we designed and fabricated Si-coated tetragonal microlattices purposely structured to promote lateral in-plane buckling. Using the resulting buckled patterns along with the varying constituent material properties due to alloying, we numerically study the evolving dynamic response of these materials at different lithiation stages by computing their dispersion relations.

5.2.1 Fabrication and Experimental Lithiation of Si Microlattices

To create micro-architectures with a propensity for collective in-plane buckling, we designed a periodic three-dimensional (3D) lattice comprised of tetragonal unit cells with slender horizontal beams connected to stubby vertical posts. Fig. 5.1a shows a schematic of this lattice geometry and the fabrication process. We first printed the polymer tetragonal lattice on a glass substrate using two-photon lithography, then sputtered a ~100 nm-thick Ni conductive layer and deposited a ~300 nm-thick amorphous Si layer onto each beam within the structure using plasma-enhanced chemical vapor deposition (PECVD). Each sample contained $79 \times 79 \times 5$ unit cells in the x-, y-, and z-directions, respectively (with the xy-plane corresponding to the substrate), and each tetragonal unit cell had a width of $20\,\mu m$ (horizontal beam

length) and a height of 5 μm (vertical post length) (Fig. 5.1b-e). The horizontal beams had an elliptical cross-section with a vertical major axis of ~2.6 μm and a minor axis of ~1.3 μm; the vertical posts had a circular cross-section with a diameter of ~2.6 μm. A square grid with 5 μm spacing was also patterned on the substrate to prevent delamination of the Si thin film underneath the microlattice (Fig. 5.1c). Each sample contained ~8.0 μg of Si as the electrochemically active component, with an areal Si loading of 0.25 mg cm^{-2}.

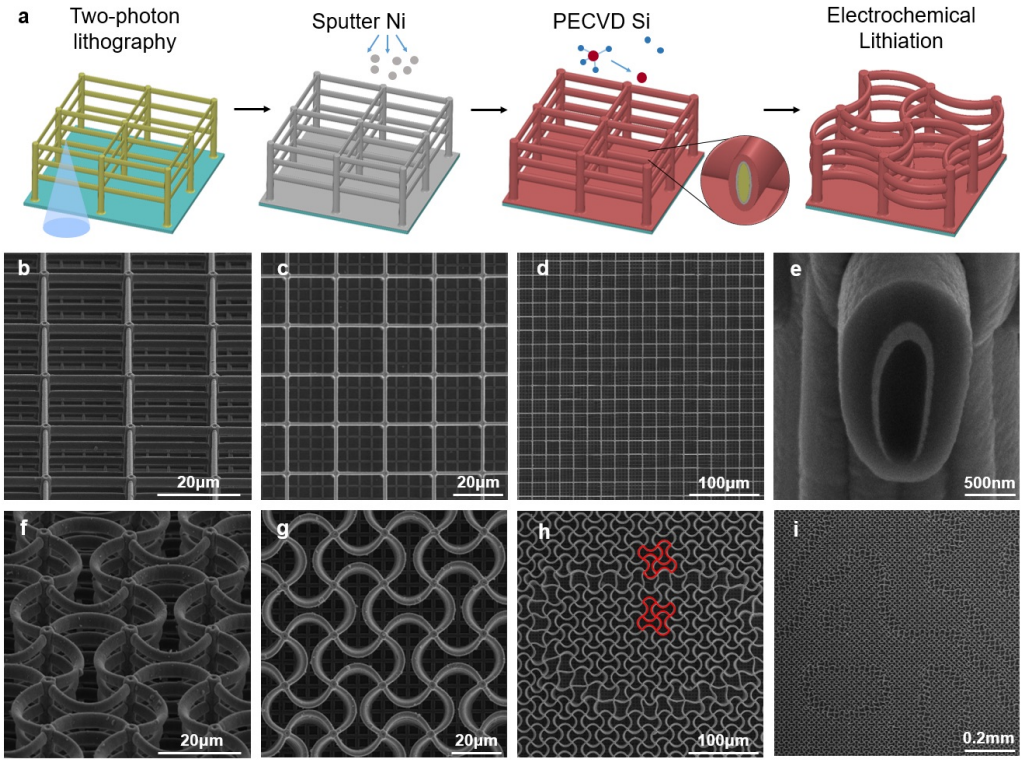

Figure 5.1 | Fabrication Process and SEM Characterization of Si Microlattices Before and After Lithiation
(a) Illustration of the fabrication process of Si microlattices and their structural transformation after lithiation. **(b)**-**(d)** SEM images of as-fabricated Si microlattices at different magnifications and tilts. **(e)** SEM image of a FIB-milled cross-section of a representative horizontal Si-Ni-polymer beam that shows a slight variation in the Ni and Si layer thickness. **(f)**-**(i)** SEM images of Si microlattices lithiated at a current of $C/6$ and a cutoff voltage of 0.01 V vs. Li/Li$^+$ at different magnifications and tilts. (b, e, f) are at a tilt angle of 52°. (c, d, g, j, i) are top-down views. (f, g) show the orthogonal sinusoidal pattern formed via cooperative buckling. (h, i) show multiple bistable domains adjoined by clearly visible boundaries. (h) contains an overlaid illustration of the two bistable states for a four-unit-cell group.

Lithiation of Si microlattices inside modified coin cells was conducted galvanos-

tatically at a constant current of 5 μA with a Li counter electrode until the voltage dropped to a cutoff voltage of 0.01 V vs. Li/Li^+ (see Xia et al. [144] for details). This applied current corresponds to a current density of 0.15 mA cm^{-2} and a *C*-rate of ~*C*/6, where a *C*-rate of 1*C* represents the current at which it takes 1 hour to attain the theoretical capacity of the electrode (3600 mA h g^{-1}Si [102]). Under these conditions, an average of ~80% of the theoretical capacity was attained after the first lithiation, which corresponds to ~240% of volumetric expansion in the Si shell [58]. SEM images in Fig. 5.1f-i demonstrate that Si microlattices deformed via cooperative beam buckling to result in an orthogonal sinusoidal pattern with pairwise opposite concavity upon lithiation. Each horizontal beam accommodated the volumetric expansion through radial growth of the cross-sectional area and axial elongation, which prompted in-plane beam buckling. The two ends of each beam were connected to two nodes, which rotated in opposite directions in response to buckling-induced torque. We did not observe any cracking or failure of the beams after lithiation, and the lattice remained in this stable, buckled state after removing the applied current. The buckling directions of four neighboring horizontal beams at each node were coupled through the node's in-plane rotation, and such cooperative buckling led to the formation of the ordered sinusoidal pattern in the lateral planes (Fig. 5.1g), which is known for its auxetic behavior [27, 28, 68]. The bistability of in-plane beam buckling led to the formation of multiple domains in the microlattice, with the domain boundaries defined by second-mode buckled beams (Fig. 5.1h, i). The buckling pattern transcended vertically across all out-of-plane layers through twisting of the vertical posts (Fig. 5.1f).

5.2.2 *In situ* Observation and Reversibility of Lithiation-induced Buckling

We constructed an *in situ* optical setup to capture the dynamics of cooperative buckling and domain formation in real-time. A custom-made electrochemical cell with a quartz window was used to visualize structural transformations at a constant current of *C*/6 under a digital optical microscope. Fig. 5.2a,b present real-time snapshots of a typical in situ experiment at progressively lower voltages during lithiation (Fig. 5.2a) and at progressively higher voltages during delithiation (Fig. 5.2b). Lithiation was conducted until a cutoff voltage of 0.01 V, and delithiation was conducted until a cutoff voltage of 1.5 V. *In situ* lithiation observation revealed that incipient slight buckling initiated at a few lattice sites and rapidly spread onto all horizontal beams, which continued to buckle simultaneously as the lithiation proceeded. Domain boundaries emerged spontaneously between mismatched domains.

During delithiation, the horizontal beams almost fully unbuckled, and fracture occurred at the nodes when the voltage increased above ~0.6 V. The Si-Li alloying reaction is a spontaneous discharge process, which implies that the observed lithiation-induced cooperative buckling does not require an external energy supply.

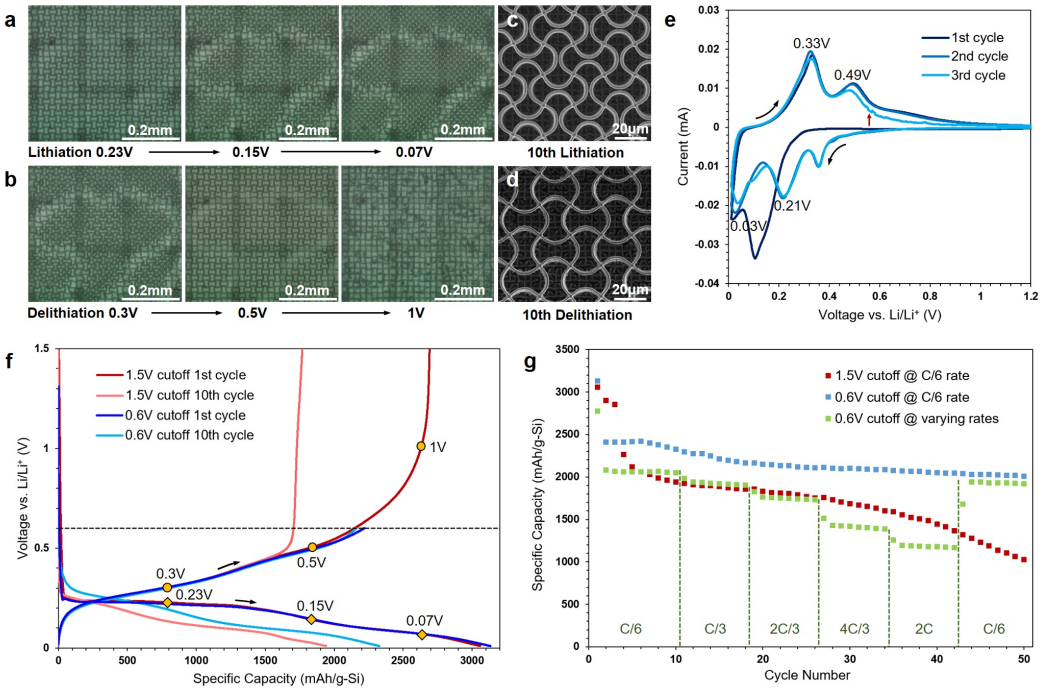

Figure 5.2 | *In Situ* Optical and Electrochemical Characterization of Lithiation-Induced Cooperative Buckling in Si Microlattices
(a),(b) Progressive optical snapshots during in situ (a) lithiation and (b) delithiation at different voltages that reveal cooperative buckling, unbuckling, and domain formation. **(c),(d)** SEM images of Si microlattices after (c) the 10th lithiation and (d) the 10th delithiation in modified coin cells with a 0.6 V delithiation cutoff voltage. **(e)** A cyclic voltammogram of a representative Si microlattice with a Li counter electrode at a scan rate of 0.1 mV s^{-1} between 0.01 V and 1.5 V. The red arrow points out the current fluctuation starting around 0.55 V in the 3rd delithiation. **(f)** Voltage profiles of the 1st and 10th cycles with 1.5 V and 0.6 V delithiation cutoff voltages in modified coin cells. The voltages labeled in (f) correspond to the voltages shown in (b, c) during *in situ* experiments. **(g)** Cycling performance of Si microlattices with 1.5 V and 0.6 V delithiation cutoffs at $C/6$ and at varying rates up to $2C$.

Fig. 5.2e shows a cyclic voltammogram (CV) of the first three cycles by scanning the voltage at a rate of 0.1 mV s^{-1} between 0.01 V and 1.5 V in a modified coin cell. It conveys the reversible Si-Li alloying and dealloying reactions indicated by the reduction peaks around 0.03 V and 0.21 V and the oxidation peaks around 0.33 V and 0.49 V respectively [24, 82]. The initial lithiation of pristine Si occurred at a lower

voltage of 0.11 V, and weak reduction peaks around 0.40 V appeared in the second and third cycles possibly caused by irreversible Li insertion; these features are consistent with reports for various binder-free amorphous Si electrodes [82, 114, 150]. Noticeable current fluctuations occurred during the third delithiation around 0.55 V, which correlates with the local fracture events observed at a voltage of ~0.6 V in the in situ delithiation experiment. To investigate if preventing these unstable events could improve cycling reversibility, we conducted galvanostatic cycling tests with two delithiation cutoff voltages of 1.5 V and 0.6 V. Fig. 5.2f compares the voltage vs. specific capacity profiles of the 1st and 10th cycles for two samples with these two delithiation cutoff voltages; the voltages that correspond to the *in situ* snapshots in Fig. 5.2a,b are also labeled. This plot indicates that restricting the delithiation voltage to below 0.6 V retained ~30% of the inserted Li during the 1st lithiation inside the microlattice and significantly improved the reversible capacity of the Si-Li alloying/dealloying reactions. SEM images of Si microlattices after the 10th lithiation and the 10th delithiation with a 0.6 V delithiation cutoff voltage in Fig. 5.2c,d reveal structural integrity and reversibility of geometric transformations in Si microlattices during stable electrochemical cycling. The Li storage capacity vs. cycle number plot in Fig. 5.2g demonstrates stable lithiation and delithiation cycling of Si microlattices, with a 50th cycle capacity retention of 2010 mA h g^{-1}-Si for a 0.6 V delithiation cutoff voltage compared with that of only 1025 mA h g^{-1}-Si for a 1.5 V delithiation cutoff voltage at a constant current of $C/6$. Fig. 5.2g also shows the good rate capability of Si microlattices with a specific capacity of 1300 mA h g^{-1}-Si at a high cycling rate of $2C$.

5.2.3 Numerical Dynamic Analysis

The demonstrated electrochemically driven cooperative buckling in Si microlattices uncovers a new regime for dynamic structural reconfiguration in architected materials. Most of the existing reconfigurable materials are soft polymer structures that rely on persistent external stimuli to stay in the deformed geometry [4, 27, 30, 64, 66, 104, 125]. The Si microlattices in this work are electrochemically lithiated to induce simultaneous buckling and plastic deformation, which locks-in the buckled geometry. The degree of buckling can be continuously tuned and even reversed by simple electrical control. The Si-Li alloying reaction is an electrochemical discharge process that releases energy, which implies that the lithiation-induced buckling mechanism can be used as a building block for self-powered deployable structures that spontaneously transform into the desired geometry while providing

energy for lighting or heating. Through the interactions among neighboring beams, cooperative buckling transforms a simple tetragonal lattice into a well-studied sinusoidal lattice with intriguing mechanical metamaterial properties. These structures have been shown to have a negative Poisson's ratio [27, 28, 68] and deform synclastically upon out-of-plane bending [81]. In the dynamic realm, they provide an efficient platform for designing tunable phononic crystals.

Elastic Dispersion Relations

To understand the effect of structural reconfiguration on the dynamic response of this tunable material, we conducted an eigenfrequency analysis on the three-dimensional unit cells at different stages of lithiation using the commercial finite element package COMSOL Multiphysics. We considered an extended unit cell consisting of 2×2 tetragonal unit cells for the buckled configurations to maintain compatibility and periodicity, while simulations for the initial as-fabricated configuration were done on a single unit cell (Fig. 5.3). The geometry was represented using linear tetrahedral elements, with 18,600 to 110,000 elements per unit cell depending on geometry and the required discretization to ensure mesh-independent results. For simplicity, all material properties (i.e., Young's modulus E, Poisson's ratio ν, and density ρ) for a given beam were homogenized following a weighted volume average. This resulted in the elements corresponding to the horizontal beams (elliptical cross-section) and the vertical beams (circular cross-section) having different constituent material properties due to different volume ratios of Si, Ni, and polymer in each.

For a comprehensive understanding of the dynamic response of this material, we considered three different cases: (*i*) as-fabricated Si microlattices (Fig. 5.3a), (*ii*) lithiated Si microlattices (Fig. 5.3b), and (*iii*) delithiated Si microlattices (Fig. 5.3c). For as-fabricated Si microlattices, we used the same geometry of the experimental samples described above. For lithiated Si microlattices, we considered a realistic 80% state of charge (SOC) that corresponds to the Li_3Si phase. For delithiated Si microlattices, we considered a realistic 70% Coulombic efficiency with a 0.6 V delithiation voltage cutoff in the first cycle that leads to the $Li_{0.9}Si$ phase. We assumed 240% volumetric expansion for Li_3Si and 60% for $Li_{0.9}Si$ (compared to Si volume) based on simulation results by Huang and Zhu [58] and used those values to calculate the corresponding material densities. Poisson's ratios for $Li_{0.9}Si$ and Li_3Si were estimated by the rule of mixtures of the atomic ratios of Si and Li.

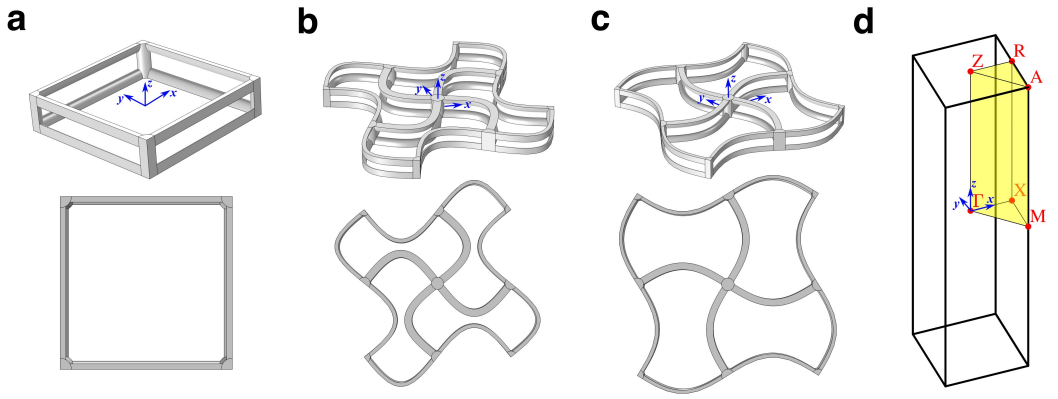

Figure 5.3 | Real- and Reciprocal-Space Unit Cells for Dispersion Relations
(a) Initial, as-fabricated unit cell matching the dimensions of the fabricated samples, **(b)** lithiated unit cell with buckled beams approximated by sinusoidal functions, resembling an 80% state of charge state corresponding to a Li_3Si phase, **(c)** delithiated unit cell corresponding to a 70% Coulombic efficiency and 0.6 V cutoff corresponding to $Li_{0.9}Si$, **(d)** first Brillouin zone (reciprocal space, black outline) and irreducible Brillouin zone (yellow). The real-space coordinate system is shown in blue.

The Young's moduli of Si, $Li_{0.9}Si$, and Li_3Si were chosen to be 110 GPa, 85 GPa, and 50 GPa, respectively, based on nanoindentation test results of amorphous Si thin films undergoing lithiation [32]. The calculated material properties for each material phase are summarized in Table 5.1.

	Polymer	**Ni**	**Si**	**$Li_{0.9}Si$**	**Li_3Si**	**Li**
E [GPa]	5	200	110	85	50	–
ν	0.38	0.31	0.22	0.31	0.33	0.36
ρ [kg/m^3]	1,180	8,080	2,330	1,784	1,199	–

Table 5.1 | Material Properties for Reconfigurable Material's Phases
Calculated material properties for each material phase and the Li-Si alloy at different states-of-charge.

The geometry of the buckled beams was approximated using sinusoidal functions for simplicity, although slightly smaller curvatures were observed at the center of some beams in the samples, and the amplitudes of these functions were chosen based on experimental SEM images. To estimate the material volume ratios in each beam, the thickness of the $Li_{0.9}Si$ and Li_3Si layers were calculated from the sinusoidal geometry and the corresponding volumetric expansion ratios using SolidWorks (Daussault Systèmes). Using these volume ratios, along with the calculated properties presented in Table 5.1, we calculated the homogenized material proper-

ties for the horizontal and vertical beams using a rule-of-mixtures and utilized those values to compute the disperion relations (Table 5.2).

	Initial		**Lithiated**		**Delithiated**	
	Horizontal	Vertical	Horizontal	Vertical	Horizontal	Vertical
E [GPa]	95.4	69.8	55.2	47.1	81.6	63.1
ν	0.28	0.31	0.34	0.34	0.33	0.34
ρ [kg/m^3]	2,874	2,425	1,718	1,674	2,404	2,145

TABLE 5.2 | HOMOGENIZED MATERIAL PROPERTIES FOR RECONFIGURABLE MATERIAL'S DISPERSION RELATIONS
Calculated homogenized material properties for horizontal- and vertical-beam domains in the simulations. These values were calculated using the individual phases' properties presented in Table 5.1 and the volume ratios obtained from CAD models.

Bloch boundary conditions, as described in section 1.5.2, were applied to the corresponding faces of the simulated unit cells. Using the corresponding irreducible Brillouin zone (IBZ) depicted in Fig. 5.3d, we swept the wavevector through the edges and calculated the first 30 eigenfrequencies at each state to construct the dispersion relations. Fig. 5.4 demonstrates that lithiation-induced cooperative buckling creates two 6 MHz-wide partial band gaps centered at 16 MHz and 44 MHz for waves propagating in the x- or y-directions of the microlattice, compared to no band gaps in the as-fabricated lattice. Upon partial delithiation to a 0.6 V cutoff, the center of the first band gap moves to 22 MHz, and that of the second one to 53 MHz, showing a correlation between the state of charge and the dynamic response. Sweeping the wavevector along the edges of the IBZ corresponding to all xy-plane direction (i.e., Γ-M-X-Γ) confirms the existence of the two partial band gaps in all in-plane directions for both the lithiated and delithiated configurations (Fig. 5.5c,d). The formation and tunability of these band gaps are attributed to both the lattice geometry transformations, potentially triggering Bragg scattering behavior, as well as changes in material properties due to alloying/dealloying. Due to the electrochemical capabilities of this material, the frequencies of the band gaps can be reversibly tuned by repeated lithiation and delithiation in a non-volatile fashion with a minimum switching time of a few minutes.

Besides confirming the partial band gaps in all in-plane directions, the dispersion relations presented in Fig. 5.5 provide insight into the changes in phase and group velocities for the three configurations. As expected, group velocities in the long-wavelength limit (i.e., in the vicinity of Γ) for the first few modes are much higher for the initial configuration than for the buckled ones, since this architecture is stiffer

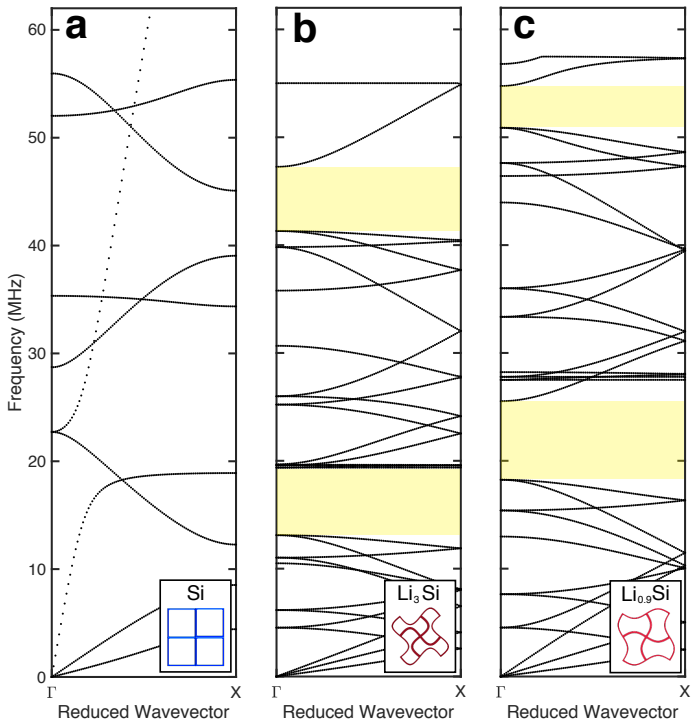

FIGURE 5.4 | SI MICROLATTICE ELASTIC DISPERSION RELATIONS
(a) as-fabricated Si microlattices, **(b)** lithiated Li_3Si microlattices, and **(c)** partially delithiated $Li_{0.9}Si$ microlattices using Bloch boundary conditions. The Γ-X wavevector path consists of that along the edge of the irreducible Brillouin zone, coinciding with the x-direction (equivalent to y-direction due to symmetry).

and stretching-dominated (as opposed to bending-dominated). To decouple the effects of geometry and material properties on the formation of band gaps, we constructed the dispersion relations of the lithiated and delithiated configurations with the as-fabricated material parameters (i.e., without changes in the chemical composition of the Si layer). As shown in Fig. 5.5a, using these material properties still presents two band gaps in each configuration, with mid-band frequencies changing from 18 MHz and 49 MHz to 23 MHz and 54 MHz in the lithiated and delithiated states, respectively. This corresponds to relative center-frequency shifts ranging from 2 % to 13 %, without any significant qualitative changes in the dispersion. This marginal change in the dynamic response indicates that the geometric transformations play a more dominant role than varying material properties in enabling the formation of band gaps, and strengthen the case for Bragg scattering mechanisms (as opposed to local resonance).

To better understand the mechanism that gives rise to these band gaps, we study

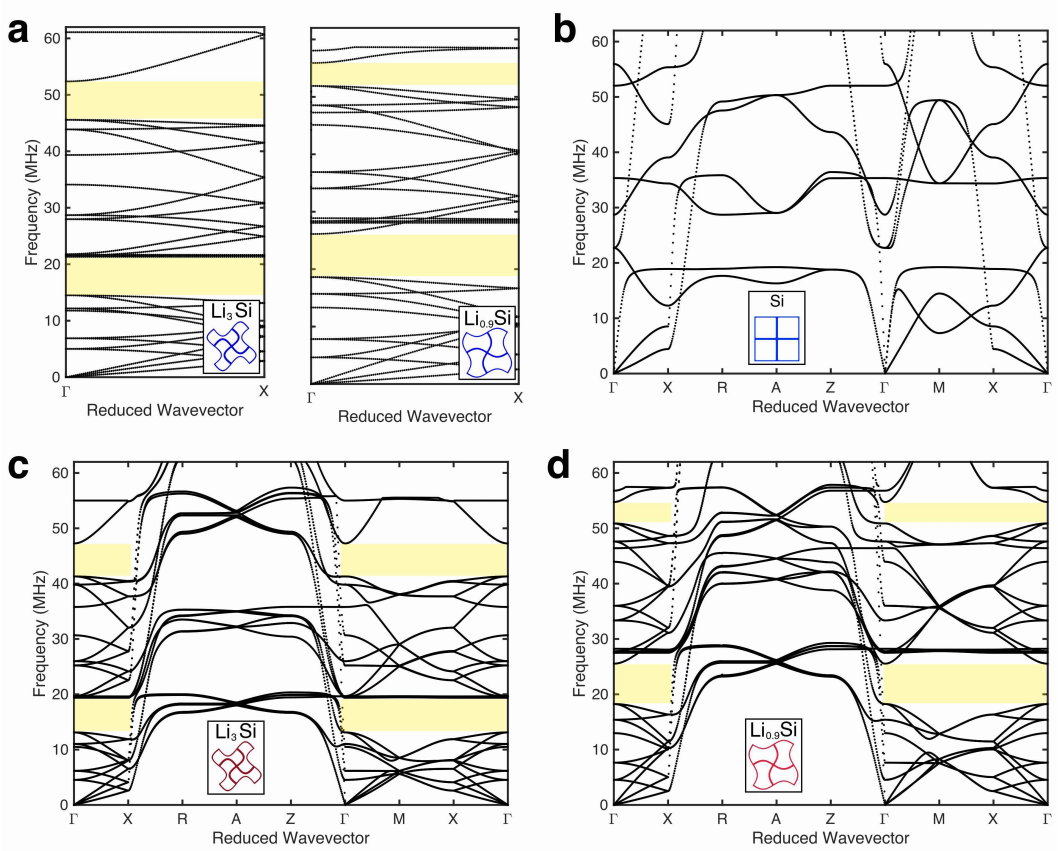

Figure 5.5 | Extended Si Microlattice Elastic Dispersion Relations
(a) Dispersion relations of the lithiated and delithiated states without accounting for the inherent mechanical property changes upon alloying, **(b)**–**(d)**, extended dispersion relations for the as-fabricated, lithiated, and delithiated unit cells, respectively. The band gaps shown in (c) and (d) prove their existence in all directions within the *xy*-plane.

the first-order approximation of an Euler-Bernoulli beam in free vibration under pinned-pinned boundary conditions as a potential source of local resonance in the unit cell. Applying the appropriate boundary conditions to the general solution of this problem yields a first resonant frequency of $f_0 = \frac{\pi}{2}\sqrt{EI/\rho AL}$, where I is the second area moment, A is the cross-sectional area, and L is the length of the beam. Assuming an initially straight geometry (which might over-predict the frequency by up to ~30-40% for the curvatures in our samples [25]), and using the effective parameters for in-plane bending of the horizontal beams in the Si microlattices (Table 5.2), we calculated the resonant frequencies to be 11 MHz and 8.6 MHz for the lithiated and delithiated cases, respectively. Since these frequencies are well below the first band gaps in each configuration (especially accounting for possible over-estimation) and do not agree with the trend of the first band gap's frequency

increasing upon delithiation, it is likely that the dominating mechanism for band gap formation is Bragg scattering instead of local resonance due to beams.

Elastoacoustic Dispersion Relation

Since microdevices that utilize the reconfigurable properties of the Si microlattices can be readily fabricated as enclosed microlattice-electrolyte systems, we also studied the dynamic response of such devices. To this end, we computed the dispersion relation of the lithiated microlattice submerged in the electrolyte, while accounting for coupling between the fluid and the solid. Linear tetrahedral elements were used for the fluid domain, with a total of 296,000 elements in the geometry. In a similar fashion to the elastic dispersion relations, we enforce Bloch boundary conditions of the form $(\boldsymbol{u}^+, p^+) = (\boldsymbol{u}^-, p^-)\boldsymbol{e}^{i\boldsymbol{k}\boldsymbol{x}}$, where $\boldsymbol{u}^{+/-}$ and $p^{+/-}$ correspond to the displacement vector and the pressure of a point on the plus and minus faces of the unit cell, applied to the solid and fluid domains respectively, $\boldsymbol{k}$ is the wave vector, and $\boldsymbol{x} = \boldsymbol{x}^+ - \boldsymbol{x}^-$ is the vector between the plus and minus faces. For simplicity, we approximated the electrolyte's properties to be those of water, and we coupled the fluid and solid domains by applying the fluid pressure as a normal traction boundary condition to the solid elements while shear stresses and viscous effects in the fluid were neglected.

When compared to the elastic dispersion relation, the elastoacoustic one (Fig. 5.6a) shows a higher density of states at lower frequencies. In addition, we see the emergence of initially non-dispersive fast and slow Biot waves [71] at low frequencies. To focus our analysis on the modes that could potentially be experimentally measured, we selected those with the largest displacements in the Γ-X-direction (Fig. 5.6b).

These modes were selected by applying an x-direction participation metric of the form

$$M_x = \frac{1}{2}\int_{\Omega_s} \frac{|u_x|}{|\boldsymbol{u}|} dV + \frac{1}{2}\int_{\Omega_f} \frac{|U_x|}{|\boldsymbol{U}|} dV, \tag{5.1}$$

where $\boldsymbol{u}$ and $\boldsymbol{U}$ are the displacement vectors in the solid and fluid domains, respectively. Fig. 5.6 shows these modes with transparencies linked to M_x and color-coded to *qualitatively* depict the solid-fluid displacement phase, i.e., $\phi = \text{sign}\left(\frac{\int_{\Omega_s} u_x dV}{\int_{\Omega_f} U_x dV}\right)$, with red and blue signifying in- and out-of-phase, respectively. This different dynamic response is marked by the emergence of two acoustic band gaps (in yellow), corresponding to a hybridization of the fast Biot mode with elastic modes of the

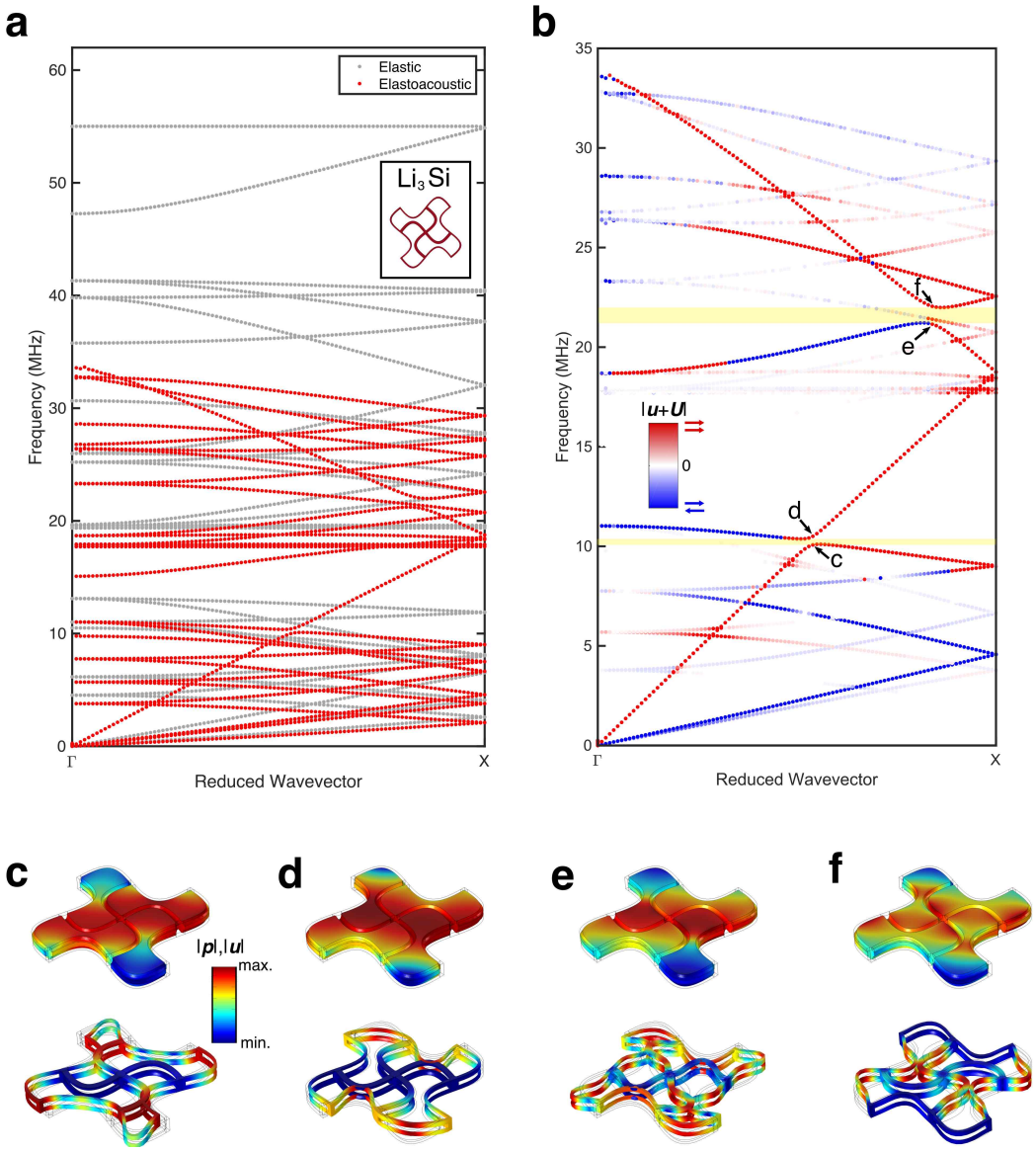

FIGURE 5.6 | SI MICROLATTICE ELASTOACOUSTIC DISPERSION RELATION
Numerical study corresponding to the lithiated microlattice submerged in an electrolyte. **(a)** Overlaid elastic and elastoacoustic dispersion relations for the same geometry, **(b)** detailed view of the elastoacoustic dispersion relation in (a), whose bands have modified transparency depicting the magnitude of their x-direction participation and have been color-coded to depict in-phase (red) or out-of-phase (blue) solid-fluid motion. **(c)–(f)** Fluid pressure fields and elastic modes corresponding to the bands below and above each acoustic band gap (yellow). The electrolyte was simplified to have the properties of water, and its pressure field was coupled to the elastic displacements of the microlattice.

microlattice, at ~10.3 MHz and ~21.5 MHz. The resulting modes above and below these band gaps, shown in Figs. 5.6c-f, depict the strong coupling between the fluid

pressure field and the resulting elastic displacements. The observed strong coupling between the fluid and solid hints at the beam geometry as an additional tuning parameter to shift or widen the acoustic band gaps. Although the acoustic band gaps are narrower and at different frequencies from the elastic ones shown in Fig. 5.4, this proves the potential of using reconfiguration to create more complex, tunable acoustic band gaps.

Outlook

We envision that tunable phononic band gaps of architected materials, combined with the versatility and flexibility of additive manufacturing, could empower novel non-linear microelectromechanical systems (MEMS) in the RF domain [23]. Engineering defects in the architected materials also allows for accurate programing of the transformed configurations as well as the formation of domain boundaries between several transformed domains, which could also forbid the propagation of waves at certain frequencies. This opens up opportunities to trap and control phonon modes inside the domain boundaries, which could potentially enable topological metamaterials [123, 124]. Even though the proof-of-concept material system used in this work (Si-Li) is air-sensitive, other bi-metallic alloying systems with compatible phase diagrams and realistic diffusion kinetics can be explored in aqueous electrolytes [42], potentially embedded in dehydration-resistant hydrogels [146].

5.3 Vibration Band Gaps Enabled by Added Micro-inertia

The emergence of band gaps in truss architectures via reconfiguration, as shown in Section 5.2, can enable the formation of band gaps commonly through Bragg scattering mechanisms. Another potential route consists of designing structural components or lumped inertia which act as local resonators to also give way to band gaps. This concept has been extensively studied both numerically and experimentally in a variety of periodic 2D materials and structures [5, 59, 105, 140] and has been shown to effectively provide mechanisms to introduce band gaps and wave directionality. This analysis has also been done numerically for 3D truss-based materials whose unit cells contain some sort of localized micro-inertia [2, 70, 83] wwith tunable geometry such that the resulting band gaps can be shifted or even widened.

Experimental validation of band gap formation in 3D truss materials has been achieved with samples at the cm-scale [88, 141], targeting frequencies in the kHz

range. Current efforts in this field seek to work with mechanical vibrations in the MHz regime [23], which requires a substantial downscale of material dimensions as well as reliable techniques to validate their response. Few works have achieved experimental measurements of 3D truss materials in this frequency range [69, 71], and have only achieved them while the materials are submerged in a fluid (to avoid impedance mismatching), inherently studying the coupled fluid-solid response and not that of the material alone.

In this Section we provide a custom method to experimentally measure wave propagation in micro-architected 3D materials while in vacuum, and use it to characterize the dynamic response of a periodic 3D truss-based material. Using advanced fabrication techniques, we include μm-scale resonators in the unit cells of the material and experimentally show the existence of numerically predicted band gaps.

5.3.1 Micro-scale Ultrasonic Transmission Method

Experimentally measuring the dynamic response of micro-architected materials presents several challenges due to the high frequencies associated with these length scales as well as the small sample sizes. In light of these difficulties, we designed and built a custom setup termed the *Micro-scale Ultrasonic Transmission Method* (μUTM) that enables dynamic probing of micro-architected materials with overall dimensions of just a few mm^3.

The μUTM setup analyzes the transmission of a signal through a material of interest using two ultrasonic transducers which come in contact with the sample on opposite sides. These transducers are mounted inside a scanning electron microscope (SEM) chamber (Quanta SEM, FEI), which enables *in situ* observation of the material while in a high vacuum environment. The two ultrasonic transducers are fully interchangeable, which allows for a wide range of transducer sizes and nominal frequencies ranging from ~1 MHz to 125 MHz. For the work presented in this chapter, we utilized two 10 MHz delay line transducers with a nominal element size of 0.25 inches and polystyrene delay lines with a nominal 10 μs delay (V202-RM, Olympus). The receiving transducer is mounted on the SEM stage and the sample material is fixed onto the transducer's delay line surface with colloidal graphite paste (Fig. 5.7a). The transmitting transducer is mounted on a nanoindenter arm, which enables positioning with nm-precision. Imaging with the electron beam then allows for accurate sample pre-strain measurements (Fig. 5.7b).

The two transducers are connected to an external lock-in amplifier equipped with

an arbitrary waveform generator (UHFLI, Zurich Instruments) via a BNC vacuum feedthrough. Depending on the desired signal power, a high frequency voltage amplifier may be connected between the lock-in amplifier and the transmitting transducer. Since each transducer's position can be fully adjusted, the relative distance between the two transducers may be tuned for the desired sample pre-strain. A schematic of the full setup is shown in Fig. 5.8

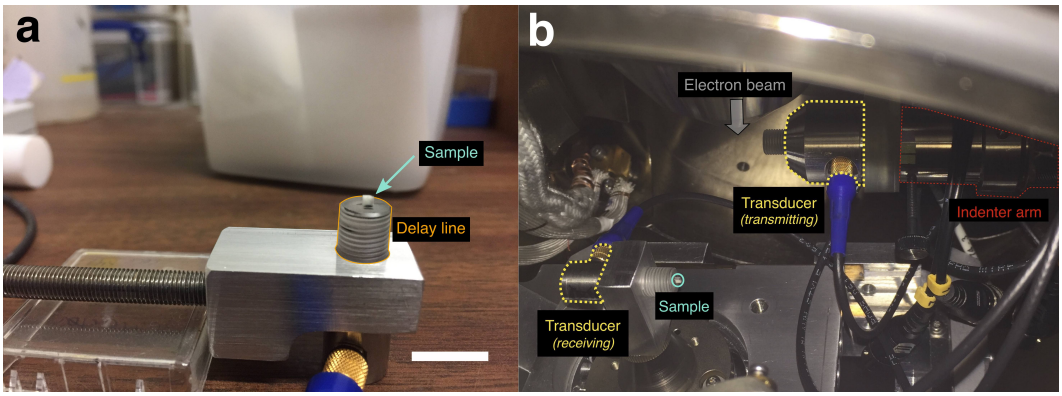

FIGURE 5.7 | MICRO-SCALE ULTRASONIC TRANSMISSION METHOD (μUTM) SETUP
(a) Close-up view of the transmitting transducer, the polystyrene delay line, and a micro-architected sample, and **(b)** photograph of the setup inside the SEM chamber, while the chamber is open and the transducers are not aligned. Scale bar, 1 cm.

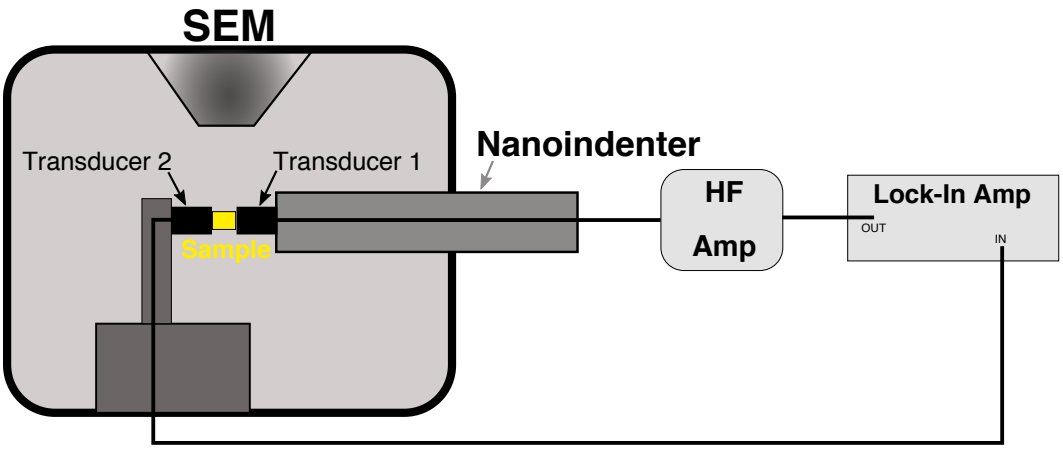

FIGURE 5.8 | μUTM SETUP SCHEMATIC
The full setup, with both transducers contacting the sample, is depicted. Depending on the amplitude of signal to be transmitted, a high frequency amplifier is connected between the the lock-in's output waveform and the transducer.

Method Validation

To validate the μUTM setup, we characterized the transmission through a homogeneous elastomer, *aqualene* dry couplant (Olympus), through a frequency-space ranging from 1 MHz to 3 MHz. A cylindrical puck of *aqualene* with a diameter of 0.64 mm and a 2 mm-thickness was placed between the two transducers with minimal pre-strain. The first test consisted of transmitting a high-frequency sinusoidal waveform and observing the transmitted waveform using an oscilloscope (DPO 3014, Tektronix), which confirmed low distortion of the signal and an appropriate delay corresponding to the two delay lines and the *aqualene* couplant (Fig. 5.9). As expected, a lower signal amplitude was measured by the receiving transducer due to the inherent damping in the elastomer as well as a relatively low contact force between both transducers.

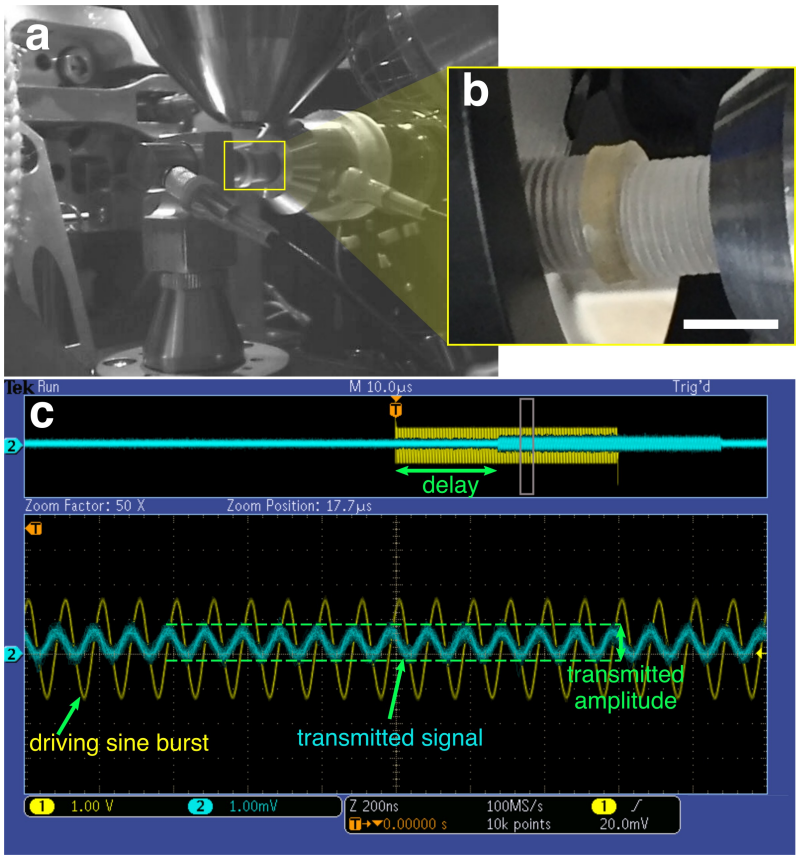

FIGURE 5.9 | μUTM VALIDATION WITH SINGLE-FREQUENCY SIGNAL
(a) Image of the setup under vacuum with **(b)** a 2 mm *aqualene* puck between the two transducers. **(c)** Oscilloscope observation of a 10 MHz pulse transmission, depicting the expected delay associated with the delay lines and the elastomeric puck.

The second test consisted of emitting a chirp signal with a 1 MHz to 3 MHz frequency content and analyzing the frequency content of the transmitted signal. This was done to ensure that the transducers could properly send and receive signals in this frequency range, and to confirm the non-dispersive response of a homogeneous elastomer such as *aqualene*.

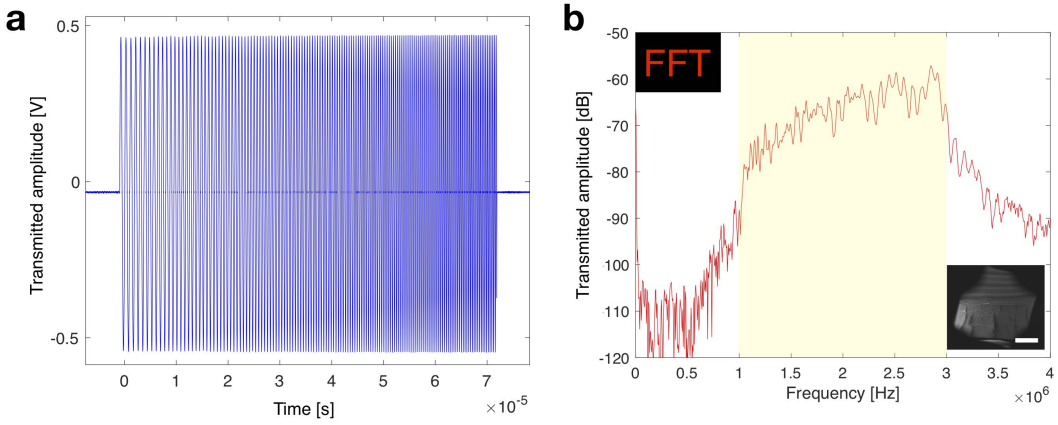

FIGURE 5.10 | μUTM VALIDATION WITH CHIRP SIGNAL
(a) Chirp with frequency content from 1 to 3 MHz and **(b)** Fast Fourier Transform (FFT) of the transmitted signal, showing proper tranmission and reception of the signal. Scale bar, 1 mm.

Fig. 5.10 shows the emitted chirp and the resulting transmitted frequency content, which was obtained by computing the fast Fourier transform (FFT) of the signal from the receiving transducer. As expected, the frequency content of the signal was between 1 MHz to 3 MHz, showing proper functioning of the transducers and no dispersion from the elastomer.

5.3.2 Auxetic Material with Resonators

To design architected materials with band gaps, we used a variation of the auxetic unit cell design presented by Krödel et al. [70]. We implemented the concept of a resonator by including a cantilever beam at the center of the unit cell with a sphere attached at its end. To target frequencies in the MHz regime, we selected the tetragonal unit cell dimensions to be $l_x = l_y = 60$ µm and $l_z = 209$ µm, with a junction angle $\theta = 70°$ (Fig. 5.11a). The strut diameters were kept constant at $r = 6$ µm between the unmodified unit cell and the one with the resonator. The resonator's cantilever beam, placed at the center of the unit cell, was chosen to have length $l_r = 53$ µm and a sphere with radius $r_s = 24$ µm. These parameters were

selected to optimize the band gap response of the material as well as the fabrication process.

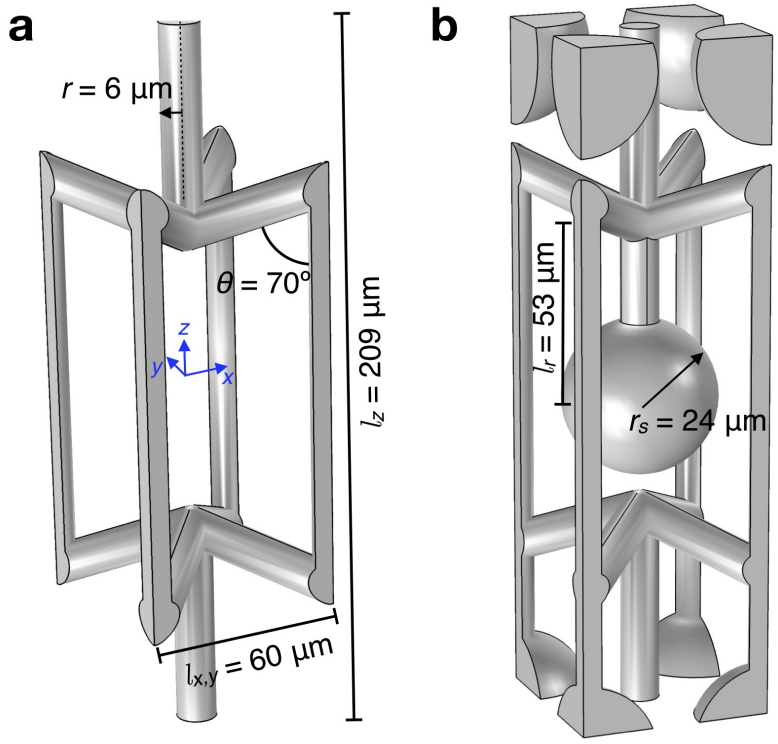

Figure 5.11 | Auxetic Unit Cell Design with Resonators
(a) Auxetic unit cell without a resonator and **(b)** modified unit cell with a cantilever beam and a spherical mass at its end, acting as the resonator.

Elastic Dispersion Relations

We computed the elastic dispersion relations for the unit cells in Fig. 5.11 in the same manner as in Section 5.2.3. This analysis was restricted to the Γ-*X* direction since this was the direction of experimental interest. The dispersion relation for the unmodified unit cell (Fig. 5.12) shows no band gaps, while that of the resonator-containing unit cell showed the emergence of a band gap centered at ~1.4 MHz.

The modes corresponding to the bands above and below the band gap (insets in Fig. 5.12b) show coupling between the resonator and the rest of the unit cell, meaning that the emergence of the band gap is not due to the resonator's contribution alone. To further analyze this response, we approximate the resonator in Fig. 5.11b as a clamped Euler-Bernoulli beam with a lumped mass at its free end (equivalent

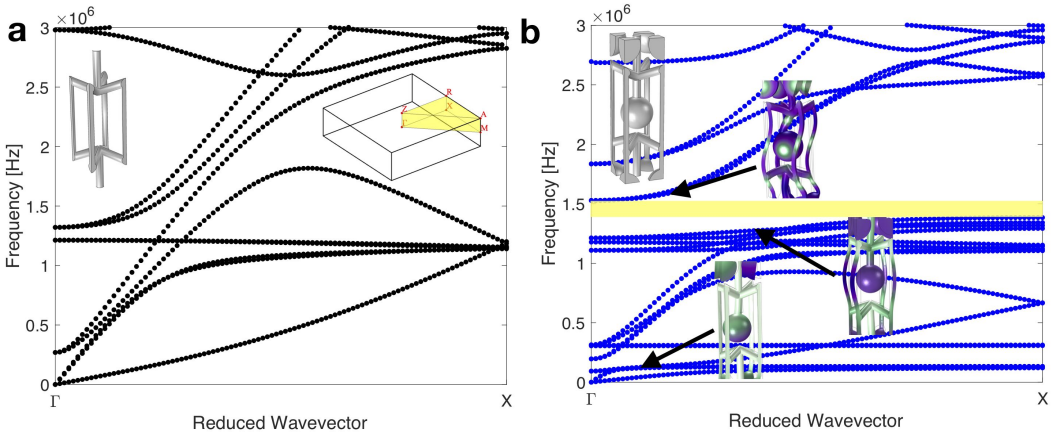

Figure 5.12 | Dispersion Relation of Auxetic Unit Cells
(a) Dispersion relation of unmodified unit cell from Γ to X showing no band gap, and **(b)** dispersion relation of the resonator-containing unit cell showing the emergence of a band gap, which seems to appear due to the coupled interaction of the resonator and the supporting lattice. Pure resonance of the cantilever beam is observed in the kHz regime.

to a spring-mass system), whose resonant frequency can be approximated as

$$f_0 = \frac{1}{2\pi}\sqrt{\frac{k_{\text{bend}}}{m_{\text{tot}}}}, \tag{5.2}$$

where k_{bend} is the stiffness of the beam in bending, $m_{\text{tot}} = \frac{33}{140}m + M$ is the participating fraction of the beam mass m plus the lumped mass M at the end. Taking $k_{\text{bend}} = 3EI/l_r^3$, where E is the constituent material's Young's modulus and $I = \pi r^4/4$ is the second area moment, and using the dimensions and material properties for the cantilever beam in this work ($E = 2.7$ GPa, $\rho = 1,200$ kg m^{-3}), yields an expected resonant frequency of $f_0 \approx 140$ kHz. This approximate resonant frequency is confirmed by the flat band corresponding to $f = 124$ kHz in Fig. 5.12b, whose mode shows the expected motion of the resonator alone. Given the dimensions associated with the auxetic unit cell as well as the material properties of polymer, it is impossible to achieve a feasible cantilever configuration within the volume of the unit cell to have f_0 in the MHz range, hence the need to recur to resonator-unit cell coupled modes for band gap emergence.

μUTM Testing

To experimentally measure the band gap in the dispersion relation, we fabricated $10 \times 48 \times 16$ tessellations (in the x-, y-, and z-directions, respectively) of the unit cells in Fig. 5.11 out of IP-S photoresist using a two-photon lithography system

(Nanoscribe, GmbH). A laser power of 25 mW and a scan speed of 20 mm s^{-1} were used on a Si substrate, leading to overall sample dimensions of ~0.6 × 2.9 × 3.3 mm. To promote proper contact with the transducers, a 6 µm plate was printed on the plus and minus x-faces of the microlattices. Following sample development in propylene glycol monomethyl ether acetate (PGMEA) and isopropyl alcohol (IPA), the samples were dried using a critical point dryer (Autosamdri 931, Tousimis) and carefully delaminated from the substrate using tweezers. Using colloidal graphite on one of the x-faces as a binder, the sample was then attached to the receiving transducer and put in contact with the transmitting transducer under vacuum as shown in Fig. 5.13a,b. This orientation ensured probing the microlattices in the Γ-X direction.

To probe the transmission response of the microlattices, we performed a frequency sweep of a continuous sine wave from 1 MHz to 3 MHz at a compression strain of ~10 % (Fig. 5.13d,e). Fabrication defects in the unmodified microlattice prevented testing of this sample due to improper contact and failure of truss members. The resonator-containing microlattice, on the other hand, showed an ~200 kHz-wide band gap indicated by a signal amplitude drop of more than an order-of-magnitude centered at ~2.4 MHz. The shift in the band gap center-frequency compared to the numerically predicted one is attributed to an under-estimation of the photoresist's Young's modulus as well as the effect of prestress on the propagation of waves in the material, which was not accounted for in the dispersion relations.

To confirm the existence of the band gap, we probed the material using a chirp with a frequency content from 1 MHz to 3 MHz. Applying a fast Fourier transform on the signal from the receiving transducer (Fig. 5.14) indicated the same band gap as the one observed in Fig. 5.13c.

5.3.3 Outlook

The implementation of the μUTM setup has allowed for previously unachievable dynamic characterization of nano- to micro-architected 3D materials. This ability to validate the exotic properties of such metamaterials could pave the way for a range of explorations towards information transport through mechanical waves, reconfigurable architected materials (as discussed in Section 5.2), or waveguiding and energy focusing for nanoelectromechanical devices. The concept of introducing micro-inertia (i.e., resonators) has proven to be effective for frequency ranges beyond those of the resonator's frequencies if proper coupling with the surrounding

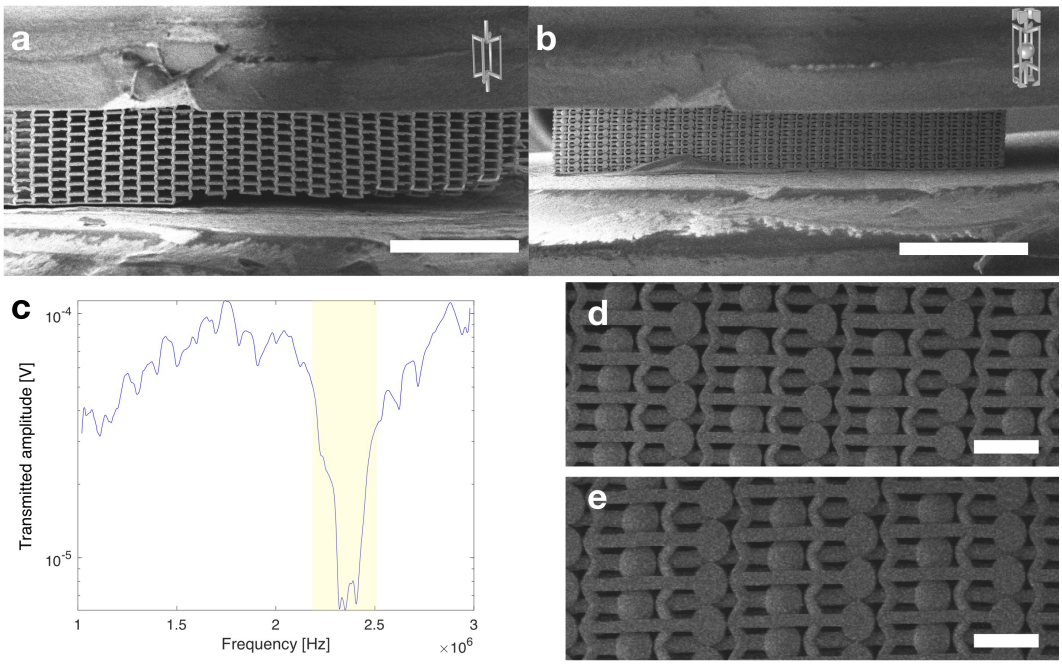

FIGURE 5.13 | FREQUENCY SWEEP OF AUXETIC MICROLATTICES
SEM image of the **(a)** unmodified and **(b)** resonator-containing microlattices upon contact with the transducers. **(c)** Frequency sweep from 1 MHz to 3 MHz, detailed view of sample **(c)** prior to contact, and **(d)** with some compressive strain due to contact. Scale bars in (a), (b), 1 mm and (d), (e), 100 µm.

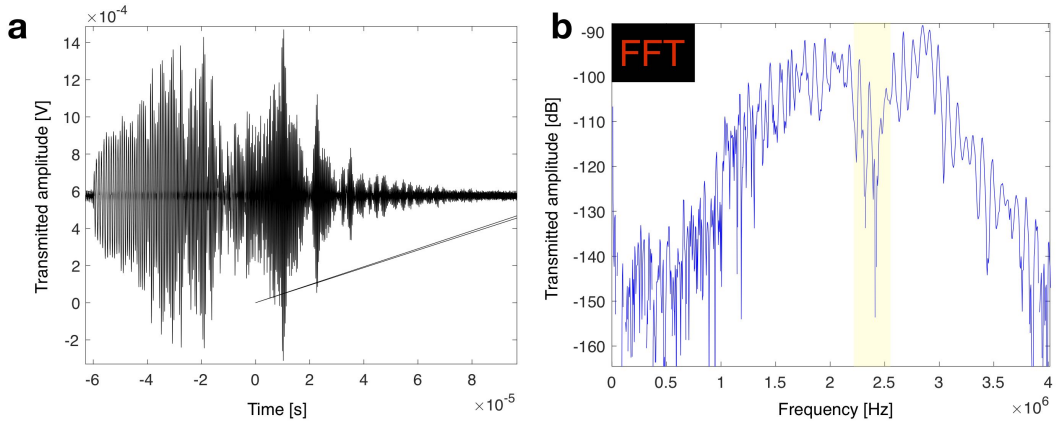

FIGURE 5.14 | FREQUENCY CHIRP THROUGH AUXETIC MICROLATTICES
(a) Signal from the receiving transducer and **(b)** FFT of the signal in (a), indicating the existence of a band gap at ~2.4 MHz. This transform was computed on an oscilloscope with no filtering, resulting more signal noise than the sweep conducted by the lock-in amplifier.

structure is achieved. Combining these capabilities with those of a reconfigurable material could lead to realizations with both tunable and permanent band gaps,

drastically expanding the achievable dynamic parameter space.

Chapter 6

DYNAMIC LOADING ON CARBON-BASED LATTICE ARCHITECTURES

This chapter has been adapted from:

C.M. Portela, A. Vyatskikh & J.R. Greer. "Fabrication and Design of Composites with Architected Layers". *U.S. Patent Application No. 16/206,163 and PCT International Patent Application No. PCT/US18/63306* (November 30, 2018)
Contributions: participated in the conception and design of the project, fabricated samples, performed mechanical tests and analyzed the data, and partially wrote the application;

C.M. Portela, B.W. Edwards, D. Veysset, Y. Sun, K. Nelson, D.M. Kochmann & J.R. Greer. "Supersonic Impact on Nano-architected Carbon Materials". *In Preparation* (2019)
Contributions: participated in the conception and design of the project, designed and fabricated samples, participated in the mechanical testing and analyzed the data, and wrote the manuscript;

and section 6.5 was done in collaboration with Christopher J. Cummins and Jeffrey T. Lloyd (ARL), who conducted the blast experiments.

6.1 Chapter Summary

This chapter provides further exploration into the dynamic realm of architected materials by studying the impact and blast responses of lattice architectures at the nanometer and centimeter scales, respectively. We outline fabrication methods that enable the creation of carbon-based architected materials for these studies at both scales, and perform quasi-static characterization prior to dynamic loading.

The first exploration pertains to supersonic impact of micro-particles onto nano-architected carbon materials, where we analyze cratering on carbon materials of different geometric parameters and at impact velocities ranging from ~40 m/s to ~900 m/s. Using dimensional analysis, we obtain a predictive tool that estimates cratering as a function of the initial impact conditions.

We conclude this chapter by studying the blast loading response of beam-based carbon and carbon-epoxy architected materials with sample sizes on the order of

a few centimeters and feature sizes on the order of ~100 μm, which are shown to provide significant energy dissipation while at densities of ~285 kg/m^3.

6.2 Fabrication Processes

The fabrication process of carbon-based materials at the nano- to micro- to macro-scale revolves around optimized pyrolysis processes, i.e., controlled high-temperature processing in inert atmospheres. Most commonly, the precursor material is a polymer whose organic components decompose during the pyrolysis process. Since this process involves significant mass reduction and volumetric shrinkage, special care needs to be taken such that minimal warping occurs. Depending on the precursor material and processing temperatures, the resulting pyrolyzed carbon material can increase in elastic modulus and strength by more than an order of magnitude, while also substantially decreasing in density. In this section, we present the methods to fabricate carbon-based materials at two different scales.

6.2.1 Nano-Scale Carbon Materials

We fabricated nano-architected carbon materials using a polymeric precursor material with nm-scale features. The precursor architecture was fabricated out of IP-Dip photoresist using a two-photon lithography (TPL) Photonic Professional GT (Nanoscribe GmbH) system. Due to the high temperatures associated with the pyrolysis process, the samples were printed on a Si substrate (as opposed to SiO_2) to prevent unwanted substrate warping or melting.

As mentioned above, the significant mass reduction and volumetric shrinkage of the precursor material presents fabrication challenges, since significant warping occurs if the material is not properly decoupled from the substrate. This issue arises from the lack of shrinkage in the Si substrate that effectively imposes an unwanted zero-displacement boundary condition to the precursor material in contact with it. To mitigate this, Bauer et al. [9] and Zhang et al. [152] printed the precursor material of interest on top of a monolithic pillar of the same material, such that the pillar undergoes warping at the point of contact with the substrate while little-to-no warping occurs at the top. This is a satisfactory solution since the effective substrate of the precursor material becomes the top of the pillar, which undergoes shrinkage at the same rate as the precursor material itself. Although it has proven to be an effective approach to study these materials, it is only viable for precursor samples with footprint dimensions of ~100×100 μm due to the extensive print times associated with the monolithic pillar.

Alternatively, we developed a method to print precursor materials with footprint areas greater than 300×300 µm with the use of an ultra-low-density elastic foundation to decouple the precursor material from the substrate. This elastic foundation consisted of an array of vertically aligned helical springs made of IP-Dip resist which were connected to the substrate at the bottom and the precursor material at the top. For a 300×300 µm footprint material, we utilized nine helical springs per 100×100 µm section, each with a beam radius $r = 2.6$ µm, helix radius $r_h = 5$ µm, pitch $\lambda = 7$ µm, and height $h = 28$ µm (Fig. 6.1). To anchor the precursor sample to the substrate, one spring in the central 100×100 µm section was replaced by a 10 µm-radius monolithic pillar.

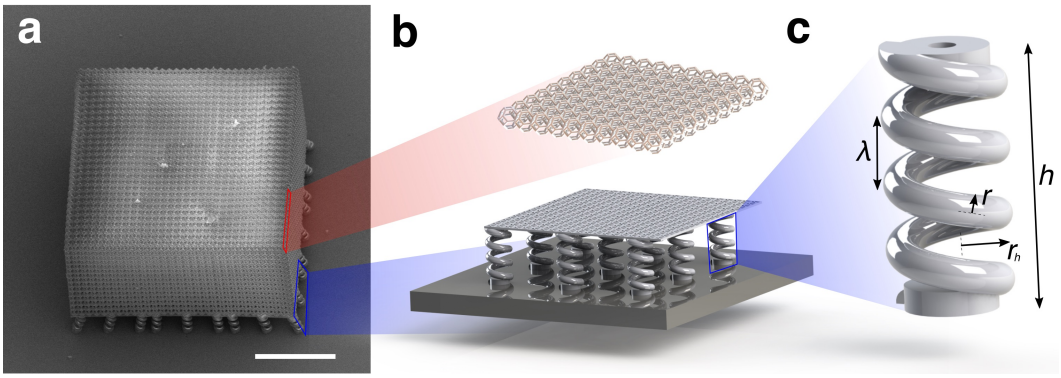

Figure 6.1 | Pre-Pyrolysis Sample Configuration
(a) Polymeric tetrakaidecahedron sample with overall dimensions of $\sim 300 \times 300 \times 150$ µm. **(b)** Diagram of spring elastic foundation, and **(c)** detailed view of a single helical spring with its characteristic dimensions. Scale bar, 100 µm.

We fabricated polymeric lattice materials of octet and tetrakaidecahedron geometries with unit cell sizes of 5 µm or 10 µm, resulting in $60 \times 60 \times n$ or $30 \times 30 \times n$ tessellations, respectively, where n was any z-tessellation of choice. Depending on the desired relative density for each material, the beam diameters were chosen to range from 800 nm to 2.3 µm. These cross-linked IP-Dip lattice materials were developed for 4 hours in propylene glycol monomethyl ether acetate (PGMEA), followed by a 10-minute rinse in isopropyl alcohol (IPA), and subsequent drying using a critical point dryer (Autosamdri 931, Tousimis). Upon drying, the samples were pyrolyzed in a vacuum furnace (OTF-1500, MTI) fitted with a 4-inch-diameter quartz tube. The process consisted of a hold at 900 °C for 5 hours, with constant heating and cooling rates of 10 °C min^{-1}. An initial pressure at room temperature of 50 mTorr or less was required to ensure minimal sample warping during the pyrolysis process. The final carbon materials underwent isotropic shrinkage of 80% in

each dimension, resulting in unit cell sizes of ~1 µm and ~2 µm, and beam diameters ranging from ~200 nm to 600 nm.

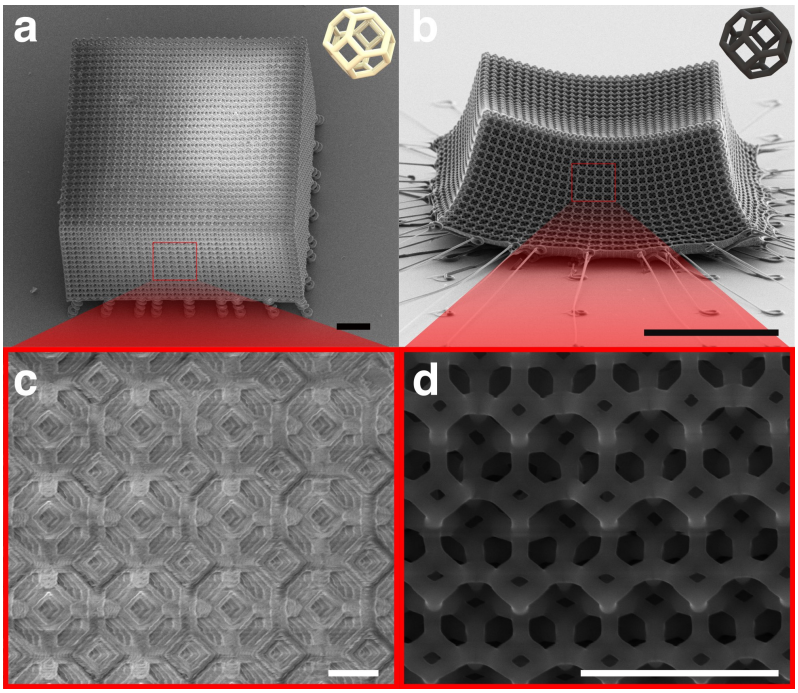

FIGURE 6.2 | CARBON-BASED NANOLATTICE MATERIAL OBTAINED VIA PYROLYSIS
(a) Sample polymeric tetrakaidekahedron material with 26% relative density and ~10 µm unit cells, and **(b)** resulting carbon tetrakaidekahedron material after pyrolysis with ~2 µm unit cells. **(c)**,**(d)** Magnified views of (a) and (b), respectively. Black scale bars 40 µm, white scale bars 5 µm.

6.2.2 Macro-Scale Carbon Materials

We fabricated the polymeric precursor materials out of PR-48 resin (Colorado Photopolymer Solutions) using an Ember DLP 3D printer (Autodesk). The resulting materials were rinsed with IPA after printing and then dried with compressed nitrogen. The overall sample dimensions ranged from a few cubic centimeters to the full 13 × 6 × 4 cm build volume of the printer. Besides fabricating typical lattice materials with unit cells of ~1 mm, and beam diameters ranging from 100 µm to 200 µm (Fig. 6.4), we fabricated shell-based architectures with wall thicknesses of ~300 µm to showcase the versatility of this method.

Compared to the pyrolysis process from section 6.2.1, these larger volumes of polymeric precursor material (with masses up to ~20 g) required a more controlled temperature profile to minimize warping during pyrolysis. This temperature profile was

optimized based on simultaneous thermogravimetric analysis (TGA) and differential thermal analysis (DTA) performed on a PR-48 block in an N_2 environment and a heating rate of 5 °C min^{-1} to 900 °C (Fig. 6.3). These results indicated the critical temperatures at which decomposition took place, which resulted in extended holds at those temperatures during the pyrolysis process. Analogous to the nanoscale sample process, pyrolysis was done in vacuum at pressures below 100 mTorr but to a peak temperature of 1300 °C inside a 4-inch-diameter mullite tube. The tailored holds at the critical temperatures, along with a total temperature cycle of ~24 h, significantly minimized warping of the resulting carbon materials and enabled isotropic shrinkage in each dimension of ~66% and a mass reduction of 95%.

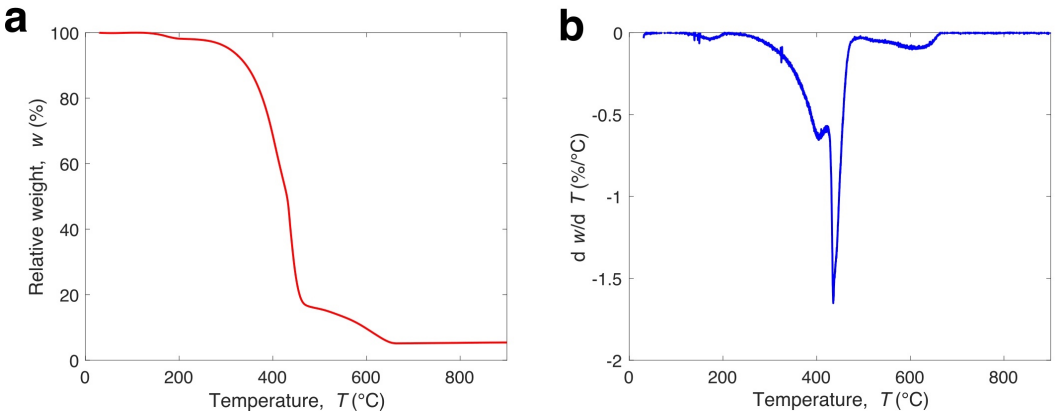

Figure 6.3 | TG/DT-Analysis on PR-48
Simultaneous thermogravimetric (TG) and differential thermal analysis (DTA) on a PR-48 sample, in a N_2 environment and a heating rate of 5 °C min^{-1} to a maximum temperature of 900 °C. **(a)** Relative weight evolution as a function of temperature, and **(b)** relative weight differential per degree Celsius as a function of temperature. Data courtesy of Kai Narita.

As mentioned previously, the versatility of this method was demonstrated by the fabrication of periodic beam- and shell-based carbon architected materials with densities ranging from 123 kg m^{-3} to 400 kg m^{-3} based on the chosen geometric parameters (Figs. 6.4 & 6.5). Additionally, the fabrication of architected carbon net-shape components was demonstrated by printing and pyrolyzing a tubular structure made up of tetrakaidecahedron unit cells (Fig. 6.6).

Carbon-Epoxy 3D Composites

As an alternative material system, we fabricated carbon-epoxy composites using the carbon materials from section 6.2.2 as continuous reinforcing phases, as described by the general process in Fig. 6.7. The architected carbon reinforcing phases in this

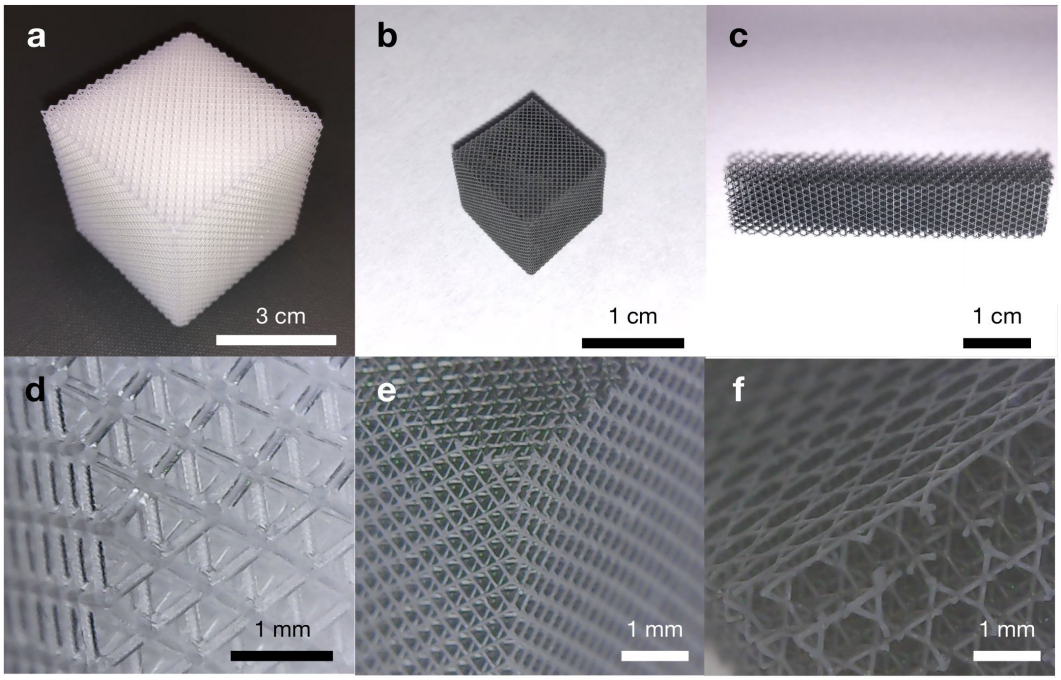

Figure 6.4 | Carbon-Based Lattice Materials Obtained via Pyrolysis
(a) Polymeric octet material with a relative density of 15% consisting of a 17 × 17 × 17 tessellation, and **(b)** resulting carbon octet material after pyrolysis, **(c)** 3D kagome beam, **(d)**–**(f)** close-up images of (a)–(c), respectively.

study were infiltrated with a low-viscosity epoxy (635 3:1 thin epoxy, US Composites) and cured at room temperature for 8 hours.

The bi-continuous columnar shell material depicted in Figs. 6.8a,d underwent a density transition from $\rho = 123.7$ kg/m^3 to 1152 kg/m^3, while the octet-cube in Figs. 6.8c,f transitioned from 255 kg/m^3 to 1160 kg/m^3. The resulting composite materials had an average density of at least two times lower than that of light metals (e.g., aluminum, $\rho_{Al} = 2700$ kg/m^3), and at least 40% lower than some carbon fiber reinforced polymers, which commonly have a density of 1600 – 1800 kg/m^3.

6.3 Baseline Quasi-static Characterization

Before dynamically testing the nano- and macro-scale materials described above, we characterized their quasi-static response at both scales using well-established methods.

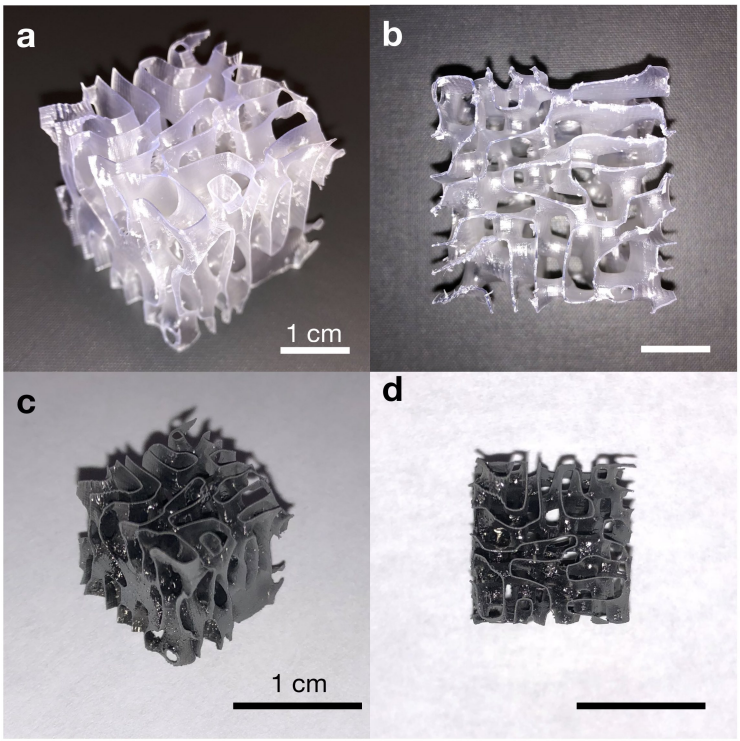

Figure 6.5 | Bi-Continuous Shell-Based Carbon Material
(a),**(b)** Polymeric shell-based geometry of the columnar type from chapter 4, and **(c)**,**(d)** resulting carbon material after pyrolysis.

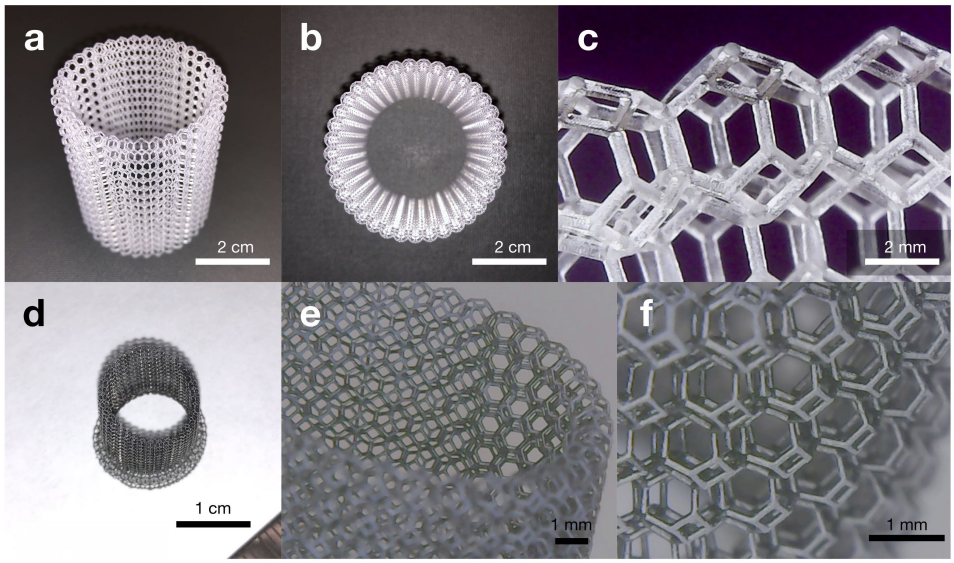

Figure 6.6 | Carbon Tubular Part with Tetrakaidecahedron Architecture
(a)–**(c)** Tubular part in its polymeric form, **(d)**–**(f)** resulting carbon tube.

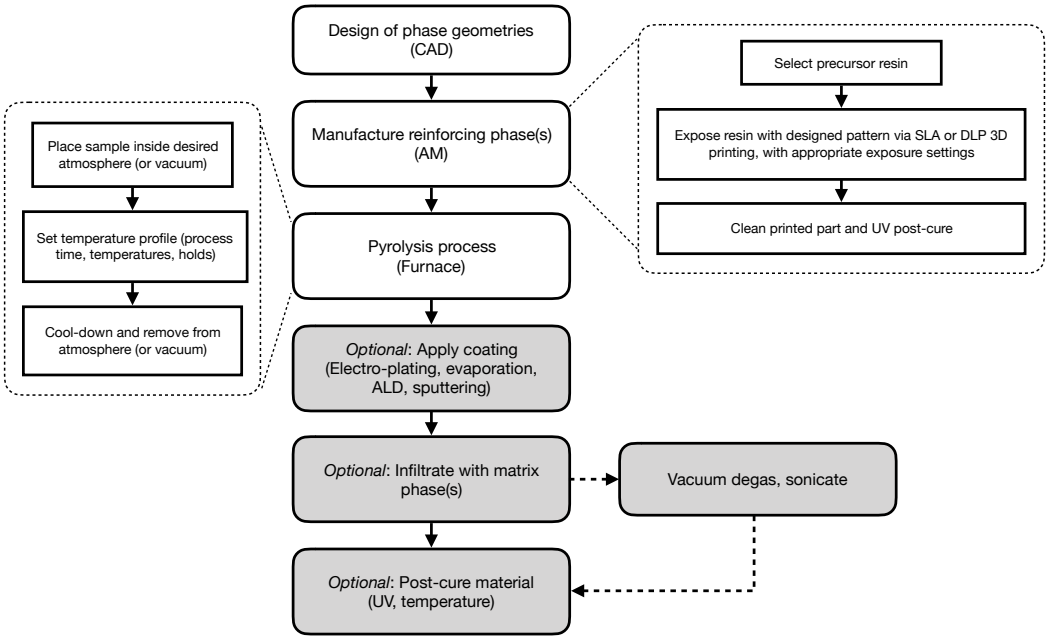

Figure 6.7 | Fabrication Process of Continuous-Phase 3D Carbon Composites
Flow chart depicting the fabrication process of continuous-phase 3D architected carbon composites. Optional processes are shown in grey.

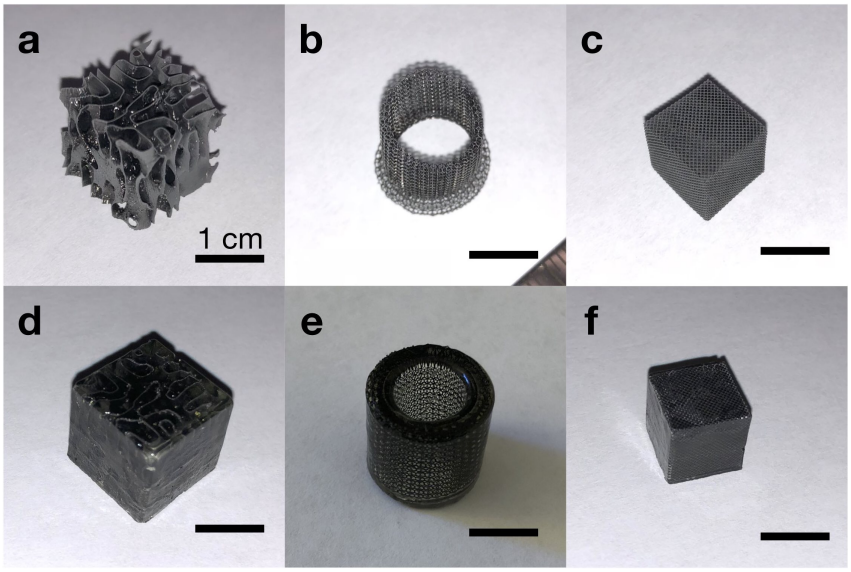

Figure 6.8 | Carbon-Epoxy Composites
(a)–**(c)** Carbon phases prior to infiltration, and **(d)**–**(f)** resulting composite materials.

6.3.1 Nanomechanical Testing

To obtain the static mechanical properties of the nano-architected carbon materials, we fabricated representative $10 \times 10 \times 10$ tessellations of the tetrakaidecahedron architecture with relative densities of $\overline{\rho} = 8\%$ and 17%, and performed *in situ* nanomechanical compression experiments[1]. Following the pyrolysis step, the samples were supported by a sacrificial central pillar, which was designed to fail upon the initial loading regime to allow proper contact between the substrate and the sample (Fig. 6.9). A minimum of seven samples per configuration were compressed in a custom nanomechanical instrument inside of an SEM chamber (Quanta 200 FEG, Thermo Fisher), which provided load-displacement data along with real-time observation of the experiment at quasi-static strain rates of $\dot{\varepsilon} = 10^{-3}$ s^{-1}. The load-displacement data was converted to stresses and strains by normalizing by the sample footprint area and height, respectively. Since pillar failure did not occur at the same point for all samples, zero-strain was defined to be the start of the test for consistency.

All samples exhibited a linear loading regime once proper contact was established, with some sporadic settling events, as well as brittle, catastrophic failure. The settling events and brittle failure are both depicted as sudden strain bursts (i.e., horizontal lines with few data points) in the stress-strain response presented in Fig. 6.9. This response was used to compute the effective Young's moduli and strength of the two material configurations, which were defined as the slope of the response after pillar collapse and the maximum stress prior to catastrophic failure, respectively. Effective Young's moduli of 0.43 ± 0.09 GPa and 1.1 ± 0.1 GPa were obtained for the 8% and 17% relative density configurations, respectively, which are consistent with the values reported by Bauer et al. [9] and Zhang et al. [152] when accounting for the difference in architecture and relative density compared to the samples in those works. We also calculated effective strength values of 25 ± 4 MPa and 79 ± 13 MPa for the 8% and 17% relative density configurations, respectively, which were expectedly lower than those reported for octet carbon nanolattices [9, 152].

6.3.2 Macro-scale Testing

Uniaxial Compression of Octet Phases and Composites

We performed quasi-static uniaxial compression on octet carbon reinforcing phases ($\overline{\rho} \approx 15\%$) with and without epoxy infiltration at a strain rate of $\dot{\varepsilon} = 10^{-3}$ s^{-1} using

[1] We tested these configurations specifically since they represent the types of materials that were tested dynamically later in this chapter.

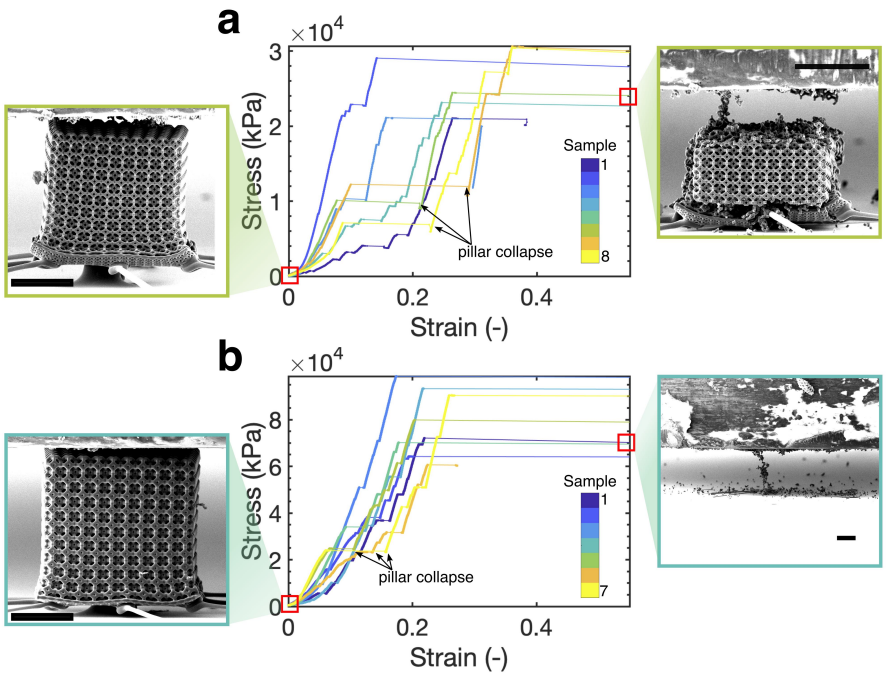

FIGURE 6.9 | QUASI-STATIC COMPRESSION OF CARBON NANOLATTICES
Uniaxial *in situ* compression of **(a)** ~8% relative density samples, and **(b)** ~17% relative density samples, with insets showing a representative sample before and after compression. In both cases catastrophic, brittle failure was observed. All samples were fabricated on a sacrificial pillar which collapsed at low loads to enable proper sample contact with the substrate. Zero-strain was defined as the beginning of the experiment for consistency. Scale bars, 10 μm.

an Instron load frame. Since the underlying tessellation consisted of $17 \times 17 \times 17$ unit cells (with a characteristic unit cell size of $\sim$ 590 μm), we assume sufficient separation of scales to discuss effective *material* (rather than structural) properties.

The experiments depicted in Fig. 6.10 were used to obtain an effective modulus and yield strength for this octet carbon material with approximately 15% relative density. Young's moduli of 669.7 and 495 MPa were calculated, while the yield strengths—defined as the stress at the initial catastrophic fracture event—were calculated to be 11.33 and 8.67 MPa. These carbon phases, without a matrix phase, were susceptible to defects such as minimal warping at the top surface which affected contact with the compression head.

Upon infiltration with epoxy, the mechanical behavior of these materials changed significantly. Most notably, the material did not undergo any catastrophic events and underwent significant strain hardening past $\varepsilon > 0.1$. Fig. 6.11 shows the response

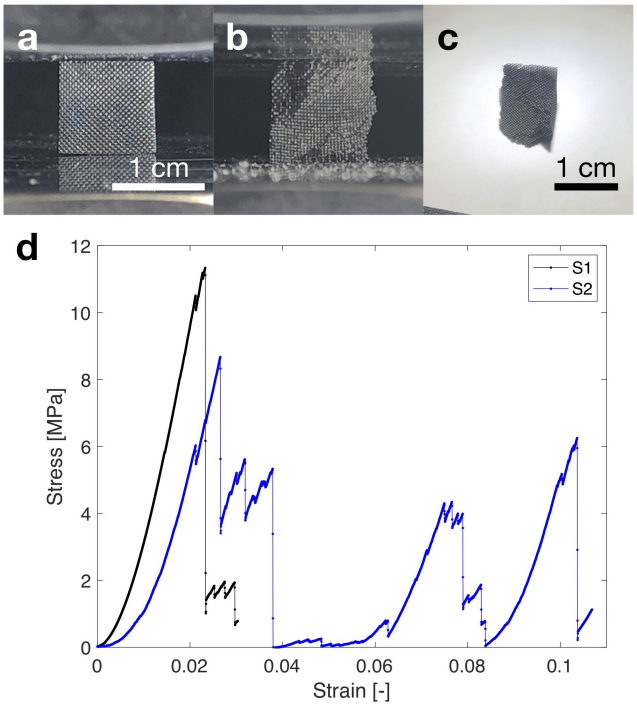

FIGURE 6.10 | QUASI-STATIC COMPRESSION OF CARBON MACRO-LATTICES
(a) Carbon octet material prior to loading, and **(b)**,**(c)** representative samples after catastrophic failure, **(d)** stress-strain response of two representative samples, depicting discrete failure events.

of the material under compression, with significant densification after $\varepsilon = 0.5$ but no catastrophic failure or through-sample cracks.

These experiments resulted in Young's moduli of 1.82 and 2.24 GPa, and yield strengths of 59.8 and 69.6 MPa. At these strength values, this material has a strength comparable to some metals (e.g., copper), while at 13% of their density. We define the yield strength σ_y for these materials using the 0.2% strain offset method, and we also define a flow stress σ_f corresponding to the maximum stress before a negative tangent modulus was observed (i.e., before a decrease in stress). The flow stress for these samples were calculated to be 71.9 and 78.2 MPa. These values and comparisons to some metals are summarized in Table 6.1.

Although the fill fraction of the carbon phase was low in these materials, infiltration proved to be a potential route to mitigate catastrophic failure while still enabling a material with relatively low density to be produced. The non-catastrophic and strain-hardening response for these composites makes them well suited for energy absorption applications. For instance, in these quasi-static experiments the specific

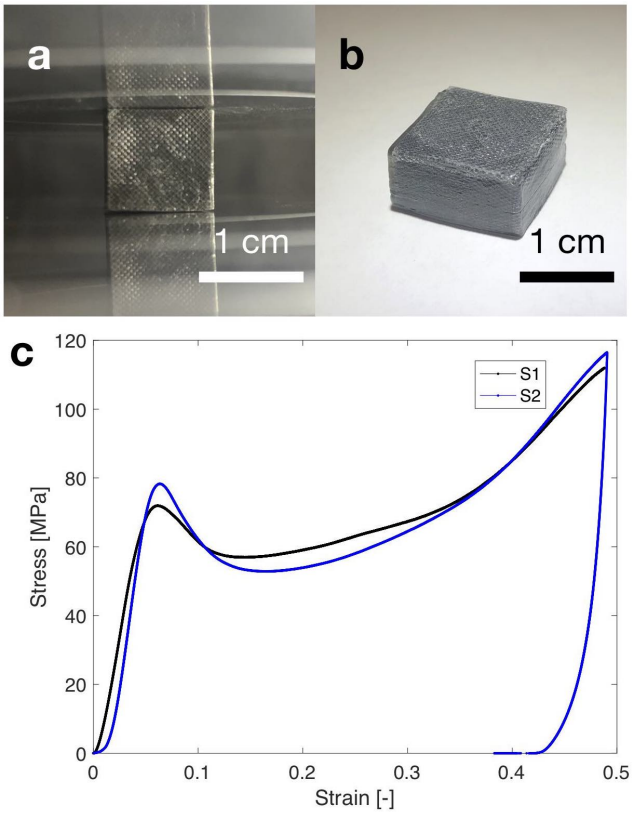

Figure 6.11 | Quasi-Static Compression of Carbon-Epoxy Composite
(a) Sample prior to loading, and **(b)** final sample configuration after compression to $\varepsilon = 50\%$. **(c)**, Stress-strain response of two representative samples exhibiting significant strain hardening beyond $\varepsilon = 10\%$.

energy absorption (SEA) can be defined as

$$\psi = \frac{W}{\rho},$$

where W is the strain energy density, defined as $W = \int \sigma \mathrm{d}\varepsilon$, and ρ is the material density. Calculating this metric for the experiments in Fig. 6.11c yielded $W = 30.9$ MJ/m^3 and $\psi = 26.7$ J/g, at a density of $\rho = 1159$ kg/m^3. Comparing these metrics to those of stainless steel 316L octets [127], whose reported values were $\psi = 10.1$ J/g and $\rho = 2160$ kg/m^3, shows that the carbon octet composites have twice the SEA capacity while at half the density.

Four-point Bending of Octet Phases and Composites

We also explored the bending behavior of the same octet carbon materials using a 4-point bending setup following ASTM standard D6272.

Material	Density, ρ [kg/m^3]	E	σ_y [MPa]	σ_f [MPa]
Carbon octets 1	291	669.7 MPa	11.33	-
Carbon octets 2	273	495 MPa	8.67	-
Composite octets 1	1157	1.82 GPa	59.8	71.9
Composite octets 2	1159	2.24 GPa	69.6	78.2
Aluminum	2700	69 GPa	95	-
Copper	8960	117 GPa	70	-

Table 6.1 | Mechanical parameters of tested carbon octet materials including comparison to some metals, where E corresponds to the Young's modulus, and σ_y and σ_f represent the yield strength and flow stress, respectively.

Bending of the carbon phase without a matrix showed catastrophic failure, as observed in the compression experiments. Fig. 6.12 shows the experiment and corresponding data, which yielded an approximate flexural strength of 10.34 MPa, and a bending modulus of $E_B = 1.4$ GPa.

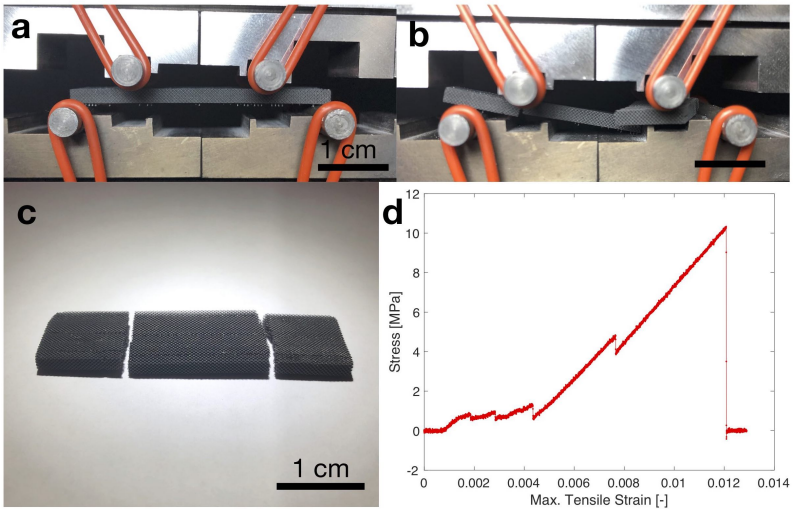

Figure 6.12 | **Four-Point Bending of Carbon Phase**
(a) Sample prior to bending, and **(b)**,**(c)** failed sample morphology. **(d)** Corresponding stress-strain response.

The same experiment was performed on epoxy-infiltrated materials (Fig. 6.13), which resulted in bending moduli of 3.3 and 3.9 GPa. A flexural strength value was not calculated since no failure was observed within the allowable strain limit of this ASTM standard. After undergoing significant bending, the samples returned to their original shape with no evident permanent deformation or cracks.

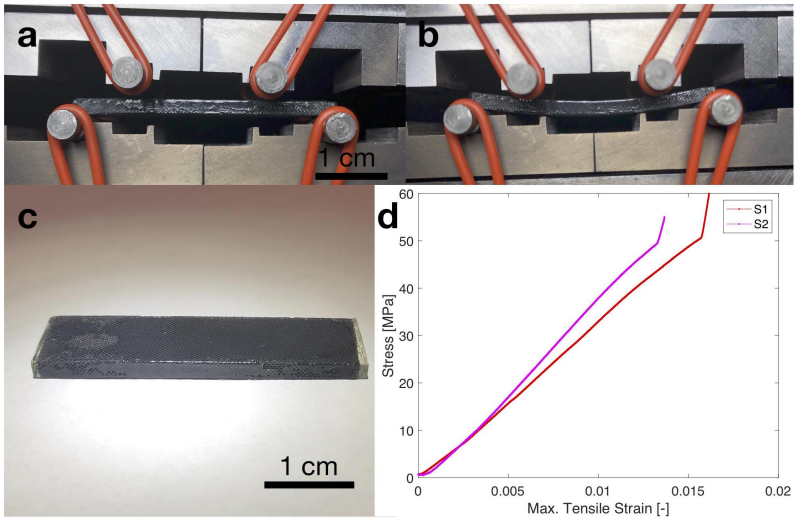

Figure 6.13 | Four-Point Bending of Composite Material
(a) Sample prior to bending, and **(b)** sample at the maximum allowable bending, and **(c)** sample after experiment. **(d)** Corresponding stress-strain response with no indication of failure. The drastic stiffening beyond strains of 1% corresponded to the sample contacting the bottom support.

6.4 Supersonic Impact on Nano-scale Carbon Lattice Architectures

As presented in previous chapters, the use of architecture in materials has been reported to enable novel combinations of static mechanical properties such as high stiffness- and strength-to-density ratios [15, 93, 153]. In the dynamic regime, beam-based architected materials with features on the order of hundreds of micrometers have been reported to exhibit high energy absorption under low-velocity impact [12, 95, 149], which was highly dependent on the type of architecture used. On the other hand, ballistic impact experiments to velocities of ~1,300 m/s on larger metallic truss-core sandwich materials showed a transition ballistic velocity beyond which architecture did not significantly affect the material response, hinting to different physical phenomena in these two regimes. Evidence of this regime transition was also shown at smaller scales in compaction experiments of polymeric micro-lattices [52, 73], which ranged in velocity from 0.15 m/s to ~300 m/s.

While most of the underlying physics that describe this unique response are scale-independent, i.e., applying to materials with centimeter- to micrometer-scale feature sizes, interesting size effects appear when nanometer-scale features are achieved. Two examples of these size effects have been reported in truss-based materials with hollow thin-walled ceramic struts [92] and monolithic carbon struts [9, 152],

whose feature sizes span from tens of nm to approximately 600 nm. Each of these studies independently observed enhanced structural recovery and almost-theoretical strength, each directly attributable to the nano-scale feature dimensions. While this size effect has been thoroughly explored in the quasi-static response of architected materials, no work has explored its implications in the dynamic response of these materials. Exploiting these size effects in the dynamic regime has potential to enable ultralightweight impact-resistant materials for a variety of applications such as ballistic impact, blast loading, and micrometeoroid shielding in space.

One of the challenges associated with mechanical testing of nano-architected materials is that these materials rarely achieve a proper separation of scales between the unit cell size and a relevant sample dimension [9, 52, 94, 152]. Several nano-architected materials have been limited to tessellations of just a few (i.e., < 7) unit cells in each direction, which can fall short in approximating the true continuum material response. For example, this lack of separation of scales can become detrimental in impact testing when the time scale associated with impact allows elastic waves to propagate information from the free boundaries back to the projectile. Another difficulty in dynamic testing of nano-architected materials is associated with the lack of reliable methods that achieve consistent loading conditions while being able to capture nanosecond- and (at least) micrometer-scale response of the samples.

Here, we propose a method to design, fabricate, and test nano-architected carbon materials at supersonic impact speeds of up to ~1 km/s, while properly addressing the challenges described above. Using tetrakaidecahedron architectures as the periodic building-blocks, we fabricated these materials by the two-photon polymerization and pyrolysis process described in section 6.2.1, which ultimately yielded a carbon-based nano-architected material as shown in Fig. 6.14. The resulting carbon unit cell size was ~2 μm, with beam diameters ranging from ~300 nm to 500 nm, achieving relative densities (i.e., fill fractions) of $\overline{\rho} \approx 8\%$ and 17%. To achieve proper separation of scales, the material tessellation consisted of a minimum of $30 \times 30 \times 15$ unit cells and the SiO_2 projectile diameter was approximately an order of magnitude larger that the unit cell size. In this work, we explore the effects of relative density on the impact response of nano-architected carbon materials at impact velocities ranging from 40 m/s to 900 m/s and provide an analytical predictive tool for material cratering based on dimensional analysis.

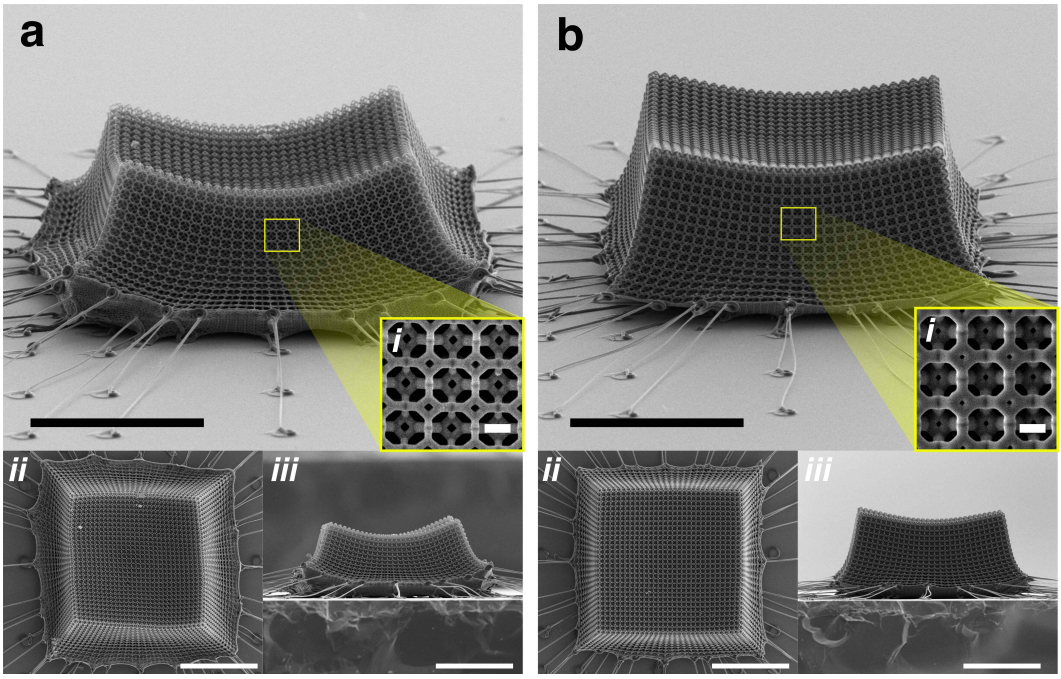

FIGURE 6.14 | NANO-ARCHITECTED CARBON SAMPLES FOR SUPERSONIC IMPACT
Representative carbon samples for dynamic testing of **(a)** $\overline{\rho} \approx 8\%$, and **(b)** $\overline{\rho} \approx 17\%$. Sub-figures labeled as (*i*), (*ii*), and (*iii*) correspond to a magnified unit cell view, a top view, and a side view, respectively. All scale bars are 40 μm except those in (*i*) sub-figures which are 1 μm.

6.4.1 Laser Induced Particle Impact Test

The impact experiments were conducted using the laser induced particle impact test (LIPIT) method in which 14 μm-diameter SiO_2 spheres were accelerated by a pulsed laser to velocities of up to 1.2 km/s [78, 135]. To accelerate the impactors (i.e., the spheres), the laser was focused on a glass launching pad containing thin layers of Au and polydimethylsiloxane (PDMS) which caused ablation of the gold film and rapid expansion of the elastomer film. The projectiles located at the focus sites attained their kinetic energy from the expansion of the elastomer with tunable speeds depending on the power of the laser pulse. The impact event was captured using 16 frames from a high-frame-rate camera (SIMX 16, Specialised Imaging) which was connected to a microscope objective, allowing for exposure times as short as 3 ns and ~300 nm-pixel resolution. To decouple any nonlinear processes associated with the impactor, we preformed a series of impact experiment of the SiO_2 particles onto a thick Si substrate prior to impacting carbon nanolattices. All projectiles were aimed to impact the samples as close to the center as possible to minimize the effect of boundaries. By varying impact velocity over 1.5 decades

(40–1,100 m/s), we probed different impact regimes while maintaining the impactor geometry, material, and size constant. Following the impact experiments, we performed post-mortem analysis on the samples via confocal and scanning electron microscopy (SEM), which allowed for qualitative and quantitative characterization of the impact cratering process on the carbon materials.

6.4.2 Particle-Substrate Impact

The impact response of the SiO_2 spheres onto Si was characterized by distinct rebound and shattering regimes. Representative frames from a rebound-regime impact are shown in Fig. 6.15a, corresponding to impact and rebound velocities of $v_0 = 514$ m/s and $v_r = 339$ m/s, respectively. This regime extended to impact velocities of ~650 m/s, around which the shattering regime emerged. A representative impact in this regime is presented in Fig. 6.15b, corresponding to an impact velocity of 646 m/s. The last frames in this sequence show catastrophic failure of the particle which disintegrated into several pieces as the one shown in Fig. 6.15d.

Using the velocities obtained from the camera frames, and assuming a density $\delta = 2650\ \mathrm{kg\,m^{-3}}$ for SiO_2, a radius $r = 14\mu$m, and a mass $m = \frac{4}{3}\delta\pi r^3$ for all particles, the impact energy $W_0 = \frac{1}{2}mv_0^2$ and rebound energy $W_r = \frac{1}{2}mv_r^2$ for each impact was calculated. Additionally, the dissipated or inelastic energy was computed as the difference between the impact and rebound energies, $W_i = W_0 - W_r$. Normalizing the rebound and inelastic energies by the impact energy and plotting those values as a function of the impact energy in Fig. 6.16a shows a non-linear increase in dissipation with increasing impact energy, which reaches a maximum value prior to reaching the particle shatter regime.

To understand this anomalous behavior of the SiO_2 particles upon high-velocity impact, we refer to the continuum plasticity model proposed by Schill et al. [119]. By applying this model, we assume that inelastic energy is primarily accounted for by densification (i.e., consolidation) of the SiO_2 spheres due to the high pressures associated with supersonic impact, and thereby neglect contributions of heat loss or damage in the Si substrate (no damage was visible in post-mortem SEM micrographs). The consolidation energy density in SiO_2 as a function of J_p can be obtained by integrating the consolidation relation presented in this model

$$p_c = p_0 + \frac{A}{\alpha}\left(1 - J_p^{-\alpha}\right), \tag{6.1}$$

where p_c is the consolidation pressure (i.e., maximum pressure attained), J_p is the permanent volumetric deformation factor (i.e., the resulting fraction of the orig-

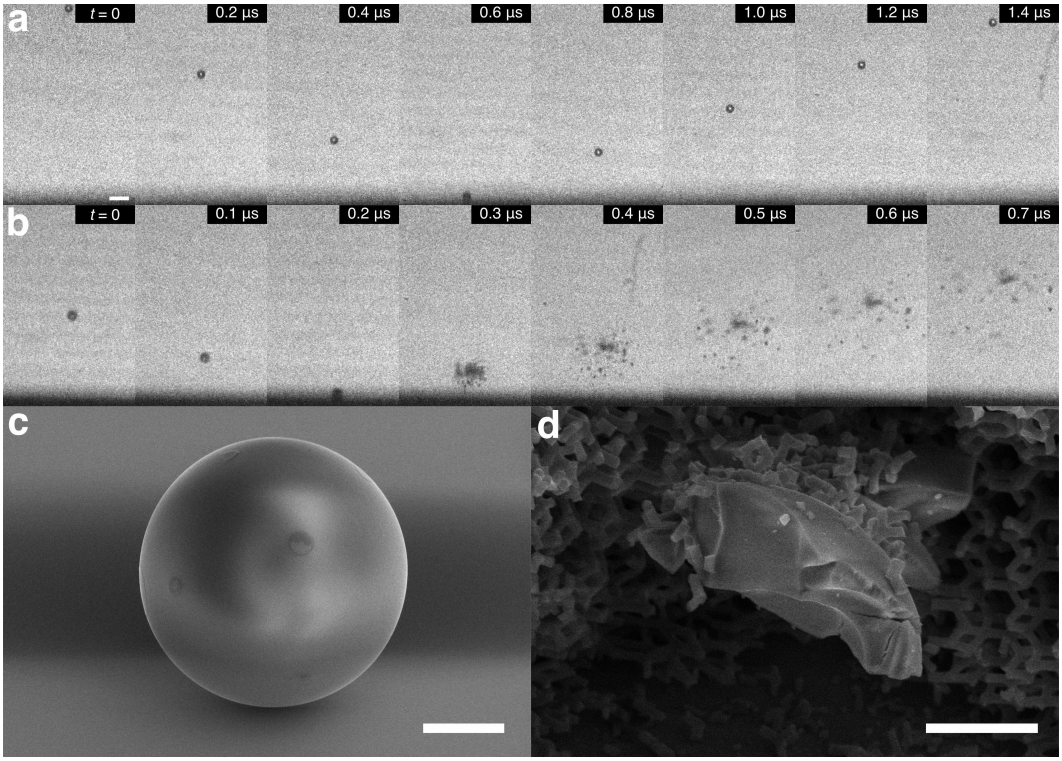

FIGURE 6.15 | SiO_2-Si IMPACT EXPERIMENTS
Impact of 14 µm-diameter SiO_2 onto a Si substrate. **(a)** Impact and rebound speeds of 514 m/s and 339 m/s, respectively, and **(b)** impact speed of 646 m/s causing particle shatter. **(c)** Micrograph of initial SiO_2 particle, and **(d)** fragment of a shattered particle. Scale bar in (a),(b), 30 µm, (c),(d), 4 µm.

inal volume after impact), and A, p_0, and α are fit parameters provided by the model [119]. Taking this energy density and multiplying it by the particle volume provides an inelastic energy estimate assuming an on-average particle consolidation J_p, which is plotted in Fig. 6.16b. Matching the maximum inelastic energy observed experimentally to the energies predicted by the model, corresponding to an impact velocity of $v_0 = 656$ m/s, indicates that an on-average volume reduction of up to ~10% (for $J_p \approx 0.9$) occurred for particles that did not shatter. Impact velocities beyond the shatter limit are assumed to have caused an on-average consolidation pressure higher than ~4.6 GPa, as shown in Fig. 6.16c, which could lead to unstable behavior at a defect to initiate fracture. This model validates our approximation that internal processes of the SiO_2 particles can account for the dissipated energy in these SiO_2-Si impacts.

Since the energy loss associated with inelastic processes in SiO_2 is not negligible,

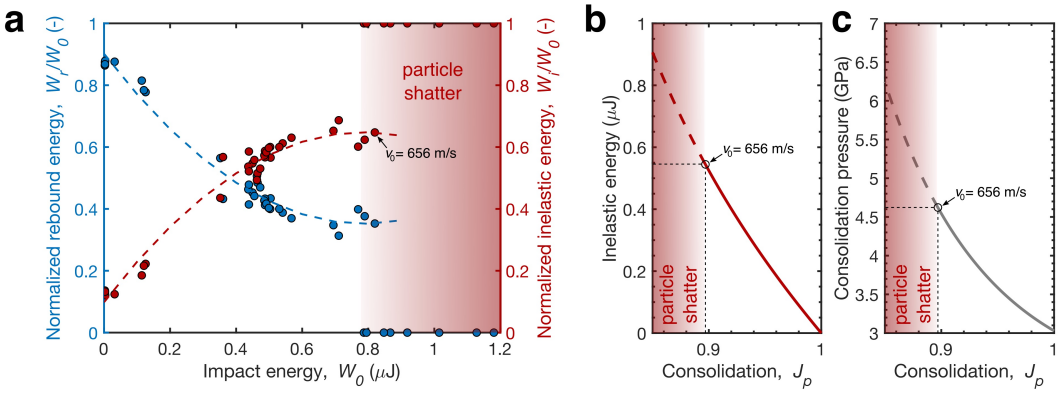

Figure 6.16 | SiO_2-Si Impact Energetics
(a) Normalized rebound and inelastic energies, W_r/W_0 and W_i/W_0, respectively, as a function of impact energy showing a non-linear dissipation response and an abrupt transition to the particle shatter regime. **(b)** Estimation of average consolidation J_p of the particles that result in comparable inelastic energies to those measured experimentally, applying the model provided by Schill et al. [119], and **(c)** corresponding estimated consolidation pressures. The velocity of the experimental point with the maximum absolute inelastic energy is labeled in all plots.

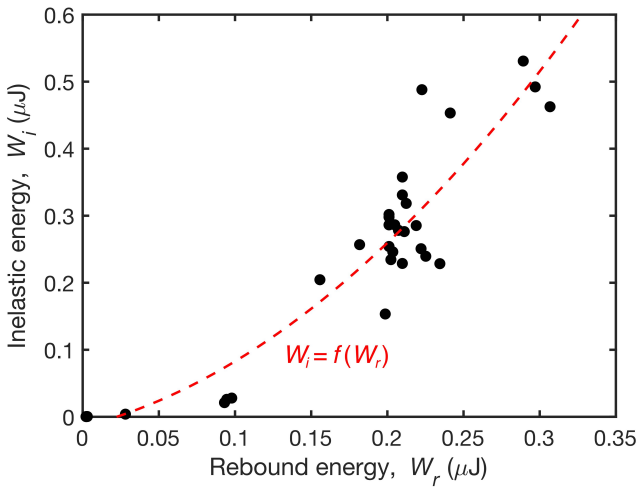

Figure 6.17 | Inelastic Energy as a Function of Rebound Energy
Impact onto a tetrakaidekahedron carbon material with 17% relative density with **(a)** impact speed of 676 m/s and particle embedding, and **(b)** impact and rebound speeds of 238 m/s and 50 m/s, respectively. **(c)** 17% relative density sample after elastic impact and no permanent deformation at 50 m/s, **(d)** post-impact micrograph of sample from (a), and **(e)** post-impact micrograph of sample from (b) showing cratering. White scale bars 20 µm, black scale bars 5 µm.

we fit the experimental data to a second-order polynomial of the form[2] $W_{i,SiO_2} = f(W_r)$ to provide a function that related the rebound and inelastic energies, as shown in Fig. 6.17. The motivation behind this fit was to provide an expression to estimate the dissipation energy of the SiO_2 particles when the impact energy at rebound was unknown, such as the case when the particles penetrate a foreign object and rebound after substantial penetration (assuming the pressures experienced at rebound are the only source of densification). This function was later used to decouple the inelastic contributions from the impactors and the target material.

6.4.3 Nanolattice Impact Response

Impact of the SiO_2 particles onto tetrakaidekahedron architectures exhibited three distinct response regimes: (*i*) elastic impact, (*ii*) cratering and particle rebound, and (*iii*) cratering and particle capture, depending on the relative density of the carbon material as well as the impact energy. In the elastic impact regime, no permanent deformation occurred and the impactor rebounded with a high coefficient of restitution $\alpha = |v_r|/|v_0|$, defined as the ratio of the rebound and impact velocities. The cratering and particle rejection regime consisted of permanent deformation in the form of a localized crater and a non-zero α, as shown in Fig. 6.18a,d. Lastly, the cratering and particle capture regime was characterized by permanent deformation in the form of a crater, with $\alpha = 0$ due to the particle remaining embedded inside the material, as depicted in Fig. 6.18b,e. Permanent deformation consisted mostly of craters with diameters of ~15 μm and varying depths, without any visible cracks or damage emanating from them.

Impacts on the $\overline{\rho} \approx 8\%$ samples exhibited cratering and rebound for all probed impact velocities above 50 m/s, with full sample penetration beyond velocities around ~490 m/s. Post-mortem analysis via confocal microscopy and electron microscopy confirmed full penetration in some samples and enabled the calculation of crater volumes. Using the velocities from the high-speed frames we computed the impact and rebound energies for each experiment, and calculated the inelastic energy corresponding to lattice cratering as

$$W_{i,lat} = W_0 - W_r - W_{i,SiO_2}(W_r), \tag{6.2}$$

where $W_{i,SiO_2}(W_r)$ is the fit function for SiO_2-Si impacts presented in Fig. 6.17. For simplicity, W_i will correspond to the inelastic energy due to the lattices (including

[2]With fit parameters $a = 3.95 \times 10^6$, $b = 0.582$, and $c = -1.5 \times 10^{-8}$, corresponding to the second-, first-, and zeroth-order coefficients, respectively.

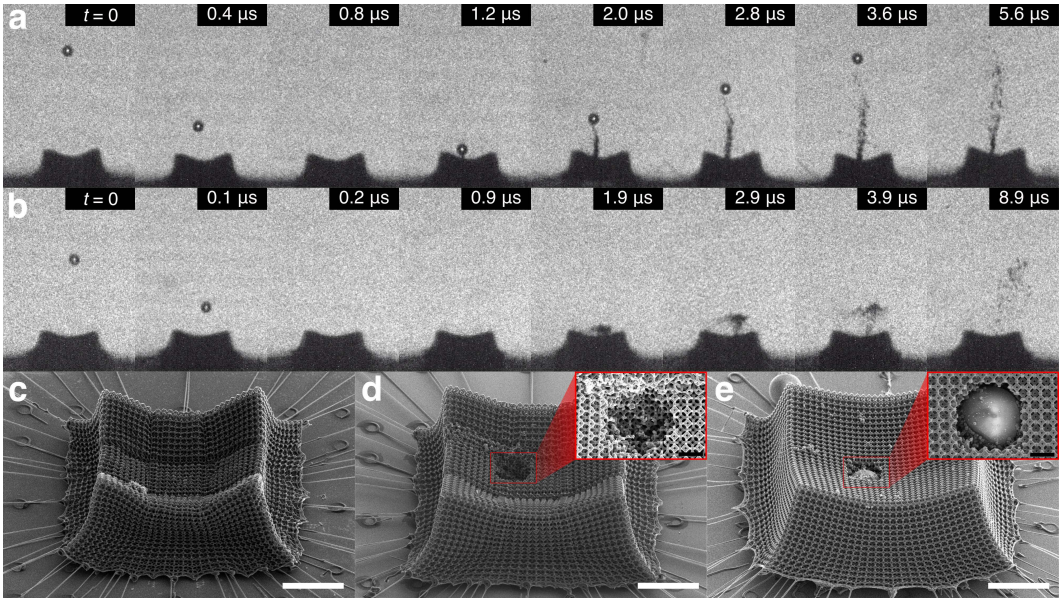

FIGURE 6.18 | IMPACT RESPONSE REGIMES
Impact onto a tetrakaidekahedron carbon material with ~17% relative density with **(a)** impact and rebound speeds of 238 m/s and 50 m/s, respectively, and **(b)** impact speed of 676 m/s and particle embedding. **(c)** ~17% relative density sample after elastic impact and no permanent deformation at 50 m/s, **(d)** post-impact micrograph of sample from (a) showing cratering, and **(e)** post-impact micrograph of sample from (b) showing embedded particle. White scale bars 20 µm, black scale bars 5 µm.

the correction for W_{i,SiO_2}) in the remainder of this work. Plotting the energetics of these impacts (Fig. 6.19a) shows an increase in rebound velocities in the full penetration regime, indicative of rebound taking place from the Si substrate. The slope of 0.69 corresponding for the inelastic energies indicates an on-average ability of this material to dissipate ~69% of the impact energy in the probed regime.

The $\overline{\rho} \approx 17\%$ samples exhibited both cratering and rebound as well as particle embedding for all impact velocities beyond the elastic regime, while no full-sample penetration was observed. Partial cratering was observed at velocities below ~515 m/s before transitioning to an embedding-dominated regime that extended to velocities of up to ~820 m/s (Fig. 6.19b). Performing a linear fit on the inelastic energy approximations for these samples yielded a slope of 1.00, indicating an on-average close-to-perfect energy dissipation response of these materials in the probed regime.

The distinct response regimes for the $\overline{\rho} \approx 8\%$ and $\overline{\rho} \approx 17\%$ came with similar crater morphologies, as shown in Fig. 6.20. Craters at both relative densities generally had a cylindrical shape, with a diameter of approximately 15 µm, and depths depending

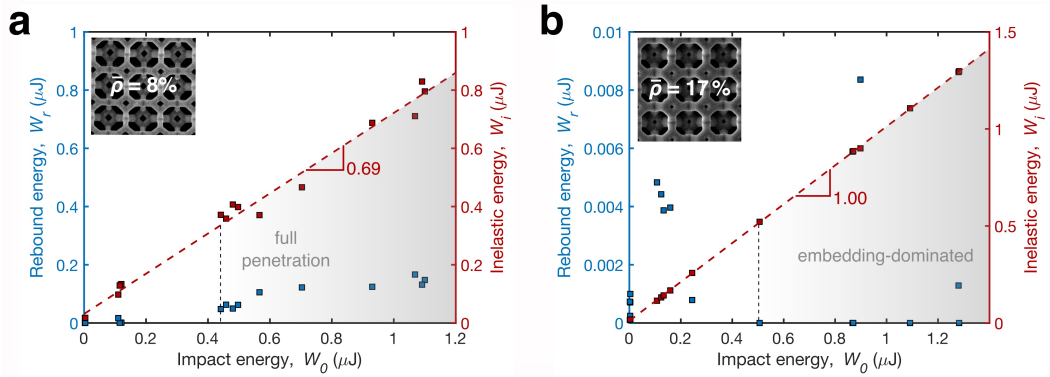

FIGURE 6.19 | SiO_2-NANOLATTICE IMPACT ENERGETICS
Energetic distribution of impacts onto samples with **(a)** 8%, and **(b)** 17% relative density. Rebound and full penetration regimes were observed for the $\overline{\rho}$ = 8% samples, while the $\overline{\rho}$ = 17% samples exhibited a particle embedding regime in addition to the rebound regime (no full penetration observed). Performing a linear fit of W_i as a function of W_0 (red dotted lines) yielded an on-average 69% and 100% effectiveness at dissipating impact energy for the 8% and 17% samples, respectively.

on the impact velocity. No significant spalling or fracture was observed beyond the cylindrical craters for any of the probed velocities, allowing the materials to retain overall structural integrity. The $\overline{\rho} \approx 8\%$ samples exhibited larger crater volumes and generally lower ejecta velocities (i.e., velocities of debris ejected from the crater) than the $\overline{\rho} \approx 17\%$ samples at the same velocity, resulting in more debris remaining in the craters after the impact process. Close-up view of the crater base on the $\overline{\rho} \approx 17\%$ sample impacted at 255 m/s shows characteristic indications of brittle failure in the carbon struts.

6.4.4 Dimensional Analysis of Impact Processes: from planetary impact to nano-impact

Several works in planetary sciences have extensively used dimensional analysis to formulate approximate prediction tools for planetary impact processes [54]. In this field, accurate measurement or even observation of impact processes is almost impossible, limiting researchers to post-mortem analysis of craters. Additionally, experiments performed on earth can fail to replicate conditions such as low gravity, km-diameter impactors, or hyper-velocities, leaving dimensional analysis as the preferred tool to bridge the gap between *dimensionally similar* experiments and planetary impacts.

Although the impact processes presented in this chapter do not face the challenges

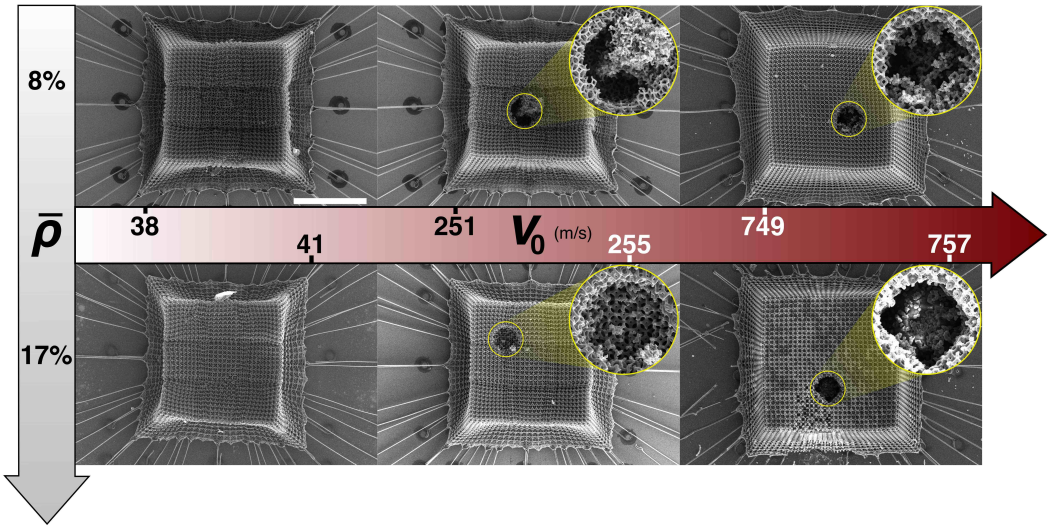

Figure 6.20 | Effect of Relative Density and Impact Velocity on Cratering
Crater evolution as a function of relative density $\bar{\rho}$ and impact velocity v_0. Full penetration of the $\bar{\rho} = 8\%$ sample was observed for the impact at 749 m/s, and deep particle embedding was observed in the $\bar{\rho} = 17\%$ sample at 757 m/s. White scale bar 40 μm, inset diameters 18 μm.

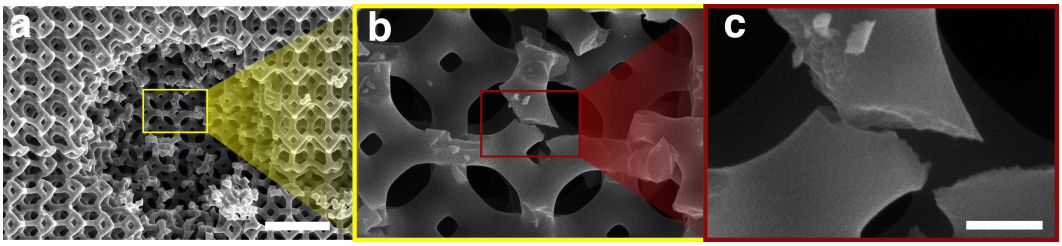

Figure 6.21 | Close-Up of Crater Base
Micrographs of the crater base for a $\bar{\rho} \approx 17\%$ sample impacted at 255 m/s showing brittle failure in its nanometer-diameter beams. Scale bar in (a), 5 μm, and in (c), 300 nm.

described above, the nanometer and nanosecond spatial and temporal scales associated with these experiments prevent full characterization of values of interest such as the time-dependent stress and strain fields, limiting us to just two velocities and the resulting crater volume. Since this constitutes the first time a micro- or nano-architected 3D material is tested at such high impact velocities, and no guiding principles exist to interpret this response, in this section we utilize principles of dimensional analysis in planetary impact to relate the cratering response to the strength of the material, the impact energy, and the ratio of densities between the impactor and the material.

Impact Scaling Relations

Analogous to a standard planetary impact, the objective is to relate the volume of the crater V to the parameters relating to the impactor (radius r, velocity v_0, and density δ) and those relating to the underlying material (strength σ_y and density ρ) at some gravitational acceleration g in some form

$$V = f\big[\underbrace{\{r, v_0, \delta\}}_{\text{particle}}, \underbrace{\{\rho, \sigma_y\}}_{\text{target material}}, g\big]. \tag{6.3}$$

Applying the Buckingham-Π theorem to these variables, plus accounting for porosity (i.e., relative density $\overline{\rho}$) in the target material, admits a total of 5 non-unique dimensionless groups which are chosen to be [54, 55]

$$\underbrace{\frac{\rho V}{m}}_{\Pi_v} = f\Bigg[\underbrace{\frac{gr}{v_0^2}}_{\Pi_g}, \underbrace{\frac{\sigma_y}{\rho v_0^2}}_{\Pi_\sigma}, \underbrace{\frac{\rho}{\delta}}_{\Pi_\rho}, \overline{\rho}\Bigg]. \tag{6.4}$$

Π_v represents the ratio between the mass expelled from the crater and the mass of the impactor m, i.e., the *cratering efficiency*, which is related to a gravity term Π_g, a strength term Π_σ, a density term Π_ρ, and the relative density $\overline{\rho}$.

To provide a form for the function $\Pi_v = f\left(\Pi_g, \Pi_\sigma, \Pi_\rho, \overline{\rho}\right)$, some works have assumed that the impactor behaves as a point source [54–56] such that the energy and momentum are coupled into a volume that is small compared to other features of interest. As a first-order approximation, we assume this point-source simplification is applicable to our nano-architected impact experiments, which allows us to replace the particle-related variables in Eq. 6.3 with a single measure $C = r v_0^{\mu} \delta^{\nu}$, where the exponents μ and ν are specific to a given target material. The bounds for $\mu \in [\frac{1}{3}, \frac{2}{3}]$ represent a momentum- or energy-dominated response [56], respectively, while ν has been typically found to be ~0.4. Values for μ have experimentally been found to range from ~0.4 for dry sands ($\overline{\rho} \approx 0.65$) to ~0.55 for water or metals [54], but no value has been obtained for low relative-density materials.

Assuming these experiments are done in a strength-dominant regime with $\sigma_y \gg \rho g r$, which we confirm to be valid since σ_y[3] for our materials (see section 6.3.1) is nine orders of magnitude larger than $\rho g r$ (with $\rho = 1{,}400$ kg/m^3 [9]), we can neglect the dependence on Π_g and express Eq. 6.4 as [56]

$$\Pi_v = \Pi_\sigma^{-\frac{3\mu}{2}} \Pi_\rho^{3\nu-1} f(\overline{\rho}), \tag{6.5}$$

[3] ranging from 25 ± 4 MPa to 79 ± 13 MPa.

where for simplicity we will assume $f(\overline{\rho}) = \overline{\rho}^{\,\gamma}$.

Using confocal microscopy we calculated Π_v for all $\overline{\rho} \approx 17\%$ impacts and fit the data to the expression in Eq. 6.5, as shown in Fig. 6.22. Restricting μ to its physical bounds provided best-fit values of $\mu = \frac{1}{3}$, $\nu \approx \frac{1}{3}$, and $\gamma = 1.185$, hinting to a momentum-dominated response.

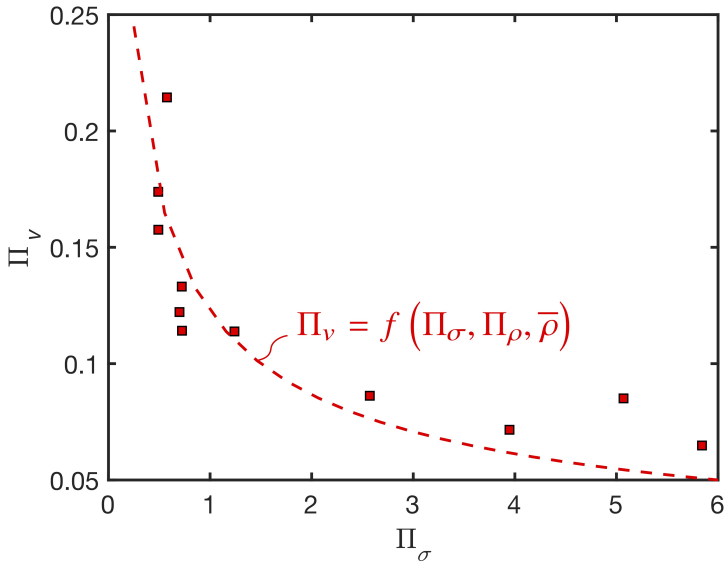

Figure 6.22 | Cratering Scaling Law for $\overline{\rho} \approx 17\%$ Nanolattices

Fit of the form $\Pi_v = \Pi_\sigma^{-\frac{3\mu}{2}} \Pi_\rho^{3\nu-1} \overline{\rho}^{\,\gamma}$ for the $\overline{\rho} \approx 17\%$ carbon nanolattice impacts. The fit parameters were $\mu = \frac{1}{3}$, $\nu \approx \frac{1}{3}$, and $\gamma = 1.185$.

6.4.5 Outlook

The experiments presented in this section constitute the first exploration of a nano-architected material under supersonic impact conditions. Besides observing different impact regimes, the overarching outcome was the ability to use dimensional analysis to provide a predictive tool for cratering in these materials. Performing these experiments for different geometries and relative densities could provide insight on the driving mechanisms for cratering and could facilitate the design of nano-architected materials for impact applications without requiring preliminary experiments. The nano-architected materials presented in this section present a lightweight solution for impact absorption of high-velocity micro-particle impacts, e.g., micrometeoroids, and could be readily used as protective coatings if they can be manufactured in larger volumes. Since no size-dependent assumptions went into

the dimensional analysis, these predictive tools could potentially apply to dimensionally similar impacts at larger scales.

6.5 Blast-loading on Macro-scale Carbon and Composite Lattice Architectures

Analytical and numerical explorations on the blast response of truss-core sandwich metallic materials have shown that these materials are able to sustain significantly larger blast impulses than monolithic plates of the same weight [145]. At smaller scales, hollow metallic microlattices have been predicted to benefit from plastic buckling of its tubes to dissipate more than twice the energy than a typical foam of the same mass [41].

To expand on the explorations described above, we studied the blast response of brittle 3D carbon architected materials and composites under buried blast conditions. The objective was to qualitatively observe the failure modes of these materials and assess the energy absorption capabilities with and without epoxy infiltration. We fabricated octet and tetrakaidecahedron carbon samples with a relative density of $\overline{\rho} \approx 15\%$ and a density of $\rho = 285 \pm 9$ kg/m^3 as shown in Fig. 6.23, and selected the octet configuration for these experiments due to its rigid architecture. After epoxy infiltration, the material density increased to $\rho = 1130 \pm 40$ kg/m^3 (see section 6.2.2 for details). These samples were fabricated to conform to an approximate $1 \times 0.56 \times 0.08$ aspect ratio, to conform to larger-scale blast experiments, and had final dimensions of $\sim 38 \times 19 \times 3.2$ mm corresponding to a $63 \times 32 \times 5$ tessellation of $\sim 600\,\mu$m unit cells.

6.5.1 Experiments

Buried blast experiments were performed on the carbon and carbon-epoxy octet materials which were suspended ~5 mm above the soil, as shown in Fig. 6.24. The sandwich configuration was achieved by encompassing the carbon-based materials between two 300 µm-thick stainless steel plates which were clamped together using screws.

To ensure controlled soil conditions, a 2.76 specific-gravity soil was passed through a #40 sieve (0.425 mm), oven dried for 24 hours, and wetted to 10% moisture content. The treated soil was pressed in ~10 mm layers to a nominal bulk density of 2.11 g cm^{-3}, until a controlled-soil cylinder of 311 mm in diameter and 50 mm in height was obtained. The explosive device (Teledyne RISI RP-3 EBW) was buried at a depth of ~1 mm within the controlled-soil cylinder.

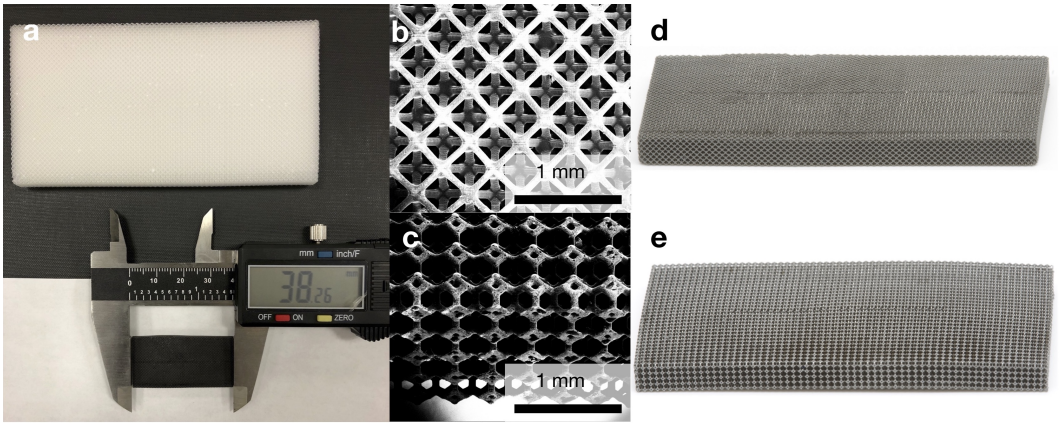

Figure 6.23 | Carbon Samples for Blast Loading
(a) Precursor polymeric material (white) and resulting carbon material (in caliper). **(b)** Micrograph of octet carbon material with ~600 µm unit cells, and **(c)** micrograph of tetrakaidecahedron carbon material with ~600 µm unit cells.**(d)**,**(e)** Photographs of the samples in (b),(d).

To capture the deflection of the truss-core sandwich plate, two high-speed cameras (HPV-X2, Shimadzu) were mounted above the blast setup to enable in situ digital image correlation (DIC).

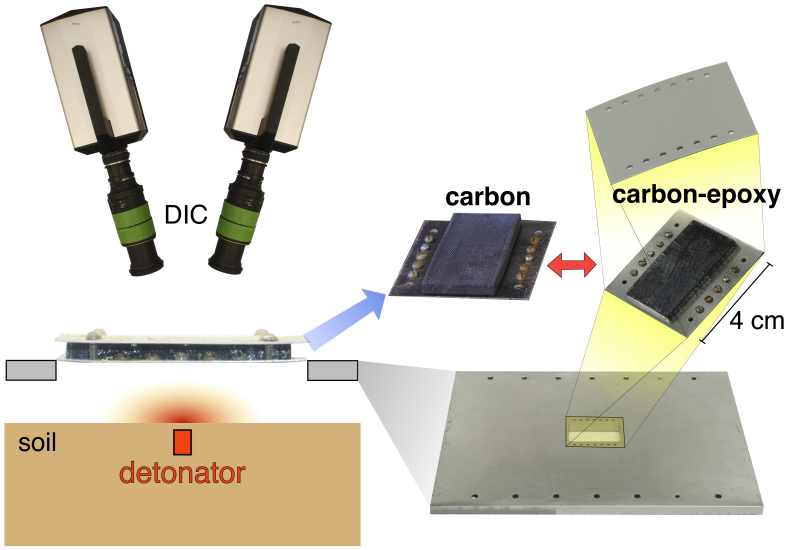

Figure 6.24 | Buried Blast Experimental Setup
A truss-core sandwich plate was assembled using stainless steel plates clamped together with screws. The test material was suspended ~5 mm above the soil, and two high-speed cameras were used to capture the in situ deflection of the plate. The detonator was buried ~1 mm below the soil.

In addition to blast experiments on the carbon and carbon-epoxy octet materials (see Supplementary Videos 21 & 22), an identical experiment was performed on two clamped stainless steel plates without a core as a control. Selecting a representative pixel from the DIC data at the center of each plate provided the deflection-time response shown in Fig. 6.25 (see Supplementary Videos 23–25). The control setup exhibited significant plastic deformation on the top and bottom plates of ~3 mm, most of which occurred within the first ~40 μs of the experiment. In contrast, both the carbon and carbon-epoxy sandwich plates only underwent elastic deformation on the stainless steel plates with maximum deflections of ~1 mm, confirmed upon disassembling the sandwich. Remarkably, both carbon-material configurations exhibited the same qualitative deflection response regardless of their different densities, Young's moduli, or effective strengths. However, they did present different failure mechanisms, with the carbon-epoxy sample exhibiting significantly fewer cracks than the carbon sample. Both architected materials seemed to have distributed the blast energy throughout a large fraction of the plate, possibly due to the inherent connectivity between unit cells.

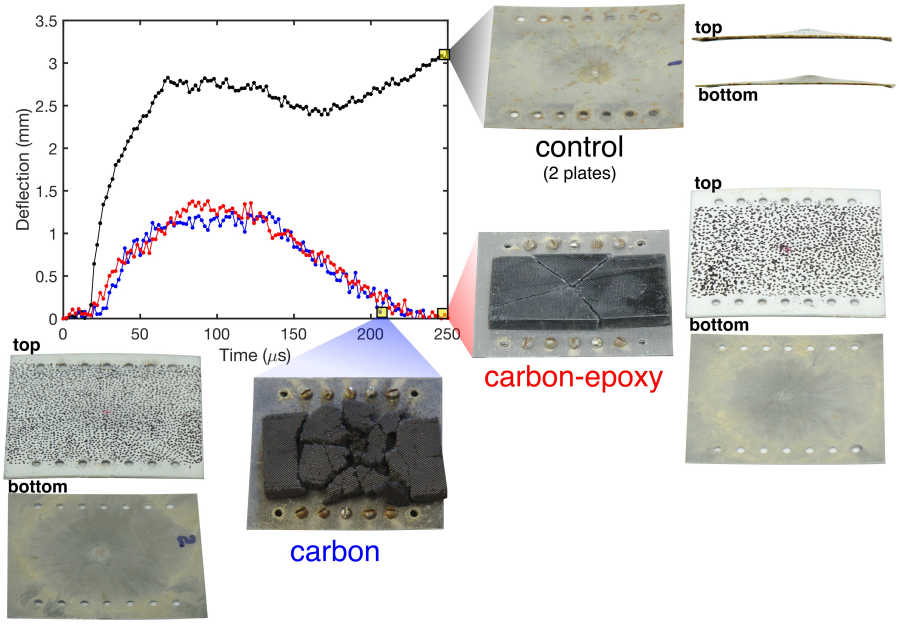

Figure 6.25 | Deflection of Sandwich Plates Upon Blast Impulse
Time-dependent deflection of the center of the top face plate for all configurations. A control sample consisted of the two face plates clamped together, which exhibited significant plastic deformation. The carbon and carbon-epoxy cores fractured, but prevented plastic deformation of the face plates.

6.5.2 Outlook

Although the exact mechanisms for energy dissipation in these materials remain to be understood, these experiments show the potential of lightweight architected carbon materials to be used blast shields. In particular, understanding the effect of architecture and epoxy infiltration on this response could allow for tunable failure mechanisms that might enable the material to endure more than one blast impulse, e.g., with military applications in mind. Future work will include comparison of this response to that of equal-density stochastic metallic and ceramic foams to assess the benefits of architecture in energy dissipation. Additionally, the effect of strain rate on the infiltrated epoxy could provide insight on the observed response.

Chapter 7

SUMMARY & OUTLOOK

7.1 Summary

The objective of this thesis was to probe beyond the current limits of nano- and micro-architected materials by numerically and experimentally exploring new geometries and loading regimes. As a result, we were able to thoroughly characterize the effect of nodes on the mechanical response of lattice architectures, and we provided an extension to the classical stiffness scaling laws that accounts for non-slender geometries such as the ones currently realizable by additive manufacturing techniques.

An important step was moving beyond solid and hollow beam-based architectures and exploring the doubly curved shells and their mechanical benefits. In doing so, we were able to exploit self-assembly techniques which enabled the fabrication of node-less architectures with features on the order of ~10 nm and sample volumes on the order of cubic centimeters. Using numerical tools and advanced fabrication techniques, we demonstrated the potential of this method to produce tunable nano-architected materials with extreme resilience by harnessing material size effects.

We were able to venture into previously unexplored dynamic mechanical regimes at these scales through the implementation and application of custom methods such as the micro-scale ultrasonic transmission method (μUTM) and the laser induced particle impact test (LIPIT). In the mechanical-wave regime, we explored the implications of structural reconfiguration and added micro-inertia to the dynamic response of the material and numerically & experimentally showed the emergence of vibrational band gaps. In the impact regime, we were able to probe nano-architected materials at supersonic speeds for the first time, and showed their potential to dissipate energy from these impacts.

Lastly, the knowledge gathered from the explorations mentioned above enabled the design and fabrication of centimeter-scale lightweight 3D carbon materials and composites through novel fabrication routes. These materials were tested under blast conditions and showed significant energy dissipation while at considerably lower densities than commonly used components for these applications.

7.2 Outlook

7.2.1 Self-Assembly

In light of all recent accomplishments in the architected materials community, true applicability of these materials is still highly dependent on their scalable fabrication. Additive manufacturing can be deemed satisfactory for specialized applications, but widespread use of these materials will rely on novel fabrication techniques. It is my opinion that several self-assembly methods have the potential to form large volumes of architected materials (as shown in chapter 4), which will require better understanding and control of the obtained morphologies. Closing the gap between large-scale fabrication and nanoscale mechanical effects will be crucial in enabling the realization of nano-architected materials beyond lab settings.

7.2.2 Compliant, Tunable, Resilient Materials

Most of the explorations in the nano-architected materials realm have been guided by the search for stiff, strong, and deformation-resistant materials. On the other hand, I believe the search for compliant and tunable materials that can selectively undergo deterministic forms of deformation is also worthwhile. Such materials can be particularly useful for multi-physics applications that require careful control of deformation. Additionally, the use of architecture in compliant materials could provide novel pathways to explore bio-mechanics problems where low stiffness but high resilience are necessary.

7.2.3 MHz and Beyond

Studying nano-architected materials under dynamic stimuli has opened the door for the exploration of mechanical waves in the MHz regime. This presents a significant accomplishment since these frequencies encompass a variety of ultrasound medical applications, which could benefit from wave-guiding or focusing enabled by architecture.

Beyond mechanical waves, the dynamic response of nano-architected materials is a largely unexplored field. We have recently witnessed the emergence of techniques that enable the study of these materials at previously inaccessible strain rates. Further work along this path might reveal that nanoscale architecture could provide significant benefits in the dynamic regime, similar to what has been observed in quasi-statics.

7.2.4 Carbon

Lastly, I believe that carbon has proven to be a versatile constituent material for architected materials as a whole. The possibility to 'shape' carbon into deterministic architectures could provide an alternative to carbon-fiber-based parts that are not easily manufactured. Furthermore, the high strength- and stiffness-to-density ratios concomitant with carbon enable these architected materials to achieve efficient material response. Additional work on the processing of this material system might enable us to fully control the atomic structure of the resultant constituent carbon while pushing for scalable fabrication of carbon-based architected materials.

BIBLIOGRAPHY

[1] Oraib Al-Ketan, Rachid Rezgui, Reza Rowshan, Huifeng Du, Nicholas X. Fang, and Rashid K. Abu Al-Rub. Microarchitected Stretching-Dominated Mechanical Metamaterials with Minimal Surface Topologies. *Advanced Engineering Materials*, 20(9):1800029, sep 2018. ISSN 14381656. doi: 10.1002/adem.201800029. URL http://doi.wiley.com/10.1002/adem.201800029.

[2] Ignacio Arretche and Kathryn H. Matlack. On the Interrelationship Between Static and Vibration Mitigation Properties of Architected Metastructures. *Frontiers in Materials*, 5(November):68, 2018. ISSN 2296-8016. doi: 10.3389/fmats.2018.00068. URL https://www.frontiersin.org/article/10.3389/fmats.2018.00068/full.

[3] Michael F. Ashby. The properties of foams and lattices. *Philosophical transactions. Series A, Mathematical, physical, and engineering sciences*, 364(1838):15–30, 2006. ISSN 1364-503X. doi: 10.1098/rsta.2005.1678. URL http://rsta.royalsocietypublishing.org/cgi/doi/10.1098/rsta.2005.1678.

[4] Sahab Babaee, Jongmin Shim, James C. Weaver, Elizabeth R. Chen, Nikita Patel, and Katia Bertoldi. 3D soft metamaterials with negative poisson's ratio. *Advanced Materials*, 25(36):5044–5049, 2013. ISSN 09359648. doi: 10.1002/adma.201301986.

[5] Emanuele Baravelli and Massimo Ruzzene. Internally resonating lattices for bandgap generation and low-frequency vibration control. *Journal of Sound and Vibration*, 332(25):6562–6579, 2013. ISSN 0022460X. doi: 10.1016/j.jsv.2013.08.014. URL http://dx.doi.org/10.1016/j.jsv.2013.08.014.

[6] Francois Barthelat, Huang Tang, Pablo D. Zavattieri, Chunming. Li, and Horacio D. Espinosa. On the mechanics of mother-of-pearl: A key feature in the material hierarchical structure. *Journal of the Mechanics and Physics of Solids*, 55(2):306–337, 2007. ISSN 00225096. doi: 10.1016/j.jmps.2006.07.007.

[7] Frank S. Bates, Wayne W. Maurer, Paul M. Lipic, Marc A. Hillmyer, Kristoffer Almdal, Kell Mortensen, Glenn H. Fredrickson, and Timothy P. Lodge. Polymeric Bicontinuous Microemulsions. *Physical Review Letters*, 79(5):849–852, aug 1997. ISSN 0031-9007. doi: 10.1103/PhysRevLett.79.849. URL https://link.aps.org/doi/10.1103/PhysRevLett.79.849.

[8] Jens Bauer, Stefan Hengsbach, Iwiza Tesari, Ruth Schwaiger, and Oliver Kraft. High-strength cellular ceramic composites with 3D microarchitecture. *Proceedings of the National Academy of Sciences*, 111(7):2453–2458, 2014. ISSN 0027-8424. doi: 10.1073/pnas.1315147111. URL http://www.pnas.org/cgi/doi/10.1073/pnas.1315147111.

[9] Jens Bauer, Almut Schroer, Ruth Schwaiger, and Oliver Kraft. Approaching theoretical strength in glassy carbon nanolattices. *Nature Materials*, 15(4):438–443, apr 2016. ISSN 1476-1122. doi: 10.1038/nmat4561. URL http://www.nature.com/doifinder/10.1038/nmat4561http://www.nature.com/articles/nmat4561.

[10] Alireza Bayat and Stavros Gaitanaros. Wave Directionality in Three-Dimensional Periodic Lattices. *Journal of Applied Mechanics*, 85(1):011004, nov 2017. ISSN 0021-8936. doi: 10.1115/1.4038287. URL http://appliedmechanics.asmedigitalcollection.asme.org/article.aspx?doi=10.1115/1.4038287.

[11] Lars A.A. Beex, Ron H.J. Peerlings, and Marc G.D. Geers. A quasicontinuum methodology for multiscale analyses of discrete microstructural models. *International Journal for Numerical Methods in Engineering*, 87(7):701–718, aug 2011. ISSN 00295981. doi: 10.1002/nme.3134. URL http://arxiv.org/abs/1010.1724http://doi.wiley.com/10.1002/nme.3134.

[12] Amer Beharic, Rafael Rodriguez Egui, and Li Yang. Drop-weight impact characteristics of additively manufactured sandwich structures with different cellular designs. *Materials and Design*, 145:122–134, 2018. ISSN 18734197. doi: 10.1016/j.matdes.2018.02.066. URL https://doi.org/10.1016/j.matdes.2018.02.066.

[13] Joel R. Bell, Kwanho Chang, Carlos R. Lopez-Barron, Christopher W. Macosko, and David C. Morse. Annealing of Cocontinuous Polymer Blends: Effect of Block Copolymer Molecular Weight and Architecture. *Macromolecules*, 43(11):5024–5032, jun 2010. ISSN 0024-9297. doi: 10.1021/ma902805x. URL http://pubs.acs.org/doi/abs/10.1021/ma902805x.

[14] Maria Berdova, Tuomo Ylitalo, Ivan Kassamakov, Jouni Heino, Pekka T. Törmä, Lauri Kilpi, Helena Ronkainen, Jari Koskinen, Edward Hæggström, and Sami Franssila. Mechanical assessment of suspended ALD thin films by bulge and shaft-loading techniques. *Acta Materialia*, 66:370–377, 2014. ISSN 13596454. doi: 10.1016/j.actamat.2013.11.024.

[15] Jonathan B. Berger, Hayden N.G. Wadley, and Robert M. McMeeking. Mechanical metamaterials at the theoretical limit of isotropic elastic stiffness. *Nature*, 543(7646):533–537, 2017. ISSN 14764687. doi: 10.1038/nature21075. URL http://dx.doi.org/10.1038/nature21075.

[16] Katia Bertoldi and Mary C. Boyce. Mechanically triggered transformations of phononic band gaps in periodic elastomeric structures. *Physical Review B*, 77(5):1–4, 2008. ISSN 1098-0121. doi: 10.1103/physrevb.77.052105.

[17] Katia Bertoldi, Vincenzo Vitelli, Johan Christensen, and Martin Van Hecke. Flexible mechanical metamaterials. *Nature Reviews Materials*, 2, 2017. ISSN 20588437. doi: 10.1038/natrevmats.2017.66.

[18] Juergen Biener, Andrea M. Hodge, Joel R. Hayes, Cynthia A. Volkert, Luis A. Zepeda-Ruiz, Alex V. Hamza, and Farid F. Abraham. Size Effects on the Mechanical Behavior of Nanoporous Au. *Nano Letters*, 6(10): 2379–2382, oct 2006. ISSN 1530-6984. doi: 10.1021/nl061978i. URL http://pubs.acs.org/doi/abs/10.1021/nl061978i.

[19] Colin Bonatti and Dirk Mohr. Large deformation response of additively-manufactured FCC metamaterials: From octet truss lattices towards continuous shell mesostructures. *International Journal of Plasticity*, 92: 122–147, may 2017. ISSN 07496419. doi: 10.1016/j.ijplas.2017.02.003. URL http://dx.doi.org/10.1016/j.ijplas.2017.02.003https://linkinghub.elsevier.com/retrieve/pii/S0749641917300840.

[20] Colin Bonatti and Dirk Mohr. Mechanical performance of additively-manufactured anisotropic and isotropic smooth shell-lattice materials: Simulations & experiments. *Journal of the Mechanics and Physics of Solids*, 122:1–26, 2019. ISSN 00225096. doi: 10.1016/j.jmps.2018.08.022. URL https://doi.org/10.1016/j.jmps.2018.08.022.

[21] Léon Brillouin. *Wave Propagation in Periodic Structures: Electric Filters and Crystal Lattices*. Dover phoenix editions. Dover Publications, 2003. ISBN 9780486495569. URL https://books.google.com/books?id=m2WmGiU5nUwC.

[22] Christopher R. Calladine. *Theory of Shell Structures*. Cambridge University Press, Cambridge, 1983. ISBN 9780511624278. doi: 10.1017/CBO9780511624278. URL http://ebooks.cambridge.org/ref/id/CBO9780511624278.

[23] Jinwoong Cha, Kun Woo Kim, and Chiara Daraio. Experimental realization of on-chip topological nanoelectromechanical metamaterials. *Nature*, jun 2018. ISSN 0028-0836. doi: 10.1038/s41586-018-0764-0. URL http://arxiv.org/abs/1806.10680http://dx.doi.org/10.1038/s41586-018-0764-0.

[24] Candace K Chan, Hailin Peng, Gao Liu, Kevin McIlwrath, Xiao Feng Zhang, Robert A Huggins, and Yi Cui. High-performance lithium battery anodes using silicon nanowires. *Nature nanotechnology*, 3(1):31–5, 2008. ISSN 1748-3395. doi: 10.1038/nnano.2007.411. URL http://www.ncbi.nlm.nih.gov/pubmed/18654447.

[25] Chong-seok Chang and Dewey Hodges. Vibration characteristics of curved beams. *Journal of Mechanics of Materials and Structures*, 4(4):675–692, 2009. ISSN 1559-3959. doi: 10.2140/jomms.2009.4.675.

[26] Yanyu Chen and Lifeng Wang. Periodic co-continuous acoustic metamaterials with overlapping locally resonant and Bragg band gaps. *Applied Physics Letters*, 105(19), 2014. ISSN 00036951. doi: 10.1063/1.4902129.

[27] Yanyu Chen, Tiantian Li, Fabrizio Scarpa, and Lifeng Wang. Lattice Metamaterials with Mechanically Tunable Poisson's Ratio for Vibration Control. *Physical Review Applied*, 7(2):1–11, 2017. ISSN 23317019. doi: 10.1103/PhysRevApplied.7.024012.

[28] Anders Clausen, Fengwen Wang, Jakob S. Jensen, Ole Sigmund, and Jennifer A. Lewis. Topology Optimized Architectures with Programmable Poisson's Ratio over Large Deformations. *Advanced Materials*, 27(37):5523–5527, 2015. ISSN 15214095. doi: 10.1002/adma.201502485.

[29] Robert D. Cook, David S. Malkus, and Michael E. Plesha. *Concepts and Applications of Finite Element Analysis*. Wiley, 1989. ISBN 9780471503194. URL https://books.google.ch/books?id=irZHPgAACAAJ.

[30] Corentin Coulais, Eial Teomy, Koen De Reus, Yair Shokef, and Martin Van Hecke. Combinatorial design of textured mechanical metamaterials. *Nature*, 535(7613):529–532, 2016. ISSN 14764687. doi: 10.1038/nature18960. URL http://dx.doi.org/10.1038/nature18960.

[31] Corentin Coulais, Chris Kettenis, and Martin Van Hecke. A characteristic length scale causes anomalous size effects and boundary programmability in mechanical metamaterials. *Nature Physics*, 14(1):40–44, 2018. ISSN 17452481. doi: 10.1038/NPHYS4269.

[32] Luize Scalco de Vasconcelos, Rong Xu, and Kejie Zhao. Operando Nanoindentation: A New Platform to Measure the Mechanical Properties of Electrodes during Electrochemical Reactions. *Journal of The Electrochemical Society*, 164(14):A3840–A3847, 2017. ISSN 0013-4651. doi: 10.1149/2.1411714jes.

[33] Bolei Deng, Jordan R. Raney, Vincent Tournat, and Katia Bertoldi. Elastic Vector Solitons in Soft Architected Materials. *Physical Review Letters*, 118 (20):1–5, 2017. ISSN 10797114. doi: 10.1103/PhysRevLett.118.204102.

[34] Vikram S. Deshpande, M. F. Ashby, and Norman A. Fleck. Foam topology: Bending versus stretching dominated architectures. *Acta Materialia*, 49(6): 1035–1040, 2001. ISSN 13596454. doi: 10.1016/S1359-6454(00)00379-7.

[35] Vikram S. Deshpande, Norman A. Fleck, and M. F. Ashby. Effective properties of the octet-truss lattice material. *Journal of the Mechanics and Physics*

of Solids, 49(8):1747–1769, 2001. ISSN 00225096. doi: 10.1016/S0022-5096(01)00010-2.

[36] Albert Desmoulins and Dennis M. Kochmann. Local and nonlocal continuum modeling of inelastic periodic networks applied to stretching-dominated trusses. *Computer Methods in Applied Mechanics and Engineering*, 313: 85–105, 2017. ISSN 00457825. doi: 10.1016/j.cma.2016.09.027. URL http://dx.doi.org/10.1016/j.cma.2016.09.027.

[37] Albert Desmoulins, Alex J. Zelhofer, and Dennis M. Kochmann. Auxeticity in truss networks and the role of bending versus stretching deformation. *Smart Materials and Structures*, 25(5), 2016. ISSN 1361665X. doi: 10.1088/0964-1726/25/5/054003.

[38] Leon S. Dimas, Graham H. Bratzel, Ido Eylon, and Markus J. Buehler. Tough composites inspired by mineralized natural materials: Computation, 3D printing, and testing. *Advanced Functional Materials*, 23(36):4629–4638, 2013. ISSN 1616301X. doi: 10.1002/adfm.201300215.

[39] Nicholas G. Dou, Robert A. Jagt, Carlos M. Portela, Julia R. Greer, and Austin J. Minnich. Ultralow Thermal Conductivity and Mechanical Resilience of Architected Nanolattices. *Nano Letters*, 18(8):4755–4761, 2018. ISSN 15306992. doi: 10.1021/acs.nanolett.8b01191. URL https://dx.doi.org/10.1021/acs.nanolett.8b01191.

[40] Horacio D. Espinosa, Jee E. Rim, Francois Barthelat, and Markus J. Buehler. Merger of structure and material in nacre and bone - Perspectives on de novo biomimetic materials. *Progress in Materials Science*, 54(8):1059–1100, 2009. ISSN 00796425. doi: 10.1016/j.pmatsci.2009.05.001. URL http://dx.doi.org/10.1016/j.pmatsci.2009.05.001.

[41] Anthony G. Evans, Ming Y. He, Vikram S. Deshpande, John W. Hutchinson, Alan J. Jacobsen, and William B. Carter. Concepts for enhanced energy absorption using hollow micro-lattices. *International Journal of Impact Engineering*, 37(9):947–959, 2010. ISSN 0734743X. doi: 10.1016/j.ijimpeng.2010.03.007. URL http://dx.doi.org/10.1016/j.ijimpeng.2010.03.007.

[42] Eli Fahrenkrug, Junsi Gu, and Stephen Maldonado. Electrochemically gated alloy formation of crystalline InAs thin films at room temperature in aqueous electrolytes. *Chemistry of Materials*, 26(15):4535–4543, 2014. ISSN 15205002. doi: 10.1021/cm501752n.

[43] Norman A. Fleck, Vikram S. Deshpande, and Michael F. Ashby. Micro-architectured materials: past, present and future. *Proceedings of the Royal Society A: Mathematical, Physical and Engineering Sciences*, 466(2121): 2495–2516, jun 2010. ISSN 1364-5021. doi: 10.1098/rspa.2010.0215.

[44] Haoran Fu, Kewang Nan, Wubin Bai, Wen Huang, Ke Bai, Luyao Lu, Chaoqun Zhou, Yunpeng Liu, Fei Liu, Juntong Wang, Mengdi Han, Zheng Yan, Haiwen Luan, Yijie Zhang, Yutong Zhang, Jianing Zhao, Xu Cheng, Moyang Li, Jung Woo Lee, Yuan Liu, Daining Fang, Xiuling Li, Yonggang Huang, Yihui Zhang, and John A. Rogers. Morphable 3D mesostructures and microelectronic devices by multistable buckling mechanics. *Nature Materials*, 17(3):268–276, 2018. ISSN 14764660. doi: 10.1038/s41563-017-0011-3. URL http://dx.doi.org/10.1038/s41563-017-0011-3.

[45] Tochukwu George, Vikram S. Deshpande, and Haydn N.G. Wadley. Mechanical response of carbon fiber composite sandwich panels with pyramidal truss cores. *Composites Part A: Applied Science and Manufacturing*, 47:31–40, apr 2013. ISSN 1359835X. doi: 10.1016/j.compositesa.2012.11.011.

[46] Lorna J. Gibson and Michael F. Ashby. *Cellular Solids: Structure and Properties*. Cambridge University Press, Cambridge, 2 edition, 1999. ISBN 978-0521499118. URL https://doi.org/10.1017/CBO9781139878326.

[47] Andrew Gross, Panos Pantidis, Katia Bertoldi, and Simos Gerasimidis. Correlation between topology and elastic properties of imperfect truss-lattice materials. *Journal of the Mechanics and Physics of Solids*, 124:577–598, 2019. ISSN 00225096. doi: 10.1016/j.jmps.2018.11.007. URL https://linkinghub.elsevier.com/retrieve/pii/S0022509618308615.

[48] Gérald Gurtner and Marc Durand. Stiffest elastic networks. *Proceedings of the Royal Society A: Mathematical, Physical and Engineering Sciences*, 470 (2164):20130611–20130611, 2014. ISSN 1364-5021. doi: 10.1098/rspa.2013.0611. URL http://rspa.royalsocietypublishing.org/cgi/doi/10.1098/rspa.2013.0611.

[49] Seung Chul Han, Jeong Woo Lee, and Kiju Kang. A New Type of Low Density Material: Shellular. *Advanced Materials*, 27(37):5506–5511, oct 2015. ISSN 09359648. doi: 10.1002/adma.201501546. URL http://doi.wiley.com/10.1002/adma.201501546.

[50] Seung Chul Han, Jeong Myung Choi, Gang Liu, and Kiju Kang. A microscopic shell structure with schwarz's D-Surface. *Scientific Reports*, 7 (1):1–8, 2017. ISSN 20452322. doi: 10.1038/s41598-017-13618-3. URL http://dx.doi.org/10.1038/s41598-017-13618-3.

[51] Jonathan A. Harris, R. E. Winter, and Graham J. McShane. Impact response of additively manufactured metallic hybrid lattice materials. *International Journal of Impact Engineering*, 104:177–191, 2017. ISSN 0734743X. doi: 10.1016/j.ijimpeng.2017.02.007.

[52] James A. Hawreliak, Jonathan Lind, Brian Maddox, Matthew I. Barham, Mark C. Messner, Nathan Barton, Brian J. Jensen, and Mukul Kumar. Dynamic Behavior of Engineered Lattice Materials. *Scientific Reports*, 6:

28094, 2016. ISSN 2045-2322. doi: 10.1038/srep28094. URL http://www.nature.com/articles/srep28094.

[53] Andrea M. Hodge, Reed T. Doucette, Monika M. Biener, Juergen Biener, Octavio Cervantes, and Alex V. Hamza. Ag effects on the elastic modulus values of nanoporous Au foams. *Journal of Materials Research*, 24(4):1600–1606, 2009. ISSN 08842914. doi: 10.1557/jmr.2009.0184.

[54] Keith A. Holsapple. The Scaling of Impact Processes in Planetary Sciences. *Annual Review of Earth and Planetary Sciences*, 21 (1):333–373, 1993. ISSN 0084-6597. doi: 10.1146/annurev.ea.21.050193.002001. URL http://www.annualreviews.org/doi/10.1146/annurev.ea.21.050193.002001.

[55] Kevin R. Housen and Keith A. Holsapple. Impact cratering on porous asteroids. *Icarus*, 163(1):102–119, 2003. ISSN 00191035. doi: 10.1016/S0019-1035(03)00024-1.

[56] Kevin R. Housen, William J. Sweet, and Keith A. Holsapple. Impacts into porous asteroids. *Icarus*, 300:72–96, jan 2018. ISSN 00191035. doi: 10.1016/j.icarus.2017.08.019. URL http://dx.doi.org/10.1016/j.icarus.2017.08.019https://linkinghub.elsevier.com/retrieve/pii/S0019103517305948.

[57] Meng-Ting Hsieh, Bianca Endo, Yunfei Zhang, Jens Bauer, and Lorenzo Valdevit. The mechanical response of cellular materials with spinodal topologies. *Journal of the Mechanics and Physics of Solids*, 125:401–419, 2019. ISSN 0022-5096. doi: 10.1016/J.JMPS.2019.01.002. URL https://www.sciencedirect.com/science/article/pii/S0022509618307750?dgcid=raven{_}sd{_}aip{_}email{#}sec0007.

[58] Shan Huang and Ting Zhu. Atomistic mechanisms of lithium insertion in amorphous silicon. *Journal of Power Sources*, 196(7):3664–3668, 2011. ISSN 03787753. doi: 10.1016/j.jpowsour.2010.11.155. URL http://dx.doi.org/10.1016/j.jpowsour.2010.11.155.

[59] Mahmoud I. Hussein, Michael J. Leamy, and Massimo Ruzzene. Dynamics of Phononic Materials and Structures: Historical Origins, Recent Progress, and Future Outlook. *Applied Mechanics Reviews*, 66(4):040802, 2014. ISSN 0003-6900. doi: 10.1115/1.4026911. URL http://appliedmechanicsreviews.asmedigitalcollection.asme.org/article.aspx?doi=10.1115/1.4026911.

[60] Alan J. Jacobsen, William Barvosa-Carter, and Steven Nutt. Micro-scale Truss Structures formed from Self-Propagating Photopolymer Waveguides. *Advanced Materials*, 19(22):3892–3896, nov 2007. ISSN 09359648. doi: 10.1002/adma.200700797.

[61] Alan J. Jacobsen, Sky Mahoney, William B. Carter, and Steven Nutt. Vitreous carbon micro-lattice structures. *Carbon*, 49(3):1025–1032, 2011. ISSN 00086223. doi: 10.1016/j.carbon.2010.10.059. URL http://dx.doi.org/10.1016/j.carbon.2010.10.059.

[62] Dongchan Jang, Lucas R Meza, Frank Greer, and Julia R Greer. Fabrication and deformation of three-dimensional hollow ceramic nanostructures. *Nature materials*, 12(10):893–898, oct 2013. ISSN 1476-1122. doi: 10.1038/nmat3738.

[63] Wen Yea Jang, Stelios Kyriakides, and Andrew M. Kraynik. On the compressive strength of open-cell metal foams with Kelvin and random cell structures. *International Journal of Solids and Structures*, 47(21):2872–2883, 2010. ISSN 00207683. doi: 10.1016/j.ijsolstr.2010.06.014. URL http://dx.doi.org/10.1016/j.ijsolstr.2010.06.014.

[64] Sung Hoon Kang, Sicong Shan, Wim L. Noorduin, Mughees Khan, Joanna Aizenberg, and Katia Bertoldi. Buckling-induced reversible symmetry breaking and amplification of chirality using supported cellular structures. *Advanced Materials*, 25(24):3380–3385, 2013. ISSN 09359648. doi: 10.1002/adma.201300617.

[65] Syed N. Khaderi, Maik R.J. Scherer, C. E. Hall, Ullrich Steiner, Upradrastra Ramamurty, Norman A. Fleck, and Vikram S. Deshpande. The indentation response of Nickel nano double gyroid lattices. *Extreme Mechanics Letters*, 10:15–23, 2017. ISSN 23524316. doi: 10.1016/j.eml.2016.08.006. URL http://dx.doi.org/10.1016/j.eml.2016.08.006.

[66] Yoonho Kim, Hyunwoo Yuk, Ruike Zhao, Shawn A Chester, and Xuanhe Zhao. Printing Ferromagnetic Materials. *Letter*, 2018. ISSN 0028-0836. doi: 10.1038/s41586-018-0185-0.

[67] Charles Kittel. *Introduction to Solid State Physics*. Wiley series on the science and technology of materials. Wiley, 1956. URL https://books.google.com/books?id=K1dAAAAAIAAJ.

[68] Carolin Korner and Yvonne Liebold-Ribeiro. A systematic approach to identify cellular auxetic materials. *Smart Materials and Structures*, 24(2), 2015. ISSN 1361665X. doi: 10.1088/0964-1726/24/2/025013.

[69] Sebastian Krödel and Chiara Daraio. Microlattice Metamaterials for Tailoring Ultrasonic Transmission with Elastoacoustic Hybridization. *Physical Review Applied*, 6(6):064005, 2016. ISSN 2331-7019. doi: 10.1103/PhysRevApplied.6.064005. URL http://link.aps.org/doi/10.1103/PhysRevApplied.6.064005.

[70] Sebastian Krödel, Tommaso Delpero, Andrea Bergamini, Paolo Ermanni, and Dennis M. Kochmann. 3D auxetic microlattices with independently

controllable acoustic band gaps and quasi-static elastic moduli. *Advanced Engineering Materials*, 16(4):357–363, 2014. ISSN 15272648. doi: 10.1002/adem.201300264.

[71] Sebastian Krödel, Antonio Palermo, and Chiara Daraio. Acoustic properties of porous microlattices from effective medium to scattering dominated regimes. *The Journal of the Acoustical Society of America*, 144(1):319–329, 2018. ISSN 0001-4966. doi: 10.1121/1.5046068.

[72] Yongwoo Kwon, K. Thornton, and P.W. Voorhees. Morphology and topology in coarsening of domains via non-conserved and conserved dynamics. *Philosophical Magazine*, 90(1-4):317–335, jan 2010. ISSN 1478-6435. doi: 10.1080/14786430903260701. URL http://www.tandfonline.com/doi/abs/10.1080/14786430903260701.

[73] Chang Quan Lai and Chiara Daraio. Highly porous microlattices as ultra-thin and efficient impact absorbers. *International Journal of Impact Engineering*, 120(December 2017):138–149, 2018. ISSN 0734743X. doi: 10.1016/j.ijimpeng.2018.05.014. URL https://doi.org/10.1016/j.ijimpeng.2018.05.014.

[74] Ryan M. Latture, Matthew R. Begley, and Frank W. Zok. Design and mechanical properties of elastically isotropic trusses. *Journal of Materials Research*, 33(3):249–263, 2018. ISSN 20445326. doi: 10.1557/jmr.2018.2.

[75] Ryan M. Latture, Ricardo X. Rodriguez, Larry R. Holmes, and Frank W. Zok. Effects of nodal fillets and external boundaries on compressive response of an octet truss. *Acta Materialia*, 149:78–87, 2018. ISSN 13596454. doi: 10.1016/j.actamat.2017.12.060. URL https://doi.org/10.1016/j.actamat.2017.12.060.

[76] K. H. Law and Leroy Gardner. Lateral instability of elliptical hollow section beams. *Engineering Structures*, 37:152–166, 2012. ISSN 01410296. doi: 10.1016/j.engstruct.2011.12.008. URL http://dx.doi.org/10.1016/j.engstruct.2011.12.008.

[77] A Lazarus, H C B Florijn, and P M Reis. Geometry-Induced Rigidity in Nonspherical Pressurized Elastic Shells. *Physical Review Letters*, 109 (14):144301, oct 2012. ISSN 0031-9007. doi: 10.1103/PhysRevLett.109.144301. URL https://link.aps.org/doi/10.1103/PhysRevLett.109.144301.

[78] Jae Hwang Lee, Jonathan P. Singer, and Edwin L. Thomas. Micro-/nanostructured mechanical metamaterials. *Advanced Materials*, 24(36):4782–4810, 2012. ISSN 09359648. doi: 10.1002/adma.201201644.

[79] Matthew N. Lee and Ali Mohraz. Bicontinuous macroporous materials from bijel templates. *Advanced Materials*, 22(43):4836–4841, 2010. ISSN 09359648. doi: 10.1002/adma.201001696.

[80] Haiyi Liang and L Mahadevan. The shape of a long leaf. *Proceedings of the National Academy of Sciences*, 106(52):22049–22054, dec 2009. ISSN 0027-8424. doi: 10.1073/pnas.0911954106. URL http://www.pnas.org/lookup/doi/10.1073/pnas.0911954106.

[81] Yvonne Liebold-Ribeiro and Carolin Körner. Phononic band gaps in periodic cellular materials. *Advanced Engineering Materials*, 16(3):328–334, 2014. ISSN 15272648. doi: 10.1002/adem.201300064.

[82] Jinyun Liu, Nan Li, Matthew D. Goodman, Hui Gang Zhang, Eric S. Epstein, Bo Huang, Zeng Pan, Jinwoo Kim, Jun Hee Choi, Xingjiu Huang, Jinhuai Liu, K. Jimmy Hsia, Shen J. Dillon, and Paul V. Braun. Mechanically and chemically robust sandwich-structured C@Si@C nanotube array Li-ion battery anodes. *ACS Nano*, 9(2):1985–1994, 2015. ISSN 1936086X. doi: 10.1021/nn507003z.

[83] Ying Liu, Xiu-zhan Sun, Wen-zheng Jiang, and Yu Gu. Tuning of Bandgap Structures in Three-Dimensional Kagome-Sphere Lattice. *Journal of Vibration and Acoustics*, 136(2):021016, 2014. ISSN 0739-3717. doi: 10.1115/1.4026211. URL http://vibrationacoustics.asmedigitalcollection.asme.org/article.aspx?doi=10.1115/1.4026211.

[84] Carlos R. Lopez-Barron and Christopher W. Macosko. Direct Measurement of Interface Anisotropy of Bicontinuous Structures via 3D Image Analysis. *Langmuir*, 26(17):14284–14293, sep 2010. ISSN 0743-7463. doi: 10.1021/la102314r. URL http://pubs.acs.org/doi/abs/10.1021/la102314r.

[85] K. R. Mangipudi, E. Epler, and C. A. Volkert. Topology-dependent scaling laws for the stiffness and strength of nanoporous gold. *Acta Materialia*, 119:115–122, 2016. ISSN 13596454. doi: 10.1016/j.actamat.2016.08.012. URL http://dx.doi.org/10.1016/j.actamat.2016.08.012.

[86] I. Maskery, L. Sturm, A. O. Aremu, A. Panesar, C. B. Williams, C. J. Tuck, R. D. Wildman, I. A. Ashcroft, and R. J.M. Hague. Insights into the mechanical properties of several triply periodic minimal surface lattice structures made by polymer additive manufacturing. *Polymer*, 152:62–71, 2018. ISSN 00323861. doi: 10.1016/j.polymer.2017.11.049. URL https://doi.org/10.1016/j.polymer.2017.11.049.

[87] Arturo J. Mateos, Wei Huang, Yong-Wei Zhang, and Julia R. Greer. Discrete-Continuum Duality of Architected Materials: Failure, Flaws, and Fracture. *Advanced Functional Materials*, 1806772:1806772, 2018. ISSN 1616-301X. doi: 10.1002/adfm.201806772. URL https://onlinelibrary.wiley.com/doi/abs/10.1002/adfm.201806772.

[88] Kathryn H. Matlack, Anton Bauhofer, Sebastian Krödel, Antonio Palermo, and Chiara Daraio. Composite 3D-printed metastructures for low-frequency and broadband vibration absorption. *Proceedings of the National Academy of Sciences*, 113(30):8386–8390, jul 2016. ISSN 0027-8424. doi: 10.1073/pnas.1600171113. URL http://arxiv.org/abs/1511.09465{%}0Ahttp://dx.doi.org/10.1073/pnas.1600171113http://www.pnas.org/lookup/doi/10.1073/pnas.1600171113.

[89] Matthew T. McDowell, Seok Woo Lee, William D. Nix, and Yi Cui. 25th anniversary article: Understanding the lithiation of silicon and other alloying anodes for lithium-ion batteries. *Advanced Materials*, 25(36):4966–4985, 2013. ISSN 09359648. doi: 10.1002/adma.201301795.

[90] Mark C. Messner, Matthew I Barham, Mukul Kumar, and Nathan R Barton. Wave propagation in equivalent continuums representing truss lattice materials. *International Journal of Solids and Structures*, 73-74:55–66, 2015. ISSN 0020-7683. doi: 10.1016/j.ijsolstr.2015.07.023. URL http://dx.doi.org/10.1016/j.ijsolstr.2015.07.023.

[91] Lucas R. Meza and Julia R. Greer. Mechanical characterization of hollow ceramic nanolattices. *Journal of Materials Science*, 49(6):2496–2508, 2014. ISSN 00222461. doi: 10.1007/s10853-013-7945-x.

[92] Lucas R. Meza, Satyajit Das, and Julia R. Greer. Strong, lightweight, and recoverable three-dimensional ceramic nanolattices. *Science*, 345 (6202):1322–1326, sep 2014. ISSN 0036-8075. doi: 10.1126/science.1255908. URL http://www.sciencemag.org/cgi/doi/10.1126/science.1255908.

[93] Lucas R. Meza, Alex J. Zelhofer, Nigel Clarke, Arturo J. Mateos, Dennis M. Kochmann, and Julia R. Greer. Resilient 3D hierarchical architected metamaterials. *Proceedings of the National Academy of Sciences of the United States of America*, 112(37):11502–7, 2015. ISSN 1091-6490. doi: 10.1073/pnas.1509120112. URL http://www.pnas.org/content/112/37/11502.abstract.

[94] Lucas R. Meza, Gregory P. Phlipot, Carlos M. Portela, Alessandro Maggi, Lauren C. Montemayor, Andre Comella, Dennis M. Kochmann, and Julia R. Greer. Reexamining the mechanical property space of three-dimensional lattice architectures. *Acta Materialia*, 140:424–432, 2017. ISSN 1359-6454. doi: 10.1016/j.actamat.2017.08.052. URL http://dx.doi.org/10.1016/j.actamat.2017.08.052.

[95] R. A.W. Mines, S. Tsopanos, Y. Shen, R. Hasan, and S. T. McKown. Drop weight impact behaviour of sandwich panels with metallic micro lattice cores. *International Journal of Impact Engineering*, 60:120–132, 2013. ISSN 0734743X. doi: 10.1016/j.ijimpeng.2013.04.007. URL http://dx.doi.org/10.1016/j.ijimpeng.2013.04.007.

[96] Michael A. Monn, James C. Weaver, Tianyang Zhang, Joanna Aizenberg, and Haneesh Kesari. New functional insights into the internal architecture of the laminated anchor spicules of Euplectella aspergillum. *Proceedings of the National Academy of Sciences*, 112(16):4976–4981, 2015. ISSN 0027-8424. doi: 10.1073/pnas.1415502112.

[97] Lauren C Montemayor and Julia R. Greer. Mechanical Response of Hollow Metallic Nanolattices: Combining Structural and Material Size Effects. *Journal of Applied Mechanics*, 82(July):1–10, 2015. ISSN 0021-8936. doi: 10.1115/1.4030361. URL http://appliedmechanics.asmedigitalcollection.asme.org/article.aspx?doi=10.1115/1.4030361.

[98] R.K. Nalla, J.H. Kinney, and R.O. Ritchie. Mechanistic fracture criteria for the failure of human cortical bone. *Nature Materials*, 2(3):164–168, 2003. ISSN 1476-1122. doi: 10.1038/nmat832.

[99] Utpal Nath, Brian C W Crawford, Rosemary Carpenter, and Enrico Coen. Genetic control of surface curvature. [Science. 2003] - PubMed result. *Science (New York, N.Y.)*, 299(5611):1404–7, 2003. ISSN 1095-9203. doi: 10.1126/science.1079354. URL http://www.ncbi.nlm.nih.gov/pubmed/12610308.

[100] Sokol Ndoni, Martin E. Vigild, and Rolf H. Berg. Nanoporous Materials with Spherical and Gyroid Cavities Created by Quantitative Etching of Polydimethylsiloxane in Polystyrene-Polydimethylsiloxane Block Copolymers. *Journal of the American Chemical Society*, 125(44):13366–13367, 2003. ISSN 00027863. doi: 10.1021/ja0360034.

[101] Ban Dang Nguyen, Seung Chul Han, Yoon Chang Jung, and Kiju Kang. Design of the P-surfaced shellular, an ultra-low density material with micro-architecture. *Computational Materials Science*, 139:162–178, 2017. ISSN 09270256. doi: 10.1016/j.commatsci.2017.07.025. URL http://dx.doi.org/10.1016/j.commatsci.2017.07.025.

[102] M. N. Obrovac and V. L. Chevrier. Alloy Negative Electrodes for Li-Ion Batteries. *Chemical Reviews*, 114(23):11444–11502, 2014. ISSN 0009-2665. doi: 10.1021/cr500207g. URL http://pubs.acs.org/doi/10.1021/cr500207g.

[103] M. R. O'Masta, L Dong, L. St-Pierre, H. N.G. Wadley, and V S Deshpande. The fracture toughness of octet-truss lattices. *Journal of the Mechanics and Physics of Solids*, 98(October 2016):271–289, 2017. ISSN 00225096. doi: 10.1016/j.jmps.2016.09.009. URL http://dx.doi.org/10.1016/j.jmps.2016.09.009.

[104] Johannes T.B. Overvelde, James C. Weaver, Chuck Hoberman, and Katia Bertoldi. Rational design of reconfigurable prismatic architected materials. *Nature*, 541(7637):347–352, 2017. ISSN 14764687. doi: 10.1038/nature20824. URL http://dx.doi.org/10.1038/nature20824.

[105] Raj Kumar Pal and Massimo Ruzzene. Edge waves in plates with resonators: an elastic analogue of the quantum valley Hall effect. *New J. Phys*, 19, 2017. URL http://iopscience.iop.org/article/10.1088/1367-2630/aa56a2/pdf.

[106] Raj Kumar Pal, Massimo Ruzzene, and Julian J. Rimoli. A continuum model for nonlinear lattices under large deformations. *International Journal of Solids and Structures*, 96:300–319, 2016. ISSN 00207683. doi: 10.1016/j.ijsolstr.2016.05.020. URL http://dx.doi.org/10.1016/j.ijsolstr.2016.05.020.

[107] C.-L. Park, J.W. Gibbs, P.W. Voorhees, and K. Thornton. Coarsening of complex microstructures following spinodal decomposition. *Acta Materialia*, 132:13–24, jun 2017. ISSN 13596454. doi: 10.1016/j.actamat.2017.03.020. URL http://dx.doi.org/10.1016/j.actamat.2017.03.020.

[108] Cheolmin Park, Jongseung Yoon, and Edwin L. Thomas. Enabling nanotechnology with self assembled block copolymer patterns. *Polymer*, 44 (22):6725–6760, oct 2003. ISSN 00323861. doi: 10.1016/j.polymer.2003.08.011. URL http://linkinghub.elsevier.com/retrieve/pii/S0032386103007432.

[109] Ganesh U. Patil and Kathryn H. Matlack. Effective property evaluation and analysis of three-dimensional periodic lattices and composites through Bloch-wave homogenization. *The Journal of the Acoustical Society of America*, 145(3):1259–1269, 2019. ISSN 0001-4966. doi: 10.1121/1.5091690. URL http://asa.scitation.org/doi/10.1121/1.5091690.

[110] S. Pellegrino and C. R. Calladine. Matrix Analysis of Statically and Kinematically Indeternimate Frameworks. *International Journal of Solids and Structures*, 22(4):409–428, 1986.

[111] Minh-Son Pham, Chen Liu, Iain Todd, and Jedsada Lertthanasarn. Damage-tolerant architected materials inspired by crystal microstructure. *Nature*, 2019. ISSN 0028-0836. doi: 10.1038/s41586-018-0850-3. URL http://www.nature.com/articles/s41586-018-0850-3.

[112] Gregory P. Phlipot and Dennis M. Kochmann. A quasicontinuum theory for the nonlinear mechanical response of general periodic truss lattices. *Journal of the Mechanics and Physics of Solids*, 124:758–780, 2019. ISSN 00225096. doi: 10.1016/j.jmps.2018.11.014. URL https://doi.org/10.1016/j.jmps.2018.11.014.

[113] V Pini, J J Ruz, P M Kosaka, O Malvar, M Calleja, and J Tamayo. How two-dimensional bending can extraordinarily stiffen thin sheets. *Scientific Reports*, 6(June):1–6, 2016. ISSN 20452322. doi: 10.1038/srep29627. URL http://dx.doi.org/10.1038/srep29627.

[114] Elad Pollak, Gregory Salitra, Valentina Baranchugov, and Doron Aurbach. In situ conductivity, impedance spectroscopy, and ex situ Raman spectra of amorphous silicon during the insertion/extraction of lithium. *Journal of Physical Chemistry C*, 111(30):11437–11444, 2007. ISSN 19327447. doi: 10.1021/jp0729563.

[115] Carlos M Portela, Julia R Greer, and Dennis M Kochmann. Impact of node geometry on the effective stiffness of non-slender three-dimensional truss lattice architectures. *Extreme Mechanics Letters*, 22:110–138, 2018. ISSN 2352-4316. doi: 10.1016/j.eml.2018.06.004. URL https://doi.org/10.1016/j.eml.2018.06.004.

[116] E. Ramm and W. A. Wall. Shell structures - A sensitive interrelation between physics and numerics. *International Journal for Numerical Methods in Engineering*, 60(1):381–427, 2004. ISSN 00295981. doi: 10.1002/nme.967.

[117] Ladan Salari-Sharif and Lorenzo Valdevit. Accurate Stiffness Measurement of Ultralight Hollow Metallic Microlattices by Laser Vibrometry. *Experimental Mechanics*, 54(8):1491–1495, 2014. ISSN 17412765. doi: 10.1007/s11340-014-9917-8.

[118] Tobias A. Schaedler, Alan J. Jacobsen, A. Torrents, a. E. Sorensen, J. Lian, Julia R. Greer, Lorenzo Valdevit, and W. B. Carter. Ultralight Metallic Microlattices. *Science*, 334(6058):962–965, nov 2011. ISSN 0036-8075. doi: 10.1126/science.1211649. URL http://www.sciencemag.org/cgi/doi/10.1126/science.1211649.

[119] W. Schill, S. Heyden, S. Conti, and M. Ortiz. The anomalous yield behavior of fused silica glass. *Journal of the Mechanics and Physics of Solids*, 113:105–125, 2018. ISSN 00225096. doi: 10.1016/j.jmps.2018.01.004. URL https://doi.org/10.1016/j.jmps.2018.01.004.

[120] Almut Schroer, Jeffrey M. Wheeler, and Ruth Schwaiger. Deformation behavior and energy absorption capability of polymer and ceramic-polymer composite microlattices under cyclic loading. *Journal of Materials Research*, 33(03):274–289, 2018. ISSN 0884-2914. doi: 10.1557/jmr.2017.485.

[121] N Silvestre. International Journal of Solids and Structures Buckling behaviour of elliptical cylindrical shells and tubes under compression. *International Journal of Solids and Structures*, 45(16):4427–4447, 2008. ISSN 00207683. doi: 10.1016/j.ijsolstr.2008.03.019.

[122] A.E. Simone and L.J. Gibson. Effects of solid distribution on the stiffness and strength of metallic foams. *Acta Materialia*, 46(6):2139–2150, 1998. ISSN 13596454. doi: 10.1016/S1359-6454(97)00421-7.

[123] Roman Süsstrunk and Sebastian D Huber. Observation of phononic helical edge states in a mechanical topological insulator. *Science*, 349(6243):47 LP – 50, jul 2015. doi: 10.1126/science.aab0239. URL http://science.sciencemag.org/content/349/6243/47.abstract.

[124] Roman Süsstrunk and Sebastian D. Huber. Classification of topological phonons in linear mechanical metamaterials. *Proceedings of the National Academy of Sciences*, 113(33):E4767–E4775, aug 2016. ISSN 0027-8424. doi: 10.1073/pnas.1605462113. URL http://arxiv.org/abs/1604.01033{%}0Ahttp://dx.doi.org/10.1073/pnas.1605462113http://www.pnas.org/lookup/doi/10.1073/pnas.1605462113.

[125] A. Sydney Gladman, Elisabetta A. Matsumoto, Ralph G. Nuzzo, L. Mahadevan, and Jennifer A. Lewis. Biomimetic 4D printing. *Nature Materials*, 15 (4):413–418, 2016. ISSN 14764660. doi: 10.1038/nmat4544.

[126] Thomas Tancogne-Dejean and Dirk Mohr. Elastically-isotropic elementary cubic lattices composed of tailored hollow beams. *Extreme Mechanics Letters*, 22:13–18, 2018. ISSN 23524316. doi: 10.1016/j.eml.2018.04.005. URL https://doi.org/10.1016/j.eml.2018.04.005.

[127] Thomas Tancogne-Dejean, Adriaan B. Spierings, and Dirk Mohr. Additively-manufactured metallic micro-lattice materials for high specific energy absorption under static and dynamic loading. *Acta Materialia*, 116:14–28, 2016. ISSN 13596454. doi: 10.1016/j.actamat.2016.05.054. URL http://linkinghub.elsevier.com/retrieve/pii/S1359645416304153.

[128] Thomas Tancogne-Dejean, Marianna Diamantopoulou, Maysam B. Gorji, Colin Bonatti, and Dirk Mohr. 3D Plate-Lattices: An Emerging Class of Low-Density Metamaterial Exhibiting Optimal Isotropic Stiffness. *Advanced Materials*, 30(45):1803334, nov 2018. ISSN 09359648. doi: 10.1002/adma.201803334. URL http://doi.wiley.com/10.1002/adma.201803334.

[129] Xin Tang, Vikas Prakash, John J. Lewandowski, Gregory W. Kooistra, and Haydn N G Wadley. Inertial stabilization of buckling at high rates of loading and low test temperatures: Implications for dynamic crush resistance of aluminum-alloy-based sandwich plates with lattice core. *Acta Materialia*, 55 (8):2829–2840, 2007. ISSN 13596454. doi: 10.1016/j.actamat.2006.12.037.

[130] H. C. Tankasala, Vikram S. Deshpande, and Norman A. Fleck. Tensile response of elastoplastic lattices at finite strain. *Journal of the Mechanics and Physics of Solids*, 109:307–330, 2017. ISSN 00225096. doi: 10.1016/j.jmps.2017.02.002.

[131] Ottman A. Tertuliano and Julia R. Greer. The nanocomposite nature of bone drives its strength and damage resistance. *Nature Materials*, 15(11):1195–1202, 2016. ISSN 14764660. doi: 10.1038/nmat4719.

[132] S. Timoshenko and J.N. Goodier. *Theory of elasticity*. McGraw-Hill, New York, 1969.

[133] Norio Tsujioka, Norio Ishizuka, Nobuo Tanaka, Takuya Kubo, and Ken Hosoya. Well-controlled 3D skeletal epoxy-based monoliths obtained by polymerization induced phase separation. *Journal of Polymer Science Part A: Polymer Chemistry*, 46(10):3272–3281, may 2008. ISSN 0887624X. doi: 10.1002/pola.22665. URL http://doi.wiley.com/10.1002/pola.22665.

[134] Lorenzo Valdevit, Scott W. Godfrey, Tobias a. Schaedler, Alan J. Jacobsen, and William B. Carter. Compressive strength of hollow microlattices: Experimental characterization, modeling, and optimal design. *Journal of Materials Research*, 28(17):2461–2473, 2013. ISSN 0884-2914. doi: 10.1557/jmr.2013.160. URL http://www.journals.cambridge.org/abstract{_}S088429141300160X.

[135] David Veysset, Alex J Hsieh, Steven Kooi, Alexei A Maznev, Kevin A Masser, and Keith A Nelson. Dynamics of supersonic microparticle impact on elastomers revealed by real-time multi-frame imaging. *Scientific Reports*, 6(1):25577, jul 2016. ISSN 20452322. doi: 10.1038/srep25577. URL http://dx.doi.org/10.1038/srep25577http://www.nature.com/articles/srep25577.

[136] Thomas Vidil, Nicholas Hampu, and Marc A. Hillmyer. Nanoporous Thermosets with Percolating Pores from Block Polymers Chemically Fixed above the Order–Disorder Transition. *ACS Central Science*, 3(10):1114–1120, oct 2017. ISSN 2374-7943. doi: 10.1021/acscentsci.7b00358. URL http://pubs.acs.org/doi/10.1021/acscentsci.7b00358.

[137] A Vidyasagar, S Krödel, and D M Kochmann. Microstructural patterns with tunable mechanical anisotropy obtained by simulating anisotropic spinodal decomposition. *Proceedings of the Royal Society A: Mathematical, Physical and Engineering Science*, 474(2218):20180535, 2018. ISSN 1364-5021. doi: 10.1098/rspa.2018.0535. URL http://rspa.royalsocietypublishing.org/lookup/doi/10.1098/rspa.2018.0535.

[138] Andrea Vigliotti, Vikram S. Deshpande, and Damiano Pasini. Non linear constitutive models for lattice materials. *Journal of the Mechanics and Physics of Solids*, 64(1):44–60, 2014. ISSN 00225096. doi: 10.1016/j.jmps.2013.10.015. URL http://dx.doi.org/10.1016/j.jmps.2013.10.015.

[139] Andrey Vyatskikh, Stéphane Delalande, Akira Kudo, Xuan Zhang, Carlos M. Portela, and Julia R. Greer. Additive manufacturing of 3D nano-architected metals. *Nature Communications*, 9(1):593, 2018. ISSN 2041-1723. doi: 10.1038/s41467-018-03071-9. URL http://www.nature.com/articles/s41467-018-03071-9.

[140] Pai Wang, Filippo Casadei, Sicong Shan, James C. Weaver, and Katia Bertoldi. Harnessing buckling to design tunable locally resonant acoustic metamaterials. *Physical Review Letters*, 113(1):1–5, 2014. ISSN 10797114. doi: 10.1103/PhysRevLett.113.014301.

[141] Franziska Warmuth, Maximilian Wormser, and Carolin Körner. Single phase 3D phononic band gap material. *Scientific Reports*, 7(1):1–7, 2017. ISSN 20452322. doi: 10.1038/s41598-017-04235-1.

[142] Ulrike G.K. Wegst, Hao Bai, Eduardo Saiz, Antoni P. Tomsia, and Robert O. Ritchie. Bioinspired structural materials. *Nature Materials*, 14(1):23–36, 2015. ISSN 14764660. doi: 10.1038/nmat4089.

[143] Weidong Wu, Joseph Owino, Ahmed Al-Ostaz, and Liguang Cai. Applying Periodic Boundary Conditions in Finite Element Analysis. *Simulia Community Conference*, pages 707–719, 2014.

[144] Xiaoxing Xia, A. Afshar, Heng Yang, Carlos M. Portela, Dennis M. Kochmann, Claudio V. Di Leo, and Julia R. Greer. Electrochemically Reconfigurable Architected Materials. *Under Review*, 2019.

[145] Zhenyu Xue and John W. Hutchinson. A comparative study of impulse-resistant metal sandwich plates. *International Journal of Impact Engineering*, 30(10):1283–1305, 2004. ISSN 0734743X. doi: 10.1016/j.ijimpeng.2003.08.007.

[146] Hyunwoo Yuk, Teng Zhang, German Alberto Parada, Xinyue Liu, and Xuanhe Zhao. Skin-inspired hydrogel-elastomer hybrids with robust interfaces and functional microstructures. *Nature Communications*, 7(May):1–11, 2016. ISSN 20411723. doi: 10.1038/ncomms12028. URL http://dx.doi.org/10.1038/ncomms12028.

[147] Christian J. Yungwirth, Haydn N.G. Wadley, John H. O'Connor, Alan J. Zakraysek, and Vikram S. Deshpande. Impact response of sandwich plates with a pyramidal lattice core. *International Journal of Impact Engineering*, 35(8):920–936, aug 2008. ISSN 0734743X. doi: 10.1016/j.ijimpeng.2007.07.001. URL https://linkinghub.elsevier.com/retrieve/pii/S0734743X07001170.

[148] Alex J. Zelhofer and Dennis M. Kochmann. On acoustic wave beaming in two-dimensional structural lattices. *International Journal of Solids and Structures*, 115-116:248–269, 2017. ISSN 00207683. doi: 10.1016/j.ijsolstr.2017.03.024.

[149] Guoqi Zhang, Bing Wang, Li Ma, Jian Xiong, and Linzhi Wu. Response of sandwich structures with pyramidal truss cores under the compression and impact loading. *Composite Structures*, 100:451–463, 2013. ISSN 02638223. doi: 10.1016/j.compstruct.2013.01.012.

[150] Huigang Zhang and Paul V. Braun. Three-dimensional metal scaffold supported bicontinuous silicon battery anodes. *Nano Letters*, 12(6):2778–2783, 2012. ISSN 15306984. doi: 10.1021/nl204551m.

[151] Lei Zhang, Stefanie Feih, Stephen Daynes, Shuai Chang, Michael Yu Wang, Jun Wei, and Wen Feng Lu. Energy absorption characteristics of metallic triply periodic minimal surface sheet structures under compressive loading. *Additive Manufacturing*, 23(August):505–515, 2018. ISSN 22148604. doi: 10.1016/j.addma.2018.08.007. URL https://doi.org/10.1016/j.addma.2018.08.007.

[152] Xuan Zhang, Andrey Vyatskikh, Huajian Gao, Julia R. Greer, and Xiaoyan Li. Lightweight, flaw-tolerant, and ultrastrong nanoarchitected carbon. *Proceedings of the National Academy of Sciences*, page 201817309, 2019. ISSN 0027-8424. doi: 10.1073/pnas.1817309116. URL http://www.pnas.org/lookup/doi/10.1073/pnas.1817309116.

[153] Xiaoyu Zheng, Howon Lee, Todd H. Weisgraber, Maxim Shusteff, Joshua DeOtte, Eric B Duoss, Joshua D Kuntz, Monika M Biener, Qi Ge, Julie A. Jackson, Sergei O Kucheyev, Nicholas X. Fang, and Christopher M. Spadaccini. Ultralight, ultrastiff mechanical metamaterials. *Science*, 344(6190):1373–1377, jun 2014. ISSN 0036-8075. doi: 10.1126/science.1252291. URL http://www.sciencemag.org/cgi/doi/10.1126/science.1252291.

[154] Xiaoyu Zheng, William Smith, Julie Jackson, Bryan Moran, Huachen Cui, Da Chen, Jianchao Ye, Nicholas Fang, Nicholas Rodriguez, Todd Weisgraber, and Christopher M. Spadaccini. Multiscale metallic metamaterials. *Nature Materials*, 15(10):1100–1106, oct 2016. ISSN 1476-1122. doi: 10.1038/nmat4694. URL http://www.nature.com/doifinder/10.1038/nmat4694http://www.nature.com/articles/nmat4694.

[155] Ning Zhou, Frank S. Bates, and Timothy P. Lodge. Mesoporous membrane templated by a polymeric bicontinuous microemulsion. *Nano Letters*, 6(10):2354–2357, 2006. ISSN 15306984. doi: 10.1021/nl061765t.

Appendix A

SUPPLEMENTARY VIDEOS

The following supplementary videos are included:

CHAPTER 4

Video 1: `V1_Col[001]_t11nm_x50.mp4`
3-Cycle compression of 11-nm columnar sample along the [001] direction at ×50 playback speed.

Video 2: `V2_Iso[001]_t11nm_x50.mp4`
3-Cycle compression of 11-nm isotropic sample along the [001] direction at ×50 playback speed.

Video 3: `V3_Lam[001]_t11nm_x50.mp4`
3-Cycle compression of 11-nm lamellar sample along the [001] direction at ×50 playback speed.

Video 4: `V4_Lam[010]_t11nm_x50.mp4`
3-Cycle compression of 11-nm lamellar sample along the [010] direction at ×50 playback speed.

Video 5: `V5_Col[001]_t44nm_x50.mp4`
3-Cycle compression of 44-nm columnar sample along the [001] direction at ×50 playback speed.

Video 6: `V6_Col[100]_t44nm_x50.mp4`
3-Cycle compression of 44-nm columnar sample along the [100] direction at ×50 playback speed.

Video 7: `V7_Iso[001]_t44nm_x50.mp4`
3-Cycle compression of 44-nm isotropic sample along the [001] direction at ×50 playback speed.

Video 8: `V8_Lam[100]_t44nm_x50.mp4`
3-Cycle compression of 44-nm lamellar sample along the [100] direction at ×50 playback speed.

Video 9: `V9_Lam[010]_t44nm_x50.mp4`
3-Cycle compression of 44-nm lamellar sample along the [010] direction at ×50 playback speed.

Video 10: `V10_Col[001]_t168nm_x20.mp4`
3-Cycle compression of 168-nm columnar sample along the [001] direction at ×20 playback speed. Nanoindenter reached load limit prior to failure, so loading is purely elastic.

Video 11: `V11_Col[100]_t168nm_x20.mp4`
1-Cycle compression of 168-nm columnar sample along the [100] direction at ×20 playback speed. Catastrophic failure.

Video 12: `V12_Iso[001]_t168nm_x20.mp4`
3-Cycle compression of 168-nm isotropic sample along the [001] direction at ×20 playback speed. Nanoindenter reached load limit prior to failure, so loading is purely elastic.

Video 13: `V13_Lam[100]_t168nm_x50.mp4`
3-Cycle compression of 168-nm lamellar sample along the [100] direction at ×50 playback speed. Failure of shell but no catastrophic collapse.

Video 14: `V14_Lam[010]_t168nm_x20.mp4`
1-Cycle compression of 168-nm lamellar sample along the [010] direction at ×20 playback speed. Catastrophic failure.

Video 15: `V15_Col[001]vsOctet[001]_t11nm_x124.mp4`
Side-by-side 10-cycle compression of 11-nm columnar and $5 \times 5 \times 5$ *octet samples along the [001] direction at ×124 playback speed.*

Chapter 6

Video 16: `V16_SiO2Si_v514_vr339.mp4`
Impact of SiO_2 *particle onto a Si substrate at* $v_0 = 514$ *m/s with a rebound velocity of* $v_r = 339$ *m/s.*

Video 17: `V17_SiO2Si_v646_vrshattered.mp4`
Impact of SiO_2 *particle onto a Si substrate at* $v_0 = 646$ *m/s and shattering upon impact.*

Video 18: `V18_TkC17_v44_vr23.mp4`
Elastic impact of SiO_2 *particle onto* $\overline{\rho} \approx 17\%$ *tetrakaidecahedron carbon nanolattice at* $v_0 \approx 44$ *m/s and rebounding at* $v_r \approx 23$ *m/s. At low velocities these measured speeds are just an estimate, since the uncertainty is inversely related to the speed. No damage was observed, implying the actual rebound speed must be closer to 44 m/s.*

Video 19: `V19_TkC17_v238_vr50.mp4`
Impact of SiO_2 *particle onto* $\overline{\rho} \approx 17\%$ *tetrakaidecahedron carbon nanolattice at* $v_0 = 238$ *m/s and rebounding at* $v_r = 50$ *m/s exhibiting cratering and ejecta.*

Video 20: `V20_TkC17_v676_vrEmbedded.mp4`
Impact of SiO_2 particle onto $\overline{\rho} \approx 17\%$ tetrakaidecahedron carbon nanolattice at $v_0 = 676$ m/s exhibiting particle embedding and minor ejecta.

Video 21: `V21_BlastOctet_Side.mp4`
High-speed camera video capturing blast detonation onto a carbon octet-core sandwich plate with $300\,\mu m$ *stainless steel face sheets. The carbon octet core had a density of* $\rho = 285 \pm 9$ *kg/m*^{3}.

Video 22: `V22_BlastCompOctet_Side.mp4`
High-speed camera video capturing blast detonation onto a carbon-epoxy octet composite core sandwich plate with $300\,\mu m$ *stainless steel face sheets. The composite core had a density of* $\rho = 1130 \pm 4$ *kg/m*^{3}.

Video 23: `V23_ControlSS_2D_DIC_15fps.mp4`
2D DIC of the control sandwich plate (face sheets clamped together) showing significant plastic deformation on the top sheet.

Video 24: `V24_BlastCarbon_3D_DIC.mp4`
3D DIC of the carbon octet-core sandwich plate's top sheet.

Video 25: `V25_BlastComp_3D_DIC.mp4`
3D DIC of the composite octet-core sandwich plate's top sheet.